UNIVERSITAT POLITÈCNICA DE VALÈNCIA

DEPARTAMENTO DE COMUNICACIONES

Doctoral Dissertation

FULL-WAVE CHARACTERIZATION OF BI-DIMENSIONAL CAVITIES AND ITS APPLICATION TO THE DESIGN OF WAVEGUIDE FILTERS AND MULTIPLEXERS

Carlos Carceller Candau

Advisors:
Dr. Vicente E. Boria Esbert (Universitat Politècnica de València)
Dr. Jordi Gil Raga (Aurora Software and Testing)
Dr. Pablo Soto Pacheco (Universitat Politècnica de València)

Dissertation submitted to the Departamento de Comunicaciones, in partial fulfillment of the requirements for:
Título de Doctor por la Universitat Politècnica de València
Valencia, March 2016

Agradecimientos

A pesar de las dudas iniciales que tenía sobre cual podía ser mi aportación a un mundo tan estudiado como el de los dispositivos de microondas en guía de onda, considero que la decisión de realizar esta tesis ha sido todo un acierto. La colaboración entre la Universidad Politécnica de Valencia y la empresa de base tecnológica Aurorasat ha permitido enfrentarme a problemas de interés científico, pero que a su vez tienen aplicación práctica directa en la industria. Agradezco enormemente a Vicente Boria por haber hecho posible esta colaboración, haberme animado a embarcarme en ella y confiado en que la llevaría a cabo con éxito. Sin su liderazgo y tenacidad, esta tesis no hubiera sido posible.

Durante el desarrollo de la misma he tenido la gran suerte de contar con dos valiosos mentores, como son Jordi Gil y Pablo Soto. Para mí han sido toda una referencia tanto profesional como personal. Han sabido orientarme en momentos críticos, y su implicación ha sido total desde el primer momento. Gran parte de lo que he aprendido durante todos estos años sobre electromagnetismo y diseño de componentes de microondas se lo debo a ellos. Sin duda, este trabajo no hubiera tenido la misma calidad sin sus innumerables aportaciones.

Por otro lado, también quisiera reconocer la contribución de otras personas por las que tengo gran admiración. A Carlos Vicente, por plantar algunas de las semillas que han dado lugar a esta tesis, así como por las enriquecedoras discusiones que hemos tenido todo este tiempo y el apoyo que me ha brindado. También a Santiago Cogollos, que me introdujo en el mundo BI-RME y la teoría de filtros, y que siempre ha me ha prestado una valiosa ayuda cuando lo he necesitado.

Por supuesto, debo agradecer a Marco Guglielmi por permitirme explorar algunas de sus innovadoras ideas sobre filtros HFRW, y a la Prof. Kawthar Zaki por acogerme en su laboratorio de la University of Maryland. Asímismo, a mis compañeros de Aurorasat y el GAM, con los que he compartido muy buenos momentos.

Por último, a mi familia por todo su apoyo. Su confianza en mi capacidad para llevar a cabo esta tesis ha sido de gran ayuda para seguir adelante. A mis amigos y *brothers*, por estar ahí siempre. Y a Ellen, por todos los ánimos que me ha dado, en especial a la hora de escribir.

Con esta tesis se cierra un capítulo de mi vida y se abre uno nuevo. Espero que, sea donde sea, sigamos colaborando durante muchos años.

Carlos Carceller

Abstract

Modern communications systems impose stringent requirements on the equipment that operates at microwave frequency, especially in the case of wireless communications. The design of passive components for these applications is contingent upon the availability of accurate electromagnetic (EM) modeling tools that can efficiently handle the complex geometry of these components. Despite the widespread use of mesh-based general-purpose computer-aided engineering (CAE) tools to perform final design verifications, their application during the optimization process is limited. Optimum designs require a large number of simulations, which are computationally expensive when performed by general purpose tools. Instead, microwave designers prefer to employ faster software tools tailored to specific geometries, such as waveguide components, ferromagnetic devices, multilayer planar structures, etc. Therefore, the development of faster and more efficient specialized EM tools has a direct impact on the design of microwave components, both quantitatively and qualitatively. Increasingly complex geometries are modeled more accurately, and may be incorporated into novel designs without penalizing development time and its associated costs. By doing so, passive components become more advanced and are able to fulfill stricter requirements. At the same time, new research and development opportunities arise in order to address the challenges posed by these advanced structures.

The present PhD thesis is focused on a specific type of waveguide cavity geometry: bi-dimensional structures of arbitrary shape. Most microwave components based on rectangular waveguides include these elements (bends, T-junctions, tapers, power-dividers, etc.), thus the scope of this work is wide. To characterize these structures, an efficient full-wave modal formulation is developed. Taking into account common properties of bi-dimensional structures, such as its electromagnetic symmetry, the resulting technique is very efficient and accurate. Thanks to the integration of this formulation into a CAE tool, a designer is able to solve complex systems that combine this type of element with components of vastly different shapes.

The developed formulation is first applied to the analysis and design of passive components, such as filters, multiplexers and orthomode transducers. These

examples are employed to validate the results, as well as to demonstrate the improvement that the proposed analysis technique represents over well-known commercial EM packages. Likewise, this formulation is combined with the commercial tool SPARK3D to predict RF breakdown (multipactor and corona) in selected bi-dimensional structures.

Then, novel implementations of waveguide quasi-elliptic filters, based on the interconnection of bi-dimensional cavities, are proposed. Special attention is paid to the realization of multiple transmission zeros (TZs) with tuning-less compact structures. First, a novel family of filters, known as hybrid-folded rectangular waveguide (HFRW) structures, is studied. Simple and flexible methods to prescribe the location of the transmission zeros realized by these structures are presented. Practical aspects related to their physical implementation are also discussed. Secondly, a compact and purely capacitive obstacle, capable of realizing multiple TZs, is presented and discussed. In both cases, multiple examples are given to illustrate the step-by-step process involved in the design of these structures.

Finally, a systematic procedure for the design of wideband manifold-coupled multiplexers is proposed. To avoid the generation of undesired resonances, stubs that connect the filters to the manifold are removed. Likewise, the manifold length is kept as short as possible. Following a simple step-by-step procedure, based on analytical formulas and EM simulations, a good starting point for the final optimization of these structures is obtained. Ultimately, all of the technology and developments presented in this PhD thesis converge into the design of a wideband quadruplexer for passive intermodulation measurements at C-band.

Resumen

En la actualidad, los sistemas de comunicaciones imponen unos requisitos muy estrictos sobre el equipamiento en la banda de microondas. El diseño de estos componentes está supeditado, muchas veces, a la disponibilidad de herramientas de modelado electromagnético (EM) que sean capaces de analizar geometrías complejas. A pesar del amplio uso de herramientas CAE (en inglés, computer-aided engineering) de propósito general para la verificación final de prototipos, su posible aplicación durante el proceso de diseño es limitada. Los diseños óptimos exigen realizar una gran cantidad de simulaciones EM. Dado que las simulaciones con estas técnicas tienen un alto coste computacional, los diseñadores suelen optar por emplear herramientas software especializadas en las estructuras que diseñan, ya sean componentes en guía de onda, dispositivos ferromagnéticos, estructuras planares multicapa, etc. Por tanto, el desarrollo de nuevas herramientas más precisas y eficientes ayudará a reducir el tiempo de diseño de estos productos, y con ello los costes asociados. Además, permitirá abrir nuevas líneas de investigación para responder a los retos que plantean geometrías cada vez más complejas.

Esta tesis se centra en el desarrollo de una herramienta de análisis EM para un tipo muy concreto de estructuras. Se trata de cavidades bidimensionales, con independencia de la forma que tengan. Es habitual encontrar este tipo de estructuras en la mayoría de componentes implementados en guía rectangular (codos, uniones en T, divisores de potencia, etc). Por tanto, el rango de aplicación de la teoría desarrollada en esta tesis es muy amplio. En concreto, se ha desarrollado una nueva formulación basada en métodos modales que permite realizar una caracterización de onda completa de estas estructuras de forma eficiente y precisa. Al aprovechar su simetría geométrica y electromagnética, la herramienta desarrollada puede minimizar los cálculos a realizar, consiguiendo grandes velocidades de computación pero manteniendo una alta precisión. Gracias a la integración de esta formulación dentro de una herramienta CAE basada en métodos modales, se ofrece la posibilidad a los diseñadores de resolver sistemas muy complejos que combinan este tipo de cavidades con otros componentes de geometrías distintas.

Esta formulación se aplica, en primer lugar, al análisis y diseño de componentes pasivos comunes, tales como filtros, multiplexores y transductores ortomodales.

Estos ejemplo sirven para validar la herramienta desarrollada, así como demostrar la significativa mejora que supone el uso de esta nueva técnica con respecto a otros paquetes software de análisis electromagnético. Asímismo, al combinar esta formulación con la herramienta SPARK3D se abre la posibilidad de predecir la aparición de fenómenos de descarga de alta potencia (multipactor y corona) en determinadas estructuras bidimensionales.

Seguidamente, se proponen nuevas formas de implementar filtros cuasi-elípticos basados en la interconexión de cavidades bi-dimensionales. Se hace especial hincapié en la realización de múltiples ceros de transmisión mediante estructuras compactas que no requieran sintonía. Por una parte se estudian los filtros hybrid-folded rectangular waveguide (HFRW por sus siglas en inglés). Este trabajo incluye una discusión en profundidad sobre distintas implementaciones de este tipo de filtros. En ella se consideran aspectos prácticos relacionados con su uso e implementación física, que ofrecen al diseñador unos criterios claros para elegir la estructura que más se ajuste a sus especificaciones. Por otra parte se presenta un nuevo obstáculo de naturaleza capacitiva extremadamente compacto, que permite la realización de multiples ceros de transmisión incluso en estructuras "en línea". En ambos casos se incluyen ejemplos de aplicación y se describe, paso por paso, la metodología seguida para su diseño.

Finalmente, se expone un procedimiento sistemático para diseñar multiplexores de banda ancha. Para prevenir la generación de resonancias indeseadas (un problema habitual en este tipo de componentes) se evita, en la medida de lo posible, la interconexión de las diferentes partes mediante tramos de guía (stubs). Siguiendo una metodología simple, basada en fórmulas analíticas y simulaciones electromagnéticas, se consigue un excelente punto inicial para la última fase del diseño: la optimización. La tesis culmina aplicando todos los avances y la tecnología desarrollados al diseño de un cuadruplexor para medidas de intermodulación pasiva en banda C (4-8 GHz).

Resum

Els actuals sistemes de comunicacions sense fils imposen uns requisits molt estrictes sobre l'equipament de la banda de microones. El disseny d'aquests components està supeditat, moltes vegades, a la disponibilitat de ferramentes de modelatge electromagèntic (EM) que siguen capaços de gestionar geometries complexes. Tot i l'ampli ús de ferramentes CAE (del anglés, computer-aided engineering) de propòsit general per a la verificació final de prototips, la seua aplicació durant el procés de disseny és limitada. Els dissenys òptims exigeixen realitzar una gran quantitat de simulacions. Les simulacions amb aquestes tècniques tenen un alt cost computacional, per tant els dissenyadors solen optar per utilitzar ferramentes software especialitzades en les estructures que dissenyen, ja siguen components en guía d'ona, dispositius ferromagnètics, estructures planars multicapa, etc. Per tant, el desenvolupament de noves tècniques d'anàlisi més precises i eficients ajudarà a reduir el temps de desenvolupament d'aquests productes, així com dels seus costos associats. A més permetrà obrir noves línies d'investigació per respondre els reptes que plantegen geometries cada vegada més complexes.

Aquesta tesi es centra en el desenvolupament d'una ferramenta d'anàlisi EM per a un tipus molt concret d'estructures. Es tracta de cavitats bidimensionals, amb independència de la forma que tinguen. És habitual trobar aquestes estructures en la majoria de components implementats en guia rectangular. Per tant, el rang d'aplicació de la teoria presentada en esta tesi és molt ampli. En concret, s'ha desenvolupat una nova formulació basada en mètodes modals que permet realitzar una caracterització d'ona completa d'aquestes estructures de forma eficient i precisa. Aprofitant la seua simetria geomètrica i electromagnètica, la ferramenta desenvolupada pot minimitzar els càlculs a realitzar, aconseguint grans velocitats de càlcul però sempre mantenint una alta precisió. Gràcies a la integració d'aquesta formulació dins d'una ferramenta CAE basada en mètodes modals, s'ofereix la possibilitat als dissenyadors de resoldre sistemes molt complexos que combinen aquest tipus de cavitats amb altres components de diferent geometria.

Aquesta formulació s'aplica, en primer lloc, a l'anàlisi i disseny de components passius comuns, com ara filtres, multiplexors i transductors ortomodals. Aquests exemples serveixen per validar la ferramenta desenvolupada, així com demostrar

la significativa millora que suposa l'ús d'aquesta nova tècnica respecte d'altres paquets software d'anàlisi electromagnètic. Així mateix, mitjançant la combinació d'aquesta formulació amb la ferramenta SPARK3D s'obri la possibilitat de predir l'aparició de fenòmens de descàrrega d'alta potència (multipactor i corona) en estructures bidimensionals.

A continuació, es proposen noves formes d'implementar filtres quasi el.líptics en guia d'ona basats en la interconnexió de cavitats bidimensionals. Es fa especial èmfasi en la realització de múltiples zeros de transmissió mitjançant estructures compactes que no requereixen de sintonia. D'una banda s'estudien els filtres hybrid folded rectangular waveguide (HFRW per les sigles en anglès). Aquest treball inclou una discussió en profunditat sobre diferents implementacions d'aquest tipus de filtres. S'hi consideren aspectes pràctics relacionats amb el seu ús i implementació física, que ofereixen al dissenyador uns criteris clars per triar l'estructura que més s'ajuste a les seues especificacions. D'altra banda es presenta un nou obstacle de naturalesa capacitiva extremadament compacte, que permet la realització de múltiples zeros de transmissió fins i tot en estructures "en línia ". En els dos casos s'inclouen exemples d'aplicació i es descriu, pas per pas, la metodologia seguida per al seu disseny.

Finalment, s'exposa un procediment sistemàtic per dissenyar multiplexors de banda ampla. Per prevenir la generació de ressonàncies no desitjades, un problema que és habitual en aquest tipus de components, s'evita, en la mesura del possible, la interconnexió de les diferents parts mitjançant trams de guia (stubs). Seguint una metodologia simple, basada en fórmules analítiques i simulacions electromagnètiques, s'aconsegueix un excel.lent punt inicial per a l'última fase del disseny: l'optimització. La tesi culmina aplicant tots els avanços i la tecnologia desenvolupats al disseny d'un cuadruplexor per a mesures d'intermodulació passiva en banda C (4-8 GHz).

Contents

1 Introduction **1**
- 1.1 State of the art . . . 4
- 1.2 Objectives . . . 12
- 1.3 Thesis structure . . . 14

2 Full-wave characterization of bi-dimensional cavities **17**
- 2.1 Mode spectrum and expansion of electromagnetic fields . . . 18
  - 2.1.1 Electric field expansion . . . 21
  - 2.1.2 Magnetic field expansion . . . 22
  - 2.1.3 Application to bi-dimensional cavities . . . 23
  - 2.1.4 Convergence of the direct representation: Rectangular cavity 32
- 2.2 Hybrid field representation . . . 35
  - 2.2.1 Fields under LSE excitation . . . 38
  - 2.2.2 Fields under LSM excitation . . . 48
  - 2.2.3 Convergence of the hybrid representation: Rectangular cavity 56
- 2.3 GAM characterization . . . 57
  - 2.3.1 General Admittance Matrix for LSE modes . . . 59
  - 2.3.2 General Admittance Matrix for LSM modes . . . 60

3 Analysis, design and RF breakdown prediction **63**
- 3.1 Analysis and design of waveguide components . . . 64
  - 3.1.1 Inductive filter with rounded corners . . . 64
  - 3.1.2 Triplexer for PIM measurement setups . . . 67
  - 3.1.3 Narrowband taper/branching OMT . . . 69
  - 3.1.4 Wideband turnstile-junction OMT . . . 71
  - 3.1.5 Dual-band OMT . . . 73
- 3.2 High-power RF breakdown prediction . . . 76
  - 3.2.1 Lowpass filter . . . 77
  - 3.2.2 H-plane diplexer . . . 80

4 Novel quasi-elliptic filter implementations 83
4.1 Hybrid-folded rectangular waveguide filters . . . 85
4.1.1 Coupling mechanisms in HFRW filters . . . 88
4.1.2 Wideband modeling of HFRW trisections . . . 95
4.1.3 Design procedure for HFRW filters . . . 99
4.1.4 Physical implementation of HFRW filters . . . 106
4.1.5 Example: design of a five-pole four-TZ filter . . . 115
4.2 Practical implementation of capacitive irises with TZs . . . 120
4.2.1 Practical design examples . . . 124

5 Design of wideband manifold-coupled multiplexers 131
5.1 Wideband and narrowband multiplexer comparison . . . 132
5.2 Design methodology for wideband multiplexers . . . 136
5.2.1 First cycle . . . 138
5.2.2 Additional design cycles . . . 144
5.2.3 Example: design of a Ka-band triplexer . . . 145
5.3 Design of a quadruplexer for PIM measurement . . . 151
5.3.1 Channel filters . . . 152
5.3.2 Final design . . . 156

6 Conclusions and future work 161

A Transformation between LSE/LSM and TE/TM modes 167
A.1 Coupling between LSE and TE modes . . . 169
A.2 Coupling between LSE and TM modes . . . 169
A.3 Coupling between LSM and TE modes . . . 170
A.4 Coupling between LSM and TM modes . . . 170

B Derivation of the IE for the scalar potential 171
B.1 General Integral Equation . . . 171
B.2 Integral Equation for points on the contour . . . 173

C Singular Integrals 177
C.1 Fields under LSE excitation . . . 177
C.1.1 Singularity of $\mathbf{M}^F$ . . . 177
C.1.2 Singularity of $\mathbf{G}^F$ . . . 181
C.1.3 Singularity of $\mathbf{N}^F$ . . . 184
C.1.4 Singularity of $\mathbf{T}^F$ . . . 186
C.2 Fields under LSM excitation . . . 186
C.2.1 Singularity of $\mathbf{M}^A$ . . . 186
C.2.2 Singularity of $\mathbf{G}^A$ . . . 189
C.2.3 Singularity of $\mathbf{N}^A$ . . . 189
C.2.4 Singularity of $\mathbf{T}^A$ . . . 189

D Relationship between potentials and BI-RME modal currents 191
D.1 TE modes 191
D.2 TM modes 194

E Publications 195
E.1 Journal publications 195
E.2 Conference publications 196

Bibliography 199

Chapter 1

Introduction

Nowadays, global telecommunications services are experiencing large growth rates worldwide. In the last decades, the demand for capacity in these systems has escalated. At the same time, many of these services are moving towards wireless solutions. Given the excellent propagation properties of the atmosphere for signals in the microwave frequency range, the amount of microwave devices required to fulfill this remarkable demand has soared. Simultaneously, lack of standardization of key components (for instance, filters and multiplexers for satellite applications) and demand for custom-engineered products often force microwave engineers to start new designs almost from scratch. In a dynamic sector like the microwave industry, first-pass success (i.e. the ability to design, build, tune, and succeed on the first try) is highly sought after in order to reduce costs and improve product time to market [1]. To achieve this goal, research and development of more efficient computer-aided engineering (CAE) tools and advanced design procedures are fundamental. As will be shown, both topics have gone hand-in-hand throughout much of the microwave components history.

With the advent of radar systems in the 1940s, microwave components started to receive considerable interest. Radio frequencies employed until that point in time were low enough that circuits could be simply built with conventional lumped elements, such as coils and capacitors. However, as applications shifted to microwave frequencies, the implementation of passive devices with coils and capacitors became impractical, due to the small size of the components involved, radiation from two-wired lines and the large parasitic effects of the wiring, amongst other practical limitations.

At microwave frequencies, waveguides substituted the former two-wired line, cavity resonators replaced lumped LC elements and reactances became waveguide discontinuities. It was an important change in the design approach, since the distributed nature of the elements that formed the components had to be taken into

account. In those years when computers were not readily available, the design of passive components was aided by approximated closed-form expressions and synthesis techniques [2]. A major contribution was made by N. Marcuvitz, who compiled in his book [3] the equivalent-circuit parameters for a large number of microwave structures. The simple and elegant formulas contained in this publication, based on the solution of an integral-equation formulation of field problems [4] and experimental data, offered valuable insight on how to transform synthesized lumped-circuit elements into physical waveguide structures. An in-depth study of the main design procedures for microwave passive components is compiled in the well-known book by Matthaei, Young and Jones [5], published in the late years of this period. As can be seen there, the role of graphs and tables was predominant in those early years.

The space race and rapid development of commercial satellite communications in the 1960s and 1970s brought along numerous advances in the area of microwave components. To fulfill the increasing demand for these new systems, regulators were forced to move the allocated frequency band for satellites towards higher frequencies. Associated with the frequency shift, there were many technological challenges that had to be addressed. For example, filter requirements became more stringent, in terms of in-band linearity and out-of-band selectivity, which inspired the development of folded filters with transmission zeros (TZs) [6]. Size and mass of the components were severely limited for space applications. To minimize them, the implementation of filters that employ multiple degenerate modes in each cavity (nowadays known as dual-mode filters) was proposed [7, 8]. At the same time, the combination of contiguous channel filters in a single multiplexer was made possible thanks to the design of singly-terminated filters [9, 10]. These advances enabled the reduction, in half, of the number of antennas required to transmit and receive all channels, with a consequent reduction of the satellite mass and size [11].

Improvements in computational capacity and the increasing availability of time-shared mainframe computers prompted engineers to adopt more automated design approaches for filters and multiplexers. Early computer-aided design (CAD) tools can be traced back to this era [12–15]. One of the few commercially-available tools at the time was COMPACT (which stands for Computer Optimization of Microwave Passive and Active Circuits), since most CAD tools were developed in-house [16]. Typically, the analysis of microwave networks was based on a combination of lumped and distributed elements, that were cascaded using ABCD, impedance or admittance matrices [17]. As the complexity of the guided structures increased to meet more demanding specifications, filter design demanded more accurate analysis tools. It was during these two decades that the foundations for the numerical solution of Maxwell's equations (the basis of most modern commercial EM-field solver tools) were laid. For instance, the mode matching (MM) technique was first described by Wexler [18] in 1967, and a year later Harrington published his well-known book presenting the powerful Method of Moments

(MoM) [19]. General techniques for the solution of partial differential equations, such as the Finite Element Method (FEM) [20] and the Finite-Difference Time-Domain method (FDTD) [21] (although not known by that name at the time), were first applied to solve electromagnetic problems in the late 1960s. Likewise, in the early 1970s Johns and Beurle published a paper describing the solution of bi-dimensional scattering problems by the Transmission-Line Method (TLM) [22]. Some of these contributions came in the form of mathematical formulations, while others went a step further and even included computer programs that implemented some of the novel analysis methods. However, the popularization of these methods did not arrive until decades later.

In the 1980s and 1990s, the commercialization of UNIX workstations and the personal computer (PC) provided increasing resources in terms of availability, memory and computational capacity. Technology had evolved enough to support commercial versions of the CPU- and memory-intensive methods of the 1970s. For instance, popular EM solvers such as HFSS [23] and Sonnet [24] (currently used in many microwave designs) were first introduced to the public in the mid-1980s. Despite the great technological advances in computers and the automation of meshing algorithms, EM mesh-based methods were still not efficient enough to design most components of the 1980s. Instead, most analysis tools developed during this time were focused on specific and widely used structures that were commonly found in a large number of designs [25–29]. At the same time, these techniques were often combined with optimization routines in order to minimize the time devoted to the final tuning of the components [30–32].

This trend has continued over the last two decades, with computers taking a central role in the design of high-frequency components. Neural networks [33], genetic algorithms [34] or aggressive space mapping [35] are frequently combined with full-wave EM analysis tools to facilitate the design of complex components with a large amount of variables, combining several materials or with very stringent geometrical and mechanical specifications. At the same time, general purpose 3D EM simulators, such as Ansys' HFSS [23] or CST Microwave Studio [36], have evolved tremendously and, nowadays, they can be applied to model almost any component. However, their direct use in combination with gradient-based optimization techniques is still not recommended for large or sensitive structures, due to the excessive time required in each iteration. For complex waveguide components, the actual design is usually performed with full-wave simulators tailored to the specific structure (typically, modal-based simulators such as FEST3D [37], Microwave Wizard [38], WASP-NET [39], etc.) and then the final result is exported into a mesh-based simulator to perform the final verification.

As demonstrated, new developments in microwave devices have been frequently aided by advances in analysis and modeling tools. In the current digital era, the use of computers both to analyze and design modern microwave components is indeed fundamental. In this context, the present PhD thesis makes significant contribu-

tions in both areas: a very efficient EM simulation tool is first developed, and then applied to the design of filters and multiplexers for high-power applications.

1.1 State of the art

Electromagnetic problems, and also the analysis techniques used to solve them, can be classified according to the number of space variables upon which the field magnitudes depend:

- One-dimensional (1D) problems: The unknown magnitudes in these problems depend on one space dimension only. Typical examples are transmission-line problems, where the unknown to be determined is either the voltage or current along the transmission line.
- Two-dimensional (2D) problems: The objective in these problems is to find the unknowns defined in two space dimensions. Examples of these types of problems include the determination of the modal field patterns in waveguides, TE_{n0} propagation in rectangular waveguide structures and scattering from cylindrical obstacles.
- Three-dimensional (3D) problems: These are the most general problems, where the unknown field magnitudes and the excitations depend on the three space dimensions. Modern design of microwave components require the solution of these sort of problems. A particular case of 3D problems is the field computation in a 3D region where the excitation is confined to one or more planes. These problems are known as 2.5D problems, and are found in planar structures such as microstrip circuits or co-planar circuits.

The present PhD thesis deals with a specific type of 3D problems. The structures under study are metallic cavities that are constant in one space variable and have an arbitrary shape in the other two dimensions. Figure 1.1 depicts one of these cavities, which is constant along the $\hat{y}$ direction. The cavity can be interconnected to other elements through openings (known as ports) in the lateral walls. Throughout this thesis, these types of structures will be referred to as bi-dimensional cavities. Examples of bi-dimensional cavities include, amongst many others, bends, Y-junctions, compensated T-junctions, rat-race couplers, corrugated sections, inductive/capacitive windows and posts in rectangular cavities and tapers. When these cavities are connected with other waveguide and discontinuities, and all of them share the same constant dimension, the component is known as H-plane or E-plane (depending on the constant dimension and nature of the excitation). In those cases, the use of 2D techniques is possible[1]. Otherwise,

[1]For E-plane problems, the electromagnetic fields depend on three space variables. However, the dependence on one of these variables is analytical, therefore it is not an unknown of the problem. The core of the problem can be considered, effectively, 2D.

general components containing bi-dimensional cavities need to be solved by 3D analysis techniques to take into account all the interactions in the structure.

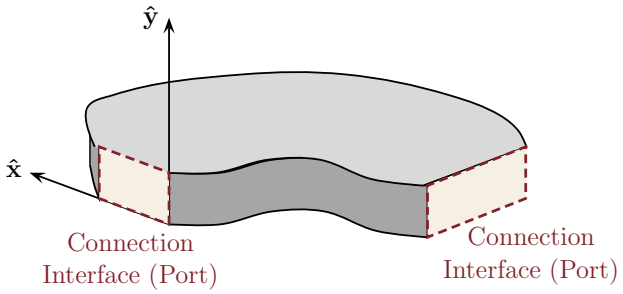

Figure 1.1: Example of a general bi-dimensional cavity.

The 3D analysis techniques implemented in modern CAD/CAE software tools can be classified in three groups: modal techniques, discretization techniques and hybrid techniques.

Modal techniques stem from the work by Wexler [18]. These techniques divide a microwave device in different regions or building blocks (typically, waveguides, planar discontinuities and cavities). They describe the electromagnetic field within each region as a superposition of modes, and characterize each building block by an equivalent multimode network representation (in terms of generalized impedance, admittance or scattering parameters). The resulting matrices model the interaction between the modes in the different regions, so the response from a complete component is computed by the interconnection of the matrices in all the regions. The main advantage of these techniques is that they are computationally very efficient and accurate, thus being ideal candidates to be the core analysis methods for CAD tools. This group of techniques has been widely used to analyze bi-dimensional cavities [40–43], since they can take full advantage of the electromagnetic properties of these structures. However, they do not offer as much flexibility as discretization techniques, and can only be applied to canonical shapes.

The second group of analysis techniques is based on the discretization of a certain electromagnetic magnitude (such as the electric field, the magnetic field or the surface current) that represents the unknown of the problem. This process is also called meshing, and requires the division of the geometry into a large number of small elements (1D segments, 2D triangles or 3D tetrahedra or hexahedra). Within each element, the unknown is assumed to have a linear dependence with a certain set of functions, known as basis functions. The discretization process transforms Maxwell's equations, along with the boundary conditions of the problem, into a linear system of equations. The solution of this system establishes the amplitude

and phase of the basis functions, thus providing an approximated representation of the electromagnetic field in each mesh element. Therefore, these techniques are suitable to analyze any 3D geometry. However, the accuracy of the results is entirely dependent on the density of the mesh, and how well it can be adapted to the geometry of the component (for instance, generating an accurate mesh for curved surfaces is a challenging task for these methods). Fine meshes generally provide more accurate results at the expense of larger computation times. However, the density of the mesh cannot be indefinitely increased. The maximum mesh size (in terms of number of elements) is limited by the available computational resources, especially memory. Likewise, mesh-based methods analyze structures as a whole, and do not permit the decomposition of a component into smaller parts. Thus, any change in the geometry of the structure (even if it is small) causes the algorithm to generate a new mesh for the complete geometry. For that reason, these methods are rarely used to design large and complex components, which require constant modifications of the geometry. Instead, they are widely applied at the end of the design cycle to verify the final result. Nowadays, the most frequently used discretization techniques are Finite Element Method (FEM), Finite Differences in Time Domain (FDTD) and Method of Moments (MoM). An in-depth study of these three methods can be found in [44]. Bi-dimensional cavities are suitable to be analyzed with any of these methods, and several examples can be found in the technical literature [45–51].

Hybrid approaches that combine several of the aforementioned techniques have also been proposed as a way to overcome the limitations of the individual techniques. For instance, the characterization of complex-shaped bi-dimensional cavities that require a large number of modes can benefit from the combination of the mode-matching technique with FEM [29, 52, 53].

Despite the maturity of the computational electromagnetics field, the efficient analysis of bi-dimensional cavities with arbitrary shape has not been properly addressed. Most publications propose very efficient algorithms that are only tailored to a few basic geometries [41, 54, 55]. Therefore, their scope of application is limited. Some methods are flexible enough to describe more arbitrary shapes [56, 57], but do not take full advantage of the 2D nature of the structure: the frequency dependence of the solution is not properly treated. As a result, these algorithms involve a large number of time-consuming operations per frequency point. Finally, formulations that perform the bulk of the computation independent of the analysis frequency [58, 59], are limited to certain excitations and, therefore, do not provide a full-wave representation. Moreover, they only allow the description of the contour in terms of straight segments. Thus, one of their main advantages (their efficiency to obtain very accurate results) is lost when analyzing cavities that include circular posts and rounded corners.

The main objective of this thesis is to contribute to the development of a hybrid analysis technique for bi-dimensional cavities that addresses most of these issues.

This technique combines the Boundary Integral - Resonant Mode Expansion (BI-RME) method [26] for waveguides with the Integral Equation technique developed by Okoshi and Miyoshi [60] for planar circuits. With the aid of a frequency transformation, the 3D problem can be divided into two independent 2D problems that, conveniently combined, provide an accurate full-wave representation.

The BI-RME method is a modal technique based on the solution of a boundary integral (BI) equation by the MoM that involves a two-dimensional dyadic Green's function. Instead of the free-space Green's function for two-dimensional domains, this method utilizes the Green's function of an auxiliary two-dimensional resonator. For efficiency purposes, this function is divided in two parts: a static term and a rapidly converging resonant mode expansion (RME). The expansion is expressed as a series involving the resonant modes of the auxiliary resonator (either a rectangular or circular waveguide). As a result, the EM problem is transformed into a linear eigenvalue problem of moderate size, amenable for a fast and accurate solution by standard linear algebra tools (for instance, LAPACK [61]). This method was originally applied to the determination of the modal chart and modal field patterns of arbitrarily-shaped waveguides with metal inserts composed of linear arcs [26]. Later, this formulation was improved in order to solve more accurately waveguides with increasingly complex contours [62]. In addition, the BI-RME method was expanded to consider 3D cavities of arbitrary shape [63], and rectangular cavities containing cylindrical metallic [64, 65] and dielectric elements [66].

The BI-RME method has also been used to analyze H-plane [67] and E-plane [68] cavities in the past. Making use of Kurokawa's field representation as an expansion of solenoidal and irrotational modes of the closed cavity [69], the authors obtained an adequate approximation for the Generalized Admittance Matrix (GAM) of a bi-dimensional cavity. Although this method has proven to be very efficient in the analysis of filters with simple inductive or capacitive windows, posts or metal sheets, its application to more complex structures is limited. The main limitation of these formulations is that they require the excitations to be located at a certain distance from the body of the cavity. This means using sections of rectangular waveguide with a considerable length to connect the excitations to the cavity. In practical cases, this reduced the scope of application of this methodology to components having only single-mode interactions between their different building blocks. Despite these limitations, the European Space Agency (ESA) funded a project to develop an EM software tool based on this application. It became known as ANAPLAN-W [70, 71].

To overcome the limitations of the original BI-RME formulation applied to bi-dimensional cavities, the same authors proposed years later to combine this formulation with the analysis methodology of planar circuits proposed by Okoshi [60]. As a result, two methods were successfully developed to analyze H-plane [59] and E-plane [58] cavities. Despite the considerable increase in the accuracy of the

analysis and the broader range of application of the new formulations, there were still some requirements that were not addressed:

1. The improved BI-RME formulations were completely based on the excitation of a limited number of modes. Components with a constant height could only be excited by the H-plane family of modes (this is, TE_{m0} modes), whereas constant-width components had to be excited by the E-plane family of modes (i.e., LSE_{1n} modes). Therefore, they could not be considered actual full-wave formulations, since they could only be applied to analyze components maintaining such symmetry throughout the entire structure. This meant that, for example, constant-width and constant-height blocks could not be interconnected in a single component.

2. The original formulation was focused on efficiently computing the GAM, in order to obtain the frequency response of the cavity. The computation of the electric and magnetic fields within the cavity was not considered. Nowadays, it is increasingly important to predict high-power failures (multipactor and corona) in microwave components [72–74]. Advanced prediction tools receive the electromagnetic fields as inputs [75]. Therefore it becomes critical for a modern full-wave analysis tool to generate these EM data.

3. The methods of [58, 59] required the contour of the bi-dimensional cavity to be described by a collection of straight segments. For eminently curved components, such as bends, rat-race couplers or cylindrical posts in rectangular cavities, the efficiency of the analysis decreased as the curved elements had to be approximated by many straight lines to increase the accuracy of results.

In this context, the present thesis will develop an efficient full-wave formulation for the analysis of bi-dimensional cavities. This new formulation will capitalize on the strengths of the improved ANAPLAN-W implementations, while simultaneously overcoming its main limitations. It will be based on the combination of the 2D version of the BI-RME method and the Okoshi formulation for planar circuits, but considering general excitations. The problem will be efficiently solved thanks to a frequency transformation that reduces the size of the problem and accelerates the computation of its solution. Both the frequency response and the electromagnetic fields will be provided. In addition to straight segments, the use of circular and elliptical arcs will be specifically considered.

The potential scope of application of this tool is very wide. Many waveguide structures include building blocks with one constant dimension (see Fig. 1.2). Due to its widespread use, specific analysis tools for the most common 2D building blocks can be found in the literature. Amongst others, we can mention rectangular irises [76, 77], posts [78–80], T-junctions with [81] and without [42] compensation posts, Y-junctions [82, 83], bends [56, 84, 85], tapered waveguides [86, 87],

waveguide steps [88, 89], branch-line couplers [90, 91], rat-races [92, 93] and power dividers [94, 95]. All these stand-alone blocks can be easily found in waveguide complex devices. For example, manifold-coupled multiplexers typically employ T-junctions to model the connection of filters to the manifold [96]. Alternative implementations of multiplexer manifolds have also been proposed, such as tapered guides [97] to aid in the spatial distribution of the different channels or Y-junctions [98,99] to cover wider frequency bands. The latter have also been used in the literature to implement circulators [100] and narrowband orthomode transducers (OMTs) [101, 102]. Wideband OMTs typically employ bends, tapered waveguides and directional couplers [103–105] or, alternatively, power dividers [106]. Likewise, numerous filters, from band-pass [107, 108] to low-pass [109–111], high-pass [112] and even band-stop [113] filters include bi-dimensional building blocks.

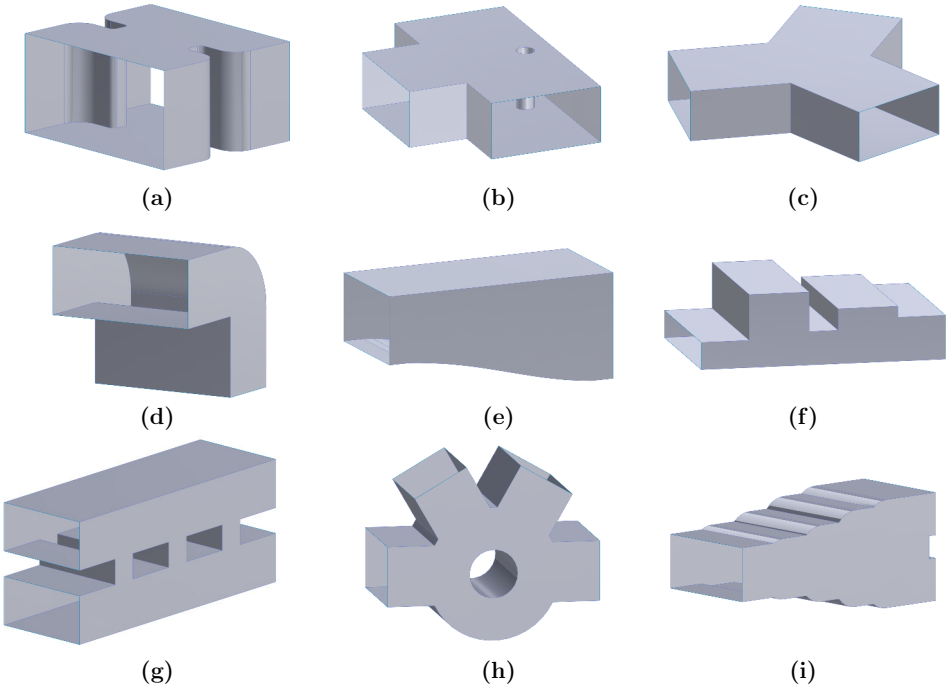

Figure 1.2: Some common building blocks. a) Inductive iris. b) Compensated T-junction. c) Y-junction. d) Bend. e) Tapered waveguide. f) Waveguide steps. g) Branch-line coupler. h) Rat-race. i) Power divider.

Given that this formulation will be integrated within a CAD tool for microwave components, this thesis will also consider its application to the design of two types of components:

- Quasi-elliptic filters.
- Wideband manifold-coupled multiplexers.

Firstly, quasi-elliptic filters, containing multiple transmission zeros (TZs) in their frequency response, will be studied. These filters are the preferred solution in applications that have strong isolation requirements at certain frequency bands. Typically, filters with TZs either use bandstop cavities to generate them (a method known as the extracted-pole technique [114]) or implement multiple signal paths by creating couplings between adjacent and non-adjacent resonators [115]. The former, combined with non-resonating nodes [116–118], becomes a highly modular procedure, but requires intense optimization to obtain the final physical dimensions. The latter often requires the ability to produce both electric and magnetic couplings, which may not be simple in some applications (for instance, high-power coaxial resonator filters), and normally produces a more intricate layout for the hardware to be manufactured. However, it is the most extended way of providing TZs in rectangular and circular waveguide filters. Furthermore, thanks to the creation of singlets [119], triplets and quadruplets [120,121] (i.e. low-order structures that introduce one or more TZs and can be cascaded with others to create higher-degree filters) the design of these types of filters has become highly modular as well.

The selection of a topology to implement the filter is one of the most important aspects of the design process. It determines the specific couplings that can be physically realized and the range of coupling levels that can be achieved. This has a direct influence on the type of response that can be implemented, especially in relation with the number of TZs and their location. The choice of an adequate topology is especially critical in tuning-less implementations, where the manufactured structure cannot be altered to compensate deviations in the physical dimensions. In these situations, low-order filters are preferred in order to improve sensitivity to manufacturing. Likewise, compact and simple structures, with a high degree of symmetry, are usual choices to facilitate its accurate and quick simulation and design with full-wave analysis tools, as well.

Hybrid Folded Rectangular Waveguide (HFRW) filters [122], like the one shown in Fig. 1.3, have been recently proposed as a robust alternative to classical cross-coupling configurations. One of the major strengths of this filter topology is its flexibility. It allows the designer to include as many resonators as required and physically arrange them in a variety of ways. This ensures an optimum utilization of the physical space available. At the same time, HFRW structures are able to provide large coupling levels between adjacent as well as non-adjacent resonators, which enables the generation of TZs in a wide frequency range. In addition, the structure is simple enough to be simulated considerably fast and is amenable to clam-shell manufacturing, which minimizes the insertion losses and the passive intermodulation (PIM) that may be generated. In this PhD thesis, the design of

this family of filters is investigated and a simple systematic design procedure is proposed. Moreover, different configurations are studied, and their capabilities, advantages and potential limitations are discussed at length.

Complementary to the design of HFRW filters, this PhD thesis also investigates a novel coupling window formed by a capacitive iris and several rectangular stubs, as a simple method for generating additional TZs without significantly increasing the number of resonators or the total length of the filter. This novel constant-width window, which can be used in a wide variety of filters including HFRW ones, is inspired by the work of Amari and Bornemann [123]. In that work, a stub is used to implement the filter input/output coupling window while simultaneously introducing a TZ. Although feasible, the window in [123] is not very practical, since it tends to be very large, spurring undesired resonances and limiting the range of coupling values that can be implemented. With the coupling window proposed in this thesis, almost any coupling window can be achieved while maintaining short stub lengths. In addition, multiple stubs can be connected in parallel, thus increasing the number of TZs implemented with the same coupling element.

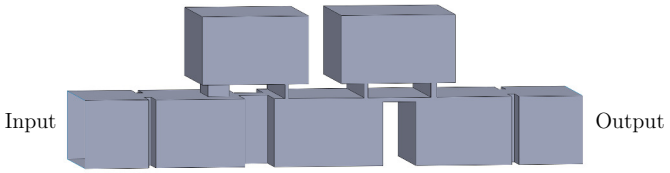

Figure 1.3: Structure of a fifth-order HFRW filter.

As a second CAD application, the design of tuning-less wideband multiplexers will be examined in this PhD thesis. Multiplexers are passive networks with multiple ports employed to separate or combine a number of radio frequency (RF) channels. These components are formed by the interconnection of a series of filters, each one assigned to extract one channel. A long waveguide, known as manifold, is typically used to interconnect the filters. If all the channels in the multiplexer cover more than 20% of the central frequency of operation, the multiplexer is known as wideband. If they cover less than 10%, they are usually referred to as narrowband. In contrast with their narrowband counterparts, wideband multiplexers have been developed to a much smaller extent.

Classical multiplexer design techniques [96, 102] assume a limited variation of the multiplexer reactance in the passband of any filter. Consequently, they are adequate in narrowband scenarios. However, a series of issues arise during the design of wideband multiplexers. The main one is due to the interaction between the different filters and the manifold, which is much stronger than in the narrowband case. Thus, undesired resonances are more problematic. In addition, they must be avoided in a wider frequency range. Another issue involves the physi-

cal implementation of the input coupling for each filter. The coupling structure must provide the high coupling level required and, at the same time, compensate for the frequency-dependent loading effect of adjacent filters. These two issues become more concerning as the number of channels increases. For that reason, most publications related to the design of wideband multiplexers are focused on diplexers [124–126]. As far as multiplexers are concerned, a manifold based on a cascade connection of Y-junctions for wideband applications has been proposed in [98], along with a tailored design technique. The solution requires interconnecting stubs and a bulky and intricate manifold (that can reduce the available coupling from the common port to the last channel filters). Also, a hybrid technique combining circuit models and full-wave simulations [127] has been proposed for multiplexers with a moderate bandwidth. However, none of these techniques provides a satisfactory solution, thus there is still demand for an efficient wideband multiplexer design technique. The present thesis contributes to this topic by proposing a simple systematic procedure that addresses most of the issues associated with this type of component.

1.2 Objectives

The main objective of the work in this thesis is the development of an efficient and rigorous analysis technique for the full-wave characterization of complex waveguide cavities that maintain one of its dimensions (either its width or height) constant, i.e. bi-dimensional cavities of arbitrary shape. This technique must take advantage of the electromagnetic symmetry of these types of discontinuities to solve the electric and magnetic fields in a fraction of the time that takes general-purpose numerical methods. It must provide the electromagnetic fields within the cavities under analysis, as well as their characterization in terms of the Generalized Admittance Matrix (GAM). Likewise, this tool must explicitly consider straight segments as well as circular and elliptical arcs, in order to describe the contour of the cavity under analysis.

After the development and implementation of this analysis technique it will be integrated in the EM solver FEST3D [37]. Given the possibilities that this software brings to the analysis and design of complete microwave components, this thesis will consider three specific topics, based on the implemented tool.

The first topic is the prediction of high-power breakdown levels in waveguide structures. In order to do so, the electromagnetic field obtained with this formulation is used as input of the prediction algorithm for high power phenomena implemented by SPARK3D [128]. This software models multipactor accurately thanks to the use of an electron tracking algorithm, along with an adequate secondary electron yield model. Corona, also known as gas discharge or arcing, is analyzed through the solution of the free electron density continuity equation by

means of the Finite Element method. The predicted threshold levels will be compared with measurements to validate the accuracy of the field computation.

A second area of interest is the design of HFRW filters. These components find wide application in low PIM and high-isolation environments. For that reason, they are ideally suited to implement the channel filters in PIM measurement setups. The design of this type of filter is greatly benefited from the use of an efficient analysis tool, since there can be many couplings of different natures (capacitive and inductive) placed close to each other. The number of modes in these structures is high, thus classical modal techniques tend to be relatively slow to provide convergent results. Regarding this class of filters, a simple design procedure will be provided and different implementations will be studied. To complement this topology of filters, a new coupling structure, based on the combination of stubs with capacitive windows, will be studied. With it, HFRW filters can increase the total number of TZs in the stopband without increasing the filter size significantly.

The third application involves the design of wideband manifold-coupled multiplexers. These components are generally used in PIM measurement setups. This thesis will present a systematic procedure for the critical stage of the design: the spacing of the filters along the manifold and initial adjustment of all the interconnections. This simple and fast methodology provides an adequate starting point for the successful optimization of wideband multiplexers. Specific issues associated with the design of multiplexers for wideband applications will be addressed.

In conclusion, the main objectives of the work in this thesis can be summarized as follows:

1. Development of a full-wave formulation to efficiently compute the electromagnetic fields within bi-dimensional cavities of arbitrary shape. The excitation of these cavities will be expressed as an expansion of modes in a rectangular waveguide. The shape of the cavity will be described by any combination of straight, circular and elliptical arcs defining a closed line. The case of multiple conductors within a cavity will also be considered.

2. Extension of the formulation to provide a circuit description of the cavity under analysis, in terms of the Generalized Admittance Matrix (GAM). This extension is required in order to generate the frequency response of complex passive devices that contain bi-dimensional cavities.

3. Validation and integration of this formulation with FEST3D. A variety of passive components featuring, predominantly, bi-dimensional structures will be analyzed. Results will be compared with measurements taken from the literature (when available), and otherwise with results from other commercial software tools such as Ansys' HFSS and CST Microwave Studio.

4. Application of the formulation, in combination with SPARK3D, to the prediction of RF breakdown: multipactor and corona thresholds.

5. Study of HFRW filters in different configurations. Proposal of specific implementations that allow the realization of multiple transmission zeros either in the upper or the lower stopbands.

6. Proposal of a new coupling window for rectangular waveguide filters that generates multiple transmission zeros and an adjustable coupling level.

7. Development of a design procedure for wideband multiplexers. Application of this procedure to the design of multiplexers with HFRW filters for Passive Intermodulation setups.

1.3 Thesis structure

The thesis is organized in six chapters. This first chapter has presented an overview of the topic developed within the framework of this thesis. A review of the methodologies currently used to analyze and design waveguide filters and multiplexers is given. The objectives set for this work are also presented. All this gives the reader a perspective into the strategic value of efficient computer-aided design (CAD) tools and methodologies in the context of modern passive microwave components.

Chapter 2 deals with the full-wave characterization of bi-dimensional cavities. It explains how to derive the electromagnetic field within any type of cavity as a series expansion of resonant modes, coupled to the sources of excitation in the contour of the cavity. This formulation is then particularized for the case of cavities having one constant dimension. As will be shown, the problem of determining the fields given a certain excitation can be split into two contributions: one for Longitudinal Section Electric (LSE) modes and another for Longitudinal Section Magnetic (LSM) modes. The field problems associated with each excitation can be solved independently. This chapter proposes a new and efficient methodology to solve these two problems. The novelty of proposed methodology is that it reduces the complexity of the analysis thanks to a proper frequency transformation. The EM fields under excitation of high-order modes can be derived directly from the fields associated with low-order modes, simply by evaluating them at particular frequencies. The low-order modes that this formulation employs are those typically involved in the solution of purely E-plane and H-plane cavities. Therefore, the proposed formulation can be directly applied to any numerical method dealing with E-plane and H-plane cavities. In the framework of this thesis, a hybrid method combining an Integral Equation for planar circuits with the BI-RME method for arbitrarily-shaped waveguides is employed to solve the partial E-plane and H-plane problems. The analysis capabilities of this method are also expanded. To increase its precision when dealing with structures that contain circular and elliptical contours, singular integrals associated with these segments are solved. In addition to its application to the computation of EM fields, this novel methodol-

ogy is also applied to efficiently compute the GAM of bi-dimensional cavities, at the end of the chapter.

Chapter 3 presents a series of components that are analyzed in order to validate the accuracy of the electromagnetic formulation developed in chapter 2. They cover a wide range of applications, from filters and multiplexers to orthodomode transducers. In some instances, measured data taken from the literature is employed to compare results. In other instances, the components are analyzed with commercial EM solvers for comparison.

Chapter 4 is focused on the study of quasi-elliptic filters. HFRW implementations offer great flexibility to choose the number and location of the TZs in the response. Depending on the specific combination of couplings, the TZs are located above or below the transmission zeros. Several implementations of these couplings are proposed. A thorough investigation of the coupling mechanisms between resonators reveals that some of these mechanisms are capable of providing an excess of TZs. This phenomenon is studied, and guidelines are given to help designers control the position of all TZs available. Moreover, a new coupling structure formed by stubs connected to a capacitive window is studied. Two examples are given to illustrate its use in practical filter design.

Chapter 5 describes a systematic procedure for the design of wideband manifold-coupled multiplexers. As opposed to the classical narrowband multiplexers, in wideband applications it is critical to have short manifolds and avoid the use of long stubs to connect the different filters to the manifold. In the proposed technique, filters are directly connected to the manifold, following a sequential procedure. In each stage, only a few variables are adjusted. By the end of this procedure, an adequate initial point is obtained. Further optimization by classical methods is able to provide the desired response of the multiplexer. Several examples will be shown to validate this procedure.

Chapter 6 summarizes the conclusions of this work. Likewise, it describes potential research and development lines associated with the work performed in the framework of this thesis.

Chapter 2

Full-wave characterization of bi-dimensional cavities

A resonant cavity is a metallic enclosure (such as those shown in Fig. 2.1) of a lossless - or low-loss - medium in which an infinite number of free-oscillating modes can exist. A discrete frequency is associated with each mode, indicating the condition for its resonance. Cavities are usually coupled to waveguides via apertures located in the metallic shell. In these apertures, the electric field transverse to the aperture $\hat{\mathbf{n}} \times \mathbf{E} \neq 0$ ($\hat{\mathbf{n}}$ refers to the outwardly directed normal direction), provides the external source of excitation for the fields in the cavity. However, in this thesis no additional electric or magnetic current sources are considered in the cavity.

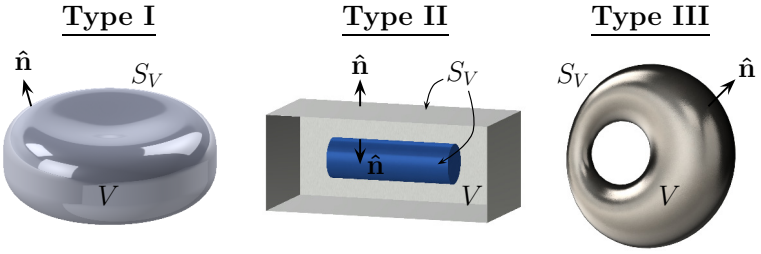

Figure 2.1: Cavities can be classified in three groups. Type I cavities are simply connected volumes with a single boundary. Type II cavities are simply connected volumes with multiple boundaries. Type III cavities are multiconnected volumes with a single boundary.

Although cavities are traditionally employed as resonators, in this thesis the concept of cavity is taken in a much broader sense. This means that the cavities

will be characterized near their resonances but also away from them. In the latter case, especially when the coupling apertures have a considerable size, cavities can represent a non-resonating discontinuity between the waveguides connected to the apertures. Consequently, the theory of cavities can be directly applied to the modeling of building blocks, such as those depicted in chapter 1.

The electromagnetic fields within aperture-coupled cavities (not containing electric or magnetic current sources) are governed by Maxwell's equations:

$$\nabla \times \mathbf{E} = -j\omega\mu\mathbf{H} \tag{2.1a}$$
$$\nabla \times \mathbf{H} = j\omega\varepsilon\mathbf{E}. \tag{2.1b}$$

By appropriate combination of both equations, the classical wave equations can be obtained:

$$\nabla^2\mathbf{E} + k^2\mathbf{E} = 0 \tag{2.2a}$$
$$\nabla^2\mathbf{H} + k^2\mathbf{H} = 0 \tag{2.2b}$$

where $k = \omega\sqrt{\mu\epsilon}$. The solution of these equations, along with the boundary conditions imposed by the cavity walls and apertures in the shell, is the objective of this chapter. The metallic walls and enclosed medium are assumed to be loss-less. Two different procedures to solve the wave equations will be shown. The first one is based on Kurokawa's field expansion in cavities [69]. As will be demonstrated, the direct application of this first procedure provides accurate results, but involves slowly converging series that deem this procedure unsuitable to develop an efficient analysis tool. As an alternative, a second formulation is proposed. It combines the theory of auxiliary potentials with the Kurokawa's expansion and an integral equation technique proposed by Okoshi [60] to model planar circuits. The application of a frequency and boundary-condition transformation to the proposed formulation results in an important reduction in the size of the problem. This accelerates the numerical computation of a solution and, therefore, the efficiency of the overall algorithm. To finalize the present chapter, this second formulation is applied to efficiently compute the Generalized Admittance Matrix (GAM) of bi-dimensional structures. Numerical results involving the analysis of this type of cavities with the proposed formulation will be presented in chapter 3.

2.1 Cavity mode spectrum and the expansion of electromagnetic fields

Given that the $\mathbf{E}$, $\mathbf{H}$, $\nabla \times \mathbf{E}$ and $\nabla \times \mathbf{H}$ functions in (2.1) and (2.2) are piecewise-continuous functions (i.e. continuous except for a finite number of surfaces each with a finite area) and square-integrable over the cavity volume V, they can be

expanded in terms of an adequate set of orthonormal functions [69, 129]: the electric and magnetic eigenvectors.

On the one hand, the electric eigenvectors are the solution of the eigenvalue problem:

$$\begin{aligned} &\nabla^2\mathbf{\Omega} + \kappa^2\mathbf{\Omega} = 0 && \text{in } V \\ &\hat{\mathbf{n}} \times \mathbf{\Omega} = 0, \qquad \nabla \cdot \mathbf{\Omega} = 0 && \text{on } S_V \end{aligned} \tag{2.3}$$

where κ are the eigenvalues of the problem. As it can be seen, the boundary conditions are of the electric type, thus the term "electric eigenvectors". Magnetic eigenvectors, on the other hand, are the solution of:

$$\begin{aligned} &\nabla^2\mathbf{\Omega} + \kappa^2\mathbf{\Omega} = 0 && \text{in } V \\ &\hat{\mathbf{n}} \cdot \mathbf{\Omega} = 0, \qquad \hat{\mathbf{n}} \times \nabla \times \mathbf{\Omega} = 0 && \text{on } S_V. \end{aligned} \tag{2.4}$$

The boundary conditions, in this second case, are of the magnetic type.

The solutions to the eigenvalue problems presented in (2.3) and (2.4) share the following properties:

1. There is a countable infinity of real non-negative eigenvalues and real eigenvectors.
2. Eigenvalues have a single cluster point at infinity.
3. Eigenvalues are simple or have a finite degree of degeneracy.
4. Eigenvectors are continuously differentiable to all orders.
5. The full eigenvector set constitutes an orthonormal basis. The projection between any pair of solutions must fulfill:

$$\langle \mathbf{\Omega}_i, \mathbf{\Omega}_j \rangle = \int_V \mathbf{\Omega}_i \cdot \mathbf{\Omega}_j^* \; dV = \delta_{ij} \tag{2.5}$$

where δ_{ij} is Kronecker's delta. Consequently, any square-integrable vector field $\mathbf{F}$ defined in V can be represented by the expansion:

$$\mathbf{F} = \sum_i \mathbf{\Omega}_i \int_V \mathbf{\Omega}_i \cdot \mathbf{F} \; dV. \tag{2.6}$$

In general, the electric and magnetic eigenvectors can be classified in three groups:

- **Irrotational modes** — Satisfying:

$$\nabla \times \mathbf{\Omega} = 0 \qquad \nabla \cdot \mathbf{\Omega} \neq 0. \tag{2.7}$$

To distinguish between them, the i-th electric irrotational eigenvector are represented by the symbol $\mathbf{f}_i$ and the i-th magnetic eigenvector by $\mathbf{g}_i$.

- **Solenoidal modes** — Fulfilling:

$$\nabla \times \mathbf{\Omega} \neq 0 \qquad \nabla \cdot \mathbf{\Omega} = 0. \tag{2.8}$$

  The electric solenoidal eigenvectors are represented by the symbol $\boldsymbol{\mathcal{E}}_i$ and the magnetic eigenvectors by $\boldsymbol{\mathcal{H}}_i$.

- **Harmonic modes** — Satisfying:

$$\nabla \times \mathbf{\Omega} = 0 \qquad \nabla \cdot \mathbf{\Omega} = 0. \tag{2.9}$$

  Electric harmonic eigenvectors, denoted by $\boldsymbol{\mathcal{E}}_i^0$, only exists when the cavity region is enclosed by M (with $M > 1$) separate boundaries (type II in Fig. 2.1). In contrast, magnetic harmonic eigenvectors $\boldsymbol{\mathcal{H}}_i^0$ must only be considered in the field expansion of N-times connected cavities, with $N > 1$ (type III in Fig. 2.1).

Given the transverse electric field $\hat{\mathbf{n}} \times \mathbf{E}$ in all the apertures of the shell, the electric and magnetic field solutions of (2.1) can be expanded according to:

$$\mathbf{E} = \sum_{i=1}^{\infty} \mathcal{A}_i \, \boldsymbol{\mathcal{E}}_i + \overbrace{\sum_{i=1}^{M-1} \mathcal{A}_i^0 \, \boldsymbol{\mathcal{E}}_i^0}^{\substack{\text{in case of M} \\ \text{separate boundaries} \\ \text{(Type II)}}} + \sum_{i=1}^{\infty} \mathcal{T}_i \, \mathbf{f}_i \tag{2.10a}$$

$$\mathbf{H} = \sum_{i=1}^{\infty} \mathcal{B}_i \, \boldsymbol{\mathcal{H}}_i + \underbrace{\sum_{i=1}^{N-1} \mathcal{B}_i^0 \, \boldsymbol{\mathcal{H}}_i^0}_{\substack{\text{in case of N-times} \\ \text{connected volume} \\ \text{(Type III)}}} + \sum_{i=1}^{\infty} \mathcal{D}_i \, \mathbf{g}_i \tag{2.10b}$$

where

$$\mathcal{A}_i = \langle \boldsymbol{\mathcal{E}}_i, \mathbf{E} \rangle = \frac{\kappa_i}{k^2 - \kappa_i^2} \int_{S_V} \boldsymbol{\mathcal{H}}_i \cdot \hat{\mathbf{n}} \times \mathbf{E} \, dS \tag{2.11a}$$

$$\mathcal{B}_i = \langle \boldsymbol{\mathcal{H}}_i, \mathbf{H} \rangle = \frac{j\,k}{\eta\,(k^2 - \kappa_i^2)} \int_{S_V} \boldsymbol{\mathcal{H}}_i \cdot \hat{\mathbf{n}} \times \mathbf{E} \, dS \tag{2.11b}$$

$$\mathcal{A}_i^0 = \langle \boldsymbol{\mathcal{E}}_i^0, \mathbf{E} \rangle = 0 \tag{2.11c}$$

$$\mathcal{B}_i^0 = \langle \boldsymbol{\mathcal{H}}_i^0, \mathbf{H} \rangle = \frac{j}{k\eta} \int_{S_V} \boldsymbol{\mathcal{H}}_i^0 \cdot \hat{\mathbf{n}} \times \mathbf{E} \, dS \tag{2.11d}$$

$$\mathcal{T}_i = \langle \mathbf{f}_i, \mathbf{E} \rangle = 0 \tag{2.11e}$$

$$\mathcal{D}_i = \langle \mathbf{g}_i, \mathbf{H} \rangle = \frac{j}{k\eta} \int_{S_V} \mathbf{g}_i \cdot \hat{\mathbf{n}} \times \mathbf{E} \, dS. \tag{2.11f}$$

In these equations, $k = \omega\sqrt{\varepsilon\mu}$ is the wavenumber at the frequency of operation and $\eta = \sqrt{\mu/\varepsilon}$ is the characteristic impedance of the medium. κ_i is the i-th eigenvalue of the corresponding expansion mode. Next, each family of eigenvectors will be presented.

2.1.1 Electric field expansion

2.1.1.1 Irrotational modes

Irrotational modes $\mathbf{f}_i$ and their corresponding eigenvalues are the solutions of the eigenvalue problem defined in (2.3) subject to the conditions:

$$\nabla \times \mathbf{f}_i = 0 \qquad \nabla \cdot \mathbf{f}_i \neq 0. \tag{2.12}$$

Since the curl of these eigenvectors is null, they can be expressed as the gradient of a scalar function v_i:

$$\mathbf{f}_i = \frac{\nabla v_i}{\kappa_i}. \tag{2.13}$$

The scalar function v_i satisfies

$$\begin{aligned} \nabla^2 v_i + \kappa_i^2 \, v_i = 0 \quad & \text{in } V \\ v_i = \text{constant} \quad & \text{on } S_V. \end{aligned} \tag{2.14}$$

In order to comply with the normalization condition (2.5), the scalar function must be normalized according to:

$$\int_V |v_i|^2 \; dV = 1. \tag{2.15}$$

Although these modes are not excited in aperture-coupled cavities without electric and magnetic current sources ($\mathcal{T}_i = 0$ in (2.11)), they have been included for completeness of the solution.

2.1.1.2 Solenoidal modes

Given that their divergence is null, the eigenproblem (2.3) for electric solenoidal modes $\boldsymbol{\mathcal{E}}_i$ becomes:

$$\begin{aligned} \nabla \times \nabla \times \boldsymbol{\mathcal{E}}_i - \kappa_i^2 \boldsymbol{\mathcal{E}}_i = 0 \quad & \text{in } V \\ \hat{\mathbf{n}} \times \boldsymbol{\mathcal{E}}_i = 0 \quad & \text{on } S_V \end{aligned} \tag{2.16}$$

In addition, the eigenvectors satisfy

$$\nabla \times \boldsymbol{\mathcal{E}}_i \neq 0 \qquad \nabla \cdot \boldsymbol{\mathcal{E}}_i = 0. \tag{2.17}$$

2.1.1.3 Harmonic modes

The harmonic eigenvectors of the electric type $\boldsymbol{\mathcal{E}}_i^0$ satisfy the same equations and boundary conditions as a source-free electrostatic field in the shielded region V:

$$\begin{aligned} \nabla^2 \boldsymbol{\mathcal{E}}_i^0 &= 0 \quad \text{in } V \\ \nabla \cdot \boldsymbol{\mathcal{E}}_i^0 &= 0 \quad \text{on } S_V \\ \hat{\mathbf{n}} \times \boldsymbol{\mathcal{E}}_i^0 &= 0 \quad \text{on } S_V. \end{aligned} \tag{2.18}$$

As it is demonstrated in [130], these equations necessarily imply that

$$\nabla \times \boldsymbol{\mathcal{E}}_i^0 = 0 \qquad \nabla \cdot \boldsymbol{\mathcal{E}}_i^0 = 0 \tag{2.19}$$

as defined for harmonic solutions. These modes can only exist if the boundary S_V consists of separate parts at different potentials, as it is the case of Type II cavities in Fig. 2.1. If the boundary consists of M separate parts, there must be $M-1$ harmonic eigenvectors. Similarly to the electric irrotational modes, the harmonic ones are not excited in aperture-coupled cavities without electric and magnetic current sources ($\mathcal{A}_i^0 = 0$ in (2.11)). Nevertheless, they have been included here for completeness.

2.1.2 Magnetic field expansion

2.1.2.1 Irrotational modes

As in the electric field case, the magnetic irrotational modes $\mathbf{g}_i$ satisfy

$$\nabla \times \mathbf{g}_i = 0 \qquad \nabla \cdot \mathbf{g}_i \neq 0. \tag{2.20}$$

They can be derived from a scalar function w_i as:

$$\mathbf{g}_i = \frac{\nabla w_i}{\kappa_i}. \tag{2.21}$$

The scalar function w_i fulfills

$$\begin{aligned} \nabla^2 w_i + \kappa_i^2 \, w_i &= 0 \quad \text{in } V \\ \frac{\partial w_i}{\partial n} &= 0 \quad \text{on } S_V \end{aligned} \tag{2.22}$$

where $\partial/\partial n$ is the derivative along the outwardly directed normal $\hat{\mathbf{n}}$. To fulfill the normalization condition of the eigenfunctions $\langle \mathbf{g}_i, \mathbf{g}_i \rangle = 1$, the scalar function w_i must fulfill:

$$\int_V |w_i|^2 \, dV = 1. \tag{2.23}$$

2.1.2.2 Solenoidal modes

The magnetic field solenoidal modes $\boldsymbol{\mathcal{H}}_i$ and their eigenvalues κ_i fulfill

$$\begin{aligned} \nabla \times \nabla \times \boldsymbol{\mathcal{H}}_i - \kappa_i^2 \boldsymbol{\mathcal{H}}_i = 0 \quad &\text{in } V \\ \hat{\mathbf{n}} \times \nabla \times \boldsymbol{\mathcal{H}}_i = 0 \quad &\text{on } S_V \end{aligned} \tag{2.24}$$

in addition to the conditions

$$\nabla \times \boldsymbol{\mathcal{H}}_i \neq 0 \qquad \nabla \cdot \boldsymbol{\mathcal{H}}_i = 0. \tag{2.25}$$

These modes have the same eigenvalue spectra as the electric field solenoidal modes $\boldsymbol{\mathcal{E}}_i$. Both sets of modes are related to each other by:

$$\nabla \times \boldsymbol{\mathcal{H}}_i = \kappa_i \boldsymbol{\mathcal{E}}_i \tag{2.26a}$$

$$\nabla \times \boldsymbol{\mathcal{E}}_i = \kappa_i \boldsymbol{\mathcal{H}}_i. \tag{2.26b}$$

2.1.2.3 Harmonic modes

Lastly, the magnetic field harmonic modes $\boldsymbol{\mathcal{H}}_i^0$ correspond to the zero-eigenvalue solution of (2.4). These modes only exist in multi-connected cavities like the Type III resonator of Fig. 2.1 (which represents a 2-times connected volume). In an N-times connected volume, there are $N-1$ independent magnetic field harmonic modes. All of them satisfy

$$\nabla \times \boldsymbol{\mathcal{H}}_i^0 = 0 \qquad \nabla \cdot \boldsymbol{\mathcal{H}}_i^0 = 0 \tag{2.27}$$

and can be obtained as non-trivial solutions of the eigenvalue problem:

$$\begin{aligned} \nabla^2 \boldsymbol{\mathcal{H}}_i^0 = 0 \quad &\text{in } V \\ \hat{\mathbf{n}} \cdot \boldsymbol{\mathcal{H}}_i^0 = 0 \quad &\text{on } S_V \\ \hat{\mathbf{n}} \times \nabla \times \boldsymbol{\mathcal{H}}_i^0 = 0 \quad &\text{on } S_V. \end{aligned} \tag{2.28}$$

2.1.3 Application to bi-dimensional cavities

For bi-dimensional cavities, like the ones shown in Fig. 2.2, the determination of the electric and magnetic eigenvectors admits certain simplifications. On the one hand, the vector eigenvalue problems can be transformed into scalar eigenvalue problems via suitable auxiliary potentials [131]. On the other hand, the problems admit variable separation, thus reducing the dimensionality of the scalar problem to be solved.

Bi-dimensional cavities can be understood as a section of waveguide with short-circuited ends, therefore containing standing waves [132]. As it will be shown, the

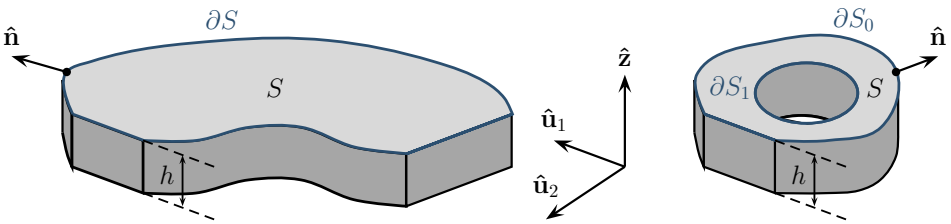

Figure 2.2: Examples of bi-dimensional cavities: simply connected (left) and multi-connected (right).

auxiliary potentials that aid in the computation of the electric and magnetic eigenvectors are directly related to the TE-to-z, TM-to-z and TEM-to-z solutions that we can find in a waveguide with the same cross-section as the bi-dimensional cavity. The construction of these solutions is analytical in highly canonical cases. In contrast, complex waveguide shapes must be solved by means of suitable numerical techniques. For instance, the efficient Boundary Integral- Resonant Mode Expansion (BI-RME) method [26] can be used to obtain the TE-to-z, TM-to-z and TEM-to-z solutions in waveguides of any arbitrary shape.

2.1.3.1 Solenoidal modes

The theory of auxiliary potentials states that, in order to obtain the solutions for the (solenoidal) electric and magnetic fields in a boundary-value problem, a pair of auxiliary vector potentials, $\mathbf{F}$ (electric vector potential) and $\mathbf{A}$ (magnetic vector potential), may be used. Each auxiliary potential provides a subset of solutions. The superposition of all of them yields the objective electric and magnetic fields. In the case of bi-dimensional cavities, the electric vector potential problem is directly related to the TE-to-z solutions of a waveguide with an equivalent cross-section, as will be shown next. The magnetic vector potential, in contrast, is related to the TM-to-z solutions of the equivalent waveguide. For multi-connected cavities, the TEM-to-z modes of the cross-section waveguide lead to a third subset of solenoidal modes. The expressions of each subset in terms of their respective waveguide potentials are developed next.

TE-mode solenoidal solutions

These modes satisfy (2.16), (2.17), (2.24) and (2.25) and can be derived from an electric vector potential $\mathbf{F}_i$ as:

$$\boldsymbol{\mathcal{E}}_i^{\mathrm{TE}} = -\nabla \times \mathbf{F}_i \tag{2.29a}$$

$$\boldsymbol{\mathcal{H}}_i^{\mathrm{TE}} = \frac{\nabla \times \boldsymbol{\mathcal{E}}_i^{\mathrm{TE}}}{\kappa_i}. \tag{2.29b}$$

The vector equation for the electric field (2.16) can be transformed into an equation for the vector potential $\mathbf{F}_i$. It has been shown in (2.26a) that the electric solenoidal modes can be related to the curl of the magnetic solenoidal modes. Equating this equation with (2.29a), we have

$$\nabla \times \left(\boldsymbol{\mathcal{H}}_i^{\mathrm{TE}} + \kappa_i \mathbf{F}_i \right) = 0. \tag{2.30}$$

From the vector identity $\nabla \times \nabla\phi = 0$, the term in parenthesis can be seen as the gradient of a certain arbitrary scalar function ϕ, thus

$$\boldsymbol{\mathcal{H}}_i^{\mathrm{TE}} = \nabla\phi - \kappa_i \mathbf{F}_i. \tag{2.31}$$

Now, the curl of (2.29a) is taken and equated with (2.26b). In the resulting expression, the magnetic field $\boldsymbol{\mathcal{H}}_i^{\mathrm{TE}}$ is substituted by its equivalent expression of (2.31), which yields,

$$\nabla^2 \mathbf{F}_i - \nabla\nabla \cdot \mathbf{F}_i = \kappa_i \nabla\phi - \kappa_i^2 \mathbf{F}_i. \tag{2.32}$$

Then, the Lorentz gauge is used to define the divergence of $\mathbf{F}_i$ in order to compensate for the term containing the gradient of ϕ (i.e. $\nabla \cdot \mathbf{F}_i = -\kappa_i \phi$). Applying this gauge in (2.32), the vector Helmholtz equation for the vector potential $\mathbf{F}_i$ becomes

$$\nabla^2 \mathbf{F}_i + \kappa_i^2 \mathbf{F}_i = 0. \tag{2.33}$$

The TE solenoidal solutions must have electric components that are transverse to the constant direction of the structure. In order to obtain these solutions, the vector potential $\mathbf{F}_i$ must be directed according to $\hat{\mathbf{z}}$. In addition, separation of variables can be applied. Consequently, $\mathbf{F}_i$ can be expressed as:

$$\mathbf{F}_i = A_{jl}\ \varphi_j(u_1, u_2)\ \sin\left(\frac{l\pi z}{h}\right) \hat{\mathbf{z}} \tag{2.34}$$

where φ_j is a certain scalar potential defined in the cross-section S and A_{jl} is a normalization factor. l indicates the number of oscillations of the mode in the z direction (standing wave condition), and h is the size of the cavity in the constant direction $\hat{\mathbf{z}}$. The index i of the vector potential $\mathbf{F}_i$ is now associated with the pair of indices (j, l). For solenoidal TE modes, $l > 0$.

Substituting the expression of the vector potential (2.34) into (2.33), the vector Helmholtz equation of the problem is transformed into an equation for the scalar potential φ_j:

$$\nabla_{\mathrm{T}}^2 \varphi_j + \left[\kappa_i^2 - \left(\frac{l\pi}{h} \right)^2 \right] \varphi_j = 0 \qquad \text{in } S \tag{2.35}$$

where $\nabla_{\mathrm{T}}^2 = \nabla^2 - \partial^2/\partial z^2$ is the transverse-to-z Laplacian operator.

Similarly, the boundary condition for the electric solenoidal modes is transformed into a boundary condition for the scalar potential.

$$\begin{aligned}\hat{\mathbf{n}} \times \boldsymbol{\mathcal{E}}_i^{\mathrm{TE}} &= \hat{\mathbf{n}} \times (-\nabla \times \mathbf{F}_i) \\ &= A_{jl} \sin\left(\frac{l\pi z}{h}\right) [\hat{\mathbf{n}} \times (\hat{\mathbf{z}} \times \nabla_{\mathrm{T}}\, \varphi_j)] \\ &= A_{jl} \sin\left(\frac{l\pi z}{h}\right) (\hat{\mathbf{n}} \cdot \nabla_{\mathrm{T}}\, \varphi_j)\, \hat{\mathbf{z}}. \end{aligned} \tag{2.36}$$

As defined by the boundary condition of the solenoidal modes (2.16), this last expression must be null on the top ($z = 0$) and bottom ($z = h$) walls of the cavity, as well as on its lateral wall. The former is fulfilled by the sinusoidal variation of the field with z. This justifies the election of a sine variation with z of the electric vector potential in (2.34). To fulfill the latter condition (i.e. $\hat{\mathbf{n}} \times \boldsymbol{\mathcal{E}}_i^{\mathrm{TE}} = 0$ on the lateral wall), the scalar potential φ_j must satisfy the following condition in the contour of the cross section of the cavity:

$$\hat{\mathbf{n}} \cdot \nabla_{\mathrm{T}}\, \varphi_j = \frac{\partial \varphi_j}{\partial n} = 0 \qquad \text{on } \partial S. \tag{2.37}$$

Combining (2.35) and (2.37), the similarity between φ_j and the scalar potential for TE modes in a waveguide of cross section S is evident. It is well known that the TE potential in a waveguide fulfills

$$\begin{aligned} \nabla_{\mathrm{T}}^2 \varphi_j^{\mathrm{TE}} + \left(\chi_j^{\mathrm{TE}}\right)^2 \varphi_j^{\mathrm{TE}} = 0 \quad &\text{in } S \\ \frac{\partial \varphi_j^{\mathrm{TE}}}{\partial n} = 0 \quad &\text{on } \partial S \end{aligned} \tag{2.38}$$

where χ_j^{TE} is the eigenvalue of the problem (and cut-off wavenumber of the corresponding TE mode). If the relationship between the eigenvalues of both problems is:

$$\kappa_i = \sqrt{\left(\chi_j^{\mathrm{TE}}\right)^2 + \left(\frac{l\pi}{h}\right)^2} = \kappa_{jl}. \tag{2.39}$$

it is immediate to see that the scalar potential of the bi-dimensional cavity problem φ_j is identical to the scalar potential of the equivalent TE problem φ_j^{TE}. To reflect that this eigenvalue is comprised of two contributions, the κ_{jl} designation is employed.

Thanks to this procedure, the computation of the solenoidal TE modes is reduced to the computation of the scalar TE problem in a waveguide of cross-section S. To enforce the normalization condition (2.5) for the solenoidal modes, the amplitude A_{jl} of the vector potential must be:

$$A_{jl} = \sqrt{\frac{2/h}{\int_S \left|\nabla_{\mathrm{T}} \varphi_j^{\mathrm{TE}}\right|^2 \, dS}}. \tag{2.40}$$

Applying Green's first identity to φ_j^{TE} and $\left(\varphi_j^{\mathrm{TE}}\right)^*$, the integral involved in (2.40) becomes:

$$\int_S \left|\nabla_{\mathrm{T}}\varphi_j^{\mathrm{TE}}\right|^2 \, dS = \left(\chi_j^{\mathrm{TE}}\right)^2 \int_S \left|\varphi_j^{\mathrm{TE}}\right|^2 \, dS. \tag{2.41}$$

It is assumed that the waveguide potentials are normalized according to:

$$\int_S \left|\varphi_j^{\mathrm{TE}}\right|^2 \, dS = 1 \tag{2.42}$$

therefore, the normalized expression for the vector potential $\mathbf{F}_i$ is

$$\mathbf{F}_i = \frac{\sqrt{2/h}}{\chi_j^{\mathrm{TE}}} \, \varphi_j^{\mathrm{TE}}(u_1, u_2) \, \sin\left(\frac{l\pi z}{h}\right) \hat{\mathbf{z}}. \tag{2.43}$$

Substituting (2.43) into (2.29) and expanding all the terms, the final expressions for the electric and magnetic solenoidal TE modes in terms of the waveguide scalar potential φ_j^{TE} are:

$$\boldsymbol{\mathcal{E}}_i^{\mathrm{TE}} = \frac{\sqrt{2/h}}{\chi_j^{\mathrm{TE}}} \left(\hat{\mathbf{z}} \times \nabla_{\mathrm{T}} \, \varphi_j^{\mathrm{TE}}\right) \sin\left(\frac{l\pi z}{h}\right) \tag{2.44a}$$

$$\begin{aligned} \boldsymbol{\mathcal{H}}_i^{\mathrm{TE}} = & \frac{-\sqrt{2/h}}{\chi_j^{\mathrm{TE}} \sqrt{\left(\chi_j^{\mathrm{TE}}\right)^2 + \left(\frac{l\pi}{h}\right)^2}} \left[\frac{l\pi}{h} \nabla_{\mathrm{T}} \, \varphi_j^{\mathrm{TE}} \cos\left(\frac{l\pi z}{h}\right)\right. \\ & + \left.\left(\chi_j^{\mathrm{TE}}\right)^2 \varphi_j^{\mathrm{TE}} \sin\left(\frac{l\pi z}{h}\right) \hat{\mathbf{z}}\right]. \end{aligned} \tag{2.44b}$$

TM-mode solenoidal solutions

As in the TE case, these modes satisfy (2.16), (2.17), (2.24) and (2.25). However, the TM-mode solenoidal eigenvectors can be derived from a magnetic vector potential $\mathbf{A}_i$ as:

$$\boldsymbol{\mathcal{H}}_i^{\mathrm{TM}} = \nabla \times \mathbf{A}_i \tag{2.45a}$$

$$\boldsymbol{\mathcal{E}}_i^{\mathrm{TM}} = \frac{\nabla \times \boldsymbol{\mathcal{H}}_i^{\mathrm{TM}}}{\kappa_i}. \tag{2.45b}$$

Following a procedure equivalent to the one developed for the solenoidal TE modes, the original eigenvalue problem can be transformed into:

$$\nabla^2 \mathbf{A}_i + \kappa_i^2 \mathbf{A}_i = 0. \tag{2.46}$$

Likewise, the vector potential $\mathbf{A}_i$ in the TM case can be expressed as the product of two contributions:

$$\mathbf{A}_i = A'_{jl}\ \varphi'_j(u_1, u_2)\ \cos\left(\frac{l\pi z}{h}\right)\hat{\mathbf{z}}. \tag{2.47}$$

For TM modes, $l \geq 0$ and $i = (j, l)$. The scalar potential φ'_j is a solution of the scalar eigenvalue problem:

$$\begin{aligned} \nabla^2_{\mathrm{T}}\varphi'_j + \left[\kappa_i^2 - \left(\frac{l\pi}{h}\right)^2\right]\varphi'_j = 0 \quad &\text{in } S \\ \varphi'_j = 0 \quad &\text{on } \partial S. \end{aligned} \tag{2.48}$$

This is identical to the eigenvalue problem for TM modes of a waveguide having a cross section equal to S:

$$\begin{aligned} \nabla^2_{\mathrm{T}}\varphi_j^{\mathrm{TM}} + \left(\chi_j^{\mathrm{TM}}\right)^2\varphi_j^{\mathrm{TM}} = 0 \quad &\text{in } S \\ \varphi_j^{\mathrm{TM}} = 0 \quad &\text{on } \partial S \end{aligned} \tag{2.49}$$

as long as the following relationship between eigenvalues holds:

$$\kappa_i = \sqrt{\left(\chi_j^{\mathrm{TM}}\right)^2 + \left(\frac{l\pi}{h}\right)^2} = \kappa_{jl}. \tag{2.50}$$

In this case χ_j^{TM} is the cut-off wavenumber of the waveguide TM eigenvalue problem. Therefore, we can substitute φ'_j by φ_j^{TM}. Likewise, it is assumed that the waveguide potentials are normalized according to:

$$\int_S \left|\varphi_j^{\mathrm{TM}}\right|^2\ dS = 1. \tag{2.51}$$

The normalization condition, in this case, can be expressed as:

$$A'_{jl} = \frac{\sqrt{\epsilon_l/h}}{\chi_j^{\mathrm{TM}}} \tag{2.52}$$

where

$$\epsilon_l = \begin{cases} 1 & \text{if } l = 0 \\ 2 & \text{if } l \neq 0. \end{cases} \tag{2.53}$$

Therefore, making use of this normalization constant, the magnetic vector potential can be expressed as:

$$\mathbf{A}_i = \frac{\sqrt{\epsilon_l/h}}{\chi_j^{\mathrm{TM}}}\ \varphi_j^{\mathrm{TM}}(u_1, u_2)\ \cos\left(\frac{l\pi z}{h}\right)\hat{\mathbf{z}}. \tag{2.54}$$

Substituting (2.54) into (2.45), the final expressions for the electric and magnetic solenoidal TM modes are:

$$\begin{aligned}\boldsymbol{\mathcal{E}}_i^{\mathrm{TM}} &= \frac{-\sqrt{\epsilon_l/h}}{\chi_j^{\mathrm{TM}}\sqrt{\left(\chi_j^{\mathrm{TM}}\right)^2+\left(\frac{l\pi}{h}\right)^2}}\left[\frac{l\pi}{h}\nabla_{\mathrm{T}}\varphi_j^{\mathrm{TM}}\sin\left(\frac{l\pi z}{h}\right)\right.\\ &- \left.\left(\chi_j^{\mathrm{TM}}\right)^2\varphi_j^{\mathrm{TM}}\cos\left(\frac{l\pi z}{h}\right)\hat{\mathbf{z}}\right] \qquad (2.55a)\\ \boldsymbol{\mathcal{H}}_i^{\mathrm{TM}} &= \frac{-\sqrt{\epsilon_l/h}}{\chi_j^{\mathrm{TM}}}\left(\hat{\mathbf{z}}\times\nabla_{\mathrm{T}}\varphi_j^{\mathrm{TM}}\right)\cos\left(\frac{l\pi z}{h}\right). \qquad (2.55b)\end{aligned}$$

TEM-mode solenoidal solutions

For N-times connected cavities, like the one shown on the right side of Fig. 2.2, there is a third set of solenoidal modes that must be considered. The modes on this set fulfill the classical solenoidal mode equations (2.16), (2.17), (2.24) and (2.25). As in the TM mode case, this third set of modes can also be derived from a magnetic vector potential $\mathbf{A}_i$:

$$\boldsymbol{\mathcal{H}}_i^{\mathrm{TEM}} = \nabla\times\mathbf{A}_i \qquad (2.56a)$$

$$\boldsymbol{\mathcal{E}}_i^{\mathrm{TEM}} = \frac{\nabla\times\boldsymbol{\mathcal{H}}_i^{\mathrm{TEM}}}{\kappa_i} \qquad (2.56b)$$

where

$$\mathbf{A}_i = A_{jl}^{''}\,\varphi_j^{''}(u_1,u_2)\,\cos\left(\frac{l\pi z}{h}\right)\hat{\mathbf{z}}. \qquad (2.57)$$

These modes are defined at eigenvalues that equal an integer number of the oscillations in the constant direction, this is:

$$\kappa_i = \frac{l\pi}{h}. \qquad (2.58)$$

Since they are solenoidal (and not harmonic) modes, the condition $l > 0$ must be fulfilled.

These modes are related to the $N-1$ TEM solutions of a waveguide with N conductors and a cross-section equal to S. To fulfill the orthonormality requirements of the solenoidal modes, this third set is not derived directly from the TEM solutions. Instead, it is expressed as a linear combination of $N-1$ independent (but not orthonormal) TEM solutions in the form:

$$\varphi_j^{''} = \sum_{r=1}^{N-1} C_{jr}\,\varphi_r^{\mathrm{TEM}} \qquad j = 1,2\cdots,N-1 \qquad (2.59)$$

where φ_r^{TEM} with $(r = 1, 2, ..., N-1)$ are the TEM potentials that fulfill:

$$\begin{aligned} \nabla_{\mathrm{T}}^2 \varphi_r^{\mathrm{TEM}} &= 0 \quad \text{in } S \\ \varphi_r^{\mathrm{TEM}} &= 1 \quad \text{on } \partial S_r \\ \varphi_r^{\mathrm{TEM}} &= 0 \quad \text{on } \partial S_i \text{ with } i \neq r \text{ (including } \partial S_0). \end{aligned} \tag{2.60}$$

In addition, coefficients C_{jr} are chosen as to ensure that:

$$\int_S \nabla_{\mathrm{T}} \varphi_j^{''} \cdot \nabla_{\mathrm{T}} \varphi_i^{''} \, dS = \delta_{ij}. \tag{2.61}$$

Once the normalization condition for $\nabla_{\mathrm{T}} \varphi_j^{''}$ is set, the normalization constant of the vector potential can be computed. Consequently, the expression of this potential is:

$$\mathbf{A}_i = \sqrt{\frac{2}{h}} \, \varphi_j^{''}(u_1, u_2) \cos\left(\frac{l\pi z}{h}\right) \hat{\mathbf{z}}. \tag{2.62}$$

Substituting (2.62) into (2.56), the final expressions for the electric and magnetic solenoidal TEM modes are:

$$\boldsymbol{\mathcal{E}}_i^{\mathrm{TEM}} = -\sqrt{\frac{2}{h}} \nabla_{\mathrm{T}} \varphi_j^{''} \sin\left(\frac{l\pi z}{h}\right) \tag{2.63a}$$

$$\boldsymbol{\mathcal{H}}_i^{\mathrm{TEM}} = -\sqrt{\frac{2}{h}} \left(\hat{\mathbf{z}} \times \nabla_{\mathrm{T}} \varphi_j^{''}\right) \cos\left(\frac{l\pi z}{h}\right). \tag{2.63b}$$

2.1.3.2 Harmonic modes

Due to their geometrical properties, bi-dimensional cavities can only have a single boundary, even if they are multi-connected. For that reason, the only set of harmonic modes that can exist in bi-dimensional cavities is the magnetic harmonic one. These modes satisfy (2.27) and (2.28) and can be derived from a magnetic vector potential $\mathbf{A}_i$:

$$\boldsymbol{\mathcal{H}}_i^0 = \nabla \times \mathbf{A}_i \tag{2.64}$$

where the auxiliary potential in now invariant with z (equivalent to (2.57) with $l = 0$):

$$\mathbf{A}_i = \sqrt{\frac{1}{h}} \, \varphi_j^{''}(u_1, u_2) \hat{\mathbf{z}}. \tag{2.65}$$

The scalar potential $\varphi_j^{''}$ is the one used to derive the TEM solenoidal magnetic modes defined (2.59). Applying the normalization conditions, these static modes can be expressed as:

$$\boldsymbol{\mathcal{H}}_i^0 = -\sqrt{\frac{1}{h}} \left(\hat{\mathbf{z}} \times \nabla_{\mathrm{T}} \varphi_j^{''}\right). \tag{2.66}$$

2.1.3.3 Irrotational modes

Magnetic irrotational modes

It was seen in section 2.1 that these modes could be described, according to (2.21), as the gradient of a scalar potential. The eigenvalue problem used to derive the scalar potential w_i (2.22) is equivalent to the one used to obtain TE waveguide modes as described in (2.38). For both problems to be exactly equal, the eigenvalues have to be related to each other by:

$$\kappa_i = \sqrt{\left(\chi_j^{\mathrm{TE}}\right)^2 + \left(\frac{l\pi}{h}\right)^2} = \kappa_{jl}. \tag{2.67}$$

Therefore, solenoidal TE modes and magnetic irrotational modes can both be derived from the TE modes of an equivalent waveguide with cross-section S. Likewise, it is possible to separate the problem into transverse and axial variables. Applying the standing wave condition for magnetic fields and ensuring the normalization condition set in (2.23), the scalar potential of this problem is expressed as:

$$w_i = \sqrt{\frac{\epsilon_l}{h}}\, \varphi_j^{\mathrm{TE}}(u_1, u_2) \cos\left(\frac{l\pi z}{h}\right) \tag{2.68}$$

where $l \geq 0$ and $i = (j, l)$.

Introducing (2.67) and (2.68) into (2.21), we obtain:

$$\mathbf{g}_i = \frac{\sqrt{\epsilon_l / h}}{\sqrt{\left(\chi_j^{\mathrm{TE}}\right)^2 + \left(\frac{l\pi}{h}\right)^2}} \left[\nabla_{\mathrm{T}} \varphi_j^{\mathrm{TE}} \cos\left(\frac{l\pi z}{h}\right) - \left(\frac{l\pi}{h}\right) \varphi_j^{\mathrm{TE}} \sin\left(\frac{l\pi z}{h}\right) \hat{\mathbf{z}}\right]. \tag{2.69}$$

Electric irrotational modes

These modes can be derived, according to (2.13), from a scalar potential v_i which fulfills (2.14). This scalar potential is equivalent to the one employed to derive TM modes in a waveguide of cross-section S, as seen by comparison of (2.14) (with $v_i = 0$ on S_V) and (2.49). The relationship between the eigenvalues of both problems must be:

$$\kappa_i = \sqrt{\left(\chi_j^{\mathrm{TM}}\right)^2 + \left(\frac{l\pi}{h}\right)^2} = \kappa_{jl}. \tag{2.70}$$

Applying separation of variables, the standing wave condition for electric fields and ensuring the normalization condition set in (2.15), the scalar potential of this problem is expressed as:

$$v_i = \sqrt{\frac{2}{h}}\, \varphi_j^{\mathrm{TM}}(u_1, u_2) \sin\left(\frac{l\pi z}{h}\right) \tag{2.71}$$

where $l > 0$ and $i = (j, l)$.

Introducing (2.70) and (2.71) into (2.13), we obtain:

$$\mathbf{f}_i = \frac{\sqrt{2/h}}{\sqrt{\left(\chi_j^{\mathrm{TM}}\right)^2 + \left(\frac{l\pi}{h}\right)^2}} \left[\nabla_{\mathrm{T}} \varphi_j^{\mathrm{TM}} \sin\left(\frac{l\pi z}{h}\right) + \left(\frac{l\pi}{h}\right) \varphi_j^{\mathrm{TM}} \cos\left(\frac{l\pi z}{h}\right) \hat{\mathbf{z}}\right]. \tag{2.72}$$

2.1.4 Convergence of the direct representation: Rectangular cavity

After presenting the different modes that conform Kurokawa's field expansion, the direct field representation presented in this section is applied to a simple bi-dimensional structure: the rectangular cavity. The cavity, shown in Fig. 2.3, is excited through a rectangular aperture located on one of the lateral walls. The TE_{10} mode of a WR-75 rectangular waveguide coinciding with this aperture sets the excitation condition $\hat{\mathbf{n}} \times \mathbf{E}$. The objective of this example is to compute the electric and magnetic fields in a finite number of points within the cavity. By comparing the results with a full-wave simulator, the convergence rate of this formulation can be studied. Based on this criteria, the potential of this formulation to model bi-dimensional cavities with more complex shapes will be discussed.

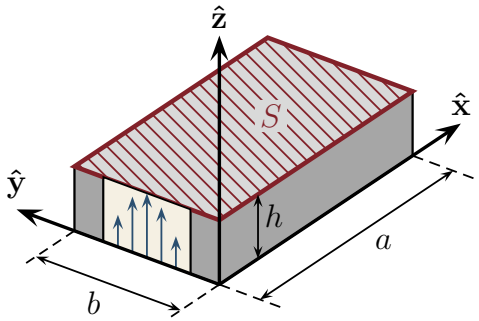

Figure 2.3: Rectangular cavity under study (a = 50 mm, b = 30 mm, h = 9.525 mm).

The electric and magnetic eigenvectors of the problem can be derived from the classical potentials of a rectangular waveguide with cross-section S:

$$\varphi_{mn}^{\mathrm{TE}} = \sqrt{\frac{\epsilon_m \epsilon_n}{a\,b}} \cos\left(\frac{m\pi x}{a}\right) \cos\left(\frac{n\pi y}{b}\right) \tag{2.73a}$$

$$\varphi_{mn}^{\mathrm{TM}} = \frac{2}{\sqrt{a\,b}} \sin\left(\frac{m\pi x}{a}\right) \sin\left(\frac{n\pi y}{b}\right) \tag{2.73b}$$

where the index j in section 2.1.3 has been replaced by the classical pair (m, n). Associated with these potentials, the eigenvalues of the problem are:

$$\chi_{mn}^{\mathrm{TE}} = \chi_{mn}^{\mathrm{TM}} = \sqrt{\left(\frac{m\pi}{a}\right)^2 + \left(\frac{n\pi}{b}\right)^2}. \tag{2.74}$$

Following (2.10)-(2.11), and given that a rectangular cavity is simply connected, three sets of eigenvectors are employed to expand the electromagnetic fields: TE solenoidal modes, TM solenoidal modes and magnetic irrotational modes. Since the excitation does not have any variations in $\hat{\mathbf{z}}$, it cannot transfer energy into the TE solenoidal modes. Therefore, they are not required to expand the electromagnetic field of this problem. Substituting the TE and TM potentials into the equations shown in 2.1.3.1 and 2.1.3.3, the field expansions are obtained (see [133] for the specific expressions). Then, the coupling amplitudes between the excitation and each mode in the cavity is computed. Finally, the field solutions are computed according to (2.10).

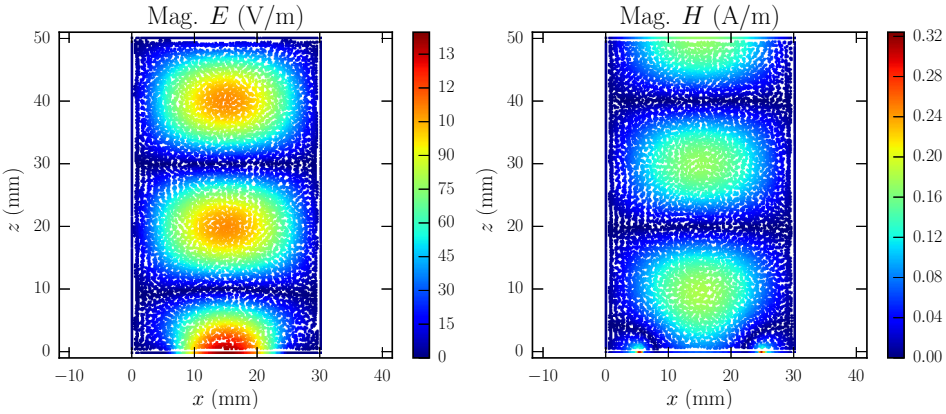

Figure 2.4: Magnitude of the electric and magnetic fields provided by FEST3D at a finite number of points in the xz-plane.

The field expansion involves infinite summations that, in practice, need to be truncated. If the number of terms considered is high enough, the addition of new terms will have a negligible impact in the field pattern. In that situation, the field has converged to the desired solution. In this example, the desired solution is known beforehand thanks to the simulation of the structure with the full-wave EM solver FEST3D (see Fig. 2.4). This commercial tool analyzes the problem as a simple short-circuited waveguide section (representing the cavity) connected to the WR-75 waveguide excitation. By comparison of the results, the convergence of series in the Kurokawa field expansion can be studied.

For this study, a maximum frequency parameter $f_{\max}$ is defined. The series are truncated according to this parameter. All the modes of the rectangular cross-section whose cut-off frequency is below this $f_{\max}$ value are added in the series. The full-wave EM solver provides the electromagnetic field solution in an array of N points distributed in a plane that is normal to $\hat{\mathbf{z}}$ (since the field solution does not depend on the z coordinates). Comparing this convergent solution with the truncated series expansion, a measure of the error in the computation of the electric and magnetic fields can be defined as:

$$\text{Error} = \frac{1}{N}\sum_{n=1}^{N}\left\{\|\mathbf{X}(x_n, y_n)\| - \|\mathbf{X}'(x_n, y_n)\|\right\}^2 \tag{2.75}$$

where N is the number of points where the field is computed, (x_n, y_n) are the coordinates of these points, $\mathbf{X}$ is either the magnitude of the electric or magnetic field obtained via the truncated field expansion, and $\mathbf{X}'$ the same magnitude computed by FEST3D. Since the electric field is orders of magnitude higher than the magnetic field, both quantities have been normalized to its maximum value in order to compute the error.

$\mathbf{f}_{\max}$ [GHz]	**No. Modes**	**Error (%) Mag.** E	**Error (%) Mag.** H
10	9	6.012	4.518
15	22	1.604	0.918
20	40	0.897	0.666
30	92	0.492	0.355
50	260	0.184	0.138
75	590	0.072	0.058
100	1,045	0.035	0.036
150	2,362	0.028	0.038
200	4,194	0.019	0.032

Table 2.1: Error in the computation of the magnitude of the electric and magnetic fields in N=17,000 points for different number of terms in the field expansion.

Table 2.1 summarizes the results obtained for different number of terms in the expansion series. Since the structure does not change its height and is only excited by one mode, the number of terms in the series expansion is coincident

with the number of modes computed in the 2D section S of the cavity (modes with $l \neq 0$ do not contribute). As shown in the table, a significantly large number of modes has to be computed in the 2D section of the cavity to obtain convergent results. Extrapolating this data to more general cases, it can be seen that the direct application of Kurokawa's field expansion is not very efficient. The time devoted to solve thousands of modes of a waveguide with an arbitrary shape is extremely high, even with very advanced and efficient numerical techniques such as the BI-RME method [26]. Therefore, further work has to be done to transform this accurate field expansion into a more efficient and robust numerical analysis method.

2.2 Hybrid field representation

As it has been shown in the previous section, Kurokawa's field expansion in cavities is accurate, but not very efficient for the computation of electromagnetic fields within bi-dimensional cavities with arbitrary shapes. In this section, an alternative procedure, combining Kurokawa's field expansion with auxiliary vector potential theory and a contour integral method, is proposed. In order to develop a systematic and efficient formulation, the excitation of the cavities is limited to rectangular apertures in the lateral walls, having the same dimension h as the cavity (see Fig. 2.5). These apertures are assumed to be connected to rectangular waveguides with the same dimensions as the apertures. Therefore, the modes of the equivalent rectangular waveguide act as individual field sources. The electric field transverse to the rectangular apertures ($\hat{\mathbf{n}} \times \mathbf{e}_s$) is considered as the only source in the problem (i.e. no equivalent sources $\mathbf{J}$ or $\mathbf{M}$ are present).

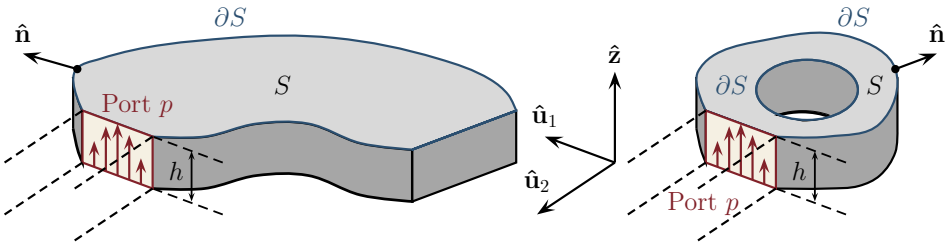

Figure 2.5: The excitation of the bi-dimensional cavities in the proposed formulation is done through rectangular apertures in the lateral walls.

Given the electromagnetic field excited by each of these modal sources, a more general problem involving apertures with other shapes and sizes can be solved. A simple projection of the desired source fields ($\hat{\mathbf{n}} \times \mathbf{E}$) into the modes of the rectangular waveguides ($\hat{\mathbf{n}} \times \mathbf{e}_s$) suffices to express any source in terms of the

equivalent rectangular waveguide modes:

$$\hat{\mathbf{n}} \times \mathbf{E} = \sum_s v_s \ (\hat{\mathbf{n}} \times \mathbf{e}_s) \tag{2.76}$$

where $\mathbf{E}$ is the desired source electric field, $\mathbf{e}_s$ is the s-th modal electric field in the rectangular aperture and $\hat{\mathbf{n}}$ is the outward normal vector. In addition, the voltage parameter is defined as:

$$v_s = \int_{S_p} (\hat{\mathbf{n}} \times \mathbf{E}) \cdot (\hat{\mathbf{n}} \times \mathbf{e}_s) \, dS \tag{2.77}$$

where S_p is the surface of the aperture of port p where $\mathbf{E}$ is defined.

According to the superposition theorem, the field within a cavity excited via multiple apertures can be expressed as the superposition of the fields due to each individual source (while the remaining sources are short-circuited). The objective of this section is to develop a formulation that is able to provide, in an efficient way, the electric and magnetic fields within the bi-dimensional cavity when it is being excited by one of these sources. The formulation will be particularized for the mode s at port p (which, in general, may represent any mode at any port).

Due to the symmetry of the problem, the electromagnetic field within bi-dimensional cavities can be separated into two independent problems, and the theory of auxiliary potentials can be applied. For the first problem, an electric vector potential $\mathbf{F}$ is used to derive the electric and magnetic fields, whereas in the second problem these fields can be derived from a magnetic vector potential $\mathbf{A}$. In both cases, the vector potentials are simply z-directed, this is, the direction where the structure is constant. Furthermore, the sources of excitation must also comply with the conditions imposed by each vector potential, if both problems are to be solved independently. Therefore, instead of the classical Transverse Electric (TE) and Transverse Magnetic (TM) modes of a rectangular waveguide, z-directed Longitudinal Section Electric (LSE) and Longitudinal Section Magnetic (LSM) modes are considered as sources. These modes form an orthonormal base; consequently, any other excitation can be described as an expansion based on these sets of modes. The orthonormalization properties of the Longitudinal Section modes can be summarized as:

$$\int_{S_p} (\hat{\mathbf{z}}_g \times \mathbf{e}_i) \cdot \mathbf{h}_j \, dS = \int_{S_p} (\mathbf{e}_i \times \hat{\mathbf{n}}) \cdot \mathbf{h}_j \, dS = \delta_{ij} \tag{2.78}$$

where δ_{ij} is Kronecker's delta. The coordinate system for these excitation modes can be seen in Fig. 2.6. Appendix A contains the formulas to transform TE and TM modes into LSE and LSM modes in a rectangular waveguide.

The particular expressions of the transverse-to-z_g components of the modal electric and magnetic fields for Longitudinal Section Electric (LSE^z_{lm}) modes are:

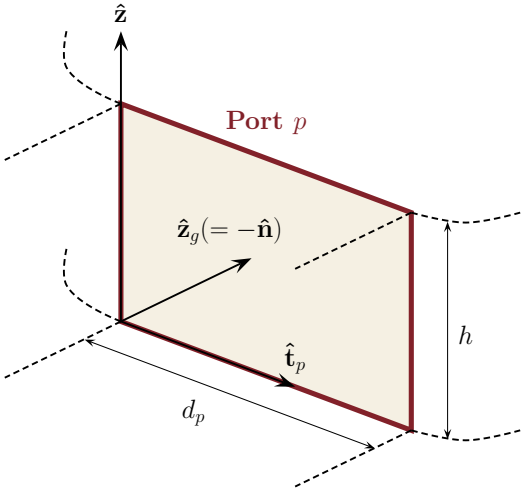

Figure 2.6: Coordinate system for the excitation modes of port p

$$\mathbf{e}_{lm}^{\mathrm{LSE}} = A_{lm}\cos\left(\frac{m\pi}{d_p}t_p\right)\sin\left(\frac{l\pi}{h}z\right)\hat{\mathbf{t}}_p \tag{2.79a}$$

$$\begin{aligned}\mathbf{h}_{lm}^{\mathrm{LSE}} &= \frac{A_{lm}\, lm\pi^2}{d_p h\left[k^2-\left(\frac{l\pi}{h}\right)^2\right]}\sin\left(\frac{m\pi}{d_p}t_p\right)\cos\left(\frac{l\pi}{h}z\right)\hat{\mathbf{t}}_p \\ &- A_{lm}\cos\left(\frac{m\pi}{d_p}t_p\right)\sin\left(\frac{l\pi}{h}z\right)\hat{\mathbf{z}}.\end{aligned} \tag{2.79b}$$

For the Longitudinal Section Magnetic modes (LSM_{lm}^{z}), the expressions of the transverse modal fields are:

$$\begin{aligned}\mathbf{e}_{lm}^{\mathrm{LSM}} &= \frac{-A_{lm}\, lm\pi^2}{d_p h\left[k^2-\left(\frac{l\pi}{h}\right)^2\right]}\cos\left(\frac{m\pi}{d_p}t_p\right)\sin\left(\frac{l\pi}{h}z\right)\hat{\mathbf{t}}_p \\ &+ A_{lm}\sin\left(\frac{m\pi}{d_p}t_p\right)\cos\left(\frac{l\pi}{h}z\right)\hat{\mathbf{z}}\end{aligned} \tag{2.80a}$$

$$\mathbf{h}_{lm}^{\mathrm{LSM}} = A_{lm}\sin\left(\frac{m\pi}{d_p}t_p\right)\cos\left(\frac{l\pi}{h}z\right)\hat{\mathbf{t}}_p. \tag{2.80b}$$

In these expressions, $k=\omega\sqrt{\mu\varepsilon}$ is the wavenumber of the medium, ϵ_i was defined

in (2.53) and the amplitude of the modes is

$$A_{lm} = \begin{cases} \sqrt{\dfrac{2\epsilon_m}{d_p h}} & \text{for LSE modes} \\ \\ \sqrt{\dfrac{2\epsilon_l}{d_p h}} & \text{for LSM modes.} \end{cases} \tag{2.81}$$

2.2.1 Fields under LSE excitation

We now first assume that the bi-dimensional cavity is excited by the s-th LSE mode on port p. The modal indices of this mode are (l, m) (i.e. $\mathbf{e}_s = \mathbf{e}_{lm}^{\text{LSE}}$). The LSE mode is directed in $\hat{\mathbf{z}}$. Since the structure is constant in this direction, the electromagnetic fields within the cavity ($\mathbf{E}_s^F$ and $\mathbf{H}_s^F$) can be derived from the same potential as the LSE mode. In this case, they can be derived from an electric vector $\mathbf{F}_s$ as:

$$\left.\begin{aligned} \mathbf{E}_s^F &= \frac{-1}{\varepsilon}\nabla \times \mathbf{F}_s \\ \mathbf{H}_s^F &= \frac{-j}{k\eta\varepsilon}\left(k^2\mathbf{F}_s + \nabla\nabla\cdot\mathbf{F}_s\right) \end{aligned}\right\} \quad \mathbf{F}_s(\mathbf{r}, z) = \varphi_s^F(k, \mathbf{r})\,\sin\left(\frac{l\pi z}{h}\right)\hat{\mathbf{z}} \tag{2.82}$$

where φ_s^F is a scalar potential defined in the surface S and $\eta = \sqrt{\mu/\varepsilon}$ is the medium impedance. Note that this field can only exist for $l > 0$. Developing the vector operators, we can obtain the different field components as:

$$\begin{aligned} \mathbf{H}_s^F \cdot \hat{\mathbf{u}}_1 &= \frac{-j}{k\eta\varepsilon}\frac{l\pi}{h}\frac{\partial\varphi_s^F(k,\mathbf{r})}{\partial u_1}\cos\left(\frac{l\pi z}{h}\right) & \mathbf{E}_s^F \cdot \hat{\mathbf{u}}_1 &= \frac{-1}{\varepsilon}\frac{\partial\varphi_s^F(k,\mathbf{r})}{\partial u_2}\sin\left(\frac{l\pi z}{h}\right) \\ \mathbf{H}_s^F \cdot \hat{\mathbf{u}}_2 &= \frac{-j}{k\eta\varepsilon}\frac{l\pi}{h}\frac{\partial\varphi_s^F(k,\mathbf{r})}{\partial u_2}\cos\left(\frac{l\pi z}{h}\right) & \mathbf{E}_s^F \cdot \hat{\mathbf{u}}_2 &= \frac{1}{\varepsilon}\frac{\partial\varphi_s^F(k,\mathbf{r})}{\partial u_1}\sin\left(\frac{l\pi z}{h}\right) \end{aligned} \tag{2.83}$$

$$\mathbf{H}_s^F \cdot \hat{\mathbf{z}} = \frac{-j\left[k^2 - \left(\frac{l\pi}{h}\right)^2\right]}{k\eta\varepsilon}\varphi_s^F(k,\mathbf{r})\sin\left(\frac{l\pi z}{h}\right) \qquad \mathbf{E}_s^F \cdot \hat{\mathbf{z}} = 0$$

where $\mathbf{r} = \mathbf{r}(r)$ is the projection of the field point into surface S and z the coordinate of the field point in the $\hat{\mathbf{z}}$ direction. The coordinate system employed is depicted in Fig. (2.5). The frequency and spatial dependence of the electromagnetic fields (with $\mathbf{r}$ and z) is omitted for compactness, and assumed throughout this chapter.

The vector wave equation for the electric field (2.2) can be transformed into an equation for the vector potential $\mathbf{F}_s$. After application of a procedure equivalent

to the one described for TE solenoidal modes in section 2.1.3.1, the wave equation for the vector potential $\mathbf{F}_s$ becomes:

$$\nabla^2 \mathbf{F}_s + k^2 \mathbf{F}_s = 0. \tag{2.84}$$

This implies that the scalar potential φ_s^F must satisfy:

$$\left\{ \nabla_{\mathrm{T}}^2 + \left[k^2 - \left(\frac{l\pi}{h} \right)^2 \right] \right\} \varphi_s^F(k, \mathbf{r}) = 0 \tag{2.85}$$

In addition, potential φ_s^F must fulfill the boundary condition (named Θ_{lm}^F) set by the metallic walls and the LSE_{lm}^z mode of excitation:

$$\Theta_{lm}^F = \hat{\mathbf{n}} \cdot \nabla_{\mathrm{T}} \varphi_s^F \Big|_{\partial S} = \begin{cases} \dfrac{\varepsilon\ \mathbf{e}_s \cdot \hat{\mathbf{t}}_p}{\sin\left(\frac{l\pi z}{h}\right)} = \varepsilon\, A_{lm}\, \cos\left(\dfrac{m\pi\, t_p}{d_p} \right) & \text{for points on port } p \\ 0 & \text{otherwise.} \end{cases} \tag{2.86}$$

From (2.85), it is apparent that we can find the solution for a certain value of l (for example, $l = 1$), and then obtain the solution for any other value of l by means of a simple transformation in the k variable [134]. For instance, given $\varphi_{s1}^F(k', \mathbf{r})$, which is the solution of

$$\left\{ \nabla_{\mathrm{T}}^2 + \left[k'^2 - \left(\frac{\pi}{h} \right)^2 \right] \right\} \varphi_{s1}^F(k', \mathbf{r}) = 0, \tag{2.87}$$

and applying the frequency transformation

$$k' = \sqrt{k^2 - \left(\frac{l\pi}{h} \right)^2 + \left(\frac{\pi}{h} \right)^2}, \tag{2.88}$$

we obtain a function that fulfills

$$\left\{ \nabla_{\mathrm{T}}^2 + \left[k^2 - \left(\frac{l\pi}{h} \right)^2 \right] \right\} \varphi_{s1}^F \left(\sqrt{k^2 - \left(\frac{l\pi}{h} \right)^2 + \left(\frac{\pi}{h} \right)^2}, \mathbf{r} \right) = 0 \tag{2.89}$$

along with the boundary condition Θ_{1m}^F. Comparing (2.89) with (2.85), and noting that the boundary conditions Θ_{1m}^F and Θ_{lm}^F are equal (since $A_{1m} = A_{lm}$), we conclude that the objective potential φ_s^F can be directly expressed in terms of φ_{s1}^F as:

$$\varphi_s^F(k, \mathbf{r}) = \varphi_{s1}^F \left(\sqrt{k^2 - k_l^2}, \mathbf{r} \right) \tag{2.90}$$

with $k_l = \sqrt{(l\pi/h)^2 - (\pi/h)^2}$. This particular potential φ_{s1}^F is the one used to derive the electromagnetic fields in a purely E-plane problem.

Substituting (2.90) into (2.83) and expressing the E-plane potential and its transverse derivatives in terms of the corresponding E-plane field components (in the transformed domain), the full-wave electromagnetic field is expressed as:

$$\mathbf{H}_s^F(k)\cdot\hat{\mathbf{u}}_1 = \frac{l\sqrt{k^2-k_l^2}}{k}\,\frac{\mathbf{H}_{s1}^F\left(\sqrt{k^2-k_l^2}\right)\cdot\hat{\mathbf{u}}_1}{\cos\left(\frac{\pi z}{h}\right)}\,\cos\left(\frac{l\pi z}{h}\right) \tag{2.91a}$$

$$\mathbf{H}_s^F(k)\cdot\hat{\mathbf{u}}_2 = \frac{l\sqrt{k^2-k_l^2}}{k}\,\frac{\mathbf{H}_{s1}^F\left(\sqrt{k^2-k_l^2}\right)\cdot\hat{\mathbf{u}}_2}{\cos\left(\frac{\pi z}{h}\right)}\,\cos\left(\frac{l\pi z}{h}\right) \tag{2.91b}$$

$$\mathbf{H}_s^F(k)\cdot\hat{\mathbf{z}} = \frac{\sqrt{k^2-k_l^2}}{k}\,\frac{\mathbf{H}_{s1}^F\left(\sqrt{k^2-k_l^2}\right)\cdot\hat{\mathbf{z}}}{\sin\left(\frac{\pi z}{h}\right)}\,\sin\left(\frac{l\pi z}{h}\right) \tag{2.91c}$$

$$\mathbf{E}_s^F(k)\cdot\hat{\mathbf{u}}_1 = \frac{\mathbf{E}_{s1}^F\left(\sqrt{k^2-k_l^2}\right)\cdot\hat{\mathbf{u}}_1}{\sin\left(\frac{\pi z}{h}\right)}\,\sin\left(\frac{l\pi z}{h}\right) \tag{2.91d}$$

$$\mathbf{E}_s^F(k)\cdot\hat{\mathbf{u}}_2 = \frac{\mathbf{E}_{s1}^F\left(\sqrt{k^2-k_l^2}\right)\cdot\hat{\mathbf{u}}_2}{\sin\left(\frac{\pi z}{h}\right)}\,\sin\left(\frac{l\pi z}{h}\right) \tag{2.91e}$$

$$\mathbf{E}_s^F(k)\cdot\hat{\mathbf{z}} = 0 \tag{2.91f}$$

where $\mathbf{E}_{s1}^F$ and $\mathbf{H}_{s1}^F$ are the electric and magnetic fields within the cavity excited by the LSE_{1m}^z mode.

By using this transformation in the variable k, the size of the problem has been reduced. Instead of computing the field for all excitation modes, only those with $l = 1$ are initially considered. Then, the field for all the other modes is immediately obtained through the proposed frequency transformation. A systematic procedure to numerically compute the electromagnetic fields in bi-dimensional cavities with arbitrary shape, under excitation of the LSE_{1m}^z mode, is explained in the following section.

2.2.1.1 Field solution in E-plane cavities

The proposed methodology to solve the electromagnetic fields within a bi-dimensional cavity excited by LSE_{1m}^z modes involves two steps. First, the potential φ_{s1}^F

and its normal derivative ($\partial\varphi_{s1}^F/\partial n$) are found on the contour ∂S of the cross-section of the cavity (see Fig. 2.5 and Fig. 2.7) at any wavenumber k in a very efficient manner. This allows the computation of the electric and magnetic fields on the walls of the cavity through the application of (2.83). Second, the integral equation

$$\varphi_{s1}^F(k,\mathbf{r}) = \oint_{\partial S}\left[G(k_0,R)\frac{\partial\varphi_{s1}^F(k,\mathbf{r}')}{\partial n} - \varphi_{s1}^F(k,\mathbf{r}')\frac{\partial G(k_0,R)}{\partial n}\right]dr' \tag{2.92}$$

and its transverse gradient

$$\nabla_{\mathrm{T}}\varphi_{s1}^F(k,\mathbf{r}) = \oint_{\partial S}\left\{\nabla_{\mathrm{T}}G(k_0,R)\frac{\partial\varphi_{s1}^F(k,\mathbf{r}')}{\partial n} - \varphi_{s1}^F(k,\mathbf{r}')\nabla_{\mathrm{T}}\left[\frac{\partial G(k_0,R)}{\partial n}\right]\right\}dr' \tag{2.93}$$

are numerically solved in order to compute the potential φ_{s1}^F and $\nabla_{\mathrm{T}}\varphi_{s1}^F$ at points $\mathbf{r}$ within S. Details on the derivation of (2.92) can be found in Appendix B. $\mathbf{r}' = \mathbf{r}(r')$ denotes a source point on the contour ∂S. R is the distance between $\mathbf{r}$ and $\mathbf{r}'$ (see Fig. 2.7). $k_0 = \sqrt{k^2 - (\pi/h)^2}$ is, according to (2.87), the eigenvalue associated with φ_{s1}^F. Note that, throughout this section, k refers to variable k' in (2.87). $G(k_0,R)$ is the two-dimensional Green's function

$$G(k_0,R) = C_0 J_0(k_0 R) - \frac{1}{4}Y_0(k_0 R) \tag{2.94}$$

where J_0 is the zero-order Bessel function of the first kind, Y_0 is the zero-order Bessel function of the second kind. C_0 is a complex constant that can be arbitrarily chosen. Appendix B contains more information on this particular form of the two-dimensional Green's function, first proposed in [135]. The choice $C_0 = -j/4$ reduces (2.94) to the classical two-dimensional free space Green's function:

$$G(k_0,R) = \frac{H_0^{(2)}(k_0 R)}{4j} \tag{2.95}$$

where $H_0^{(2)}$ is the zero-order Hankel function of the second kind. Finally, from φ_{s1}^F, the electric and magnetic fields at $\mathbf{r}$ are immediately obtained via (2.83).

As shown, the problem has now been reduced to the computation of φ_{s1}^F and its normal derivative $\partial\varphi_{s1}^F/\partial n$ on the contour ∂S. On the one hand, we have seen that the normal derivative of the scalar potential on the contour differs from zero only at the ports:

$$\left.\frac{\partial\varphi_{s1}^F}{\partial n}\right|_{\partial S} = \begin{cases} \dfrac{\varepsilon\ \mathbf{e}_{s1}\cdot\hat{\mathbf{t}}_p}{\sin\left(\frac{\pi z}{h}\right)} = \varepsilon\, A_{1m}\cos\left(\dfrac{m\pi\, t_p}{d_p}\right) & \text{for points on port } p \\ 0 & \text{otherwise.} \end{cases} \tag{2.96}$$

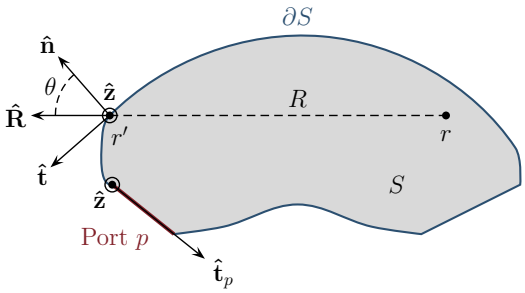

Figure 2.7: Geometry variables and vectors considered during the computation of potential φ_{s1}^F.

On the other hand, the potential φ_{s1} can be related to the z-directed magnetic field according to (2.83):

$$\varphi_{s1}^F(k,\mathbf{r}) = \frac{jk\eta\varepsilon}{\left[k^2 - \left(\frac{\pi}{h}\right)^2\right]} \frac{\mathbf{H}_{s1}^F \cdot \hat{\mathbf{z}}}{\sin\left(\frac{\pi z}{h}\right)}. \tag{2.97}$$

Kurokawa's field expansion can be used to determine the z-directed magnetic field. Only magnetic irrotational and solenoidal TE modes are coupled to the LSE_{1m}^z excitation. Starting from (2.10b), the low-frequency limit is extracted from the modal series involving solenoidal modes [133]. The z-directed component can then be written as:

$$\begin{aligned}
\mathbf{H}_{s1}^F \cdot \hat{\mathbf{z}} \;=\; & \frac{1}{jk\eta} \sum_{i=1}^{\infty} \left[\int_{S_p} (\hat{\mathbf{z}}_g \times \mathbf{e}_{s1}) \cdot \mathbf{g}_{i1} \, dS \right] \mathbf{g}_{i1} \cdot \hat{\mathbf{z}} \\
+ \; & \frac{jk}{\eta} \sum_{i=1}^{\infty} \frac{1}{\kappa_{i1}^2} \left[\int_{S_p} (\hat{\mathbf{z}}_g \times \mathbf{e}_{s1}) \cdot \boldsymbol{\mathcal{H}}_{i1}^{\mathrm{TE}} \, dS \right] \boldsymbol{\mathcal{H}}_{i1}^{\mathrm{TE}} \cdot \hat{\mathbf{z}} \\
+ \; & \frac{jk^3}{\eta} \sum_{i=1}^{\infty} \frac{1}{(\kappa_{i1}^2 - k^2)\,\kappa_{i1}^2} \left[\int_{S_p} (\hat{\mathbf{z}}_g \times \mathbf{e}_{s1}) \cdot \boldsymbol{\mathcal{H}}_{i1}^{\mathrm{TE}} \, dS \right] \boldsymbol{\mathcal{H}}_{i1}^{\mathrm{TE}} \cdot \hat{\mathbf{z}}
\end{aligned} \tag{2.98}$$

where $\kappa_{i1} = \sqrt{\left(\chi_i^{\mathrm{TE}}\right)^2 + (\pi/h)^2}$, as defined in (2.39) for $l = 1$. Note that the relationship $\hat{\mathbf{n}} = -\hat{\mathbf{z}}_g$ has been used. Isolating the rapidly converging series of solenoidal modes, as it is done in (2.98), is key to increase the efficiency of the analysis method. It was shown in section 2.1.4 that Kurokawa's field expansion requires a large number of modes to solve (2.98) accurately. However, the majority of modes are necessary to reach convergence in its first two series. They decrease the efficiency of Kurokawa's field expansion and deem its application impractical.

In contrast, the third series (associated with k^3) converges very rapidly, and thus only requires a small amount of modes. For that reason, the proposed formulation does not intend to solve Kurokawa's field expansion directly. Instead, two techniques are combined in order to increase the efficiency of the analysis. On the one hand, the integral equation formulation of [58] is employed to compute the first two terms of the expansion without actually solving any series. Then, the BI-RME method is applied to obtain the reduced number of modes in the cross section of the cavity required to evaluate the rapidly convergent series of (2.98).

From (2.98), the z-component of the magnetic field can be expressed in the form:

$$\mathbf{H}_{s1}^{F}\cdot\hat{\mathbf{z}}=\frac{\mathcal{A}_{s1}^{F}}{j\eta k}+\frac{jk}{\eta}\mathcal{B}_{s1}^{F}+\frac{jk^{3}}{\eta}\sum_{i=1}^{\infty}\frac{\left[\int_{S_p}\left(\hat{\mathbf{z}}_g\times\mathbf{e}_{s1}\right)\cdot\boldsymbol{\mathcal{H}}_{i1}^{\mathrm{TE}}\,dS\right]\boldsymbol{\mathcal{H}}_{i1}^{\mathrm{TE}}\cdot\hat{\mathbf{z}}}{\left(\kappa_{i1}^{2}-k^{2}\right)\kappa_{i1}^{2}}. \tag{2.99}$$

Introducing (2.99) in (2.97), and after some algebraical manipulations, the scalar potential φ_{s1}^{F} can be represented in terms of k as:

$$\varphi_{s1}^{F}(k,\mathbf{r})=\left[\alpha_{s1}^{F}(\mathbf{r})+k^{2}\beta_{s1}^{F}(\mathbf{r})+\frac{k^{4}}{k^{2}-\left(\frac{\pi}{h}\right)^{2}}\gamma_{s1}^{F}(k,\mathbf{r})\right]\varepsilon \tag{2.100}$$

where

$$\left(\frac{\pi}{h}\right)^{2}\alpha_{s1}^{F}(\mathbf{r}) = \frac{-\mathcal{A}_{s1}^{F}}{\sin\left(\frac{\pi z}{h}\right)} \tag{2.101a}$$

$$\left(\frac{\pi}{h}\right)^{2}\beta_{s1}^{F}(\mathbf{r})-\alpha_{s1}^{F}(\mathbf{r}) = \frac{\mathcal{B}_{s1}^{F}}{\sin\left(\frac{\pi z}{h}\right)} \tag{2.101b}$$

$$\beta_{s1}^{F}(\mathbf{r})+\gamma_{s1}^{F}(k,\mathbf{r}) = -\sum_{i=1}^{\infty}\frac{\left[\int_{S_p}\left(\hat{\mathbf{z}}_g\times\mathbf{e}_{s1}\right)\cdot\boldsymbol{\mathcal{H}}_{i1}^{\mathrm{TE}}\,dS\right]}{\left(\kappa_{i1}^{2}-k^{2}\right)\kappa_{i1}^{2}}\frac{\boldsymbol{\mathcal{H}}_{i1}^{\mathrm{TE}}\cdot\hat{\mathbf{z}}}{\sin\left(\frac{\pi z}{h}\right)}. \tag{2.101c}$$

It is clear that, in order to perfectly determine the scalar potential φ_{s1}^{F} on the contour ∂S, three functions have to be obtained: α_{s1}^{F}, β_{s1}^{F} and γ_{s1}^{F}. The first two, α_{s1}^{F} and β_{s1}^{F} (which do not depend on k), will be evaluated via an integral equation technique. Afterwards, the series in (2.101c) involving the solenoidal modes will be computed through the application of the BI-RME method [136], and γ_{s1}^{F} obtained.

2.2.1.2 Computation of α_{s1}^{F} and β_{s1}^{F}

From Green's first identity, the potential φ_{s1}^{F} at points $\mathbf{r}$ laying on the contour ∂S satisfies (see section B.2):

$$\varphi_{s1}^{F}(k,\mathbf{r})=2\oint_{\partial S}\left[G(k_0,R)\frac{\partial\varphi_{s1}^{F}(k,\mathbf{r}')}{\partial n}-\varphi_{s1}^{F}(k,\mathbf{r}')\frac{\partial G(k_0,R)}{\partial n}\right]dr'. \tag{2.102}$$

The classical two-dimensional Green's function (i.e. $C_0 = -j/4$ in (2.94)) is chosen in this particular case. This function and its normal derivative on the contour are:

$$G(k_0, R) = \frac{H_0^{(2)}(k_0\, R)}{4j} \tag{2.103a}$$

$$\frac{\partial G(k_0, R)}{\partial n} = \frac{\partial G(k_0, R)}{\partial R}\frac{\partial R}{\partial n} = \frac{j}{4} k_0\, H_1^{(2)}(k_0\, R)\cos\theta. \tag{2.103b}$$

For the purposes of this work, both functions can be approximated by their first-order expansion on k:

$$G(k_0, R) \approx \widetilde{G} = \frac{1}{2\pi}\, K_0\Big(\frac{\pi}{h}\, R\Big) + k^2 \frac{h}{\pi}\frac{R}{4\pi}\, K_1\Big(\frac{\pi}{h}\, R\Big) \tag{2.104a}$$

$$\frac{\partial G(k_0, R)}{\partial n} \approx \frac{\partial \widetilde{G}}{\partial n} = \frac{\partial \widetilde{G}}{\partial R}\cos\theta = \left[\frac{-1}{2h}\, K_1\Big(\frac{\pi}{h}\, R\Big) - k^2 \frac{R}{4\pi}\, K_0\Big(\frac{\pi}{h}\, R\Big)\right]\cos\theta \tag{2.104b}$$

where K_0 and K_1 are, respectively, the zero- and first-order modified Bessel functions of the second kind.

Substituting (2.96), (2.100) and (2.104) into (2.102), and then grouping the terms with the same power of k, we obtain the following system of integral equations:

$$\begin{aligned} k^0 \Rightarrow \frac{\alpha_{s1}^F(\mathbf{r})}{2} &= \frac{A_{1m}}{2\pi}\int_0^{d_p} K_0\left(\frac{\pi R_p}{h}\right)\cos\left(\frac{m\pi}{d_p}t_p'\right) dt_p' \\ &+ \frac{1}{2h}\oint_{\partial S}\cos\theta\, K_1\left(\frac{\pi R}{h}\right)\alpha_{s1}^F(\mathbf{r}')\, dr' \end{aligned} \tag{2.105a}$$

$$\begin{aligned} k^2 \Rightarrow \frac{\beta_{s1}^F(\mathbf{r})}{2} &= \frac{A_{1m}\, h}{4\pi^2}\int_0^{d_p} R_p\, K_1\left(\frac{\pi}{h}R_p\right)\cos\left(\frac{m\pi}{d_p}t_p'\right) dt_p' \\ &+ \frac{1}{4\pi}\oint_{\partial S}\cos\theta\, R\, K_0\left(\frac{\pi R}{h}\right)\alpha_{s1}^F(\mathbf{r}')\, dr' \\ &+ \frac{1}{2h}\oint_{\partial S}\cos\theta K_1\left(\frac{\pi R}{h}\right)\beta_{s1}^F(\mathbf{r}')\, dr'. \end{aligned} \tag{2.105b}$$

where R_p represents the distance between $\mathbf{r}$ and the point where the differential dt_p' is taken (namely $\mathbf{r}_p' = \mathbf{r}(t_p')$).

The method of moments (MoM) in its Galerkin version [19] can be applied to solve this system of integral equations. In order to do so, the unknowns α_{s1}^F and β_{s1}^F (on the contour ∂S) are discretized and expanded in a finite series of $\mathcal{K}$ basis

functions:

$$\alpha_{s1}^F(\mathbf{r}) = \sum_{\kappa=1}^{\mathcal{K}} w_{s1\kappa}^F \, f_\kappa(\mathbf{r}) \tag{2.106a}$$

$$\beta_{s1}^F(\mathbf{r}) = \sum_{\kappa=1}^{\mathcal{K}} v_{s1\kappa}^F \, f_\kappa(\mathbf{r}). \tag{2.106b}$$

The basis functions f_κ are piece-wise parabolic splines. More information about the basis functions employed can be found in chapter 5 of [133].

After simple mathematical manipulations, the system of integral equations is transformed into a matrix system in the form:

$$\left(\mathbf{L}^F + \mathbf{M}^F\right) \cdot \mathbf{w}^F = \mathbf{G}^F \tag{2.107a}$$

$$\left(\mathbf{L}^F + \mathbf{M}^F\right) \cdot \mathbf{v}^F = \mathbf{N}^F \cdot \mathbf{w}^F + \mathbf{T}^F \tag{2.107b}$$

where $\mathbf{w}^F = [w_{s11}^F, \ldots, w_{s1\mathcal{K}}^F]^T$ and $\mathbf{v}^F = [v_{s11}^F, \ldots, v_{s1\mathcal{K}}^F]^T$ are vectors with the unknown $\mathcal{K}$ expansion coefficients, and the remaining matrices and vectors of the problem are defined as:

$$L_{ij}^F = \frac{1}{2} \oint_{\partial S} f_i(\mathbf{r}) \, f_j(\mathbf{r}) \, dr \tag{2.108a}$$

$$M_{ij}^F = \frac{-1}{2h} \oint_{\partial S} \oint_{\partial S} \cos\theta \; K_1\!\left(\frac{\pi R}{h}\right) \, f_i(\mathbf{r}) \, f_j(\mathbf{r}') \, dr \, dr' \tag{2.108b}$$

$$G_i^F = \frac{A_{1m}}{2\pi} \oint_{\partial S} \int_0^{d_p} \cos\left(\frac{m\pi}{d_p} t_p'\right) K_0\!\left(\frac{\pi R_p}{h}\right) \, f_i(\mathbf{r}) \; dr \, dt_p' \tag{2.108c}$$

$$N_{ij}^F = \frac{1}{4\pi} \oint_{\partial S} \oint_{\partial S} R \, K_0\!\left(\frac{\pi R}{h}\right) \cos\theta \, f_i(\mathbf{r}) \, f_j(\mathbf{r}') \, dr \, dr' \tag{2.108d}$$

$$T_i^F = \frac{A_{1m} h}{4\pi^2} \oint_{\partial S} \int_0^{d_p} \cos\left(\frac{m\pi}{d_p} t_p'\right) R_p \, K_1\!\left(\frac{\pi R_p}{h}\right) \, f_i(\mathbf{r}) \; dr \, dt_p' \tag{2.108e}$$

where $i, j = 1, \ldots, \mathcal{K}$. Matrices $\mathbf{L}^F$, $\mathbf{M}^F$ and $\mathbf{N}^F$ are independent of the excitation modes, thus they only need to be computed once, regardless of the total number of modes. The other vectors have to be computed for all the different LSE_{1m}^z modes. However, they can be stored in a matrix form in order to use matrix algebra to solve the system simultaneously, with all the excitations present.

Regarding the construction of these matrices and vectors, it can be seen that most of the integrals involve singular integrands, therefore further work has to be done to permit their numerical solution by classical quadrature techniques. Appendix C contains a description of how the integrals in each matrix are treated. In the original formulation of [58], only straight segments were considered. In this

thesis, the singular integrals associated with circular and elliptical arcs are also solved for the first time. By doing so, the accuracy in the analysis of structures including this type of contours is significantly increased. Finally, by solving (2.107) the coefficients of the expansions for α_{s1}^F and β_{s1}^F are obtained.

2.2.1.3 Computation of γ_{s1}^F

Once β_{s1}^F has been determined, it is necessary to compute the different terms that form the series in (2.101c) to obtain γ_{s1}^F. The objective, now, is the computation of

$$\gamma_{s1}^F(k,\mathbf{r}) = -\beta_{s1}^F(\mathbf{r}) - \sum_{i=1}^{\infty} \frac{\mathcal{C}_{s1i}^F}{\kappa_{i1}\left(\kappa_{i1}^2 - k^2\right)} \frac{\boldsymbol{\mathcal{H}}_{i1}^{\mathrm{TE}} \cdot \hat{\mathbf{z}}}{\sin\left(\frac{\pi z}{h}\right)} \tag{2.109}$$

where the coefficients $\mathcal{C}_{s1i}^F$ are:

$$\mathcal{C}_{s1i}^F = \frac{1}{\kappa_{i1}} \int_{S_p} \left(\hat{\mathbf{z}}_g \times \mathbf{e}_{s1}\right) \cdot \boldsymbol{\mathcal{H}}_{i1}^{\mathrm{TE}}\, dS. \tag{2.110}$$

Making use of the modal expressions of LSE modes (2.79), these coefficients can be expressed as:

$$\mathcal{C}_{s1i}^F = \frac{-A_{1m}}{\kappa_{i1}} \int_0^{d_p} \int_0^h \cos\left(\frac{m\pi}{d_p} t_p'\right) \sin\left(\frac{\pi}{h} z\right) \boldsymbol{\mathcal{H}}_{i1}^{\mathrm{TE}} \cdot \hat{\mathbf{z}}\, dz\, dt_p'. \tag{2.111}$$

To solve the integrals and compute these coefficients, we only need to obtain the z-directed component of the solenoidal TE modes of the closed cavity. As described in (2.44), these modes can be derived from the TE potential φ_i^{TE} of a waveguide with cross-section S as:

$$\boldsymbol{\mathcal{H}}_{i1}^{\mathrm{TE}} \cdot \hat{\mathbf{z}} = \frac{-\chi_i^{\mathrm{TE}} \sqrt{2/h}}{\kappa_{i1}} \varphi_i^{\mathrm{TE}}(\mathbf{r}) \sin\left(\frac{\pi z}{h}\right) \tag{2.112}$$

with $\kappa_{i1} = \sqrt{\left(\chi_i^{\mathrm{TE}}\right)^2 + (\pi/h)^2}$, as previously determined. At this point, the BI-RME method [136] will be applied to compute the potential φ_i^{TE} for a finite number of TE modes in an equivalent waveguide with cross-section S. This method provides both the wavenumbers χ_i^{TE} of the TE modes and the modal current density tangential to the contour of the waveguide $\mathbf{J}_{\sigma i} \cdot \hat{\mathbf{t}}$. This current is also expanded as a series of basis functions. These basis functions are actually the same parabolic splines used to expand α_{s1}^F and β_{s1}^F. As explained in Appendix D, the potential φ_i^{TE} is related to the tangential current density in the walls of the equivalent waveguide as:

$$\varphi_i^{\mathrm{TE}}\Big|_{\partial S} = -\mathbf{J}_{\sigma i} \cdot \hat{\mathbf{t}} = -\sum_{\kappa=1}^{\mathcal{K}} B_{\kappa i}^{\mathrm{TE}} f_\kappa(\mathbf{r}) \tag{2.113}$$

where $B_{\kappa i}^{\mathrm{TE}}$ are expansion coefficients provided by the BI-RME method and f_κ the aforementioned parabolic spline basis functions of the current density expansion. $\mathcal{K}$ is the total number of basis functions defined in the contour ∂S.

Substituting (2.112) and (2.113) into (2.111), the coefficients $\mathcal{C}_{s1i}^F$ are:

$$\mathcal{C}_{s1i}^F = \frac{-\chi_i^{\mathrm{TE}}\sqrt{\epsilon_m/d_p}}{\kappa_{i1}^2} \sum_{\kappa=p_0}^{p_f} B_{\kappa i}^{\mathrm{TE}} \int_{\delta_k} \cos\left(\frac{m\pi}{d_p} t'_p\right) f_\kappa(\mathbf{r}'_p)\, dt'_p \tag{2.114}$$

where it is assumed that port p contains the basis functions from p_0 to p_f, each having a length of δ_k. We can define a variable $I_{\kappa m}^F$ that contains the remaining integral:

$$I_{\kappa m}^F = -\sqrt{\frac{\epsilon_m}{d_p}} \int_{\delta_\kappa} f_\kappa(\mathbf{r}'_p) \cos\left(\frac{m\pi}{d_p} t'_p\right) dt'_p. \tag{2.115}$$

To simplify the integration over all the segments, the basis functions are normalized according to a parameter $u \in [-0.5, 0.5]$. With this parametrization,

$$f_\kappa(\mathbf{r}'_p) = c_{1\kappa}\, u^2 + c_{2\kappa}\, u + c_{3\kappa} \tag{2.116a}$$

$$t'_p = t_{0\kappa} + \delta_\kappa (u + 0.5) \tag{2.116b}$$

$$dt'_p = \delta_\kappa\, du \tag{2.116c}$$

where $t_{0\kappa}$ is the initial point of segment κ along the $\hat{\mathbf{t}}$-direction at port p, and $c_{1\kappa}$, $c_{2\kappa}$ and $c_{3\kappa}$ are real coefficients. Using this parametrization, the integral in (2.115) is solved. The solution for $I_{\kappa m}^F$ is:

$$\begin{aligned} I_{\kappa m}^F &= -\sqrt{\frac{2}{d_p}}\delta_\kappa \left\{ \sin(0.5\alpha_\kappa + \beta_\kappa) \left[c_{1\kappa} \left(\frac{0.25}{\alpha_\kappa} - \frac{2}{\alpha_\kappa^3} \right) + \frac{0.5c_{2\kappa} + c_{3\kappa}}{\alpha_\kappa} \right] \right. \\ &+ \sin(-0.5\alpha_\kappa + \beta_\kappa) \left[-c_{1\kappa} \left(\frac{0.25}{\alpha_\kappa} - \frac{2}{\alpha_\kappa^3} \right) + \frac{0.5c_{2\kappa} - c_{3\kappa}}{\alpha_\kappa} \right] \\ &+ \left. \cos(0.5\alpha_\kappa + \beta_\kappa) \left[\frac{c_{1\kappa} + c_{2\kappa}}{\alpha_\kappa^2} \right] + \cos(-0.5\alpha_\kappa + \beta_\kappa) \left[\frac{c_{1\kappa} - c_{2\kappa}}{\alpha_\kappa^2} \right] \right\} \end{aligned} \tag{2.117}$$

where

$$\alpha_\kappa = \frac{m\pi\delta_\kappa}{d_p} \tag{2.118a}$$

$$\beta_\kappa = \frac{m\pi}{d_p} (t_{0\kappa} + 0.5\delta_\kappa) \tag{2.118b}$$

In the particular case of $m = 0$, this integral becomes:

$$I_{\kappa 0}^F = \frac{-1}{\sqrt{d_p}} \delta_\kappa \left[\frac{0.25c_{1\kappa}}{3} + c_{3\kappa} \right]. \tag{2.119}$$

Finally, the coefficients $\mathcal{C}^F_{s1i}$ can be expressed as:

$$\mathcal{C}^F_{s1i} = \frac{\chi^{\mathrm{TE}}_i}{\kappa^2_{i1}} \sum_{\kappa=p_0}^{p_f} B^{\mathrm{TE}}_{\kappa i} I^F_{\kappa m}. \tag{2.120}$$

Substituting these $\mathcal{C}^F_{s1i}$ coefficients, the basis function expansion of β^F_{s1} and $\boldsymbol{\mathcal{H}}^{\mathrm{TE}}_{i1} \cdot \hat{\mathbf{z}}$ into (2.109), the function γ^F_{s1} is obtained:

$$\gamma^F_{s1}(k, \mathbf{r}) = -\sum_{\kappa=1}^{\mathcal{K}} f_\kappa(\mathbf{r}) \left[v^F_{s1\kappa} + \sqrt{\frac{2}{h}} \sum_{i=1}^{\infty} \frac{\chi^{\mathrm{TE}}_i}{\kappa^2_{i1}\left(\kappa^2_{i1} - k^2\right)} B^{\mathrm{TE}}_{\kappa i}\, \mathcal{C}^F_{s1i} \right]. \tag{2.121}$$

Finally, the scalar potential φ^F_{s1} used to derive the electromagnetic fields excited by the LSE_{1m} mode can be computed, on the contour ∂S, according to (2.100):

$$\begin{aligned} \varphi^F_{s1}(k, \mathbf{r}) \;=\; & \varepsilon \sum_{\kappa=1}^{\mathcal{K}} f_\kappa(\mathbf{r}) \left[w^F_{s1\kappa} - \frac{(\pi/h)^2\, k^2\, v^F_{s1\kappa}}{k^2 - \left(\frac{\pi}{h}\right)^2} \right. \\ - \; & \left. \frac{k^4 \sqrt{2/h}}{k^2 - \left(\frac{\pi}{h}\right)^2} \sum_{i=1}^{\infty} \frac{\chi^{\mathrm{TE}}_i}{\kappa^2_{i1}\left(\kappa^2_{i1} - k^2\right)} B^{\mathrm{TE}}_{\kappa i}\, \mathcal{C}^F_{s1i} \right]. \end{aligned} \tag{2.122}$$

This potential on the contour, along with its normal derivative defined in (2.96), are then substituted into (2.92) and (2.93) to obtain the potential at any point within the cavity. From the potential, the fields under LSE^z_{1m} excitation can be computed by application of (2.83). Finally, the field excited by any LSE^z_{lm} mode is obtained via the frequency transformation of (2.91).

2.2.2 Fields under LSM excitation

Under excitation of the s-th mode, LSM^z_{lm}, at port p (i.e. $\mathbf{e}_s = \mathbf{e}^{\mathrm{LSM}}_{lm}$), the electromagnetic field within a bi-dimensional cavity ($\mathbf{E}^A_s$ and $\mathbf{H}^A_s$) can be derived from a magnetic vector potential $\mathbf{A}_s$ as:

$$\left.\begin{aligned} \mathbf{E}^A_s &= \frac{-j}{k\eta\varepsilon}\left(k^2 \mathbf{A}_s + \nabla\nabla\cdot\mathbf{A}_s\right) \\ \mathbf{H}^A_s &= \frac{1}{\mu}\nabla\times\mathbf{A}_s \end{aligned}\right\} \quad \mathbf{A}_s(\mathbf{r}, z) = \varphi^A_s(k, \mathbf{r})\, \cos\left(\frac{l\pi z}{h}\right)\hat{\mathbf{z}} \tag{2.123}$$

where φ^A_s is a scalar potential defined in the surface S. This field exists for values of $l \geq 0$. Developing the vector operators, according to the coordinate system of

Fig. 2.5, the different field components are obtained:

$$\begin{aligned}
\mathbf{H}_s^A \cdot \hat{\mathbf{u}}_1 &= \frac{1}{\mu}\frac{\partial \varphi_s^A(k,\mathbf{r})}{\partial u_2}\cos\left(\frac{l\pi z}{h}\right) \qquad \mathbf{E}_s^A \cdot \hat{\mathbf{u}}_1 = \frac{j}{k\eta\varepsilon}\frac{l\pi}{h}\frac{\partial \varphi_s^A(k,\mathbf{r})}{\partial u_1}\sin\left(\frac{l\pi z}{h}\right) \\
\mathbf{H}_s^A \cdot \hat{\mathbf{u}}_2 &= \frac{-1}{\mu}\frac{\partial \varphi_s^A(k,\mathbf{r})}{\partial u_1}\cos\left(\frac{l\pi z}{h}\right) \quad \mathbf{E}_s^A \cdot \hat{\mathbf{u}}_2 = \frac{j}{k\eta\varepsilon}\frac{l\pi}{h}\frac{\partial \varphi_s^A(k,\mathbf{r})}{\partial u_2}\sin\left(\frac{l\pi z}{h}\right) \\
\mathbf{H}_s^A \cdot \hat{\mathbf{z}} &= 0 \qquad\qquad\qquad\qquad \mathbf{E}_s^A \cdot \hat{\mathbf{z}} = \frac{-j\left[k^2 - \left(\frac{l\pi}{h}\right)^2\right]}{k\eta\varepsilon}\varphi_s^A(k,\mathbf{r})\cos\left(\frac{l\pi z}{h}\right).
\end{aligned} \tag{2.124}$$

Following a similar procedure to the one described in the previous section, it can be seen that the vector potential $\mathbf{A}_s$ must satisfy the wave equation:

$$\nabla^2 \mathbf{A}_s + k^2 \mathbf{A}_s = 0. \tag{2.125}$$

This implies that the scalar potential φ_s^A must fulfill the Helmholtz equation:

$$\left\{\nabla_{\mathrm{T}}^2 + \left[k^2 - \left(\frac{l\pi}{h}\right)^2\right]\right\}\varphi_s^A(k,\mathbf{r}) = 0 \tag{2.126}$$

along with the boundary condition (Θ_{lm}^A) set by the lateral metallic walls and LSM_{lm}^z excitation (see (2.80)):

$$\Theta_{lm}^A(k) = \varphi_s^A\Big|_{\partial S} = \begin{cases} \dfrac{jk\eta\varepsilon}{\left[k^2 - \left(\frac{l\pi}{h}\right)^2\right]}\dfrac{\mathbf{e}_s \cdot \hat{\mathbf{z}}}{\cos\left(\frac{l\pi z}{h}\right)} = \dfrac{jk\eta\varepsilon A_{lm}\sin\left[\frac{m\pi}{d_p}t_p\right]}{\left[k^2 - \left(\frac{l\pi}{h}\right)^2\right]} & \text{on port p} \\ 0 & \text{otherwise.} \end{cases} \tag{2.127}$$

As can be seen, in this case the boundary condition actually depends on the parameter l. If the solution for a certain l is derived from the solution for a different value of l, a certain correction factor has to be applied to account for the different impedance level of both excitations.

Similarly, given the solution of (2.126) for a certain value of l (for example, $l = 0$), the solution for any other value can be computed by a simple frequency transformation. In particular, given φ_{s0}^A, which is the solution of

$$\left\{\nabla_{\mathrm{T}}^2 + k'^2\right\}\varphi_{s0}^A(k',\mathbf{r}) = 0 \tag{2.128}$$

along with the boundary condition Θ^A_{0m}, the field for any other LSM excitation can be computed by applying the frequency transformation

$$k' = \sqrt{k^2 - k_l^2} \qquad \text{with } k_l = \frac{l\pi}{h}. \tag{2.129}$$

As previously mentioned, the frequency transformation is not enough, by itself, to provide the adequate solution in this case. $\varphi^A_{s0}\left(\sqrt{k^2-k_l^2}, \mathbf{r}\right)$ and $\varphi^A_s(k, \mathbf{r})$ do not fulfill the same boundary condition and a correction factor has to be applied to obtain the desired solution. This factor can be obtained by dividing the objective boundary condition $\Theta^A_{lm}(k)$ by Θ^A_{0m} evaluated at the transformed frequency $\sqrt{k^2-k_l^2}$. Finally, we can express φ^A_s as:

$$\varphi^A_s(k, \mathbf{r}) = \frac{\Theta^A_{lm}(k)}{\Theta^A_{0m}\left(\sqrt{k^2-k_l^2}\right)}\ \varphi^A_{s0}\left(\sqrt{k^2-k_l^2}, \mathbf{r}\right) = \frac{k\sqrt{\epsilon_l}}{\sqrt{k^2-k_l^2}}\ \varphi^A_{s0}\left(\sqrt{k^2-k_l^2}, \mathbf{r}\right) \tag{2.130}$$

where the relationship $A_{lm}/A_{0m} = \sqrt{\epsilon_l}$ from (2.81) has also been used. The particular solution φ^A_{s0} corresponds to the scalar potential associated with a constant-height cavity subject to excitation by an H-plane (i.e. LSM^z_{0m}) mode .

The electric and magnetic fields of the full-wave problem can be related to those in the H-plane problem by:

$$\mathbf{H}^A_s(k)\cdot\hat{\mathbf{u}}_1 = \frac{k\sqrt{\epsilon_l}}{\sqrt{k^2-k_l^2}}\ \mathbf{H}^A_{s0}\left(\sqrt{k^2-k_l^2}\right)\cdot\hat{\mathbf{u}}_1\ \cos\left(\frac{l\pi z}{h}\right) \tag{2.131a}$$

$$\mathbf{H}^A_s(k)\cdot\hat{\mathbf{u}}_2 = \frac{k\sqrt{\epsilon_l}}{\sqrt{k^2-k_l^2}}\ \mathbf{H}^A_{s0}\left(\sqrt{k^2-k_l^2}\right)\cdot\hat{\mathbf{u}}_2\ \cos\left(\frac{l\pi z}{h}\right) \tag{2.131b}$$

$$\mathbf{H}^A_s(k)\cdot\hat{\mathbf{z}} = 0 \tag{2.131c}$$

$$\mathbf{E}^A_s(k)\cdot\hat{\mathbf{u}}_1 = \frac{-j\eta\, l\pi\sqrt{\epsilon_l}}{h\sqrt{k^2-k_l^2}}\ \mathbf{H}^A_{s0}\left(\sqrt{k^2-k_l^2}\right)\cdot\hat{\mathbf{u}}_2\ \sin\left(\frac{l\pi z}{h}\right) \tag{2.131d}$$

$$\mathbf{E}^A_s(k)\cdot\hat{\mathbf{u}}_2 = \frac{j\eta\, l\pi\sqrt{\epsilon_l}}{h\sqrt{k^2-k_l^2}}\ \mathbf{H}^A_{s0}\left(\sqrt{k^2-k_l^2}\right)\cdot\hat{\mathbf{u}}_1\ \sin\left(\frac{l\pi z}{h}\right) \tag{2.131e}$$

$$\mathbf{E}^A_s(k)\cdot\hat{\mathbf{z}} = \sqrt{\epsilon_l}\ \mathbf{E}^A_{s0}\left(\sqrt{k^2-k_l^2}\right)\cdot\hat{\mathbf{z}}\ \cos\left(\frac{l\pi z}{h}\right) \tag{2.131f}$$

where $\mathbf{E}^A_{s0}$ and $\mathbf{H}^A_{s0}$ are the electric and magnetic fields under excitation of the LSM^z_{0m} mode. Note that some electric field components are related to magnetic field components of the $l = 0$ problem, since their electric field counterparts are non-existent in the $l = 0$ problem. Finally, the electromagnetic field for the H-plane problem can be solved by using the technique explained in the following section.

2.2.2.1 Field solution in H-plane cavities

The procedure to obtain the electromagnetic fields in an H-plane cavity is equivalent to the one shown in section 2.2.1.1. The scalar potential φ_{s0}^{A} satisfies (2.92) and (2.93) with $k_0 = k$ (i.e. the eigenvalue of (2.128)). Therefore, the problem of determining the fields in H-plane cavities is reduced to computing the scalar potential φ_{s0}^{A} and its normal derivative on the contour ∂S. Note that, throughout this section, k equals variable k' in (2.128).

On the one hand, the scalar potential on the contour is null on the lateral walls, except for the port of excitation, as demonstrated in (2.127). On that port it is coincident with the z-directed electric field of excitation:

$$\left.\varphi_{s0}^{A}\right|_{\partial S} = \frac{j\eta\varepsilon}{k}\mathbf{E}_{s0}^{A}\cdot\hat{\mathbf{z}} = \begin{cases} \dfrac{j\eta\varepsilon A_{0m}}{k}\sin\left[\dfrac{m\pi}{d_q}t_p\right] & \text{on port p} \\ 0 & \text{otherwise.} \end{cases} \tag{2.132}$$

On the other hand, it is clear from (2.124) with $\hat{\mathbf{u}}_1 = \hat{\mathbf{n}}$ and $\hat{\mathbf{u}}_2 = \hat{\mathbf{t}}$ (see Fig. 2.7) that the normal derivative of the scalar potential is related to the tangential magnetic field as:

$$\frac{\partial\varphi_{s0}^{A}(k,\mathbf{r})}{\partial n} = -\mu\mathbf{H}_{s0}^{A}\cdot\hat{\mathbf{t}}. \tag{2.133}$$

Magnetic irrotational, harmonic (in N-times connected cavities) and solenoidal TM modes must be considered in the field expansion (2.10)-(2.11), thus obtaining the following expression for the tangential magnetic field:

$$\begin{aligned} \mathbf{H}_{s0}^{A}\cdot\hat{\mathbf{t}} &= \frac{1}{jk\eta}\left\{\sum_{i=1}^{\infty}\left[\int_{S_p}(\hat{\mathbf{z}}_g\times\mathbf{e}_{s0})\cdot\mathbf{g}_{i0}\,dS\right]\mathbf{g}_{i0}\cdot\hat{\mathbf{t}}\right. \\ &\qquad \left. + \sum_{i=1}^{N-1}\left[\int_{S_p}(\hat{\mathbf{z}}_g\times\mathbf{e}_{s0})\cdot\boldsymbol{\mathcal{H}}_{i}^{0}\,dS\right]\boldsymbol{\mathcal{H}}_{i}^{0}\cdot\hat{\mathbf{t}}\right\} \\ &+ \frac{jk}{\eta}\sum_{i=1}^{\infty}\frac{1}{\kappa_{i0}^{2}}\left[\int_{S_p}(\hat{\mathbf{z}}_g\times\mathbf{e}_{s0})\cdot\boldsymbol{\mathcal{H}}_{i0}^{\mathrm{TM}}\,dS\right]\boldsymbol{\mathcal{H}}_{i0}^{\mathrm{TM}}\cdot\hat{\mathbf{t}} \\ &+ \frac{jk^3}{\eta}\sum_{i=1}^{\infty}\frac{1}{(\kappa_{i0}^{2}-k^2)\,\kappa_{i0}^{2}}\left[\int_{S_p}(\hat{\mathbf{z}}_g\times\mathbf{e}_{s0})\cdot\boldsymbol{\mathcal{H}}_{i0}^{\mathrm{TM}}\,dS\right]\boldsymbol{\mathcal{H}}_{i0}^{\mathrm{TM}}\cdot\hat{\mathbf{t}}. \end{aligned} \tag{2.134}$$

In this case, the relevant eigenvalues of the closed cavity are $\kappa_{i0} = \chi_i^{\mathrm{TM}}$, according to (2.50) with $l = 0$.

As shown in (2.133), the tangential magnetic field is proportional to the normal derivative of the scalar potential φ^A_{s0}. Given the field expansion in (2.134), we can express the normal derivative of the scalar potential as:

$$\frac{\partial \varphi^A_{s0}(k,\mathbf{r})}{\partial n} = -\mu \left[\frac{\alpha^A_{s0}(\mathbf{r})}{jk\eta} + \frac{jk}{\eta}\beta^A_{s0}(\mathbf{r}) + \frac{jk^3}{\eta}\gamma^A_{s0}(k,\mathbf{r}) \right] \tag{2.135}$$

where

$$\alpha^A_{s0}(\mathbf{r}) = \sum_{i=1}^{\infty} \left[\int_{S_p} (\hat{\mathbf{z}}_g \times \mathbf{e}_{s0}) \cdot \mathbf{g}_{i0}\, dS \right] \mathbf{g}_{i0} \cdot \hat{\mathbf{t}} + \sum_{i=1}^{N-1} \left[\int_{S_p} (\hat{\mathbf{z}}_g \times \mathbf{e}_{s0}) \cdot \boldsymbol{\mathcal{H}}^0_i\, dS \right] \boldsymbol{\mathcal{H}}^0_i \cdot \hat{\mathbf{t}} \tag{2.136a}$$

$$\beta^A_{s0}(\mathbf{r}) = \sum_{i=1}^{\infty} \frac{1}{\kappa^2_{i0}} \left[\int_{S_p} (\hat{\mathbf{z}}_g \times \mathbf{e}_{s0}) \cdot \boldsymbol{\mathcal{H}}^{\mathrm{TM}}_{i0}\, dS \right] \boldsymbol{\mathcal{H}}^{\mathrm{TM}}_{i0} \cdot \hat{\mathbf{t}} \tag{2.136b}$$

$$\gamma^A_{s0}(k,\mathbf{r}) = \sum_{i=1}^{\infty} \frac{1}{(\kappa^2_{i0} - k^2)\,\kappa^2_{i0}} \left[\int_{S_p} (\hat{\mathbf{z}}_g \times \mathbf{e}_{s0}) \cdot \boldsymbol{\mathcal{H}}^{\mathrm{TM}}_{i0}\, dS \right] \boldsymbol{\mathcal{H}}^{\mathrm{TM}}_{i0} \cdot \hat{\mathbf{t}}. \tag{2.136c}$$

In order to develop an efficient procedure to obtain the electromagnetic field, the series in (2.136a) and (2.136b) will not be computed due to their poor convergence rate. Instead, the integral equation formulation of [59] (which leads to a linear system of equations) will be used. However, the computation of γ^A_{s0} will be done via the rapidly convergent series of (2.136c).

2.2.2.2 Computation of α^A_{s0} and β^A_{s0}

Since φ^A_{s0} already fulfills the homogeneous Helmholtz equation, it is subject to the integral equation seen in the analysis of E-plane cavities:

$$\varphi^A_{s0}(k,\mathbf{r}) = 2 \oint_{\partial S} \left[G(k,R) \frac{\partial \varphi^A_{s0}(k,\mathbf{r}')}{\partial\, n} - \varphi^A_{s0}(k,\mathbf{r}') \frac{\partial G(k,R)}{\partial n} \right] dr' \tag{2.137}$$

where G is the general two-dimensional Green's function of (2.94). This function is approximated by the first terms of its series expansion on k as:

$$\begin{aligned} G(k,R) \approx \widetilde{G} &= C_0 - \frac{1}{2\pi}\left[\ln\frac{k}{2} + \ln R + \gamma \right] \\ &+ k^2 \frac{R^2}{4}\left[-C_0 + \frac{1}{2\pi}\left(\ln\frac{k}{2} + \ln R + \gamma - 1 \right) \right] \end{aligned} \tag{2.138a}$$

$$\frac{\partial G(k,R)}{\partial n} = \frac{\partial G}{\partial R}\frac{\partial R}{\partial n} = \cos\theta \frac{\partial G}{\partial R} \approx \cos\theta \frac{\partial \widetilde{G}}{\partial R} \tag{2.138b}$$

$$\frac{\partial \widetilde{G}}{\partial R} = \frac{-1}{2\pi R} + k^2 \frac{R}{4}\left[-2C_0 + \frac{1}{\pi}\left(\ln\frac{k}{2} + \ln R + \gamma - 1 \right) + \frac{1}{2\pi} \right] \tag{2.138c}$$

As explained in Appendix B, constant C_0 can take any arbitrary value. A wise choice of this value can aid in simplifying the expansion expressions. In particular, if the Green's function is chosen as:

$$G(k,R) = \frac{1}{2\pi}\left(\ln\frac{k}{2}+\gamma\right)\ J_0(kR) - \frac{1}{4}\,Y_0(kR) \tag{2.139}$$

the expansion in terms of k becomes:

$$\widetilde{G} = \frac{-1}{2\pi}\ln R + k^2\frac{R^2}{8\pi}\left(\ln R - 1\right) \tag{2.140a}$$

$$\frac{\partial\widetilde{G}}{\partial n} = \cos\theta\left[\frac{-1}{2\pi R} + k^2\frac{1}{8\pi}\,R\left(2\ln R - 1\right)\right] \tag{2.140b}$$

Introducing (2.132), (2.135), and then (2.140) into (2.137) and grouping the terms with the same power of k, the following system of integral equations is obtained:

$$k^0 \Rightarrow \oint_{\partial S}\alpha_{s0}^A(\mathbf{r}')\ln R\ dr' = -\pi\,\mathbf{E}_{s0}^A(\mathbf{r})\cdot\hat{\mathbf{z}} + \int_0^{d_p} A_{0m}\sin\left(\frac{m\pi}{d_q}t_p'\right)\frac{\cos\theta}{R_p}\,dt_p' \tag{2.141a}$$

$$k^2 \Rightarrow \oint_{\partial S}\beta_{s0}^A(\mathbf{r}')\ln R\ dr' = -\int_0^{d_p} A_{0m}\sin\left(\frac{m\pi}{d_q}t_p'\right)\frac{\cos\theta}{4}R_p\left(1-2\ln R_p\right)dt_p' + \oint_{\partial S}\frac{R^2}{4}\alpha_{s0}^A(\mathbf{r}')\left(1-\ln R\right)\ dr'. \tag{2.141b}$$

The MoM, in its Galerkin version, is applied to transform this system of integral equations into a matrix form. The unknown functions α_{s0}^A and β_{s0}^A are expanded in finite series of basis functions f_κ (piece-wise parabolic splines) on the contour ∂S of the cross-section of the cavity.

$$\alpha_{s0}^A(\mathbf{r}) = \sum_{\kappa=1}^{\mathcal{K}} w_{s0\kappa}^A\, f_\kappa(\mathbf{r}) \tag{2.142a}$$

$$\beta_{s0}^A(\mathbf{r}) = \sum_{\kappa=1}^{\mathcal{K}} v_{s0\kappa}^A\, f_\kappa(\mathbf{r}). \tag{2.142b}$$

Then, the inner product between each basis function in the expansion and the two equations of the system is performed. This leads to the following matrix system

$$\mathbf{M}^A\cdot\mathbf{w}^A = \left(\mathbf{L}^A+\mathbf{G}^A\right) \tag{2.143}$$

$$\mathbf{M}^A\cdot\mathbf{v}^A = \mathbf{N}^A\cdot\mathbf{w}^A + \mathbf{T}^A \tag{2.144}$$

where $\mathbf{w}^A = [w_{s01}^A,\ldots,w_{s0\mathcal{K}}^A]^T$ and $\mathbf{v}^A = [v_{s01}^A,\ldots,v_{s0\mathcal{K}}^A]^T$ are column vectors with the unknown $\mathcal{K}$ expansion coefficients, and the remaining matrices and vectors of

the problem are defined as:

$$M_{ij}^{A} = \oint_{\partial S}\oint_{\partial S} f_i(\mathbf{r})\, f_j(\mathbf{r}')\, \ln R \; dr\, dr' \tag{2.145a}$$

$$L_{i}^{A} = -\pi\sqrt{\frac{2}{h\, d_p}}\int_0^{d_p} \sin\left(\frac{m\pi}{d_p}t_p'\right)\; f_i(\mathbf{r}_p')\; dt_p' \tag{2.145b}$$

$$G_{i}^{A} = \sqrt{\frac{2}{h\, d_p}}\oint_{\partial S}\int_0^{d_p} \sin\left(\frac{m\pi}{d_p}t_p'\right)\; \frac{\cos\theta}{R_p}\, f_i(\mathbf{r})\; dr\; dt_p' \tag{2.145c}$$

$$N_{ij}^{A} = \oint_{\partial S}\oint_{\partial S} \frac{R^2}{4}\,(1-\ln R)\, f_i(\mathbf{r})\, f_j(\mathbf{r}')\; dr\; dr' \tag{2.145d}$$

$$T_{i}^{A} = \frac{-1}{4}\sqrt{\frac{2}{h\, d_p}}\oint_{\partial S}\int_0^{d_p} \sin\left(\frac{m\pi}{d_p}t_p'\right)\; \cos\theta R_p\,(1-2\ln R_p)\, f_i(\mathbf{r})\; dt_p' dr \tag{2.145e}$$

with $i, j = 1, \ldots, \mathcal{K}$. As can be seen, matrices $\mathbf{M}^A$ and $\mathbf{N}^A$ are independent of the excitation modes, thus they only need to be computed once regardless of the total number of modes. The other vectors must be computed for all the different LSM_{0m}^{z} modes, but they can be stored in a matrix form in order to use matrix algebra algorithms to solve the overall system simultaneously. As it was the case for the problem related to the LSE excitation, some of the integrals in this case also involve singular integrands. Appendix C contains further details on how to overcome this problem for contours containing straight, circular or elliptical segments.

2.2.2.3 Computation of γ_{s0}^{A}

In order to compute γ_{s0}^{A}, the series involving solenoidal TM modes of the closed cavity must be calculated:

$$\gamma_{s0}^{A}(k, \mathbf{r}) = \sum_{i=1}^{\infty} \frac{\mathcal{C}_{s0i}^{A}}{(\kappa_{i0}^2 - k^2)\,\kappa_{i0}}\, \boldsymbol{\mathcal{H}}_{i0}^{\mathrm{TM}} \cdot \hat{\mathbf{t}} \tag{2.146}$$

where

$$\mathcal{C}_{s0i}^{A} = \frac{1}{\kappa_{i0}}\left[\int_{S_p} (\hat{\mathbf{z}}_g \times \mathbf{e}_{s0}) \cdot \boldsymbol{\mathcal{H}}_{i0}^{\mathrm{TM}}\, dS\right]. \tag{2.147}$$

Since $\hat{\mathbf{z}}_g \times \mathbf{e}_{s0} = (\hat{\mathbf{z}} \cdot \mathbf{e}_{s0}) \cdot \hat{\mathbf{t}}$, and given the expression of the modal electric field for LSM_{0m}^{z} modes, the coefficients $\mathcal{C}_{s0i}^{A}$ can be written as:

$$\mathcal{C}_{s0i}^{A} = \frac{A_{0m} h}{\kappa_{i0}}\int_0^{d_p} \sin\left(\frac{m\pi}{d_p}t_p'\right) \boldsymbol{\mathcal{H}}_{i0}^{\mathrm{TM}} \cdot \hat{\mathbf{t}}\; dt_p'. \tag{2.148}$$

As shown in section 2.1, the solenoidal TM modes in a closed bi-dimensional cavity can be related to the TM scalar potential φ^{TM} of an equivalent waveguide with cross-section ∂S as (see expression (2.55b) particularized for $l = 0$):

$$\begin{aligned} \boldsymbol{\mathcal{H}}_{i0}^{\mathrm{TM}} \cdot \hat{\mathbf{t}} &= \frac{-1}{\chi_i^{\mathrm{TM}}\sqrt{h}} \left[\hat{\mathbf{z}} \times \nabla_{\mathrm{T}} \varphi_i^{\mathrm{TM}}(\mathbf{r})\right] \cdot \hat{\mathbf{t}} = \frac{-1}{\chi_i^{\mathrm{TM}}\sqrt{h}}\, \hat{\mathbf{n}} \cdot \nabla_{\mathrm{T}} \varphi_i^{\mathrm{TM}}(\mathbf{r}) \\ &= \frac{-1}{\chi_i^{\mathrm{TM}}\sqrt{h}} \frac{\partial \varphi_i^{\mathrm{TM}}(\mathbf{r})}{\partial n}. \end{aligned} \tag{2.149}$$

The TM scalar potential can be computed via application of the BI-RME method [136]. As shown in Appendix D, the normal derivative of the scalar potential on the contour is related to the z-directed current as:

$$\frac{\partial\, \varphi_i^{\mathrm{TM}}(\mathbf{r})}{\partial n} = -\chi_i^{\mathrm{TM}} J_z(\mathbf{r}) = -\chi_i^{\mathrm{TM}} \sum_{\kappa=1}^{\mathcal{K}} B_{\kappa i}^{\mathrm{TM}} f_\kappa(\mathbf{r}) \tag{2.150}$$

where $B_{\kappa i}^{\mathrm{TM}}$ are the expansion coefficients that the application of the BI-RME method provides, and $\mathcal{K}$ the total number of basis functions f_κ defined on the contour.

Combining (2.150) and (2.149) with (2.148), and knowing that $\kappa_{i0} = \chi_i^{\mathrm{TM}}$ in the H-plane case where $l = 0$, coefficients $\mathcal{C}_{s0i}^{A}$ simply become:

$$\mathcal{C}_{s0i}^{A} = \frac{\sqrt{2/d_p}}{\chi_i^{\mathrm{TM}}} \sum_{\kappa=p_0}^{p_f} B_{\kappa i}^{\mathrm{TM}} \int_{\delta_\kappa} f_\kappa(\mathbf{r}'_p) \sin\left(\frac{m\pi}{d_p} t'_p\right)\, dt'_p. \tag{2.151}$$

Similarly, a series of coefficients $I_{\kappa m}^{A}$ can be defined:

$$I_{\kappa m}^{A} = \sqrt{\frac{2}{d_p}} \int_{\delta_\kappa} f_\kappa(\mathbf{r}'_p) \sin\left(\frac{m\pi}{d_p} t'_p\right)\, dt'_p. \tag{2.152}$$

With the parametrization of the basis functions defined in (2.116), the integrals are solved and these coefficients become:

$$\begin{aligned} I_{\kappa m}^{A} &= \sqrt{\frac{2}{d_p}}\delta_\kappa \left\{ \cos\left(0.5\alpha_\kappa + \beta_\kappa\right) \left[c_{1\kappa} \left(\frac{2}{\alpha_\kappa^3} - \frac{0.25}{\alpha_\kappa} \right) - \frac{0.5c_{2\kappa} + c_{3\kappa}}{\alpha_\kappa} \right] \right. \\ &- \cos\left(-0.5\alpha_\kappa + \beta_\kappa\right) \left[c_{1\kappa} \left(\frac{2}{\alpha_\kappa^3} - \frac{0.25}{\alpha_\kappa} \right) + \frac{0.5c_{2\kappa} - c_{3\kappa}}{\alpha_\kappa} \right] \\ &+ \left. \sin\left(0.5\alpha_\kappa + \beta_\kappa\right) \left[\frac{c_{1\kappa} + c_{2\kappa}}{\alpha_\kappa^2} \right] + \sin\left(-0.5\alpha_\kappa + \beta_\kappa\right) \left[\frac{c_{1\kappa} - c_{2\kappa}}{\alpha_\kappa^2} \right] \right\} \end{aligned} \tag{2.153}$$

where

$$\alpha_\kappa = \frac{m\pi\delta_\kappa}{d_p} \tag{2.154a}$$

$$\beta_\kappa = \frac{m\pi}{d_p}\left(t_{0\kappa} + 0.5\delta_\kappa\right). \tag{2.154b}$$

Coefficients $\mathcal{C}^A_{s0i}$ are then computed as:

$$\mathcal{C}^A_{s0i} = \frac{1}{\chi^{\mathrm{TM}}_i} \sum_{\kappa=p_0}^{p_f} B^{\mathrm{TM}}_{\kappa i} I^A_{\kappa m}. \tag{2.155}$$

Introducing (2.155) into (2.146), γ^A_{s0} is obtained. Finally, substituting the basis-function expansions of α^A_{s0}, β^A_{s0} and γ^A_{s0} into (2.135), the normal derivative of the scalar potential φ^A_{s0} can be expressed as:

$$\frac{\partial\varphi^A_{s0}(k,\mathbf{r})}{\partial n} = \frac{j\mu}{k\eta}\sum_{\kappa=1}^{\mathcal{K}} f_\kappa(\mathbf{r})\left[w^A_{s0\kappa} - k^2 v^A_{s0\kappa} - \frac{k^4}{\sqrt{h}}\sum_{i=1}^{\infty}\frac{\mathcal{C}^A_{s0i}B^{\mathrm{TM}}_{\kappa i}}{(\kappa^2_{i0}-k^2)\,\kappa_{i0}}\right]. \tag{2.156}$$

Given φ^A_{s0} and its normal derivative on the contour, the integral equations of (2.92) and (2.93) are solved (exchanging φ^F_{s1} for φ^A_{s0}) , and the auxiliary potential at any point $\mathbf{r}$ within S is obtained. The electromagnetic field under excitation of the LSM^z_{0m} is computed from the auxiliary potential according to (2.124). Then, the frequency transformation described in (2.131) is applied to derive the fields under any LSM^z_{lm} mode excitation.

2.2.3 Convergence of the hybrid representation: Rectangular cavity

The hybrid field representation explained in this section can be applied to the rectangular waveguide analysis of section 2.1.4. By doing so, the convergence of results, as a function of the number of modes used in the field expansion series, can be studied. Since the example represents a purely H-plane cavity, and the term that involves irrotational modes has been evaluated following the procedure described in section 2.2.2.1, only a series involving solenoidal modes (with an improved convergence rate) must be computed in the expansion.

Comparing the results of Table 2.1 with Table 2.2, it is clear that the convergence of the only series in the hybrid field representation is much faster than the convergence of Kurokawa's field expansion series. With the proposed formulation, it is no longer necessary to compute thousands of modes in the cross-section of the cavity to have an accurate field characterization. For very simple geometries, a few dozen modes suffice. More complex structures may require up to a few hundred.

No. TM Modes	**Error (%) Mag. E**	**Error (%) Mag. H**
3	0.588	0.291
4	0.259	0.110
6	0.187	0.105
9	0.052	0.025
27	0.023	0.008
74	0.018	0.005

Table 2.2: Error in the computation of the normalized magnitude of the electric and magnetic fields using the hybrid field representation.

Nevertheless, these are manageable numbers for advanced numerical techniques, such as the BI-RME method, and can be handled very efficiently.

The importance of the frequency transformations (2.88) and (2.129) in reducing the size of the full-wave problem must also be noted. This example involves only a single-mode excitation (LSM^z_{01} mode). However, the matrices obtained in this example are enough to compute the field under excitation of any other LSM^z_{n1} mode, thanks to the frequency transformation of (2.129). If it was not applied, each index n would require to solve a new problem, which would be computationally very intensive. The same reasoning applies to LSE modes. As demonstrated, the proposed frequency transformations are also largely responsible for the high efficiency of the full-wave formulation.

2.3 General Admittance Matrix characterization

The General Admittance Matrix (GAM) of a bi-dimensional cavity can be efficiently computed as a by-product of the procedure just developed for the EM fields solution. This characterization in circuit terms provides a unique interface to interconnect building blocks. Therefore, each block may be analyzed with a different numerical method. Consequently, the frequency response of complex devices can be computed very efficiently by dividing the problem into smaller parts that are solved using the more suitable modal-based analysis technique [133]. Then, the resulting matrix system is solved by properly combining all of the blocks.

The position (r, s) of the admittance matrix (Y_{rs}) provides the relationship between the modal current I_r induced over mode r (located in an arbitrary port q) when the structure under analysis is excited by a modal voltage V_s associated

with mode s (located in port p), with all other modes short-circuited:

$$Y_{rs} = \frac{I_r}{V_s} \qquad \forall\, V_i = 0 \quad \text{with } i \neq s. \tag{2.157}$$

This definition is independent of the family of modes considered as excitation. The typical GAM for these structures would consider the classical TE/TM modes in the rectangular waveguide ports. As we have shown in the previous section, the EM analysis of these bi-dimensional cavities is much more efficient if $\text{LSE}^z/\text{LSM}^z$ modes are used as excitations. Consequently, the GAM provided in this section will consider the latter family of modes. Then, this matrix can be easily transformed into an equivalent matrix involving TE/TM modes by the simple transformations shown in Appendix A. To compact the notation, it will be assumed that the modal indices of mode r are (l', m') and for mode s they are (l, m) (as in section 2.2).

The procedure to compute the GAM is straightforward. The structure is excited by mode s in port p with $V_s = 1$, and the total magnetic field induced $\mathbf{H}_s$ is computed. Then, the magnetic field $\mathbf{H}_s$ on the surface of port q is projected into the modal vectors of the corresponding rectangular waveguide attached to this port:

$$\mathbf{H}_s\big|_{\text{Port } q} = \sum_{i=1}^{\infty} I_i\, \mathbf{h}_i \tag{2.158}$$

where $\mathbf{h}_i$ is the modal magnetic field of the i-th mode at port q. The specific expressions for the LSE/LSM modal fields can be found in (2.79) and (2.80). Multiplying both sides of (2.158) by $(\hat{\mathbf{z}}_g \times \mathbf{e}_r)$, integrating over port q and applying the orthogonality properties of LSE/LSM modes shown in (2.78), the modal current for mode r is obtained as:

$$\int_{Sq} (\hat{\mathbf{z}}_g \times \mathbf{e}_r) \cdot \mathbf{H}_s \, dS = \sum_{i=1}^{\infty} I_i \int_{Sq} (\hat{\mathbf{z}}_g \times \mathbf{e}_r) \cdot \mathbf{h}_i \, dS \Longrightarrow I_r = \int_{Sq} (\hat{\mathbf{z}}_g \times \mathbf{e}_r) \cdot \mathbf{H}_s \, dS. \tag{2.159}$$

Substituting (2.159) and $V_s = 1$ into (2.157), the general expression of the GAM becomes:

$$Y_{rs} = \int_{Sq} (\hat{\mathbf{z}}_g \times \mathbf{e}_r) \cdot \mathbf{H}_s \, dS. \tag{2.160}$$

From the study of bi-dimensional cavities performed in this chapter, we can conclude that the field generated by an LSE mode in a cavity is not coupled with any LSM modal vector at any port, and vice versa. Therefore, if r and s do not belong to the same family of modes then $Y_{rs} = 0$. Consequently, the GAM can be separated into two submatrices: one, $\mathbf{Y}^{\text{LSE}}$, involving only LSE modes and the other, $\mathbf{Y}^{\text{LSM}}$, involving only LSM modes.

2.3.1 General Admittance Matrix for LSE modes

Using the modal field expressions for LSE modes of (2.79), the GAM in this case is expressed as:

$$\begin{aligned} Y_{rs}^{\mathrm{LSE}} &= \int_0^h \int_0^{d_q} \left(\hat{\mathbf{z}}_g \times \mathbf{e}_r^{\mathrm{LSE}}\right) \cdot \mathbf{H}_s^F \, dt_q \, dz = \int_0^h \int_0^{d_q} \left(-\mathbf{e}_r^{\mathrm{LSE}} \cdot \hat{\mathbf{t}}_q\right) \mathbf{H}_s^F \cdot \hat{\mathbf{z}} \, dt_q \, dz \\ &= -A_{l'm'} \int_0^h \int_0^{d_q} \cos\left(\frac{m'\pi}{d_q} t_q\right) \sin\left(\frac{l'\pi}{h} z\right) \mathbf{H}_s^F \cdot \hat{\mathbf{z}} \, dt_q \, dz. \end{aligned} \tag{2.161}$$

Applying the transformation in the k variable (2.91), the relationship of the E-plane magnetic field with the scalar potential φ_{s1}^F of (2.97), and the expansion of the latter in terms of k (2.122), the z-directed component of this field can be expressed as:

$$\begin{aligned} \mathbf{H}_s^F \cdot \hat{\mathbf{z}}\big|_{\text{Port } q} &= \sin\left(\frac{l\pi z}{h}\right) \sum_{\kappa=q_0}^{q_f} f_\kappa(\mathbf{r}_q) \\ &\cdot \left\{ \frac{-1}{jk\eta} \left(\frac{\pi}{h}\right)^2 w_{s1\kappa}^F + \frac{j\left[k^2 - \left(\frac{l\pi}{h}\right)^2 + \left(\frac{\pi}{h}\right)^2\right]}{\eta k} \left[\left(\frac{\pi}{h}\right)^2 v_{s1\kappa}^F - w_{s1\kappa}^F\right] \right. \\ &\left. + \frac{j\left[k^2 - \left(\frac{l\pi}{h}\right)^2 + \left(\frac{\pi}{h}\right)^2\right]^2}{\eta k} \sqrt{\frac{2}{h}} \sum_{i=1}^{\mathcal{M}} \frac{\chi_i^{\mathrm{TE}} B_{\kappa i}^{\mathrm{TE}} \, \mathcal{C}_{s1i}^F}{\left[\left(\chi_i^{\mathrm{TE}}\right)^2 - k^2 + \left(\frac{l\pi}{h}\right)^2\right] \kappa_{i1}^2} \right\} \end{aligned} \tag{2.162}$$

where it is assumed that port q contains the basis functions with indices between q_0 and q_f. $\mathcal{M}$ is the number of TE modes computed in cross-section S of the cavity by the BI-RME method. Likewise, $\mathbf{r}_q = \mathbf{r}(t_q)$. Furthermore, $\chi_i^{\mathrm{TE}} = \sqrt{\kappa_{i1}^2 - (\pi/h)^2}$. Substituting (2.162) into (2.161) and solving the integral on the variable z, the LSE-mode GAM becomes:

$$\begin{aligned} Y_{rs}^{\mathrm{LSE}} &= \frac{-A_{l'm'} \, h}{2} \delta_{ll'} \sum_{\kappa=q_0}^{q_f} \left[\int_{\delta_k} \cos\left(\frac{m'\pi}{d_q} t_q\right) f_\kappa(\mathbf{r}_q) \, dt_q\right] \\ &\cdot \left\{ \frac{-1}{jk\eta} \left(\frac{\pi}{h}\right)^2 w_{s1\kappa}^F + \frac{j\left[k^2 - \left(\frac{l\pi}{h}\right)^2 + \left(\frac{\pi}{h}\right)^2\right]}{\eta k} \left[\left(\frac{\pi}{h}\right)^2 v_{s1\kappa}^F - w_{s1\kappa}^F\right] \right. \\ &\left. + \frac{j\left[k^2 - \left(\frac{l\pi}{h}\right)^2 + \left(\frac{\pi}{h}\right)^2\right]^2}{\eta k} \sqrt{\frac{2}{h}} \sum_{i=1}^{\mathcal{M}} \frac{\chi_i^{\mathrm{TE}} B_{\kappa i}^{\mathrm{TE}} \, \mathcal{C}_{s1i}^F}{\left[\left(\chi_i^{\mathrm{TE}}\right)^2 - k^2 + \left(\frac{l\pi}{h}\right)^2\right] \kappa_{i1}^2} \right\}. \end{aligned} \tag{2.163}$$

The integral in this equation is the same involved in the computation of $I^F_{\kappa m}$ defined in (2.115). Introducing these coefficients in the GAM, we finally have:

$$\begin{aligned} Y^{\mathrm{LSE}}_{rs} &= \delta_{ll'}\frac{j}{k\eta}\left\{\sqrt{h/2}\left(\frac{\pi}{h}\right)^2\sum_{\kappa=q_0}^{q_f} w^F_{s1\kappa}\, I^F_{\kappa m'}\right. \\ &+ \sqrt{h/2}\left[k^2-\left(\frac{l\pi}{h}\right)^2+\left(\frac{\pi}{h}\right)^2\right]\sum_{\kappa=q_0}^{q_f} I^F_{\kappa m'}\left[\left(\frac{\pi}{h}\right)^2 v^F_{s1\kappa}-w^F_{s1\kappa}\right] \\ &+ \left.\left[k^2-\left(\frac{l\pi}{h}\right)^2+\left(\frac{\pi}{h}\right)^2\right]^2\sum_{i=1}^{\mathcal{M}}\frac{\mathcal{C}^F_{r1i}\,\mathcal{C}^F_{s1i}}{\left[\left(\chi^{\mathrm{TE}}_i\right)^2-k^2+\left(\frac{l\pi}{h}\right)^2\right]}\right\}. \end{aligned} \tag{2.164}$$

The coefficients of the rapidly converging series of the magnetic field under excitation of mode r with $l'=1$ are:

$$\mathcal{C}^F_{r1i}=\frac{\chi^{\mathrm{TE}}_i}{\kappa^2_{i1}}\sum_{\kappa=q_0}^{q_f} B^{\mathrm{TE}}_{\kappa i} I^F_{\kappa m'}. \tag{2.165}$$

2.3.2 General Admittance Matrix for LSM modes

Similarly, and taking into account that under excitation of an LSM mode, the magnetic field within a bi-dimensional cavity does not have a z-directed contribution, the GAM in this case is defined as:

$$\begin{aligned} Y^{\mathrm{LSM}}_{rs} &= \int_0^h\int_0^{d_q}\left(\hat{\mathbf{z}}_g\times\mathbf{e}^{\mathrm{LSM}}_r\right)\cdot\mathbf{H}^A_s\, dt_q\, dz=\int_0^h\int_0^{d_q}\left(\mathbf{e}^{\mathrm{LSM}}_r\cdot\hat{\mathbf{z}}\right)\mathbf{H}^A_s\cdot\hat{\mathbf{t}}_q\, dt_q\, dz \\ &= A_{l'm'}\int_0^h\int_0^{d_q}\sin\left(\frac{m'\pi}{d_q}t_q\right)\cos\left(\frac{l'\pi}{h}z\right)\mathbf{H}^A_s\cdot\hat{\mathbf{t}}_q\, dt_q\, dz. \end{aligned} \tag{2.166}$$

Employing the transformation in the k variable (2.131), the relationship of the H-plane magnetic field with the normal derivative scalar potential φ^A_{s0} of (2.133) and the expansion of the latter in terms of k (2.156), the tangential component of the magnetic field can be expressed as:

$$\begin{aligned} \mathbf{H}^A_s\cdot\hat{\mathbf{t}}_q\big|_{\text{Port } q} &= \sqrt{\epsilon_l}\cos\left(\frac{l\pi z}{h}\right)\sum_{\kappa=q_0}^{q_f} f_\kappa(\mathbf{r}_q)\cdot\left\{\frac{1}{j\eta}\,\frac{k}{\left[k^2-\left(\frac{l\pi}{h}\right)^2\right]}\,w^A_{s0\kappa}+\frac{jk}{\eta}v^A_{s0\kappa}\right. \\ &+ \left.\frac{jk\left[k^2-\left(\frac{l\pi}{h}\right)^2\right]}{\eta}\,\frac{1}{\sqrt{h}}\sum_{i=1}^{\mathcal{M}'}\frac{B^{\mathrm{TM}}_{\kappa i}\,\mathcal{C}^A_{s0i}}{\left[\left(\chi^{\mathrm{TM}}_i\right)^2-k^2+\left(\frac{l\pi}{h}\right)^2\right]\chi^{\mathrm{TM}}_i}\right\}. \end{aligned} \tag{2.167}$$

$\mathcal{M}'$ is the number of TM modes computed in the cross-section S of the cavity by the BI-RME method.

Substituting (2.167) in (2.166), the GAM results in:

$$\begin{aligned} Y_{rs}^{\mathrm{LSM}} &= \sqrt{\frac{2h}{d_q}}\delta_{ll'}\sum_{\kappa=q_0}^{q_f}\left[\int_{\delta_\kappa}\sin\left(\frac{m'\pi}{d_q}t_q\right)f_\kappa(\mathbf{r}_q)\,dt_q\right] \\ &\cdot \left\{\frac{1}{j\eta}\frac{k}{\left[k^2-\left(\frac{l\pi}{h}\right)^2\right]}w_{s0\kappa}^A+\frac{jk}{\eta}v_{s0\kappa}^A\right. \\ &+ \left.\frac{jk\left[k^2-\left(\frac{l\pi}{h}\right)^2\right]}{\eta}\frac{1}{\sqrt{h}}\sum_{i=1}^{\mathcal{M}'}\frac{B_{\kappa i}^{\mathrm{TM}}\,\mathcal{C}_{s0i}^A}{\left[\left(\chi_i^{\mathrm{TM}}\right)^2-k^2+\left(\frac{l\pi}{h}\right)^2\right]\chi_i^{\mathrm{TM}}}\right\}. \end{aligned} \tag{2.168}$$

Making use of the integral $I_{\kappa m}^A$ defined in (2.152), the GAM can be finally expressed as:

$$\begin{aligned} Y_{rs}^{\mathrm{LSM}} &= \delta_{ll'}\frac{jk}{\eta}\left\{\frac{\sqrt{h}}{\left[\left(\frac{l\pi}{h}\right)^2-k^2\right]}\sum_{\kappa=q_0}^{q_f}w_{s0\kappa}^A\,I_{\kappa m'}^A+\sqrt{h}\sum_{\kappa=q_0}^{q_f}v_{s0\kappa}^A\,I_{\kappa m'}^A\right. \\ &+ \left.\left[k^2-\left(\frac{l\pi}{h}\right)^2\right]\sum_{i=1}^{\mathcal{M}'}\frac{\mathcal{C}_{r0i}^A\,\mathcal{C}_{s0i}^A}{\left[\left(\chi_i^{\mathrm{TM}}\right)^2-k^2+\left(\frac{l\pi}{h}\right)^2\right]}\right\} \end{aligned} \tag{2.169}$$

where

$$\mathcal{C}_{r0i}^A=\frac{1}{\chi_i^{\mathrm{TM}}}\sum_{\kappa=q_0}^{q_f}B_{\kappa i}^{\mathrm{TM}}I_{\kappa m'}^A. \tag{2.170}$$

This chapter has presented a numerical formulation to perform full-wave analysis of bi-dimensional cavities. Due to the ample range of possibilities that this technique offers, it has been deemed convenient to dedicated a specific chapter of this thesis to validate it. In chapter 3, multiple practical passive components will be considered with this objective.

Chapter 3

Application to the analysis, design and RF breakdown prediction of passive waveguide components

The EM formulation for bi-dimensional cavities developed in chapter 2 has a limited scope of application as a stand-alone module. To reach its full potential, it needs to be integrated within a Computer-Aided Engineering (CAE) environment that enables the interconnection of different building blocks. Hence, this module can be combined with other efficient methods tailored to different geometrical structures, also included in practical components. Then, the analysis and design of complex passive microwave components can be efficiently carried out.

In the framework of this thesis, the analysis module for bi-dimensional cavities has been integrated into the CAE tool FEST3D (Full-wave Electromagnetic Simulation Tool 3D) [37]. FEST3D is based on a multimode equivalent network representation of the different parts that form the structure. The device under analysis is seen as a circuit network composed of multiple building blocks, such as waveguides, cavities and planar junctions. Each block is characterized in terms of its GAM (or the analogous Generalized Impedance Matrix, GIM), which is computed by the most suitable analysis method available. Once all the building blocks are properly modeled, the cascade interconnection of the different GAMs provides a matrix system representing the complete circuit. After the excitation conditions are imposed, the scattering parameters of the overall component are computed by solving a banded matrix linear system. This last step is repeated for all frequency points in the band of interest. During the computation of the

S-parameters, FEST3D also provides the modal voltage amplitudes - v_s in (2.76) - at the interfaces between the different blocks, enabling the computation of the electromagnetic fields within the device.

FEST3D splits the GAM computation into two parts: a frequency-independent (static) part and a frequency-dependent (dynamic) one. The bulk of the computation time is dedicated to the solution of the static part. By doing so, a high-resolution frequency response can be provided without incurring a large penalty in terms of CPU time. The time required by the static analysis simply becomes a constant overhead regardless of the number of frequency points in the response. The formulation developed in chapter 2 is fully compatible with this feature, since the core of the analysis (i.e. the computation of α, β and coefficients $\mathcal{C}$ for LSE and LSM modes) can be performed independently of frequency. Likewise, the frequency-dependent operations are very simple and fast.

At the same time, the integration of this module into FEST3D enables the prediction of high-power radio-frequency (RF) breakdown (particularly, multipactor and corona discharge) in components containing bi-dimensional cavities. In recent years, there has been a renewed interest in this topic, as high-power issues are becoming a critical factor in the performance of telecommunication systems, fostering the development of more precise models for the characterization of these physical phenomena. Nowadays, breakdown prediction modules, like the one included in FEST3D, make use of the electromagnetic fields computed within the component, in order to estimate the maximum power that can be handled. Multipactor is accurately modeled by the use of an electron tracking algorithm, together with a proper secondary electron yield model. Corona discharge is analyzed through the solution of a free electron density continuity equation by means of the FEM.

The first part of this chapter presents a series of components with practical interest in the space sector. They have been analyzed, and in some instances designed, using a version of FEST3D that includes the formulation for bi-dimensional cavities developed in this thesis. An inductive filter with rounded corners, a triplexer used in PIM measurement set-ups, and three orthomode transducers will be studied. The second section is focused on the prediction of multipactor and corona discharge in two practical components: a lowpass filter and an H-plane diplexer. The reported results, successfully compared with measured and simulated data, validate the developed tool. CPU times are included for the different examples, providing insight into the numerical efficiency of the developed tool.

3.1 Analysis and design of waveguide components

3.1.1 Inductive filter with rounded corners

The first component under consideration is an inductive sixth-order bandpass filter centered at 38 GHz with a bandwidth of 3 GHz (see Fig. 3.1a). The manufactur-

ing of this filter with low-cost machining techniques, and its clam-shell assembly, introduce rounded corners. This is indeed one of the most common manufacturing effects in microwave components [137], and should be rigorously considered to obtain an accurate design of the final structure. The inductive windows (that would otherwise occupy the complete height of the cavity) are now reduced to leave space for the rounded corners, as shown in Fig. 3.1b. Given that the filter is implemented in the WR-28 rectangular waveguide (dimensions 7.112×3.556 mm), and the rounded corners have a radius of 0.5 mm, the height of the inductive windows becomes 2.556 mm. The thickness of these windows is set at 0.35 mm. The remaining dimensions can be found in Table 3.1.

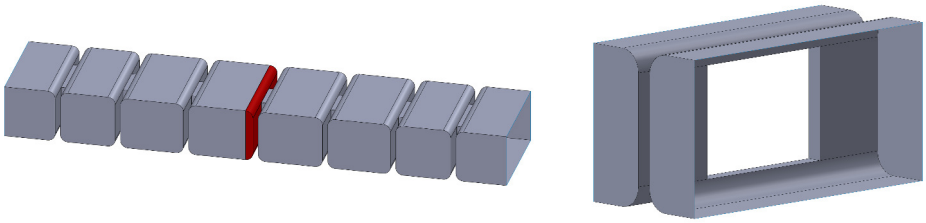

(a) **(b)**

Figure 3.1: **(a)** Structure of the inductive filter with rounded corners. One of the rounded corner sections analyzed by the EM analysis tool for bi-dimensional cavities is highlighted in red. **(b)** Inductive iris with reduced height.

Resonator lengths			**Iris widths**			
$l_1 = l_6$	$l_2 = l_5$	$l_3 = l_4$	$w_{01} = w_{67}$	$w_{12} = w_{56}$	$w_{23} = w_{45}$	w_{34}
3.701	4.235	4.342	3.515	2.515	2.239	2.192

Table 3.1: Dimensions, in mm, of the inductive filter with rounded corners.

The structure can be split into rectangular waveguides, bi-dimensional cavities and planar junctions. The bi-dimensional cavities are used to model the rounded corner sections of the filter, as depicted in Fig. 3.1a. It was mentioned in the previous chapter that the implemented formulation only permits the connection of the cavity to rectangular waveguides that have the same constant dimension (in this case, the same width). On one side, the rounded corner sections are connected with a rectangular waveguide that forms the resonator. This waveguide does have the same width as the cavity. However, the other end is connected to the

rectangular inductive iris, which has a different width. To overcome this problem, a virtual rectangular waveguide with zero thickness (and the same width as the resonator) is positioned between the bi-dimensional cavity and the iris. By doing so, the implemented formulation can be directly applied, and then, the connection between the iris and the virtual waveguide (i.e. the planar junction) can be solved via the integral equation technique presented in [138].

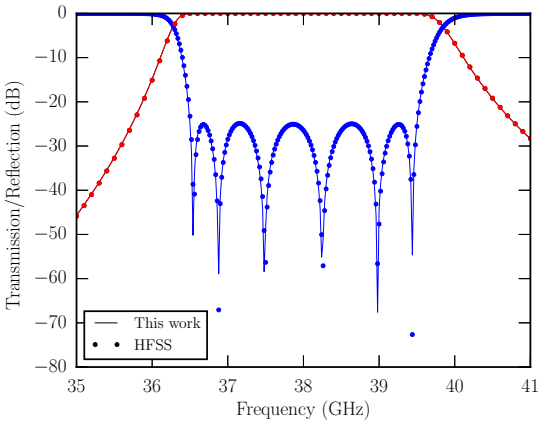

Figure 3.2: Response of the inductive filter with rounded corners compared with ANSYS HFSS.

The analysis of the filter is performed using 50 accessible modes in the rectangular irises (in particular, the modes $TE_{2m+1,2n}$ and $TM_{2m+1,2n}$ are considered, given the vertical and horizontal symmetry of the structure). Waveguides implementing the resonators and input/output ports consider 21 modes. Approximately 100 TE and TM modes are computed in the 2D section of each bi-dimensional cavity. Since all bi-dimensional cavities have the same cross-section, only one GAM is computed and stored. The other cavities can access this GAM, and use it whenever necessary. The analysis of this structure in 100 frequency points takes 25 s (5 s for the static analysis and 0.2 s per frequency point), in an AMD FX-8320 Eight-core Processor at 3.5 GHz with 32 GB RAM. All CPU times in this thesis have been obtained with this computer. To validate the results, they are compared with simulations from the well-known electromagnetic solver ANSYS HFSS (from now on simply referred to as HFSS), based on the Finite Element Method (FEM). Figure 3.2 shows that both simulators provide an equivalent response. In contrast, the simulation with HFSS requires 35 min to provide the depicted convergent results (with a discrete frequency sweep). Horizontal and vertical symmetries are employed. However, the majority of the mesh is dedicated to properly model

the curved contour of the rounded corner irises, which leads to large computation times. If these elements are not properly modeled, the filter is shifted in frequency, thus the large mesh size is justified. An interpolated frequency sweep can also be employed and, in this case, the HFSS simulation takes 10 min. Applying this technique (which is not dependent on the type of EM solver employed) to the analysis method presented in this work, results are obtained in only 10 s.

3.1.2 Triplexer for PIM measurement setups

Next, the analysis of the manifold-coupled triplexer shown in Fig. 3.3 is considered. This component is employed in a setup for passive intermodulation (PIM) measurement operating in the K-band. The specifications for the transmission (Tx) and reception (Rx) channels are as follows:

- Frequency bands:
  - Tx1 band: 11.15 GHz to 11.75 GHz
  - Tx2 band: 12.45 GHz to 12.75 GHz
  - Rx (PIM) band: 13.70 GHz to 14.55 GHz
- Common port return losses (CPRL) in band: 20 dB
- Rejection of Tx1 & Tx2 over Rx band: 80 dB
- Rejection of Rx over Tx1 & Tx2 band: 150 dB

As shown in Fig. 3.3, the triplexer is composed of two bandpass filters (BPFs), serving the Tx1 and Tx2 bands, and a high-pass filter (HPF) serving the Rx band. The former filters are implemented in the hybrid folded rectangular waveguide (HFRW) configuration (more details about this family of filters can be found in chapter 4). The coupling between adjacent resonators in these filters is implemented via capacitive windows in the top/bottom walls of each cavity. Inductive windows provide the necessary cross-coupling to implement transmission zeros in the PIM reception band. They are required to fulfill the rejection specifications. The Rx high-pass filter is implemented by means of a reduced-width rectangular waveguide with a considerable length, which is connected inline with the manifold through a stepped waveguide transformer.

This example illustrates the importance of using a good modeling technique in the design process. T-junctions are employed throughout the structure to represent the direct couplings in the HFRW filters and their connection to the manifold (see Fig. 3.3). These constant-width elements are located very close to inductive windows (that are constant in height). Therefore, there is a strong interaction between the LSE and LSM modes in the structure. During the design of the triplexer,

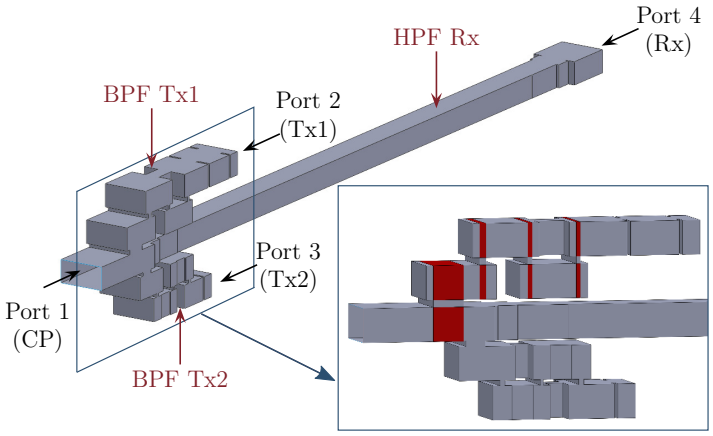

Figure 3.3: Triplexer for high-power applications. T-junctions are used to model the capacitive couplings of the HFRW filters. Some of them are located close to inductive steps, therefore requiring a full-wave representation. Areas highlighted in red in the detail of the figure indicate the T-junction blocks for the Tx1 filter.

the modal technique presented in [139] was used to model the T-junctions. However, the simulations performed during this process had, inadvertently, not reached convergence. Consequently, the measured and designed responses differed. The deviations in the measured response occurred mainly in the edges of the passbands. Fortunately, design margins had been added to the bandpass transmission filters in order to cope with manufacturing deviations. Due to the small degradations within the actual specified passbands, the component was accepted for the intended application.

Afterwards, the formulation for bi-dimensional cavities presented in this thesis was applied. It was seen that, for this particular structure, the present formulation provided more accurate results than the technique in [139], given an equivalent amount of CPU time. Therefore, convergence was reached much faster. Figure 3.4 shows the simulated response obtained with both techniques, compared with measurements from a manufactured prototype. As can be seen, both methods yield equivalent results. The response on the left, obtained after application of the formulation presented in this work, is obtained in 164 s (14 s in the static part and 0.5 s per frequency point) for a response with 300 frequency points. The response on the right, where T-junctions have been modeled by the method in [139], is obtained in 918 s (10 s in the static part and 3 s per frequency point) for quite accurate results, although full convergence is still not reached. As it becomes clear, the reduction in CPU time due to the proposed full-wave formulation is

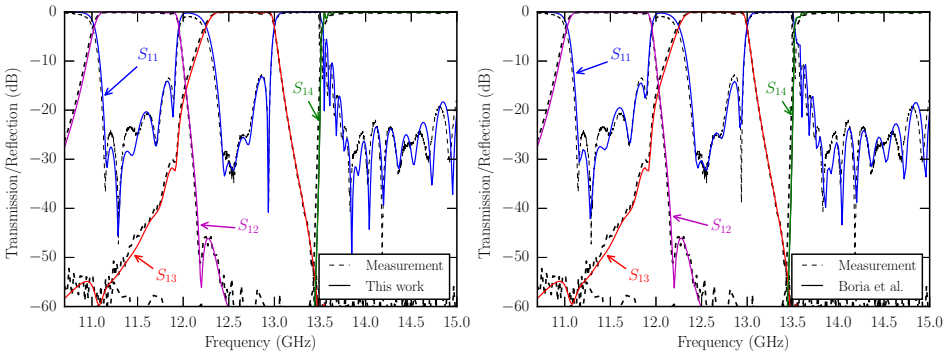

Figure 3.4: Comparison between simulations and measurements from a manufactured prototype of the triplexer in Fig. 3.3. **(a)** Simulation with the analysis technique presented in this thesis. **(b)** Simulation with the analysis technique in [139].

considerable even over other modal techniques. Besides, the accurate analysis of this triplexer by general-purpose meshing algorithms (such as those used in HFSS, CST Microwave Studio or other commercial tools), if at all possible, will certainly take several hours of computation time.

3.1.3 Narrowband taper/branching OMT

Orthomode Transducers (OMTs) are key building blocks within antenna feed systems. They are typically connected to dual-polarized antennas. These elements are tasked with the separation of two orthogonal polarizations, each carrying a different signal in the same frequency band. The presence of multiple relevant propagating modes within the main body of the OMT makes it an ideal candidate to validate the electromagnetic formulation developed in chapter 2.

The first OMT structure studied in this chapter is the narrowband taper-branching configuration shown in Fig. 3.5a. It consists of a square waveguide (Port 1) that receives both polarizations, and a smooth-profile tapered waveguide that acts as a transformer for the vertical (V) polarization. Therefore, this polarization is transferred from Port 1 to Port 3. At the same time, the horizontal (H) polarization becomes evanescent in the tapered region and is reflected and side-coupled to the branching arm (Port 2). A rectangular opening in the top wall of the OMT controls the coupling of this polarization to the branching arm.

The design of these components starts with the tapered waveguide section. In

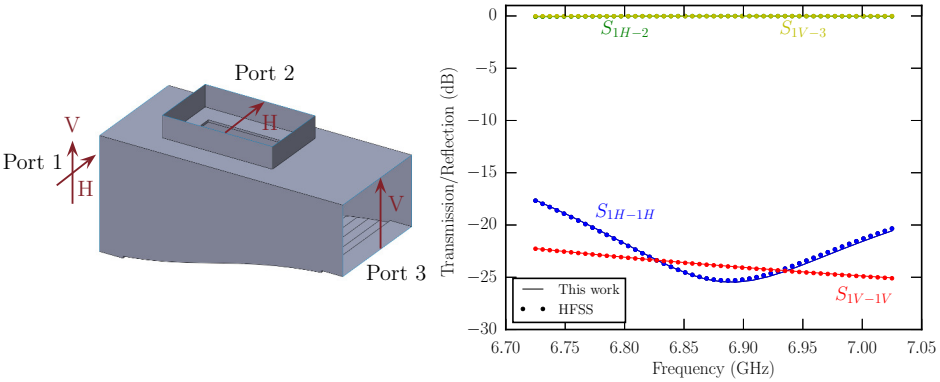

(a) **(b)**

Figure 3.5: Structure and response of the taper/branching narrowband OMT. Port 1 (25.6 × 25.6 mm square waveguide) receives both the horizontal (H) and vertical (V) polarizations. The OMT routes the horizontal polarization to Port 2 (25.6 × 15.799 mm) and the vertical one to Port 3 (25.6 × 15.799 mm).

this case, a Chebyshev taper with 20 sections and return losses of 26 dB between 6.725 and 7.025 GHz is used. The profile is continuous instead of the classical stepped implementation. In order to determine the height and separation between the different sections in the taper, formulas from [140] have been used. Once the taper is completely determined, the position and size of the side-coupled aperture are adjusted until both polarizations are properly transferred to the corresponding port in the band of interest. The dimensions of the resulting structure are shown in Fig. 3.6. In the band of interest, the common port return losses (CPRL) are better than 17.5 dB (see Fig. 3.5b).

To achieve convergent results in the analysis of this component, especially for the horizontal polarization, it is necessary to compute 1300 modes in the cross-section of the tapered waveguide. The bulk of the computation is dedicated to solving the connection from the main body of the structure (tapered waveguide) to the branching arm. Approximately 300 accessible modes are employed in solving this connection. To increase the efficiency of the analysis, the main body is split in three parts, connected by zero-length rectangular waveguides. By doing so, the section connected to the upper iris can be solved very accurately, while relaxing the accuracy in the input and output sections. With this technique, the static part of the analysis is solved in 11 s. In contrast, the frequency-dependent part

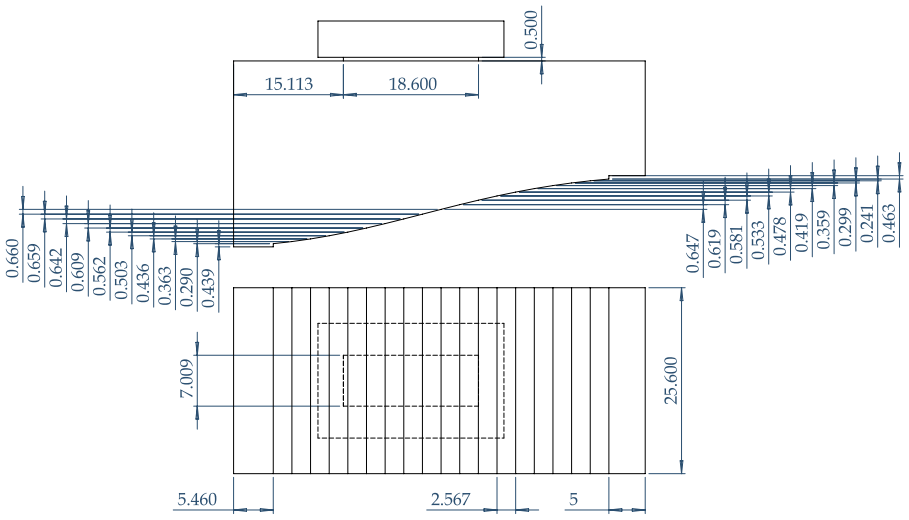

Figure 3.6: Dimensions (in mm) of the taper/branching narrowband OMT. The lower wall is composed of 18 straight segments, each with a length, in the propagation direction, of 2.567 mm. Port heights are 25.6 mm (Port 1) and 15.799 mm (Ports 2 and 3).

takes 1.25 s per frequency point. Results obtained with the new formulation are equivalent to those provided by the mesh-based simulator HFSS, as depicted in Fig. 3.5b.

3.1.4 Wideband turnstile-junction OMT

The second OMT structure, taken from the literature [141], is depicted in Fig. 3.7. It is based on a five-port turnstile-junction with a tuning post that separates both orthogonal polarizations. The signal associated with each polarization is split between two of the four arms of the turnstile, and then combined using a curved Y-junction. Once combined, the signal is guided to the output port through an E-plane bend and a linear taper.

In order to analyze the structure with FEST3D, it may be split into rectangular waveguides, bi-dimensional cavities and a turnstile-junction. This last element is not a bi-dimensional cavity, since it contains a partial-height square inset. To model this junction, the 3D version of the BI-RME method [65] is applied. Then, the arms are split into simpler building blocks to speed up the analysis. Even though each arm maintains its width constant, the analysis of the arm as a whole is not practical. To begin with, the efficiency of the BI-RME method is associated with the electrical dimensions of the cross-section under analysis, decreasing for

larger geometries. A key factor in the performance of this method is the ratio between the surface of the arbitrary contour and the surface of the canonical resonator (rectangular or circular) used in the resonant mode expansion. As this ratio increases, the results become more accurate and the analysis more efficient. Consequently, the best strategy is to split the arms into compact sections that fit a rectangle or a circle as tightly as possible. Furthermore, the parts of the arbitrary contour that coincide with the resonator do not need to be segmented (thanks to the use of an adequate Green's function that sets the boundary condition in the walls of the resonator), decreasing the size of the matrices involved in the solution. For that reason, the Y-junction combiner is split into sections that represent a rectangular cavity with two rounded corners. Other considerations that influence how proceed with the segmentation of the structure are related to the capabilities of FEST3D. As explained in section 3.1.1, FEST3D is able to identify blocks that represent the same geometry to avoid repeating simulations. Taking this into account, the 180° bends are split into two identical halves. FEST3D solves one of them using the formulation presented in this thesis, and then copies the resulting GAM into the other. At the same time, each arm has two identical 180° bends, which means that one half is analyzed and then used for the other three halves. The same applies to the tapers and the 90° bends.

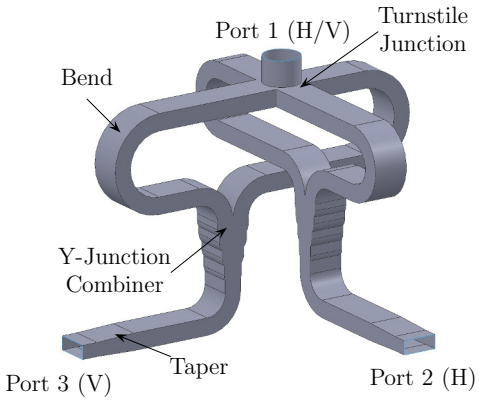

Figure 3.7: Turnstile-junction OMT.

After application of the aforementioned segmentation strategy, the OMT is solved. In Fig. 3.8, the results are compared with simulations obtained with the software tool CST Microwave Studio (based on the finite integration technique) and measurements reported in [141]. Both software tools provide an equivalent response, consistent with measurements. Metal losses have not been considered in the simulated results. The simulation with the method of this thesis takes 0.5 s per frequency point to provide the convergent results depicted, although it has

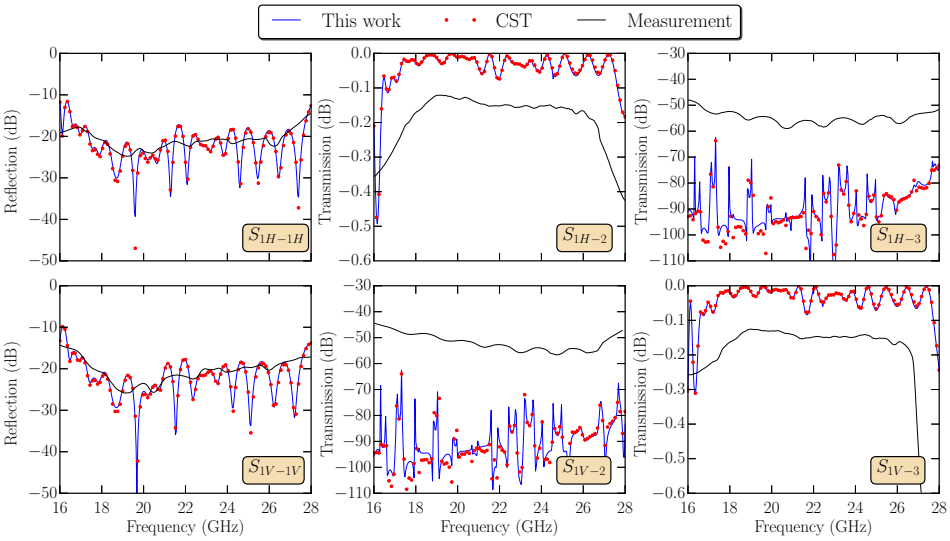

Figure 3.8: Comparison between the measured and simulated responses (with FEST3D and CST Microwave Studio) of the turnstile-junction OMT shown in Fig. 3.7.

an overhead of 2,200 s mainly due to the analysis of the turnstile junction (which requires 88% of this static time). In contrast, CST Microwave Studio requires more than 200,000 tetrahedra and takes six hours to solve the complete structure.

3.1.5 Dual-band OMT

The last example of this section involves the design of a dual-band OMT. This component must combine signals associated to two orthogonal polarizations in two different frequency bands (reception, Rx, from 4.45 to 4.8 GHz and transmission, Tx, from 6.725 to 7.025 GHz). The objective of this component is to discriminate by frequency and by polarization. Therefore, this component is a hybrid between a diplexer (which discriminates by frequency) and an orthomode transducer (which discriminates by polarization).

A schematic view of the different parts that form this OMT can be seen in Fig. 3.9. At the input port, four signals (corresponding to the two polarizations and two frequency bands) are present. The first block must be as transparent as possible for the vertical polarization, while simultaneously discriminating between the lower and upper frequency bands of the horizontally-polarized signal. The lower frequency band must be derived to the branching arm, while the upper band must pass through this block with minimal attenuation. The combination of a

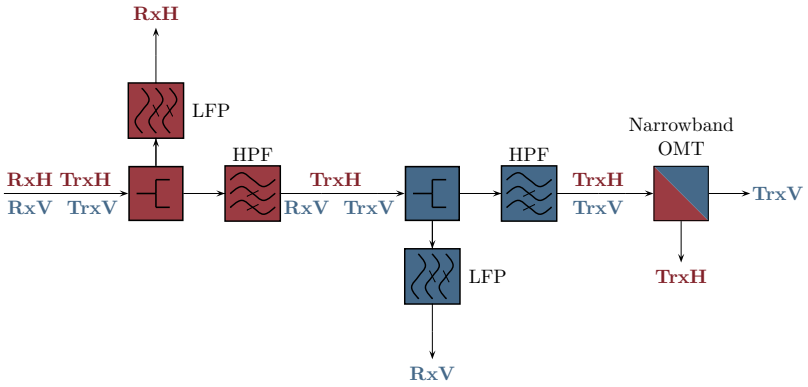

Figure 3.9: Schematic of the building blocks that form the dual-band OMT.

high-pass filter in the inline branch and a lowpass filter in the side branch is used for this purpose. The following block is identical, but derives to the branching arm the signal associated with the vertical polarization in the lower (Rx) frequency band. Finally, the last block is a narrowband OMT that separates the two polarizations in the upper frequency band.

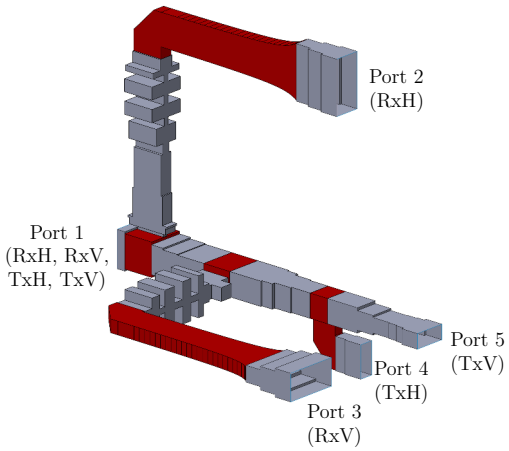

Figure 3.10: Structure of the dual-band OMT. Highlighted in red are the blocks analyzed with the formulation of this work.

This schematic is transformed into the physical structure shown in Fig. 3.10. Low-pass filters are implemented by corrugated structures, whereas the high-pass filters are simple stepped waveguide transformers. Therefore, the main body of

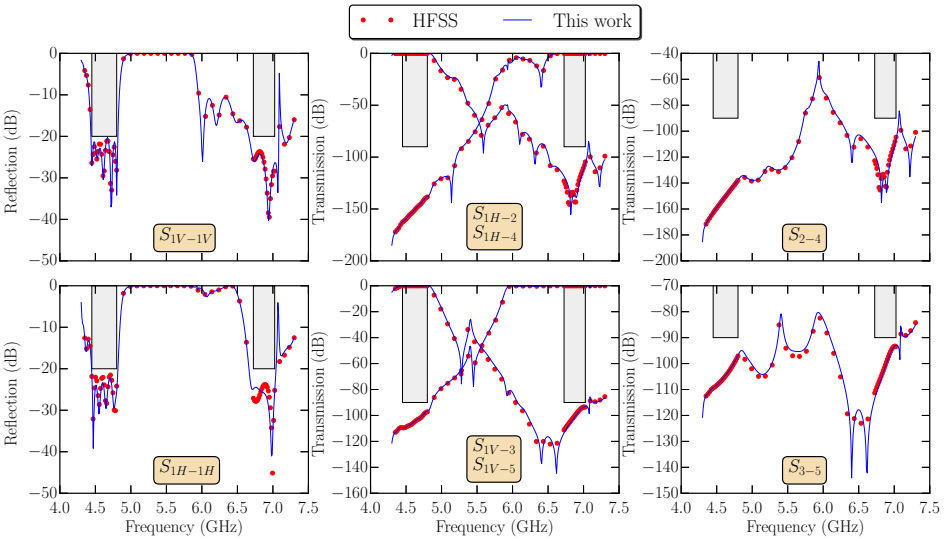

Figure 3.11: Comparison between simulated responses of the dual-band OMT of Fig. 3.10 obtained with HFSS and the formulation of this work.

the OMT consists of a cascade of transformers that alternate a reduction in height with a reduction in width. If these transformers are well designed, one polarization is reflected, while the other is transmitted. The branching arms are connected to the main body through rectangular apertures. Other elements, such as bends and tapers, are included to facilitate the proper orientation of the output ports. The complete structure is composed of bi-dimensional elements, but only a subset is analyzed by the technique developed in this work. These particular elements are highlighted in Fig. 3.10. The T-junctions are key building blocks and are certainly selected. Likewise, the tapers cannot be analyzed as a simple interconnection of rectangular waveguides, thus are also selected. The rest of the structure can be split into simple rectangular waveguides and the corresponding planar junctions that interconnect them. The analysis of these elements is simpler and faster with classical modal methods [133]. Therefore, they are not analyzed with the technique presented in this thesis in order to increase the efficiency of the design.

This dual-band OMT is designed using FEST3D. The response is then successfully compared with the one provided by HFSS after a much bigger computational effort. Figure 3.11 depicts this comparison and shows a high degree of correlation between the two simulations. Regarding the CPU time of this analysis, the convergent simulation shown in the figure requires 377 s to compute 301 frequency points (76 s for the frequency-independent computations and 1 s per point).

3.2 High-power RF breakdown prediction

Over the last decade, there has been a renewed interest in studying the physical phenomena that limit the power-handling capability of communication system at microwave frequencies. In order to satisfy the demand for higher data rates, it has been necessary to increase the transmitted power of such systems. However, once the power in a passive waveguide component exceeds a certain threshold, it can trigger two undesired effects: multipactor [142] and corona discharge [72]. The unintended consequences associated with these effects range from a temperature increase in the component to its complete destruction. Therefore, it is critical to predict this threshold level as accurately as possible [74].

The multipactor effect (or multipaction) occurs under vacuum (or near-vacuum) condition. Free electrons are accelerated by the electric field and collide with the walls of the device. If these collisions have enough energy, secondary electrons are released from the metallic surfaces. Since the electric field is time-varying, the orientation of the electric field may have reversed by the time these secondary electrons are released. In this case, both the primary and the secondary electrons will be accelerated towards the opposite wall, generating even more free electrons. Eventually, this leads to an electron avalanche that can destroy the device. As can be inferred, this effect is highly dependent upon the geometry of the device (in particular, the distance between walls, or gap), as well as the amplitude, frequency and phase of the time-varying electric field. For this reason, an accurate representation of the EM fields within the device is fundamental to obtain accurate breakdown predictions.

In contrast, the corona discharge effect occurs in devices filled with gas, under certain pressure and power conditions. It consists in the formation of an electron plasma that is generated by the ionization of a gas in the presence of high electric fields. Once the input power exceeds a certain threshold, an electron avalanche can be produced, ultimately destroying the component. Since this effect depends on the type of gas and pressure condition, it mainly affects components for terrestrial applications. Likewise, components working during the launching stage of a satellite (like the Telemetry, Tracking and Control - TT&C - system), and during the reentry stage of a space vehicle, are also susceptible to experiencing corona discharge.

The widespread use of commercial EM solvers in the microwave industry has motivated the development of more accurate breakdown prediction models. Nowadays, most of these models take advantage of the precise field solution provided by the EM solvers. However, there are still very few commercial software tools available, nowadays, with adequate capabilities to predict high-power RF breakdown. Amongst them, FEST3D, with its dedicated high-power module, and particularly SPARK3D [128] are widely known for their accurate predictions, backed by measurements. Therefore, the integration of the electromagnetic formulation presented

in chapter 2 with FEST3D, opens up the possibility of applying it to the analysis of key industrial components, that can be potentially subject to high-power RF breakdown. Since high-power issues will be a relevant limiting factor in the final performance of future communication systems, it is likely that these two areas (EM field analysis and high-power RF breakdown prediction) will be deeply integrated in a future generation of CAD tools.

3.2.1 Lowpass filter

Corrugated lowpass filters, like the one shown in Fig. 3.12, are classical examples of structures that are sensitive to RF breakdown.

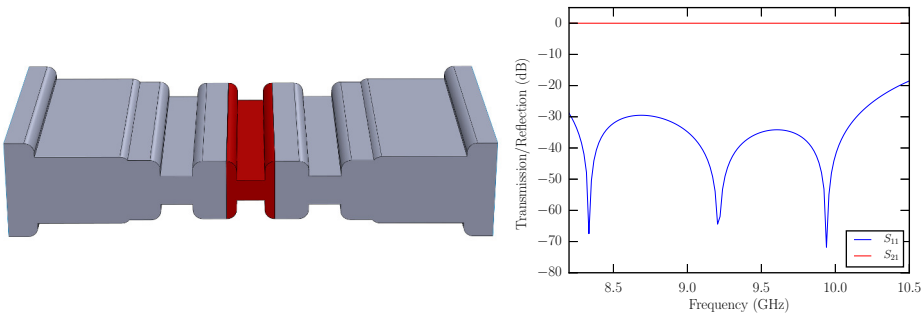

(a) **(b)**

Figure 3.12: **(a)** Physical structure of the lowpass filter. The area highlighted in red identifies the section where the corona and multipactor analysis is performed. The specific dimensions of the structure considered in this section are summarized in Table 3.2. **(b)** S-parameter response.

As opposed to filters composed of coupled resonators, lowpass filters tend to concentrate high electric fields in their low impedance sections, this is, those with a smaller height (see Fig. 3.13). At the same time, these sections have a certain length in the direction of propagation and, therefore, the fringing field effect does not aid in dispersing the free electrons that are generated, especially by multipaction. Consequently, the study of these types of filters is a logical first step in the prediction of high-power breakdown phenomena. Measured data from a manufactured prototype [143, 144], albeit not including rounded corners, will be used to validate the results. In order to perform an adequate comparison, the corners of the critical parts (i.e., the low impedance sections) are not rounded, as shown in Fig. 3.12a.

Section length				
$l_1 = l_9$	$l_2 = l_8$	$l_3 = l_7$	$l_4 = l_6$	l_5
9.513	3.0	3.230	4.420	2.840
Section height				
$h_1 = h_9$	$h_2 = h_8$	$h_3 = h_7$	$h_4 = h_6$	h_5
7.237	6.500	3.070	6.280	2.170

Table 3.2: Dimensions, in mm, of the lowpass filter. Ports are standard WR-90 waveguides. Corners in the high-impedance sections are rounded with a 1 mm radius.

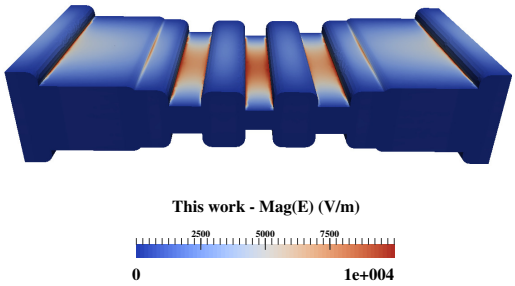

Figure 3.13: Magnitude of the electric field at 9.5 GHz.

As far as corona discharge is concerned, the regions more susceptible to experience this effect are those where the electric field is more intense. As previously mentioned, the low-impedance sections of the filter are prime candidates to experience corona discharge. Once the EM fields are computed in these sections, the continuity equation that governs the evolution of the electron density is solved, using the Finite Element Method (nitrogen has been considered as the filling gas) [144]. From this solution, the breakdown power level for different pressure conditions is predicted. Figure 3.14 depicts the predicted breakdown levels compared with the measured breakdown level (known as Paschen curve) for the manufactured prototype reported in [144]. As can be seen, the simulation agrees perfectly with measurements. The minimum power level for this component is 240 W at the critical pressure of 9 mbar.

A second high-power analysis has been performed on the lowpass filter. Given the EM field, the objective in this second case is to predict the multipactor break-

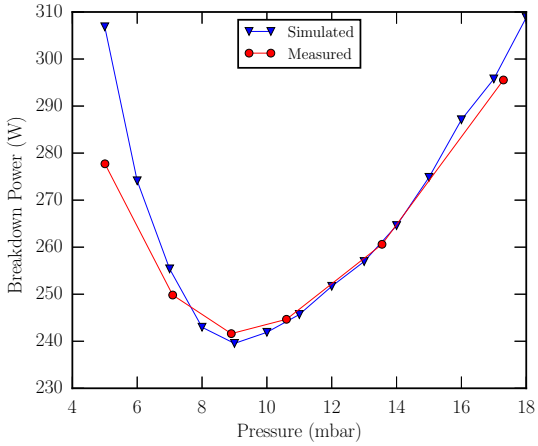

Figure 3.14: Evolution of the breakdown threshold due to corona discharge for different pressure values in the lowpass filter of Fig. 3.12.

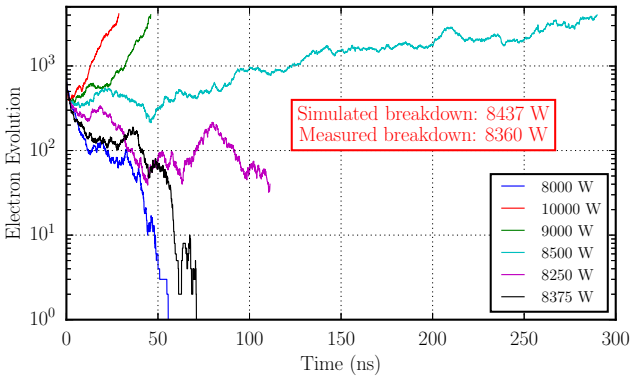

Figure 3.15: Multipactor breakdown results for the lowpass filter in Fig. 3.12. The electron evolution is shown as a function of time, along with the predicted and measured breakdown levels.

down level through the use of an electron tracker algorithm and a proper secondary emission yield (SEY) model. These two elements are integrated in FEST3D, which makes the prediction of this undesired high-power phenomena completely straightforward. Before running the simulation, the user must define the sections where multipactor may occur. In this case, the presence of an intense electric field along with the reduced gap that is present in the central section of the filter, makes

this area especially vulnerable to multipactor breakdown. Figure 3.15 depicts the electron evolution over time within this central section. Using the high-power analysis capabilities of FEST3D, the breakdown level for multipactor is predicted at 8437 W. This is an extremely accurate prediction, considering that the measured breakdown level reported in the literature was 8360 W [143].

3.2.2 H-plane diplexer

The second component considered in this section is a Ku-band H-plane diplexer for the TT&C system of a satellite. The structure of this diplexer and its S-parameter response are shown in Fig. 3.16a and Fig. 3.16b, respectively. The specific dimensions for the diplexer are defined in Fig. 3.16c. Figure 3.17 depicts the magnitude of the electric field computed with the hybrid formulation for bi-dimensional cavities developed in this thesis at 12.25 GHz. Results are successfully compared with HFSS. As can be seen, the electric field is concentrated in the center of the cavities that compose the lower-frequency band filter. Since the distance between the walls is not significantly small in that location, it is unlikely that multipactor breakdown will occur. In contrast, depending on the pressure and the input power levels, it is possible that corona discharge will occur. Consequently, this study will be focused on the corona effect.

During the first stage of the analysis, the complete channel filter is analyzed. However, the field is computed in a reduced number of spatial points to speed up the analysis. The EM fields are introduced into the corona prediction algorithm, which reveals the cavity that has a lower breakdown threshold (highlighted in red in Fig. 3.16). Since the field is computed with a weak spatial resolution, the breakdown level is simply a broad estimate, and not very accurate. Then, a second analysis is performed. This time, the field is computed only within this cavity, but in a large number of spatial points, thus increasing the accuracy in the prediction. The corona analysis algorithm provides the results shown in Fig. 3.18, where it can be seen that the critical pressure is 10 mbar and the threshold power level is 54 W. The Paschen curve obtained with HFSS is highly coincident with the results obtained using the proposed field formulation. As far as the CPU time is concerned, the EM field is computed in an array of 70,000 spatial points at one frequency point (12.25 GHz) in 85 s, a fraction of the 25 minutes dedicated by HFSS to achieve the convergent results shown in Fig. 3.17 with an equivalent mesh size.

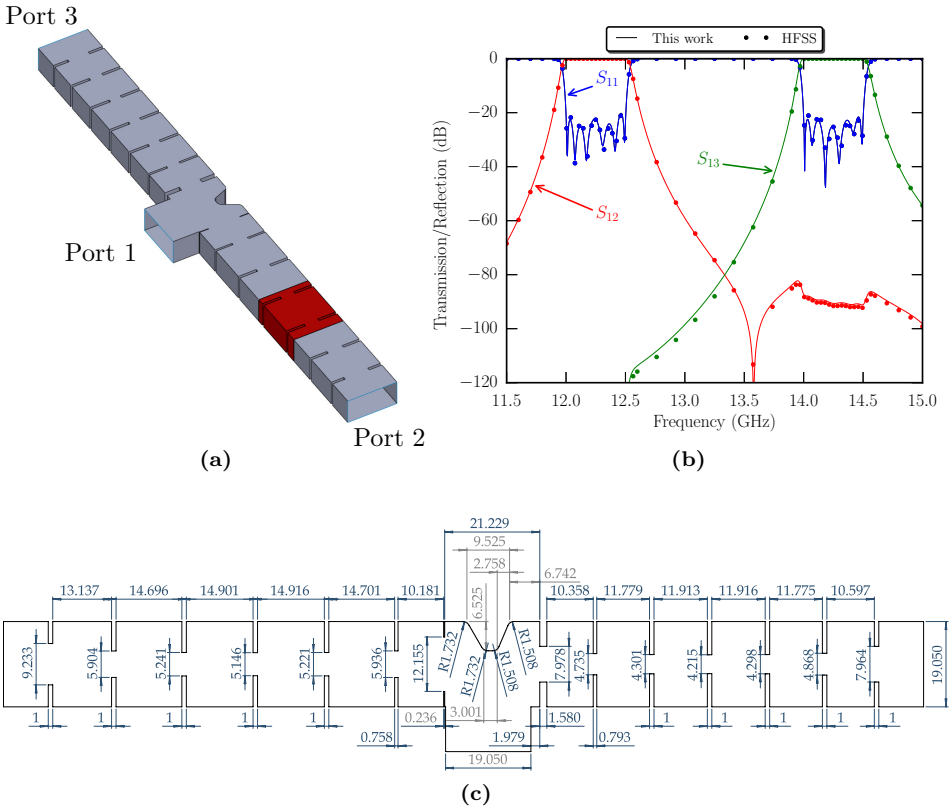

Figure 3.16: **(a)** Physical structure of the H-plane diplexer. The area highlighted in red identifies the cavity where the gas discharge prediction will be performed. **(b)** S-parameter response. **(c)** Dimensions in mm of the H-plane diplexer (height is 9.525 mm).

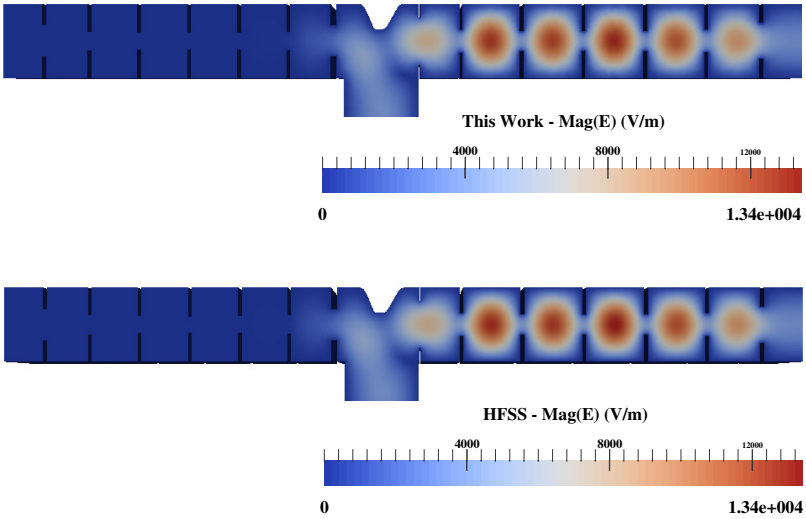

Figure 3.17: Magnitude of the electric field at 12.25 GHz, the center frequency of the lower frequency band of the diplexer. The top image represents results obtained with the formulation of this work, whereas HFSS results are depicted in the bottom. It can be seen how the electric field is concentrated in the center of the cavities, not posing a realistic threat of multipactor breakdown.

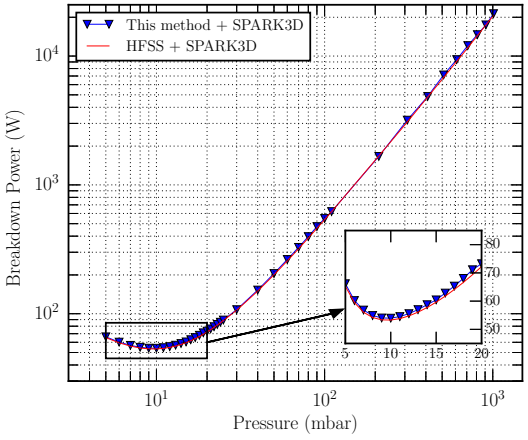

Figure 3.18: Corona breakdown power vs. pressure results for the H-plane diplexer. The inset figure shows a detail around the critical pressure.

Chapter 4

Novel quasi-elliptic filter implementations

Nowadays, a wide variety of communication systems must coexist within the limited electromagnetic spectrum allocated for commercial applications at microwave frequencies. In this crowded environment, the interference of a system into neighboring frequency bands becomes a critical issue, especially as capacity is increasingly demanded. In order to strengthen the isolation in a specific band, elliptic or quasi-elliptic filters have been the subject of intense study over the last decade. These structures are able to provide steep out-of-band rejection with a minimum number of resonators, minimizing the signal interference in adjacent channels and reducing the volume and mass of the component. Flexibility to define the number and prescribe the location of the transmission zeros (TZs) are important features for this kind of filter. They often determine whether a certain filter implementation is suitable for a particular application or not. As an example, the S-parameter response of an interference elimination quasi-elliptic filter is depicted in Fig. 4.1. This filter is employed in satellite television equipment to isolate the reception channel from external sources of interference, such as WiMAX and RADAR signals. In order to provide the required isolation, this filter introduces two TZs in the upper stopband.

In general, there are two approaches that can be employed to implement TZs: bandstop elements and the multipath effect.

The first approach is based on the use of bandstop elements, such as cavities or stubs, to interrupt the transmission of the signal at certain frequencies. This approach allows great control over the location of the TZs. For bandpass structures, a systematic design procedure that makes use of this approach is the extracted pole-technique [114]. Combined with non-resonating nodes [116–118], this design methodology becomes highly modular, although it still requires an

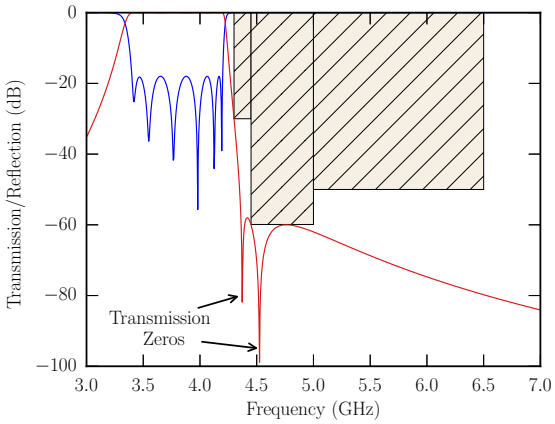

Figure 4.1: S-parameter response of an interference elimination filter operating in the standard and extended C-band (reception). Hatched areas indicate the out-of-band isolation requirements.

important optimization effort to obtain the structure physical dimensions. Corrugated lowpass and bandstop filters often employ stubs as their high-impedance sections, which can also be used to realize TZs [110, 145]. Each stub provides the adequate impedance level required by the filter in the passband. Simultaneously, the stubs become bandstop elements in the stopband, thus realizing TZs at certain finite frequencies. With this strategy, a corrugated lowpass filter composed of N waveguide sections is able to generate up to $N/2$ independent TZs (one per high-impedance section).

For waveguide bandpass filters, it is frequent to implement solutions that include cross-couplings between resonators [115]. By doing so, multiple paths are created, and the relative phase shift of the signal traveling through all of them produces a cancellation (destructive interference) at certain frequencies [146]. The TZs can be realized at specific frequencies in the complex plane ($s = \sigma + j\omega$) by adequately adjusting the coupling elements in the different signal paths. To improve selectivity, the TZs must be placed in the frequency axis ($s = j\omega$). TZs not located on this imaginary axis can be used to equalize the in-band group-delay response of the filter. In this thesis, though, the term transmission zeros will refer to those located in the imaginary axis. The frequency range (above and/or below the passband) where these TZs can be found is dependent upon the nature (electric of magnetic) of the different couplings involved in the structure. Certain coupling combinations are only able to place TZs below or above the passband. Others are flexible enough to realize TZs both in the upper and lower stopbands.

Regardless of the stopband location, coupling schemes that are relatively simple, such as singlets [119], triplets and quadruplets [120, 121], are the preferred solutions in most applications. They are amenable to a modular design, tend to be more robust to manufacturing tolerances, and are easier to tune after fabrication. Therefore, they are easier to design and manufacture than more complex schemes with multiple cross-couplings, even if the resulting physical structures are not as highly compact.

This chapter studies two novel implementation of quasi-elliptic filters. In the first part, the hybrid-folded rectangular waveguide filter topology [147] is considered. This topology makes use of the multipath effect to generate TZs that can be controlled in a wide frequency range. Several configurations will be proposed, giving the designer great flexibility to choose the one that better fits a particular set of specifications. In the second part of the chapter, a novel iris concept will be presented. This iris is formed by the interconnection of E-plane stubs and a capacitive window. The overall structure acts as a coupling element while, simultaneously, generating finite attenuation poles thanks to the bandstop stubs. Consequently, the number of TZs in a rectangular waveguide filter can be increased at will in a very simple and convenient way. All of the structures presented in this chapter are suitable to be analyzed by the full-wave EM technique already described in chapter 2.

4.1 Hybrid-folded rectangular waveguide filters

Hybrid-folded rectangular waveguide (HFRW) structures [122] are a family of filters that have been recently proposed as a powerful alternative to implement compact tuning-less quasi-elliptic filters. These structures are formed by rectangular waveguide cavities arranged in a way that enables the implementation of couplings between adjacent and non-adjacent resonators along the RF path. Figure 4.2 depicts a basic three-resonator HFRW filter. As can be seen, two adjacent resonators (for instance, resonators 1 and 2) are vertically stacked with a certain overlap between them. This overlapping allows the interconnection through apertures in the top and bottom walls of both resonators. The shape and size of these apertures control the amount of coupling between the two resonators, as well as its type (i.e. whether it is predominantly electric or magnetic coupling). Simultaneously, non-adjacent resonators (resonators 1 and 3 in the figure) are coupled via another aperture, implementing the cross-coupling. Effectively, two signal paths are created: one path goes through resonators 1, 2 and 3, and the other goes straight from resonator 1 to resonator 3 via the cross-coupling aperture. Consequently, at a certain finite frequency the signals traveling through both paths cancel each other, thus generating a transmission zero.

One of the major strengths of this filter topology is its modularity. Starting

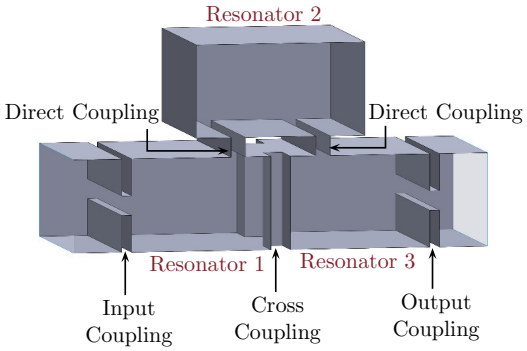

Figure 4.2: Three-pole HFRW filter, also known as a trisection. Lateral wall has been removed to permit visualization of the interior.

from the basic trisection shown in Fig. 4.2, the designer is able to include as many resonators as desired, just by stacking them above or below the preceding resonator. Each additional resonator is simply coupled to the last cavity in the structure through an opening located on its top or bottom wall. At the same time, this new resonator may be coupled to the second-to-last one, realizing a cross-coupling. Responses with multiple TZs can be obtained by simply cascading as many trisections as required, so that each trisection realizes a TZ.

In addition to selecting the number of TZs, the HFRW configuration also offers flexibility in the cavity arrangement. Filter designers that strive to achieve the most efficient use of physical space available can realize highly compact structures. Alternatively, HFRW filters can be adapted to a variety of layouts and fulfill different port-placement requirements (key in multiplexer design). For example, the classical five-resonator structure shown in Fig. 4.3a can be folded into a staircase configuration (see Fig. 4.3b) in case a purely inline port arrangement is not a viable option. Likewise, a 90° rotation of the resonators can be applied in order to place the input and output ports in the same plane, as shown in Fig. 4.3c.

The symmetry in width of the overall structure is another important characteristic of this topology. It facilitates the fabrication of the filter with a clam-shell assembly that does not interrupt current lines, and therefore reduces the insertion losses due to manufacturing effects. In addition, this manufacturing technology limits the chance of passive intermodulation, an undesired effect in high-power applications. The lack of tuning elements also aids in reducing these high-power effects. Unfortunately, this also eliminates the possibility of compensating manufacturing deviations. As a consequence, tuning-less structures are restricted to filters with relative moderate bandwidths, greater than 1-2% in Ku band. Therefore, tuning-less HFRW filters are ideally suited for the output stages of satellite

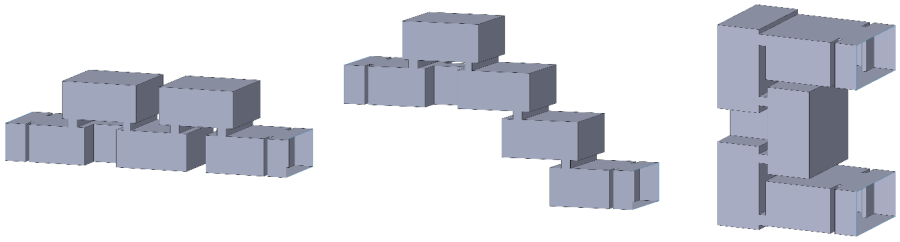

(a) **(b)** **(c)**

Figure 4.3: Five-pole HFRW filter structures. **(a)** Classical interconnection of cavities following a zig-zag arrangement. **(b)** Alternative stair-case configuration. **(c)** Configuration with rotated resonators.

communication payloads and ground-station equipment, where the filtered bands are wide and the signal intensity is considerable. In contrast, these structures find limited application in narrowband scenarios, where more compact structures, such as dual-mode filters, are preferred.

The study of HFRW filters performed in the framework of this thesis is focused on the physical realization of trisections. These elements are the basic building block to realize higher order filters. Multiple coupling combinations are available to implement trisections with the TZ located on either side of the passband. Figure 4.4 summarizes the possible coupling combinations, organized by the side of the passband where the TZ is located.

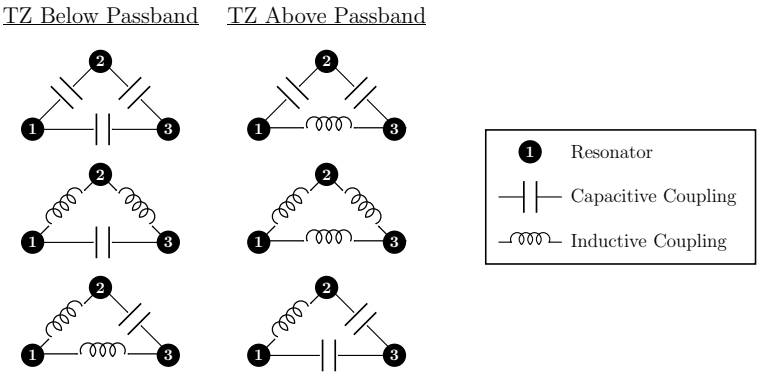

Figure 4.4: Coupling combinations in a triplet that provide TZs above or below the passband.

In the following section, certain physical apertures will be proposed to imple-

ment the inductive and capacitive elements of Fig. 4.4. The resonant nature of some of these apertures will have a strong influence on how HFRW trisections are modeled. In particular, a modification of the classical triplet coupling scheme will be proposed, to account for the resonant nature of the direct-coupling apertures. This modification proves that HFRW trisections are able to realize more than one TZ, and a design methodology to prescribe their location will be proposed. Then, practical aspects relative to the physical implementation of HFRW trisections will be discussed. Finally, a five-order filter example will be presented to validate the theoretical and practical features of this novel configuration.

4.1.1 Coupling mechanisms in HFRW filters

This section considers different physical implementations for the direct and cross-couplings elements of HFRW filters. Even though multiple coupling combinations are able to provide the same frequency response, it is important to have flexibility to look for the physical structure that is best suited to fulfill certain electrical and geometrical specifications. For that reason, different alternatives are proposed to implement the coupling elements of these filters.

4.1.1.1 Direct coupling implementations

For the most common cavity arrangement of HFRW filters (see Fig. 4.3a), direct coupling windows connect the top and bottom walls of adjacent resonators via rectangular apertures of size $d \times w$. The coupling apertures have a finite thickness t, and are separated from the short-circuited end of each cavity by a length c (see Fig. 4.5). To simplify the study of these couplings, the c dimension is assumed to be equal in the top and bottom cavities. However, since this parameter has an important influence in the coupling level provided by the structure, a filter designer can also make use of asymmetrical irises to fulfill geometrical constraints.

Figure 4.5 depicts the two apertures proposed to implement inductive and capacitive direct couplings. The two structures differ only on the size of the aperture width w. Capacitive direct couplings make use of apertures with the same width w as the cavities that are being connected, whereas inductive direct couplings contain reduced-width apertures. Both structures are resonant irises that can be modeled by the equivalent circuit proposed in [148] and shown in Fig. 4.6. Being resonant structures implies that, below the resonance, the stored magnetic energy is greater than the electric one, thus the iris behaves inductively. In contrast, the iris behaves capacitively above the resonance [149]. The width of the aperture w is mainly used to control the location of the resonance, whereas d controls the amount of coupling (in addition to influencing the resonant condition). For apertures that span the total width of the cavities (see Fig. 4.5b), the resonance condition occurs

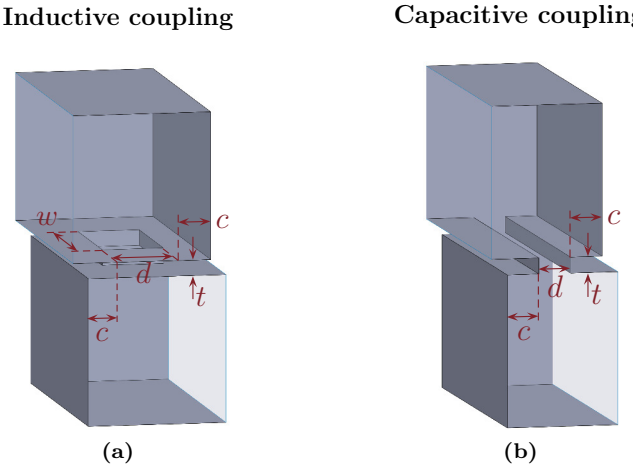

Figure 4.5: Direct coupling apertures.**(a)** Physical implementation of an inductive direct coupling. **(b)** Physical implementation of a capacitive direct coupling.

at the cut-off frequency of the port waveguides. Consequently, the iris behaves capacitively in the passband of the filter (which must be located above the cut-off of the waveguides used as resonators). As the aperture width w decreases, the resonance moves towards higher frequencies. As long as the resonance is located above the filter passband, the iris behaves inductively.

It is worth noting that the structure in Fig. 4.5a can be used to implement both capacitive and inductive irises, simply by adjusting the width w. However, it is more convenient to use an aperture that spans the width of the cavity to implement capacitive couplings. On the one hand, this discontinuity is simpler to analyze and manufacture. On the other hand, it increases the spurious-free range of the filter below the passband, since the resonance is located at or near the cut-off. Given the advantages of this second structure, in this thesis capacitive direct-couplings are assumed to be implemented by the structure depicted in Fig. 4.5b, unless otherwise noted.

Full-wave EM simulations can be employed to study the performance of a coupling structure as a function of its geometrical dimensions. From the S_{11} scattering parameter, the normalized impedance parameter $\overline{K}$ associated with the coupling structure under analysis can be computed as:

$$\overline{K} = \sqrt{\frac{1 - |S_{11}|}{1 + |S_{11}|}} \tag{4.1}$$

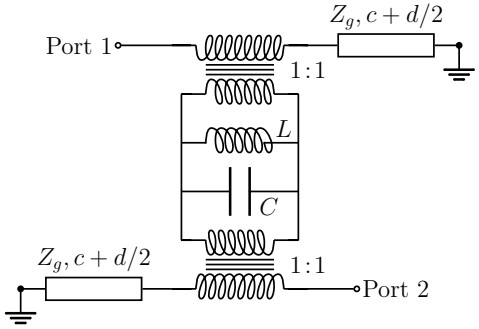

Figure 4.6: Wideband equivalent circuit proposed in [148] for the direct coupling apertures. L and C are computed from EM-simulations. Z_g is the power-voltage-defined waveguide impedance [140] of the short-circuited stubs. $c + d/2$ is the length of the transmission line, representing the distance between the short-circuit and the aperture center.

This parameter represents the inverter constant of an ideal impedance inverter with the same reflection coefficient as the physical structure under study. For filter design, this is an important parameter to transform the synthesized circuit model into a physical structure.

Fixing the aperture width w, the amount of coupling that a certain direct-coupling element provides is controlled by three dimensions: the aperture size d, its thickness t and the distance between this aperture and the short-circuit c. Figures 4.7 and 4.8 depict the normalized impedance parameter $\overline{K}$ as it relates to these three parameters. Figure 4.7 considers capacitive direct-coupling structures (w equals the resonator width), whereas Fig. 4.8 considers inductive couplings (w is set to 10 mm to locate the aperture resonance clearly above 10 GHz). As can be seen, the aperture size d provides the best adjustment range of the three physical parameters. As the aperture size d increases, so does the amount of coupling. However, when the aperture is large, there are high-order resonances that limit the maximum coupling level provided, and can interfere with the out-of-band response of the filter. For that reason, it is convenient to limit the size of the aperture and adjust other geometrical parameters to obtain very large coupling levels.

For instance, the location of the aperture along the cavity also has a significant effect in the coupling value. Moving away from the short-circuit, the capacitive aperture starts increasing the coupling it provides, until it reaches a maximum level. Minimum coupling is then obtained when the center of the aperture is located at, approximately, a quarter-wavelength from the short circuit. As it is well known, a quarter-wavelength short-circuited transmission line produces a

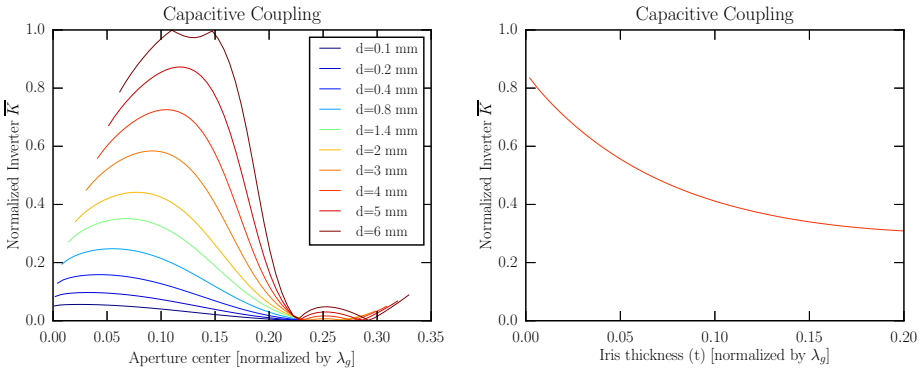

Figure 4.7: Normalized inverter parameter $\overline{K}$ as it relates to the geometrical dimensions of the capacitive direct-coupling structure. The results are obtained at 10 GHz using WR-75 waveguides. **(a)** $\overline{K}$ as a function of the position of the aperture $(c + d/2)$ with respect to the short circuit for different aperture sizes d and $t = 1$ mm. **(b)** $\overline{K}$ as a function of the thickness t for $d = 4$ mm and $c = 2$ mm.

destructive interference (or transmission zero) at the frequency where its electrical length becomes 90°. Since the structure contains two stubs (one in the upper cavity and another in the lower cavity), there is a double TZ. This can be observed in Fig. 4.7a, where the two positions of $\overline{K} = 0$ between $0.2\lambda_g$ and $0.3\lambda_g$ correspond to simulations where the TZ is located at the frequency of analysis. Ideally, the double TZ should appear at exactly $0.25\lambda_g$, but the mutual interaction between the two TZs moves them in opposite directions: one is slightly above $0.25\lambda_g$ and the other is slightly below this value. As the aperture size increases, the interaction is stronger and the shift in opposite directions is more clearly distinguished. This effect has been employed to realize all-capacitive filters with TZs that do not include cross-couplings [150, 151]. However, the resulting filters become larger in the direction of propagation, thus causing resonators to operate in the TE_{102} mode (or even higher orders) in order to implement the filter. For that reason, it is recommended to use cross-coupled HFRW structures with short stubs and TE_{101} resonators in applications that require compact structures (for instance, at low frequencies).

Finally, the thickness t of the aperture may also be employed to adjust the coupling level. However, the adjustment range is limited unless t becomes extremely short. This is evidenced by the relatively small coupling variation seen in Fig. 4.7b and 4.8b, especially compared with the coupling variation provided by dimensions

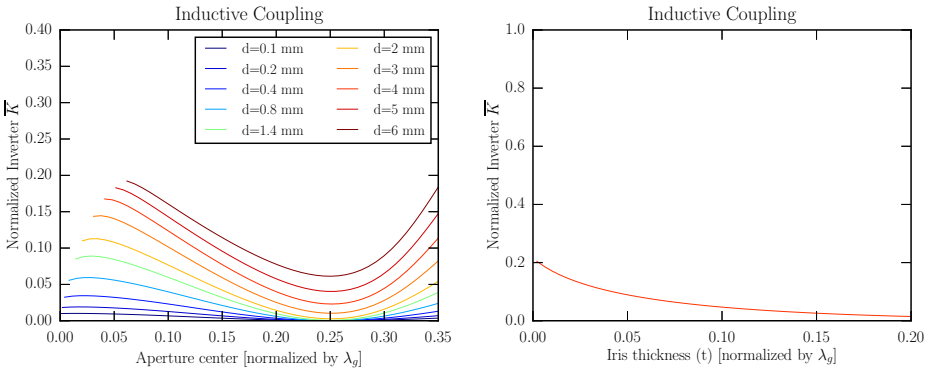

Figure 4.8: Normalized inverter parameter $\overline{K}$ as it relates to the geometrical dimensions of the inductive direct-coupling structure. Results are obtained at 10 GHz using WR-75 waveguides. **(a)** $\overline{K}$ as a function of the position of the aperture $(c + d/2)$ with respect to the short circuit in an inductive structure with $w = 10$ mm and $t = 1$ mm. **(b)** $\overline{K}$ as a function of the iris thickness t for $d = 4$ mm and $c = 2$ mm.

d and c. Therefore, this variable is normally fixed according to manufacturing and volume requirements.

4.1.1.2 Cross-coupling implementations

The main mission of the cross-coupling in a trisection is to realize a TZ and control its location. For that reason it is interesting to consider different cross-coupling implementations and classify them by the amount of coupling they tend to provide. In turn, this allows to visualize the frequency range (close or far from the passband) where each implementation realizes its TZ.

Three basic structures are first considered to implement the cross-coupling: a capacitive window, an inductive window and a resonant slot. These three structures are depicted in Fig. 4.9 along with the geometrical dimensions that adjust the amount of coupling provided. Note that cross-coupling structures occupy the physical space between non-adjacent resonators. Therefore the length of the cross-coupling iris is given by the resonator located above or below, and cannot be used to adjust the coupling value.

Figure 4.10 depicts the normalized inverter parameter $\overline{K}$ as a function of each aperture size. As can be inferred from the data, the capacitive window provides a strong coupling, especially compared with its inductive counterpart. The main

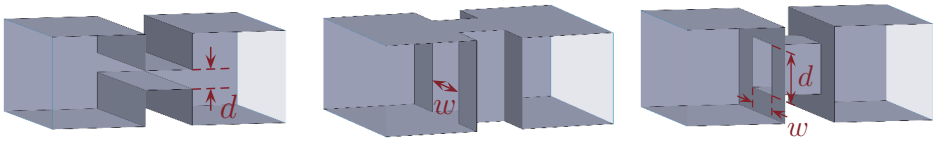

(a) Capacitive **(b)** Inductive **(c)** Mixed

Figure 4.9: Cross-coupling implementations.

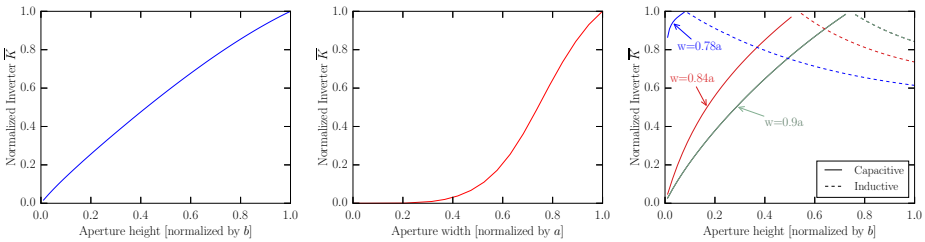

(a) Capacitive **(b)** Inductive **(c)** Mixed

Figure 4.10: Normalized inverter parameter $\overline{K}$ as a function of the geometrical dimensions for the three cross-coupling implementations. Aperture dimensions are normalized by the corresponding dimensions of the adjacent WR-75 rectangular waveguides ($a = 19.05$ mm, $b = 9.525$ mm). The three cross-coupling irises are 5 mm long in the direction of propagation. Results are obtained at 10 GHz.

reason is that the inductive window is below cut-off in the passband, thus the coupling is provided via evanescent instead of propagating modes. Strong couplings are required to locate TZs close to the passband. In those cases, structures with capacitive cross-couplings are the preferred solution. In contrast, inductive windows are able to provide small coupling values with moderate-size apertures. Combined with the fact that the structure is not very sensitive to small changes in the aperture size (i.e. the structure is robust to manufacturing tolerances), it is clear that this solution is ideal to implement filters with TZs located far from the passband.

A third solution is to combine capacitive and inductive windows in a resonant slot, as shown in Fig. 4.9c. Being a resonant structure, this solution is able to control the coupling by adjusting the resonant frequency of the LC tandem, in

addition to its size. As depicted in Fig. 4.10, this means that similar coupling levels can be obtained with much smaller dimensions of the aperture, compared to the purely capacitive and inductive window solutions.

In some instances, the opposite effect is desired: achieving a certain coupling level with apertures of considerable size. This is the case of all-capacitive filters that require low cross-coupling levels. Since capacitive windows generate such strong couplings, the size of the windows may be too small to manufacture if the TZs are to be placed far from the passband. In those cases, an alternative structure is proposed. It is also based on the combination of a capacitive and an inductive window, but instead of forming a slot, these two windows are separated by a small section of rectangular waveguide (see Fig. 4.11a). This hybrid structure can also be seen as a resonant coupling structure. Depending on the location of its resonant frequency with respect to the filter passband, it is able to provide either inductive or capacitive coupling. Three physical dimensions are employed to adjust the amount and sign of the coupling: height of the capacitive window d, width of the inductive window w and distance between windows l. As the inductive window closes, the total coupling is reduced. This loss of coupling can be compensated by increasing the size of the capacitive window, which is the ultimate objective of this structure. However, attention has to be paid to the change in the resonant condition to make sure that it is kept below the passband of the filter (to guarantee the capacitive nature of the coupling).

As was previously mentioned, the total length of the cross-coupling structure cannot be altered. Therefore, the substitution of a capacitive window by this resonant structure is not trivial. It is known that a reduction in the capacitive section length increases the total coupling. First, the inductive window has to compensate this increase in coupling, and then, the capacitive window can start increasing its height. Therefore there is a clear tradeoff between these two factors. Figure 4.11b compares the coupling value provided by a small capacitive window of length 5 mm (labeled "Ref. Capacitive") with the coupling value provided by this hybrid structure (the capacitive window in the second case has a length of 4 mm). As shown, the structure is able to provide smaller coupling values with larger apertures than the stand-alone capacitive window in a certain range of coupling values.

At the same time, the length l can be used to enhance this effect. As the two windows move away from each another, the strength of its resonant effect fades, which aids in reducing the total coupling provided. Therefore, the height of the capacitive coupling can be further increased. However, there is a limit, since the total length must remain constant. As depicted in Fig. 4.11c, when length l is relatively small, an increase in its value yields lower couplings. However, at some point the coupling lost by increasing this length is smaller than the coupling gained because the capacitive window reduces its length. Therefore, for large values of l the coupling increases with this dimension.

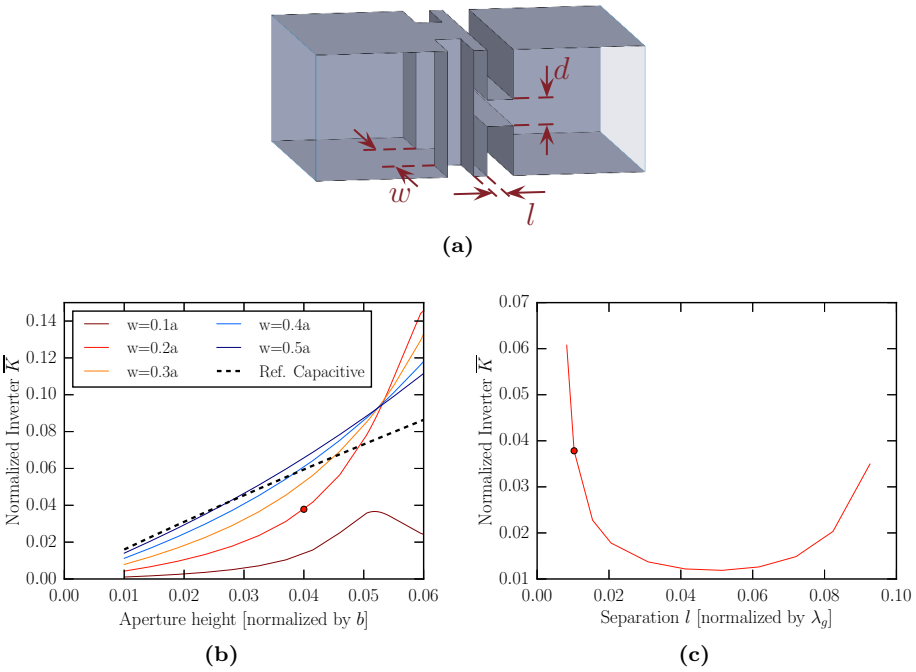

Figure 4.11: Alternative implementation of the mixed cross-coupling. **(a)** Structure and geometrical parameters. **(b)** Normalized inverter parameter as a function of the normalized height d for different widths w of the inductive window. The capacitive and inductive windows are 4 mm and 0.5 mm long, respectively. The distance between them is set at 0.5 mm. **(c)** Normalized inverter parameter as a function of the normalized length between windows l. The circled data point corresponds to the same data point as in (b) (i.e. $d = 0.04b$, $w = 0.2a$). As the length l increases, the length of the capacitive window has to be decreased, since the total length must not be altered.

4.1.2 Wideband modeling of HFRW trisections

HFRW filters are implemented by a cascade of trisections that generate the reflection and transmission zeros required to fulfill the requirements. Therefore, the basic building block for these filters is the trisection, composed of three resonators and three couplings (two direct-coupling windows and one cross-coupling element), in addition to the input/output couplings (see Fig. 4.2). The coupling scheme of a trisection is commonly known as a triplet, and is depicted in Fig. 4.12a. Depending on the particular combination of couplings, the triplet is able to generate TZs above or below the passband, as summarized in Fig. 4.4.

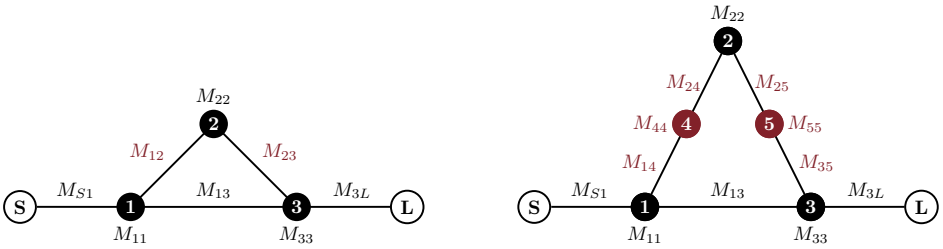

(a) Triplet coupling scheme

(b) Modified HFRW coupling scheme

Figure 4.12: Coupling schemes related to the basic building block of HFRW filters.

In the basic triplet coupling scheme, the direct-coupling apertures are represented by inductive or capacitive lumped elements that provide a certain amount of coupling between resonators. In Fig. 4.12a this corresponds to elements M_{12} and M_{23}. However, it was shown in section 4.1.1 that the direct coupling windows employed in HFRW filters are actually resonant elements (even if they resonate outside the passband). Therefore, it is convenient to include these resonators in the coupling matrix model in order to represent the behavior of HFRW trisections in a wider frequency band. The resulting coupling scheme is depicted in Fig. 4.12b. Capacitive cross-coupling windows can also be regarded as resonant elements. Consequently, an additional resonator could be placed between resonators 1 and 3 in Fig. 4.12b to account for their behavior. However, this change slightly increases the complexity of the model without providing any significant advantage. For that reason, the simpler model with 5 resonators is preferred.

The first consequence of this modification, is that the scheme in Fig. 4.12b accounts for more TZs than the scheme in Fig. 4.12a. According to the minimum path rule [152], the maximum number of TZs n_{TZ} that can be realized by a network with N resonators depends on the number of resonators $n_{\min}$ located in the shortest route between the source and load terminations. The relationship between these parameters is:

$$n_{\mathrm{TZ}} = N - n_{\min} \tag{4.2}$$

The basic triplet of Fig. 4.12a realizes one TZ, since the total number of resonators is $N = 3$ and the number of resonators in the shortest path is $n_{\min} = 2$. When accounting for the resonant behavior of the direct-coupling apertures (Fig. 4.12b), the resulting structure is capable of realizing 3 TZs (since it increases by two the total number of resonators outside the shortest path).

When dealing with resonant cross-coupling windows like the ones shown in Fig. 4.11, it is convenient to introduce an additional resonator between elements

1 and 3. Even though it does not account for any additional TZ (since the extra resonator is located in the shortest path) it can certainly influence their location. In contrast with its capacitive counterpart, the resonant cross-coupling windows is able to adjust its resonance. As it will be shown in section 4.1.4.3, if this resonance is located just above the resonances of two capacitive direct-coupling windows, the resulting trisection is able to place the 3 TZs in the desired stopband. That clearly justifies the use of a slightly more complex model when employing this type of cross-coupling window, that is not present in the purely capacitive case.

In order to illustrate the superior modeling capacity of the modified coupling matrix for HFRW trisections, an example is considered. The coupling matrix (CM) of a triplet centered at 12.6 GHz with a bandwidth of 400 MHz and a TZ at 10.6 GHz is:

$$M = \begin{bmatrix} 0 & 1.221 & 0 & 0 & 0 \\ 1.221 & -0.038 & -1.214 & 0.136 & 0 \\ 0 & -1.214 & 0.121 & 1.214 & 0 \\ 0 & 0.136 & 1.214 & -0.038 & 1.221 \\ 0 & 0 & 0 & 1.221 & 0 \end{bmatrix} \tag{4.3}$$

If this triplet is implemented in the HFRW topology, the capacitive and inductive direct couplings will become additional resonators that have to be included in the coupling scheme. A possible N+2 coupling matrix with an equivalent in-band frequency response and location of the triplet TZ is:

$$M_{\text{mod}} = \begin{bmatrix} 0 & 1.306 & 0 & 0 & 0 & 0 & 0 \\ 1.306 & 1.233 & 0 & 0.126 & -5.882 & 0 & 0 \\ 0 & 0 & 0.180 & 0 & -5.882 & 3.422 & 0 \\ 0 & 0.126 & 0 & -1.15 & 0 & 3.422 & 1.306 \\ 0 & -5.882 & -5.882 & 0 & 24.469 & 0 & 0 \\ 0 & 0 & 3.422 & 3.422 & 0 & -7.756 & 0 \\ 0 & 0 & 0 & 1.306 & 0 & 0 & 0 \end{bmatrix} \tag{4.4}$$

The diagonal elements of the coupling matrix associated with resonators 4 and 5 are large, reflecting a considerable frequency shift with respect to the filter center frequency. As expected, these elements represent the out-of-band resonances of the direct-coupling apertures.

The scattering parameter response of both coupling matrices is depicted in Fig. 4.13. The direct-coupling resonances can be easily identified (resonators 4 and 5). As expected, the coupling matrix of (4.4) provides two additional TZs, when compared with the response of (4.3). The TZ located the closest to the passband is associated with resonator 2, shared by both coupling schemes. In contrast, the two additional TZs are associated with the direct-coupling resonators of the modified coupling scheme. This association between specific TZs and specific resonators in

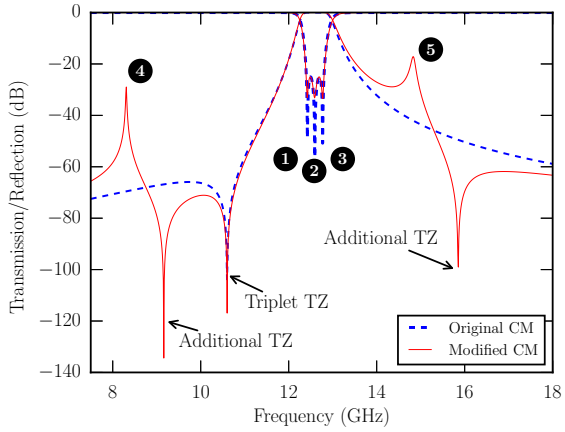

Figure 4.13: Comparison of the response of the coupling matrices in (4.3) and (4.4) for a filter centered at 12.6 GHz with 400 MHz of bandwidth.

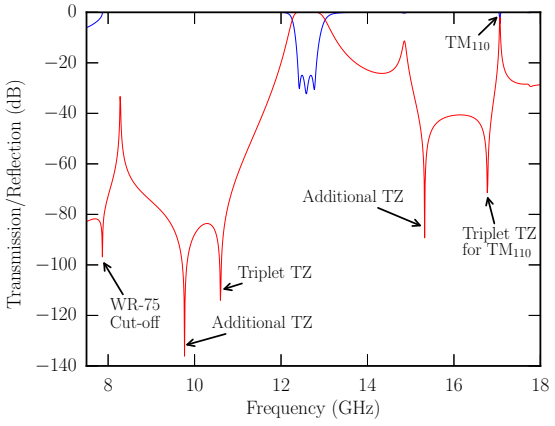

Figure 4.14: FEST3D full-wave simulation of the trisection centered at 12.6 GHz with 400 MHz bandwidth and a TZ at 10.6 GHz.

the coupling scheme can be verified by de-tuning any of them: as the resonance shifts, the TZ moves accordingly.

To ensure that the modified coupling scheme is coherent with the physical implementation of this trisection, a prototype has been constructed and simulated in FEST3D. The full-wave simulation is shown in Fig. 4.14, confirming the presence of the three TZs. In fact, the structure realizes a fourth TZ associated with the

higher order mode TM_{110} of the central resonator. Since the coupling matrix is a single-mode representation, these higher order modes are not properly considered. However, it is clear that the modified coupling scheme is a superior representation of the physical HFRW structure in a wide frequency band. Nonetheless, the accuracy of the coupling matrix representation decreases away from the passband. For that reason, the location of the additional TZs is not perfectly matched with the simulation. Therefore, the modified coupling matrix is a useful tool to understand the behavior of a particular structure, but not as useful to base the complete design process on it.

Even though it has been confirmed that the HFRW trisection is able to realize at least 3 TZs, not all of them are located in the desired stopband of the filter. Depending on the specific coupling combination, the number of TZs in the desired stopband varies. For example, the filter of Fig. 4.14 only has two TZs in the prescribed stopband (below the passband). The third TZ is above the resonance of the direct-coupling aperture, thus it is of very little use. Section 4.1.4 contains a discussion on the practical aspects associated with the physical implementation of HFRW filters. Several implementations will be proposed and, in each case, the amount of TZs in the stopband will be specified. As will be shown, only one of the additional TZs (associated with direct-coupling apertures) can be located in the same side of the passband as the TZ realized by the triplet, unless a resonant cross-coupling window is employed. Regarding the control over the location of this additional TZ, a simple method to adjust it independently of the triplet TZ is proposed in section 4.1.3.

4.1.3 Design procedure for HFRW filters

As previously discussed, the modified coupling scheme of section 4.1.2 is an interesting model to understand the wideband behavior of HFRW trisections. However, this coupling scheme has some limitations to represent the structure away from the passband, thus not being an accurate tool to prescribe the exact location of the additional TZs. In this section, an alternative design procedure is proposed. It makes use of the triplet coupling-matrix representation to perform an initial design of the different filter trisections. This initial design generates the passband of the filter and realizes the triplet TZs. From this initial design, a physical structure is extracted. Then, a simple methodology is applied to adjust the location of the additional TZs to the prescribed locations.

4.1.3.1 Initial design

From the triplet coupling matrix, the trisection distributed circuit shown in Fig. 4.15 can be constructed. It contains half-wavelength dispersive transmission lines and inverters. This model takes into account the specific dispersion introduced by

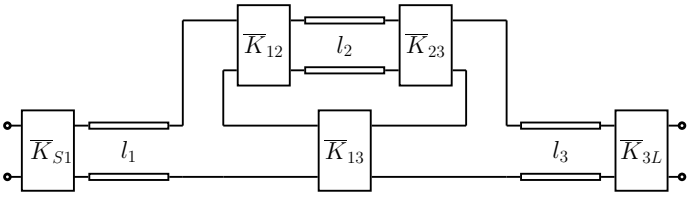

Figure 4.15: Distributed equivalent circuit representation of a triplet.

the rectangular waveguides that implement the resonators. As shown in [150], the initial values for elements in the distributed model can be extracted from the synthesized coupling matrix as:

$$\overline{K}_{S1} = M_{S1}\sqrt{\frac{\pi}{2}\mathcal{W}_{\lambda 1}} \qquad \overline{K}_{23} = M_{23}\frac{\pi}{2}\sqrt{\mathcal{W}_{\lambda 2}\,\mathcal{W}_{\lambda 3}} \quad \overline{K}_{13} = M_{13}\frac{\pi}{2}\sqrt{\mathcal{W}_{\lambda 1}\,\mathcal{W}_{\lambda 3}}$$

$$\overline{K}_{12} = M_{12}\frac{\pi}{2}\sqrt{\mathcal{W}_{\lambda 1}\,\mathcal{W}_{\lambda 2}} \quad \overline{K}_{3L} = M_{3L}\sqrt{\frac{\pi}{2}\mathcal{W}_{\lambda 3}} \tag{4.5}$$

where M_{ij} are the non-diagonal elements of the coupling matrix, and $\mathcal{W}_{\lambda i}$ is the filter factional bandwidth expressed in terms of wavelength ratios associated with resonator i. This last variable is computed as

$$\mathcal{W}_{\lambda i} = 2\frac{\lambda_{g1i} - \lambda_{g2i}}{\lambda_{g1i} + \lambda_{g2i}} \tag{4.6}$$

where λ_{g1i} and λ_{g2i} are, respectively, the guide wavelengths at the lower (f_1) and upper (f_2) passband edges of the filter. The waveguide employed to implement resonator i is used to compute λ_{g1i} and λ_{g2i}.

The diagonal components of the coupling matrix M_{ii} represent frequency-independent susceptances in the lowpass domain. Once these susceptances are transformed into the bandpass domain, the resonant condition for each resonator in the filter can be determined. The guide wavelength of each resonator is obtained as

$$\lambda_{gri} = \frac{1}{2}\left[M_{ii}\mathcal{W}_{\lambda i}\lambda_{g0i} + \sqrt{\left(M_{ii}\mathcal{W}_{\lambda i}\lambda_{g0i}\right)^2 + 4\left(\lambda_{g0i}\right)^2}\right] \tag{4.7}$$

where λ_{g0i} is guide wavelength at the filter center frequency, for resonator i, computed as:

$$\lambda_{g0i} = 2\frac{\lambda_{g1i}\lambda_{g2i}}{\lambda_{g1i} + \lambda_{g2i}}. \tag{4.8}$$

From λ_{gri}, the resonant frequency f_{ri} of each cavity can be obtained:

$$f_{ri} = c\sqrt{\left(\frac{1}{\lambda_{gri}}\right)^2 + \left(\frac{k_{ci}}{2\pi}\right)^2} \tag{4.9}$$

where k_{ci} is the cut-off wavenumber of the fundamental mode of the waveguide employed to implement resonator i, and c is the speed of light in the waveguide medium. In addition, the waveguide lengths in the distributed model are directly computed as $l_i = \lambda_{gri}/2$.

From the distributed model, the physical dimensions of the filter can be extracted by using a classical EM-based procedure [153,154]. Some dimensions in the filter must be set beforehand: the vertical distance between adjacent resonators t and the length of the stubs c (see Fig. 4.16). To simplify the design, all stub lengths can be set to the same value in the initial design. The first elements to extract are the input/output and direct couplings. In both cases, the dimension of the window that implements each coupling is adjusted until it behaves like the corresponding impedance inverter at the filter center frequency. For the direct couplings, the shaded section of Fig. 4.16a is used to compare its behavior with the inverter.

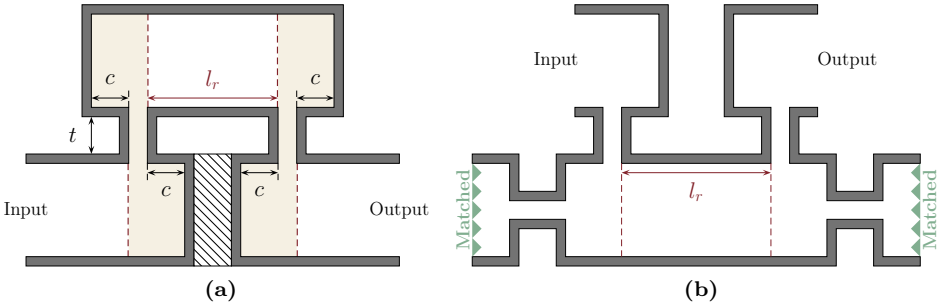

Figure 4.16: E-plane cut of filter sections. **(a)** Topology employed to tune the resonance of the central cavity. The hatched area below this cavity indicates the space that can be used to implement the cross-coupling. Prior to the resonance tuning, the beige-shaded area has been adjusted until it has the same behavior as the corresponding direct coupling impedance inverter at the filter center frequency. **(b)** Topology employed to tune the resonance of a cavity with multiple cross-coupling irises and two direct-coupling irises.

Having determined the dimensions of the direct couplings, the next step is to adjust the resonance of the cavities with cross-couplings above or below them. The reason is that, once the dimension of these cavities is determined, the space left to implement the cross-coupling above or below them will be known. This is illustrated in Fig. 4.16a, where the hatched area represents the space left to implement the cross-coupling after determination of l_r. To adjust the resonance, the distance l_r is shifted until the peak of the reflection coefficient is centered at the appropriate frequency defined by (4.9).

After tuning l_r, the length of the cross-coupling window above or below this resonator is known. Then, the iris shape is adjusted to provide the same response as the corresponding impedance inverter at the filter center frequency. Once all the cross-coupling windows are found, the remaining cavities can be adjusted. The structure employed to adjust the length of cavities having cross-coupling windows attached to them is shown in Fig. 4.16b. All irises are attached to the cavity, to compensate for their loading effect. To avoid reflections, cross-couplings are matched at their output ports.

A response very close to the desired one is obtained after the application of this systematic design procedure. Then, a final adjustment of the dimensions of the filter is performed to compensate for the mutual interactions neglected by the previous procedure. Finally, a response highly coincident with the one predicted by the coupling matrix is obtained.

As an example, this initial design procedure is applied to a simple all-capacitive triplet in WR-75 waveguide centered at 12.6 GHz with 400 MHz bandwidth, and two TZs located at 10.5 GHz and 11.6 GHz. The synthesized coupling matrix, considering only the TZ at 11.6 GHz, is:

$$M = \begin{bmatrix} 0 & 1.2214 & 0 & 0 & 0 \\ 1.2214 & -0.0791 & -1.1951 & -0.2879 & 0 \\ 0 & -1.1951 & 0.2550 & -1.1951 & 0 \\ 0 & -0.2879 & -1.1951 & -0.0791 & 1.2214 \\ 0 & 0 & 0 & 1.2214 & 0 \end{bmatrix} \tag{4.10}$$

According to (4.5) and (4.9), the inverter values and resonant frequencies are:

$$\begin{aligned} &\overline{K}_{S1} = \overline{K}_{3L} = 0.3492 \qquad \overline{K}_{13} = -0.0235 \\ &\overline{K}_{12} = \overline{K}_{23} = -0.09769 \\ &f_{r1} = f_{r3} = 12.616 \text{ GHz} \qquad f_{r2} = 12.549 \text{ GHz}. \end{aligned} \tag{4.11}$$

Following the design procedure, the circuit model is transformed into a physical structure. The response of this initial implementation can be seen in Fig. 4.17 with the label *Direct Design*. This is, indeed, an excellent starting point. Later on, the dimensions are slightly adjusted to fulfill the passband specifications. This response (labeled *Adjusted Design* in Fig. 4.17) is equivalent to the one provided by the coupling matrix from the passband up to the first TZ. Unfortunately, the location of the second TZ, at 8.9 GHz, is far from the prescribed frequency of 10.5 GHz. In the following subsection, a method to adjust the location of this additional TZ will be proposed.

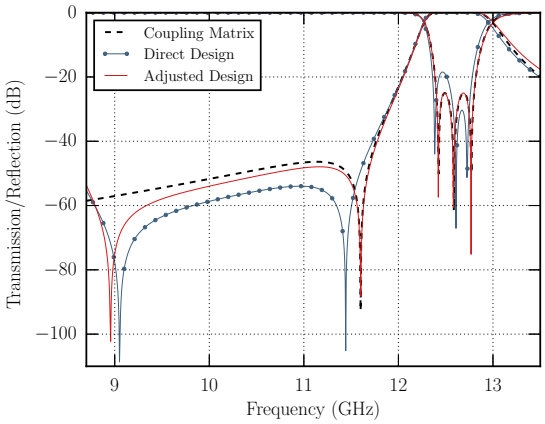

Figure 4.17: Response of example trisection after application of the initial design procedure. The triplet is centered at 12.6 GHz with 400 MHz bandwidth. The coupling matrix response is compared with the response obtained after direct application of the design procedure and, also, with the final response after optimization.

4.1.3.2 Control over the location of the additional TZ

To adjust the location of the additional TZ, the phase shift introduced by the path that crosses the direct-coupling apertures must change with respect to the path that goes through the cross-coupling window. The most direct way to do so is by modifying the cross-coupling window. This changes the location of the additional TZ but, unfortunately, it also alters the location of the triplet TZ. When the cross-coupling is reduced, the additional TZ moves towards higher frequencies whereas the triplet TZ moves towards lower frequencies, effectively approaching each other. As with any pair of TZs, when they coincide at the same finite frequency (providing a double TZ), their mutual interaction moves them away from the imaginary axis ($s = j\omega$) to paraconjugated complex frequencies. This effect is shown in Fig. 4.18a. Taking as an example the triplet whose response is depicted in Fig. 4.17, the size of the capacitive cross-coupling is changed between the original size d and half this value (the other dimensions are kept unaltered). As illustrated, both TZs approach each other until they are no longer visible in the S-parameter response.

As has been made clear, this technique is not adequate to control the location of the additional TZ independently of the location of the TZ introduced by the triplet. An alternative is to change the resonant frequency of the direct-coupling aperture, which, in turn, moves the additional TZ associated with the aperture in the same direction. This alternative is adequate for inductive direct-coupling apertures (see

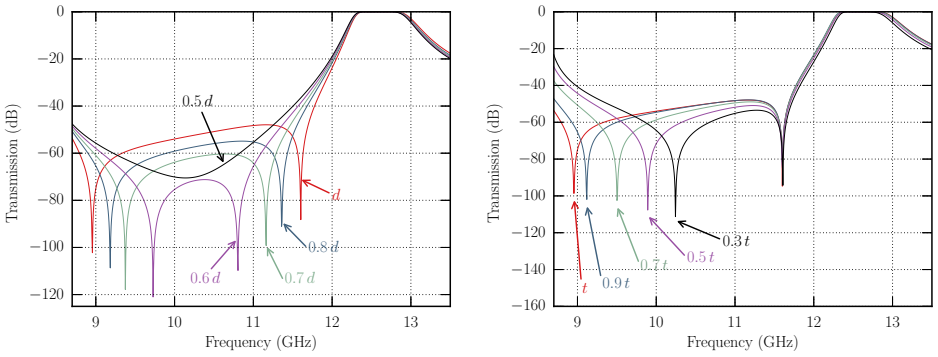

Figure 4.18: **(a)** Using as reference the adjusted design depicted in Fig. 4.17, the height d of the capacitive cross-coupling window is reduced. As this parameter decreases, the TZ introduced by the triplet moves towards lower frequencies, whereas the additional TZ moves towards higher frequencies. **(b)** Starting from the design example shown in Fig. 4.17, the length t that separates vertically the adjacent cavities is reduced. As this length decreases, the additional TZ moves towards higher frequencies (after adjustment of the couplings).

Fig. 4.5a), since they have multiple degrees of freedom to realize a certain coupling level as well as resonate at a certain frequency. However, capacitive windows that span the total width of the cavity do not have as many degrees of freedom. For these structures, a third solution is proposed. It is based on adjusting the length of the path that crosses the central resonator. In order to do so, the length of the direct coupling windows can be increased or decreased (thickness t in Fig. 4.16). Unfortunately, a change in the length of such window also affects, to some extent, the direct coupling level (as was shown in Fig. 4.7b and 4.8b). As t decreases, the direct coupling level slightly increases, thus introducing a small shift on the triplet TZ towards lower frequencies. At the same time, the additional TZ moves definitely towards higher frequencies. In this situation, the designer can readjust the direct-coupling window to recover the original coupling level. It will be immediately apparent how the additional TZ is now located at a higher frequency than initially, since the total phase shift has decreased. In some instances where a strong interaction between direct and cross-coupling windows occurs, it may also be necessary to slightly adjust the cross-coupling window to place the triplet TZ exactly at the original frequency.

The resulting effect after application of this procedure is depicted in Fig. 4.18b.

Starting from the designed triplet (see Fig. 4.17) the thickness t of the two direct-coupling windows is reduced. Then the structure is adjusted to recover the original location of the triplet TZ. As can be seen, the additional TZ has effectively moved towards higher frequencies.

For trisections with capacitive direct couplings, the change in their thickness t can be easily computed. If the additional TZ must be shifted between the original frequency f_{TZ} and the objective frequency f_{obj}, the total length increase for the complete direct-coupling path can be computed as:

$$\Delta t = \frac{\pi}{\beta(f_{\mathrm{obj}})} - \frac{\pi}{\beta(f_{\mathrm{TZ}})} \tag{4.12}$$

where $\beta(f)$ is the phase constant for the fundamental mode in the direct-coupling iris at frequency f. Since the length of both couplings must be equal, the increment Δt must be equally split between the two irises. In the case of triplets with one inductive and one capacitive direct-coupling window, this equation can be just used as a starting reference to adjust the length of the capacitive one. Additional fine tuning is required in those cases.

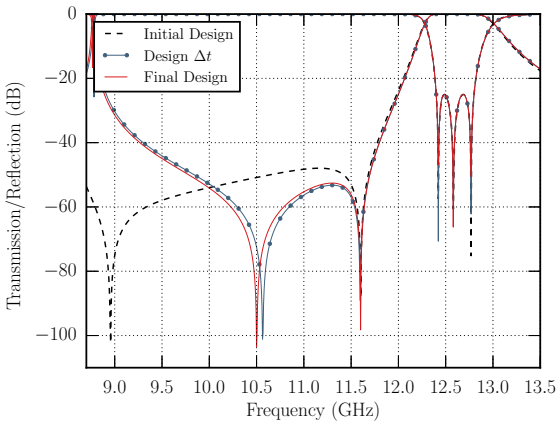

Figure 4.19: Final adjustments to the design example in order to move the additional TZ from 8.9 GHz to 10.5 GHz.

This simple method is applied to the designed filter of section 4.1.3.1 to adjust the location of the TZ from 8.9 GHz to the prescribed 10.5 GHz. Equation (4.12) is employed to estimate the length decrease of the direct coupling. Resonators and coupling windows are adjusted to recover the passband response and also the original location of the triplet TZ. The response obtained after this procedure is shown in Fig. 4.19 (labeled *Design* Δt). The additional TZ is not located exactly

at 10.5 GHz but very close to this value, at 10.57 GHz. In order to place it at exactly 10.5 GHz, the triplet is re-optimized, adjusting also the length t. The final response, having both TZs located at their prescribed frequencies, can be also seen in Fig. 4.19, labeled as *Final Design*.

4.1.4 Physical implementation of HFRW filters

When implementing HFRW filters in waveguide technology, there are certain aspects that have to be considered when selecting the most appropriate configuration to fulfill a set of requirements. The first aspect is the distribution of the TZs amongst the different trisections that form the filter. Depending on the side of the passband where the TZs are located, each trisection can be implemented by three different coupling combinations, as summarized in Fig. 4.4. At the circuit level, there is no clear benefit from using a certain coupling combination over another one. However, at the physical level, the proper choice of the coupling combination is critical. Each configuration has certain advantages and limitations and a different scope of application. Some implementations are ideally suited to realize TZs close to the passband, while others are more appropriate solutions to realize them far from the passband. Likewise, the amount of TZs that each implementation is able to generate in the stopband is another criteria for choosing the most appropriate implementation.

Other practical aspects that influence this decision are associated with design simplicity and efficiency. Given several configurations capable of fulfilling a certain set of electrical requirements, filter designers usually favor those that are simpler and faster to design. Modern filters are subject to intensive optimization to fulfill stringent requirements. Consequently, an adequate selection of the physical structure can dramatically decrease the design time. For instance, physically symmetrical structures are considerably simpler and faster to design than asymmetrical configurations. The reason is that only half the dimensions need to be adjusted (i.e. the input and output irises are equal, the first and last resonators have the same dimensions, etc). At the same time, designers must take into account the EM simulation tools employed to drive the optimization when selecting a physical implementation. Pairing a physical geometry with the right EM simulation tool goes a long way towards accelerating the design process. From this perspective, constant-width implementations are very interesting options. Since these are, in essence, 2D structures, commercial EM solvers take advantage of their electromagnetic symmetry to provide accurate results with very fast simulations. Therefore, the design of these components tends to have shorter design cycles. Unfortunately, these structures have a limited scope of application, thus designers often have to resort to slightly more complex 3D geometries (even if they are still formed by the connection of 2D blocks). In this context, it is increasingly important to employ efficient simulation tools like the one presented in chapter 2 of this PhD thesis to

succeed.

This section presents an in-depth study of multiple trisection implementations from a very practical perspective. Number and location of the TZs, ease of manufacture and simplicity in the design are all aspects considered and discussed for each topology. The objective is to offer designers a series of guidelines that help in selecting the most appropriate implementation for any given application.

4.1.4.1 Trisection with capacitive cross-coupling window providing TZs in the lower stopband

The first structure considered, shown in Fig. 4.20, is a trisection with a capacitive cross-coupling window. As previously mentioned, the location of the TZ in a trisection is strongly dependent on the value of the cross-coupling element. As a TZ moves closer to the passband, the cross-coupling value in the triplet increases. Section 4.1.1.2 showed that capacitive windows introduce strong couplings. Therefore, they are an ideal solution to place TZs close to the passband. This type of window guarantees that enough cross-coupling is provided, even if the physical distance between the non-adjacent resonators is large. In contrast, inductive apertures tend to provide lower coupling levels for similar window dimensions.

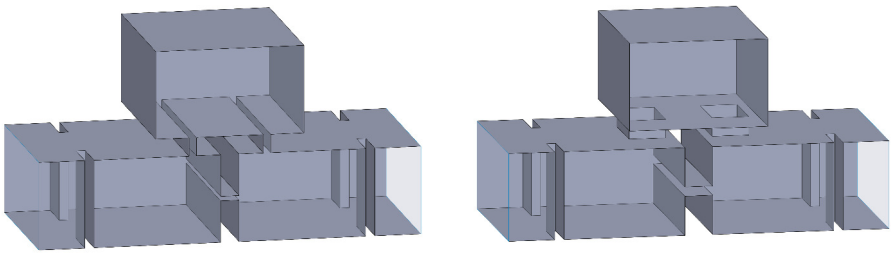

(a) **(b)**

Figure 4.20: Implementations of the trisection with capacitive cross-coupling. **(a)** Configuration with capacitive direct-couplings. **(b)** Configuration with inductive direct-couplings.

This cross-coupling window can be combined with both capacitive (Fig. 4.20a) and inductive (Fig. 4.20b) direct-coupling apertures. Generally, the trisection with all capacitive couplings in its core (this is, direct and cross-coupling windows have the same width) is easier to manufacture and design. If the input and output couplings are implemented by capacitive windows, the overall trisection is a purely bi-dimensional structure. As previously mentioned, the analysis of these structures is the fastest amongst all the possible HFRW trisections. Therefore, they are a highly desirable solution. However, being purely capacitive implies that

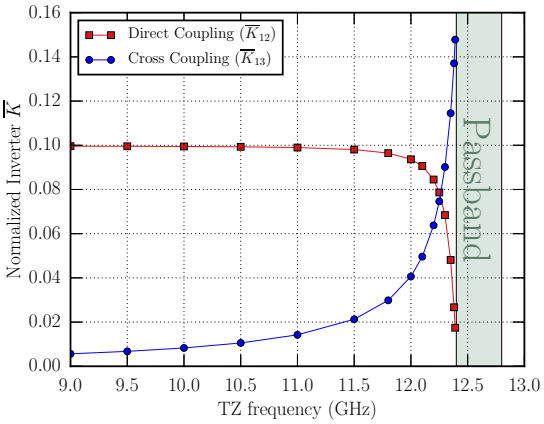

Figure 4.21: Normalized inverter parameter of the direct and cross-couplings in a trisection, as the TZ approaches the passband. Results are particularized for a WR-75 waveguide filter centered at 12.6 GHz with 400 MHz bandwidth

these implementations realize a potentially undesired passband around the cut-off frequency of the structure. This can be largely mitigated by simply changing these input and output couplings to inductive windows (as it has been done in Fig. 4.20a) in the last stage of their design.

The next factor to consider is the position of the TZ, as it affects the direct coupling value. Figure 4.21 depicts the inverter parameter $\overline{K}$ associated with the direct and cross coupling elements of a trisection for different positions of the TZ. As can be seen, when the TZ is not adjacent to the passband, the direct-coupling $\overline{K}_{12}$ is mostly flat, thus barely affected by the position of the TZ. In this case, the all-capacitive solution in Fig. 4.20a is preferred, as long as its design and implementation are feasible. However, as a TZ moves towards the passband, the direct coupling tends to zero rapidly. Implementing a small direct-coupling level with a capacitive iris can be problematic, since the size of the iris may be too small to be physically realizable. In addition, given that the electric field in these irises tends to be high, there is a considerable risk of high-power issues (such as multipactor breakdown) for very small irises.

In those situations where the required direct coupling level is too small, the best option is to use the solution depicted in Fig. 4.20b. Compared with the all-capacitive solution, the direct-coupling elements in this case are rectangular slots that behave as inductive irises in the passband. These irises are able to yield the same direct-coupling value as the all-capacitive case, but with a much bigger aperture. As a result, the inductive solution avoids the aforementioned

mechanical and power-handling issues for filters with TZs extremely close to the passband. Since this is, in nature, a resonant iris, it produces a resonance above the passband. Although it cannot be avoided, its position can be controlled by adjusting the cross-section of the iris. As an example, Fig. 4.22 shows the response of the triplet depicted in Fig. 4.20b. This triplet provides a TZ separated from the passband by 55 MHz. The passband is centered at 12.6 GHz with a 400 MHz bandwidth. In the final design, all dimensions are greater than 1 mm, which should guarantee a successful manufacture by milling.

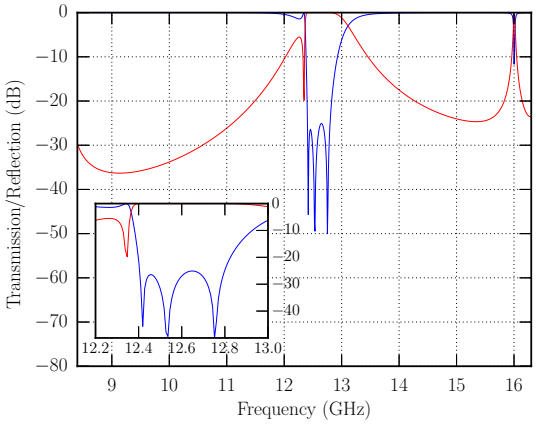

Figure 4.22: Response of the triplet with capacitive cross-coupling and inductive direct coupling of Fig. 4.20b. This triplet introduces a TZ at 12.345 GHz for a filter response centered at 12.6 GHz with a 400 MHz bandwidth. The resonant behavior of the inductive direct-coupling irises generates the undesired resonance at 16 GHz.

The last factor to consider is the amount of TZs that each option is able to provide in the lower stopband. Making use of the modified coupling scheme of Fig. 4.12, it can be proved that the solution with inductive direct-coupling apertures is only able to provide one TZ in the lower stopband. The other two TZs are located between the two direct-coupling resonances and thus cannot be used to increase the isolation in the stopband. In contrast, the all-capacitive implementation (Fig. 4.20a) is able to realize one additional TZ in the lower passband for a total of two (the second additional TZ is located below the direct-coupling resonances), as can be seen in Fig. 4.23. The location of the additional TZ can be controlled by the thickness of the direct-coupling window, as explained in section 4.1.3.2.

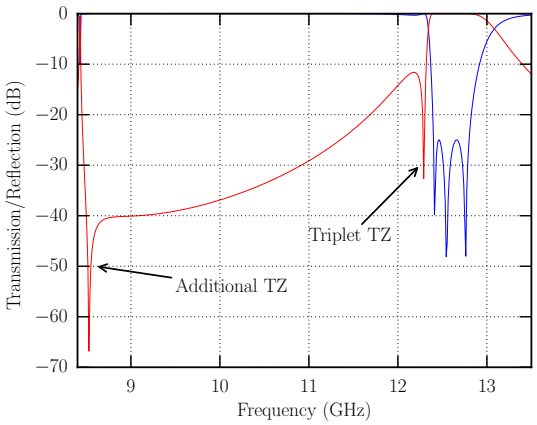

Figure 4.23: Response of the all-capacitive trisection of Fig. 4.20a. Two TZs can be easily identified below the passband.

4.1.4.2 Trisection with inductive cross-coupling window providing TZs in the lower stopband

The capacitive cross-coupling window used in section 4.1.4.1 is able to provide high coupling values with relatively small dimensions of the window. This is advantageous when a TZ is to be placed close to the passband, but becomes a burden when the TZ must be located further away. In those cases, the size of the capacitive window may be too small to be manufactured accurately, or to avoid high-power issues. There are several ways to slightly increase this size. The first one is to increase the length of the cross-coupling window, which comes at the cost of increasing the total length of the filter, and may not be feasible. In addition, it is obvious that there is a strict geometrical limitation on how much this length can be increased, since it depends on the resonator above or below the cross-coupling element. In general, this is not practical. Alternatively, the capacitive cross-coupling window can be vertically off-centered towards the central resonator in order to decrease the coupling (effectively allowing an increase in the size of the iris). The increase that can be achieved with this technique is not very large, typically 50% for very small windows.

A more powerful solution to realize TZs far from the passband is based on the scheme depicted in the bottom-left side of Fig 4.4. The cross-coupling iris is substituted by a classical inductive window. To generate a TZ below the passband, one direct coupling is a capacitive aperture whereas the other is a resonant aperture that behaves inductively in the passband. The resulting structure is shown in Fig. 4.24a. This structure is able to provide low cross-coupling levels with moderate

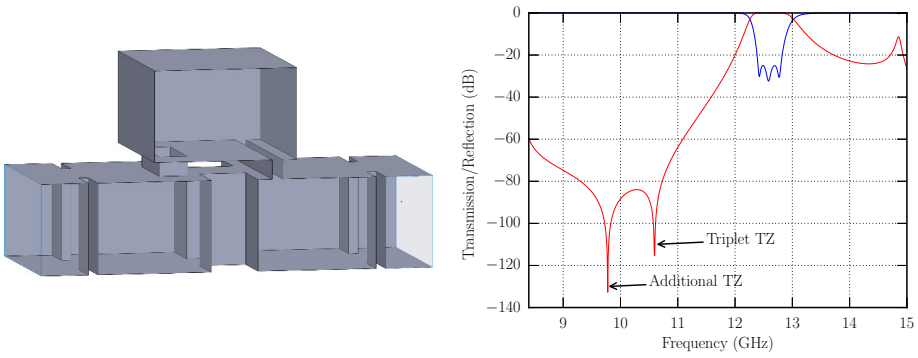

(a) **(b)**

Figure 4.24: **(a)** Trisection with inductive cross-coupling. A capacitive window implements one direct coupling whereas an inductive aperture implements the other direct coupling. **(b)** Response of this trisection. Two TZs can be identified below the passband. In addition, the inductive direct coupling generates a resonance above the passband, at 14.85 GHz.

dimensions of the inductive cross-coupling iris. Therefore, it is much more robust to manufacturing deviations than its capacitively cross-coupled counterpart (for TZs located far from the passband). As in the all-capacitive case, this particular implementation of a trisection is also able to provide two TZs below the passband (the second additional TZ is realized above the inductive resonance, as shown in Fig. 4.14). Figure 4.24b depicts the response of this trisection, where the two TZs can be identified. The higher-frequency TZ is the one associated with the triplet, whereas the lower-frequency TZ is the additional TZ associated with the capacitive direct-coupling aperture. The presence of an undesired resonance in the upper stopband (due to the inductive direct-coupling aperture) is the main drawback of this configuration.

4.1.4.3 Trisection with resonant cross-coupling window providing TZs in the lower stopband

For some applications, the presence of undesired resonances in the upper stopband is unacceptable. In those situations, HFRW filters must avoid inductive direct-coupling windows. If the specifications require the implementation of TZs far from the filter passband, the use of the resonant coupling structure presented in Fig. 4.11 is recommended. This alternative implementation provides additional degrees of freedom to generate a specific coupling, while keeping the dimensions

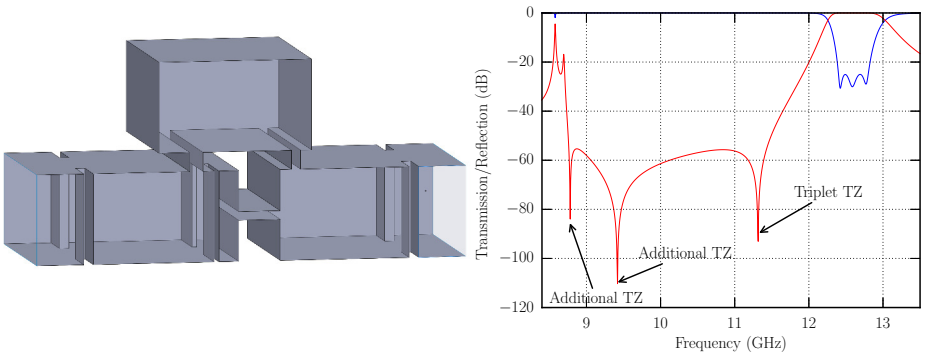

(a) **(b)**

Figure 4.25: **(a)** Trisection with resonant cross-coupling. A combination of inductive and capacitive windows implements the resonant cross-coupling. **(b)** Response of this trisection. Three TZs can be identified in the stopband.

of the structure above a certain threshold. In addition, when this resonant structure is used in combination with capacitive direct-coupling irises (as the structure shown in Fig. 4.25a), the trisection is able to provide up to three TZs in the lower stopband.

Figure 4.25b contains the S-parameter response of this structure. The three TZs can be easily identified. The higher-frequency TZ corresponds to the triplet TZ, whereas the other two are the additional TZs associated with the direct-coupling apertures. By properly adjusting the resonance of the capacitive cross-coupling window, the phase shift between the cross-coupled path and the direct-coupled path is altered, and the third TZ can be located in the lower stopband. Therefore, the simplest way to control the location of this TZ is to shift the resonance of the iris without altering the cross-coupling level. Also, the distance between the two windows that form the cross-coupling (dimension l in Fig. 4.11) can be used to make slight adjustments to the location of this third TZ. To represent this trisection, the modified coupling scheme of Fig. 4.12 must include an additional resonator in the shortest path between resonators 1 and 3. The resulting circuit is also able to generate 3 TZs, which is consistent with the minimum path rule.

4.1.4.4 Trisection with inductive cross-coupling window providing TZs in the upper stopband

To implement trisections with TZs above the passband, any one of the coupling combinations shown in the right column of Fig. 4.4 can be employed. The first two implementations contain inductive cross-coupling irises combined with two capacitive or inductive direct-coupling windows, as shown in Fig. 4.26. As mentioned before, this type of cross-coupling window allows the implementation of small couplings with relatively big apertures, thus it is a perfect solution to place TZs far from the passband.

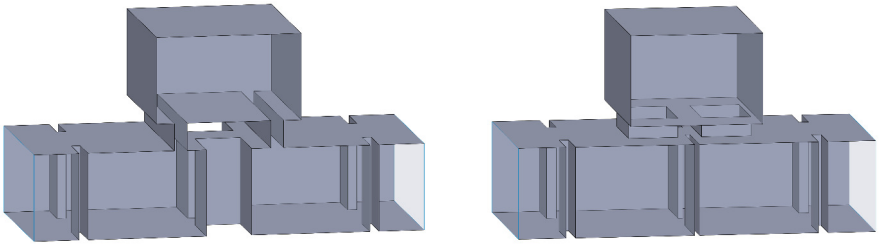

(a) **(b)**

Figure 4.26: Implementations of the trisection with inductive cross-coupling that provides TZs above the passband. **(a)** Configuration with capacitive direct-coupling. **(b)** Configuration with inductive direct coupling.

The implementation containing capacitive direct couplings (see Fig. 4.26a) has a resonance-free stopband until the first higher order mode in the central resonator (the TM_{110} mode) is excited. The two additional TZs expected from this structure are located at lower frequencies, below the resonances of the direct-coupling apertures. However, the stopband still has two TZs that can be used to increase the isolation, as shown in Fig. 4.27a. In addition to the triplet TZ, there is another TZ associated with the TM_{110} mode of the central resonator. The location of this second TZ can be controlled by adjusting the height of the central resonator. As the height increases, the resonant condition for the TM_{110} decreases, shifting the location of the second TZs towards lower frequencies. Since the triplet TZ is associated with the fundamental resonant mode TE_{101}, which has no dependence with the height of the resonator, altering this height has no effect on the location of the triplet TZ. Thus, this simple methodology can be used to prescribe the location of both TZs.

In contrast, the all-inductive implementation (see Fig. 4.26b) has a resonance-free lower stopband and an upper stopband with multiple resonances, as depicted

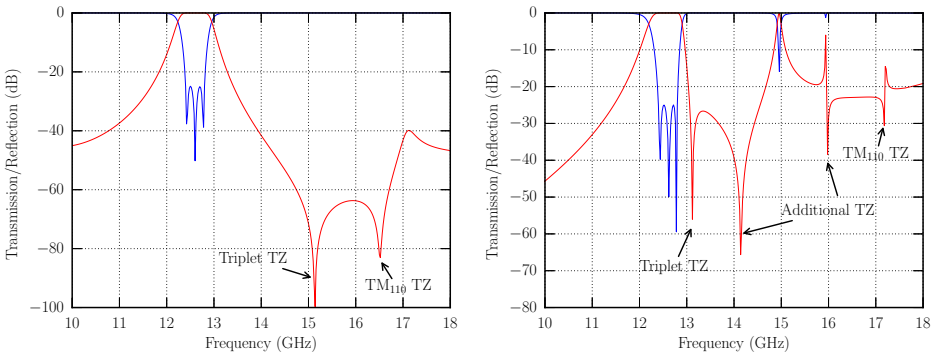

Figure 4.27: S-parameter responses of the triplet configuration with inductive cross-coupling that provides TZs in the upper stopband. **(a)** Response of the configuration with capacitive direct-couplings. **(b)** Response of the configuration with inductive direct couplings.

in Fig. 4.27b). Nevertheless, this structure is able to realize two TZs between the passband and the first resonance in the upper stopband. The additional TZ can be simply controlled by adjusting the resonance of the direct-coupling windows. However, as this resonance moves towards higher frequencies, the amount of coupling available is smaller, since the cross-section of the aperture decreases. Therefore, it is much more difficult to realize both TZs far from the passband with this implementation.

4.1.4.5 Trisection with capacitive cross-coupling window providing TZs in the upper stopband

Trisections with TZs very close to the passband ideally contain capacitive cross-coupling irises. When these TZs are above the passband, the trisection must combine a capacitive and an inductive direct-coupling aperture. The resulting structure is shown in Fig. 4.28. This configuration is able to realize one additional TZ in the stopband, associated with the inductive direct-coupling aperture. The second additional TZ is located at low frequencies, below the resonance of the capacitive direct-coupling aperture, thus it has no practical application. The triplet TZ may not be located as close to the passband as the structure of Fig. 4.20b since the capacitive direct-coupling aperture may be too small to manufacture. However, there is limited practical application to placing the TZ so close to the passband, thus this implementation is an adequate solution for filters with TZs

relatively close to the passband.

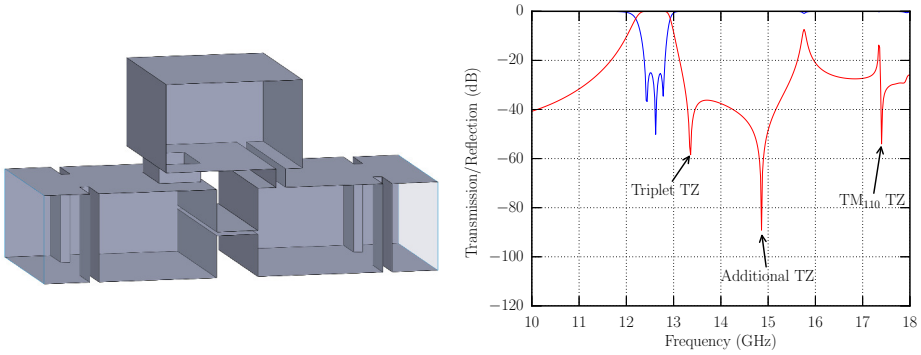

(a) **(b)**

Figure 4.28: **(a)** Trisection with capacitive cross-coupling and TZs above the passband. **(b)** S-parameter response.

4.1.5 Example: design of a five-pole four-TZ filter

In this last section, the theory of HFRW filters previously presented is applied to the design of a five-pole tuning-less filter centered at 12.6 GHz with a bandwidth of 400 MHz and return losses of 25 dB. The in-band specifications are the same as the upper-band Tx filter presented in [147]. In contrast, the filter included here must introduce 35 dB of attenuation in an adjacent channel separated 130 MHz from the lower passband edge, and at least 100 dB between 8.7 and 11 GHz. These

$M_{S1} = 1.153$	$M_{48} = -4.731$	$M_{11} = 0.806$	$M_{77} = 30.769$
$M_{16} = -5.231$	$M_{49} = 3.542$	$M_{22} = 2.072$	$M_{88} = 30.769$
$M_{26} = -5.231$	$M_{59} = 3.542$	$M_{33} = 1.141$	$M_{99} = -11.750$
$M_{27} = -4.288$	$M_{5L} = 1.153$	$M_{44} = -0.252$	
$M_{37} = -4.288$	$M_{13} = -0.495$	$M_{55} = -0.934$	
$M_{38} = -4.731$	$M_{35} = 0.064$	$M_{66} = 30.769$	

Table 4.1: Coupling matrix elements of the optimized initial coupling matrix. These values are associated with the coupling scheme of Fig. 4.29.

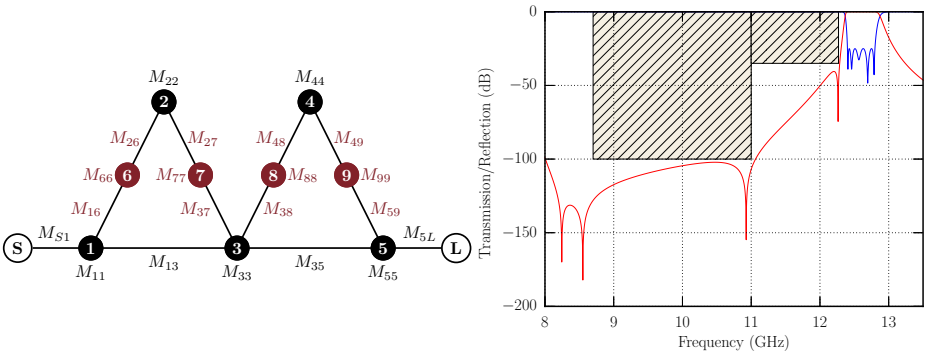

(a) **(b)**

Figure 4.29: **(a)** Coupling scheme of the initial optimized coupling matrix. The different coupling values are contained in Table 4.1. **(b)** Response of the optimized coupling matrix along with the stopband mask.

electrical specifications require the introduction of TZs both close to the passband and far from it. They can be satisfied by the cascade connection of two trisections providing 2 TZs each. To deal with the attenuation on the adjacent channel, an all-capacitive trisection is used. In addition, the extra TZ provided by this triplet can be used as an aid in providing the out-of-band rejection. A second triplet is cascaded with the all-capacitive one. It implements the coupling configuration presented in section 4.1.4.2. The objective of this triplet is to create the rejection band away from the passband. This configuration has been preferred to the one employing a resonant cross-coupling due of its simplicity and robustness.

To begin with the filter design, the cascade of two modified coupling matrices is considered. They contain resonant nodes that model the direct-coupling elements. The coupling scheme is depicted in Fig. 4.29a. This matrix is optimized until specifications are fulfilled, as shown in Fig. 4.29b. The optimized coupling elements are summarized in Table 4.1.

From this initial coupling matrix, the approximate location of the triplet TZs is extracted. They must be located around 10.93 GHz and 12.26 GHz. Given these two TZs, along with the passband and return loss requirement, a new coupling

matrix (in this case, composed of two cascaded triplets) is synthesized:

$$M = \begin{bmatrix} 0 & 1.1196 & 0 & 0 & 0 & 0 & 0 \\ 1.1196 & -0.0403 & 0.9697 & -0.0737 & 0 & 0 & 0 \\ 0 & 0.9697 & 0.0464 & 0.6795 & 0 & 0 & 0 \\ 0 & -0.0737 & 0.6795 & -0.1231 & 0.5847 & -0.4287 & 0 \\ 0 & 0 & 0 & 0.5847 & 0.5330 & 0.8729 & 0 \\ 0 & 0 & 0 & -0.4287 & 0.8729 & -0.0403 & 1.1196 \\ 0 & 0 & 0 & 0 & 0 & 1.1196 & 0 \end{bmatrix} \quad (4.13)$$

Starting from this coupling matrix, the design procedure explained in section 4.1.3.1 is applied. Then, the additional TZs are adjusted as explained in section 4.1.3.2. Optimization of the overall structure is also required. Thanks to the high degree of symmetry of this structure, it can be analyzed rigorously and efficiently with modal methods. The analysis technique for bi-dimensional cavities presented in chapter 2 is employed to model the T-junctions that form the direct-coupling windows. As was shown in section 3.1.2, convergence in the analysis of HFRW filters is achieved faster with this technique than with previously considered modal methods. Consequently, the complete design process is significantly accelerated.

A prototype of this filter has been fabricated in aluminum (alloy 6082) using a tuning-less clam-shell assembly. The physical structure of the optimized filter can be seen in Fig. 4.30 and its dimensions are summarized in Tab. 4.2. A photograph of the manufactured prototype is included in Fig. 4.31.

Resonators ($a = 19.05$, $b = 9.525$)					**Cross-couplings**			
l_1	l_2	l_3	l_4	l_5	t_7	h_7	t_8	w_8
13.555	16.081	15.324	14.976	12.553	4.631	8.934	4.141	5.105
Direct-couplings								
t_1	w_1	d_2	c_2^u	c_2^d	d_3	c_3^u	c_3^d	t_{23}
1.000	9.249	0.837	2.606	2.130	0.501	3.246	2.130	2.000
d_4	c_4^u	c_4^d	d_5	c_5^u	c_5^d	w_5	t_{45}	t_6
0.500	2.835	1.500	3.000	1.500	1.500	8.463	2.000	1.000
w_6								
8.657								

Table 4.2: Dimensions, in mm, of the HFRW filter of Fig. 4.30.

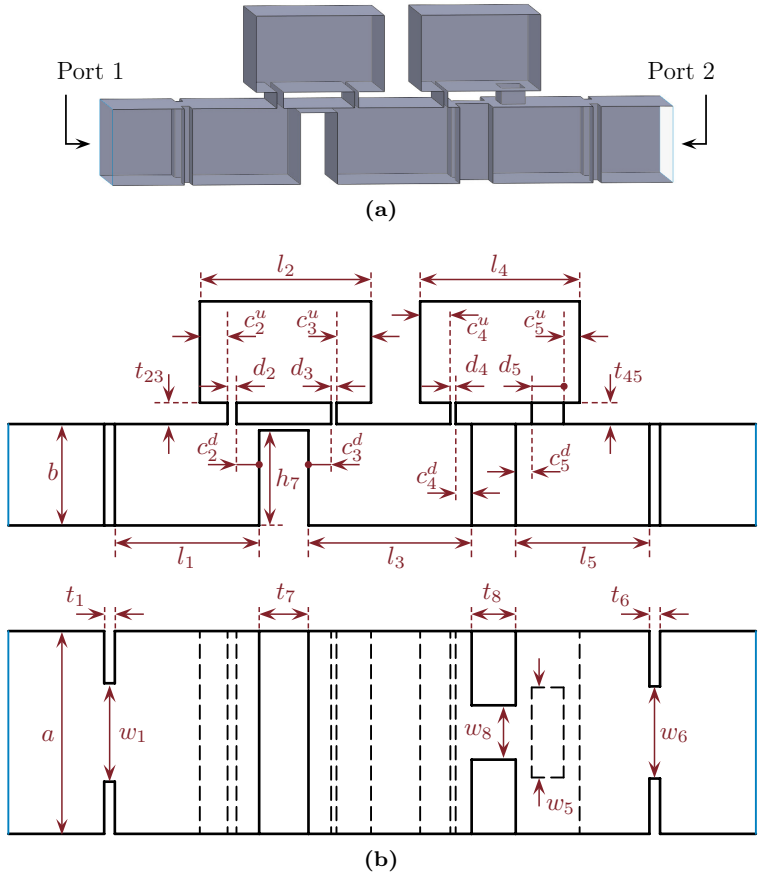

Figure 4.30: **(a)** Geometry of the designed five-pole four-TZ HFRW filter (side wall removed). Two trisections are cascaded: one includes all-capacitive couplings and the other has two inductive couplings and one capacitive. **(b)** Side and bottom view of the designed filter. Corresponding dimensions can be found in Table 4.2.

The measured response of this prototype, without any sort of tuning, is successfully compared, in Fig. 4.32, with simulations provided by FEST3D. The measured return losses are better than 20.8 dB in the passband, and the insertion losses better than 0.4 dB. A reduced frequency shift, smaller than 10 MHz, exists between the simulated and measured responses in the passband. Likewise, three of the four TZs show the same slight shift. The remaining TZ, located at 9.8 GHz in the original design, has just moved 90 MHz in the manufactured prototype. Finally,

it is also worth pointing out that the inductive iris is expected to introduce an unwanted resonance at about 15.6 GHz, beyond the recommended operation range of the filter waveguides.

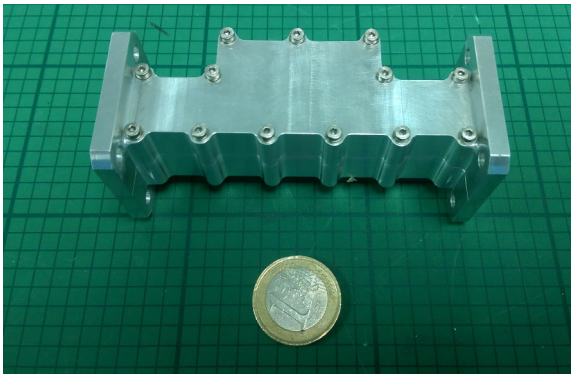

Figure 4.31: Photograph of the designed five-pole filter with four TZs.

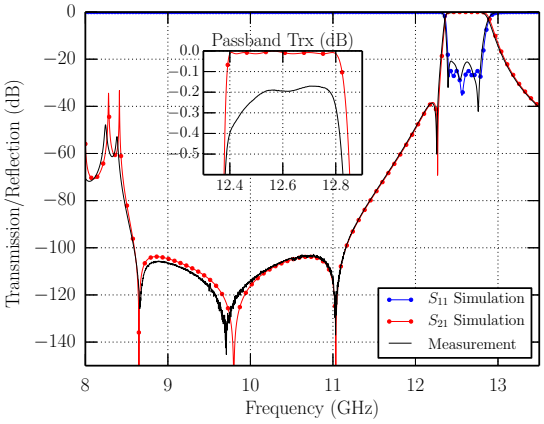

Figure 4.32: Response of the designed five-pole filter with four TZs.

4.2 Practical implementation of capacitive irises to realize additional TZs

The previous section has demonstrated that HFRW filters are an excellent solution to realize quasi-elliptic filters with multiple TZs. However, some applications require very high rejection levels in the stopband. This forces the designer to increase the number of trisections and resonators to fulfill the specifications. Consequently, the structure becomes bulkier and more sensitive to manufacturing deviations. As an alternative, certain filters (such as high-pass or low-pass filters) can be cascaded to increase the isolation. This solution allows great control over the total isolation realized, but also leads to larger component footprints. In addition, the interactions between filters must be conveniently controlled. To avoid these problems, the present section proposes the use of a new and simple 2D obstacle that can be employed to implement the input and output couplings of HFRW filters, as well as any coupling between inline adjacent resonators in rectangular waveguide structures. It is composed of a capacitive window attached to one (or more) stubs (see Fig. 4.33). This combination is able to provide a prescribed coupling level, while at the same time realizing one TZ per stub. Multiple stubs can be combined. Typically, each coupling structure will have two stubs, one attached on each side of a capacitive window. Therefore, the number of TZs can be largely increased while keeping the overall structure very compact.

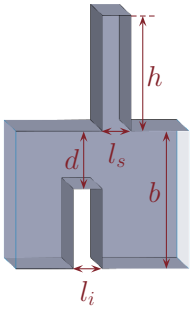

Figure 4.33: Proposed iris structure that combines a capacitive window with stubs to implement additional TZs. In the depicted structure, only one stub is considered.

Stubs have been previously proposed in the literature to implement quasi-elliptic bandpass filters without cross-couplings [123, 155, 156]. In these filters, the stubs only implement strong couplings, since no element is added to increase the degrees of freedom to control the coupling level. For that reason, these filters only have stubs in the input and output stages. In contrast, the structure proposed in this section can be used to implement both strong and weak couplings, hence they

can implement both the input/output couplings as well as intermediate couplings between adjacent resonators. In addition, the proposed coupling element is able to combine multiple stubs, thus generating more than one TZ per coupling element.

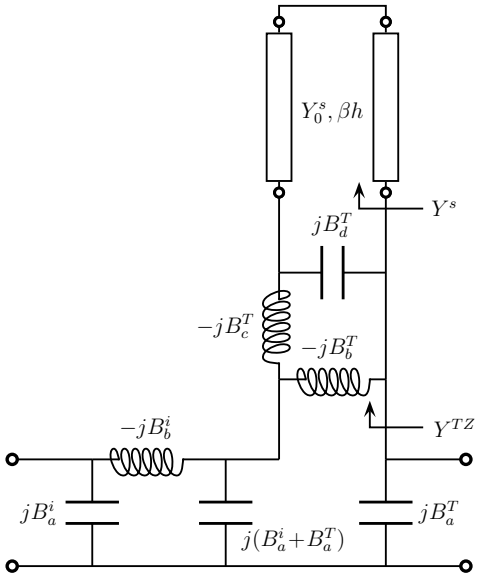

Figure 4.34: Equivalent circuit model of the stub-iris combination.

An equivalent network for the basic coupling structure depicted in Fig. 4.33 can be obtained from classical circuit models. It combines the capacitive window model from [3] (susceptances B_a^i, B_b^i) with the model of a T-junction (susceptances B_a^T, B_b^T, B_c^T, B_d^T) from the same reference and a short-circuited transmission line that represents the stub. The resulting equivalent circuit is show in Fig. 4.34. As a result, the normalized characteristic admittance of the stub transmission line is $Y_0^s = b/l_s$ and its electrical length is βh. The stub admittance has the following expression:

$$Y^s = -jY_0^s \cot(\beta h) \tag{4.14}$$

Any change in the electrical length of the stub changes the admittance seen from the branch arm of the T-junction. Combining the lumped elements of this branch with the stub, the resulting admittance becomes:

$$Y^{TZ} = -j\left(B_b^T + B_c^T \frac{B_d^T - Y_0^s \cot(\beta h)}{B_d^T - B_c^T - Y_0^s \cot(\beta h)}\right) \tag{4.15}$$

When Y^{TZ} is zero, an open circuit exists between the input and the output terminals of the circuit, thus eliminating the signal transmission between them. A TZ

has been effectively realized. For Y^{TZ} to become zero, the following relationship must hold:

$$\beta h = n\pi + \tan^{-1}\left[\frac{b}{l_s}\left(\frac{B_b^T + B_c^T}{B_c^T B_d^T + B_b^T B_d^T - B_c^T B_b^T}\right)\right] \qquad n = 0, 1, \ldots \tag{4.16}$$

Note that multiple solutions can be chosen for length h, each with a different value of the free parameter n. They are separated by half the stub wavelength (i.e. $\lambda_g/2$) and realize a TZ at the same frequency.

In addition to providing a TZ, the proposed structure must also behave like a certain impedance inverter at the filter center frequency. To compute the normalized impedance inverter parameter that this circuit represents, we start by computing its input admittance. It can be written as:

$$Y_{\text{in}} = j\left\{B_a^i - \frac{B_b^i\, C_{\text{aux}}}{C_{\text{aux}} - B_b^i\left[1 + j\left(B_a^T + B^{TZ}\right)\right]}\right\} \tag{4.17}$$

where B^{TZ} is the imaginary part of Y^{TZ} and C_{aux} is a complex term given by:

$$C_{\text{aux}} = \left(1 + jB_a^T\right)\left(B_a^i + B_a^T + B^{TZ}\right) + jB^{TZ}\left(B_a^i + B_a^T\right). \tag{4.18}$$

From Y_{in}, the S_{11} parameter can be computed as:

$$S_{11} = \frac{1 - Y_{\text{in}}}{1 + Y_{\text{in}}} \tag{4.19}$$

and applying (4.1), the normalized impedance inverter parameter of this circuit is obtained.

The circuit model suggest that the location of the TZ is only influenced by the stub and T-junction parameters, and is independent of the capacitive window. Thus, the length of the stub must be the first parameter selected to yield the proper location of the TZ. Then, the height d of the capacitive window may be adjusted to realize the desired normalized inverter value. This is confirmed, to a certain extent, by EM-simulations of the basic iris-stub structure of Fig. 4.33 performed with FEST3D. Figure 4.35a depicts the location of the TZ as a function of the stub length for different capacitive window sizes. As can be seen, the influence of the capacitive window size is limited. In contrast, Fig. 4.35b represents the variation of the normalized impedance inverter parameter with the height of the capacitive window. For each curve, the stub is slightly adjusted to keep the TZ at the same frequency. As expected, the normalized inverter value $\overline{K}$ can be controlled by adjusting the height of the capacitive window. However, for different locations of the TZ, the required window height differs.

As the TZ approaches the filter center frequency, the maximum normalized inverter value that can be achieved decreases. In Fig. 4.35b, the normalized

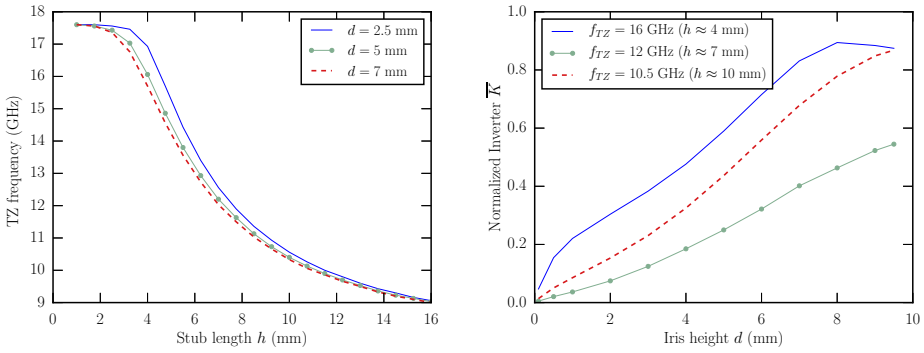

(a) **(b)**

Figure 4.35: Performance analysis of the stub-iris combination. **(a)** TZ frequency as a function of the stub length h for different values of d. In these simulations the stub and iris lengths (l_i and l_s are set to 2 mm). **(b)** Normalized impedance inverter parameter as a function the iris height. Simulations are performed at $f = 12.6$ GHz. For each curve, the length of the stub h is slightly adjusted to keep the TZ at the same frequency.

inverter is computed at 12.6 GHz. As can be seen, the curve associated with a TZ at 12 GHz has much smaller values than the other two curves, associated with TZs that are farther from the frequency of simulation. Certain scenarios may call for TZs close to the passband while simultaneously requiring large coupling levels for the aperture that is implemented by the proposed structure. For instance, a filter with relative moderate bandwidth and TZs close to the passband where the input coupling is implemented by the proposed iris-stub combination. In that scenario we can take advantage of the fact that there are multiple solutions for the stub length that yield the same TZ. Take, for instance, the S_{21} parameter response of Fig. 4.36. One curve corresponds to the simulation of a stub-iris structure with $h = 7.14$ mm, $d = 6$ mm, $l_s = l_i = 2$ mm. The other curve corresponds to the same structure except for the stub, which has increased its length by $\lambda_g/2$. The TZ associated with this longer stub has a much narrower bandwidth. This means that it can provide larger values of the S_{21} parameter for frequencies close to the TZ. Consequently, the S_{11} parameter is smaller near the TZ, and thus the normalized inverter $\overline{K}$ is larger. Effectively, by increasing the length of the stub by $\lambda_g/2$ we can implement larger coupling elements while still realizing TZs that are close to the passband. However, these long solutions may generate unwanted resonances in the stopband. For that reason, they are only employed if shorter solutions are not able to satisfy the inverter requirement.

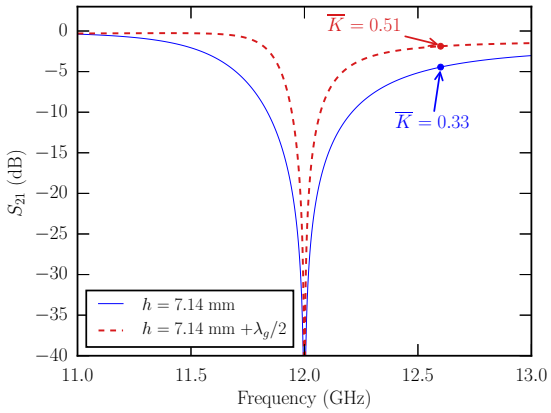

Figure 4.36: Two stub solutions, separated by $\lambda_g/2$, are able to realize the same TZ but allow the implementation of different inverter values.

Another interesting application of these obstacles is found in filters that contain very thin coupling windows, which may be difficult to manufacture. The introduction of a stub next to a capacitive window reduces the overall coupling provided by the obstacle. To compensate for the loss of coupling, the size of the capacitive window has to be increased. This is actually a positive consequence, since the window is now easier to manufacture and definitely more robust to potential manufacturing deviations.

The study of the structure carried out in this section involves only one stub. However, the conclusions drawn here can be extended to the case where the coupling structure has stubs on both sides of the capacitive window (doubling the number of TZs that the structure realizes). Once again, the height of both stubs are employed to prescribe the location of the TZs, while the height of the capacitive window controls the normalized inverter parameter at the filter center frequency. From a practical point of view, a coupling element composed of an alternate sequence of stubs and capacitive irises can be used, provided that enough coupling is finally obtained. As a result, many TZs can be realized by the same coupling structure.

4.2.1 Practical design examples

The applicability of the proposed stub-iris combination is put to the test by designing two filter structures containing these elements. The first example is a classical in-line direct-coupled resonator filter that, despite being completely con-

stant in width, is able to realize TZs. In the second example, we combine this proposed iris with an HFRW structure to realize a filter that generates TZs in both stopbands.

4.2.1.1 All-capacitive quasi-elliptic filter

The first example is a five-pole all-capacitive inline filter centered at 12.6 GHz with a bandwidth of 400 MHz and return losses better than 25 dB in the passband. It is implemented in a WR-75 waveguide with all coupling apertures realized as capacitive elements. Two of the six coupling windows have stubs attached to them, realizing a total of four TZs. These TZs are employed to increase the isolation in the lower stopband (between 11 and 12 GHz) above 75 dB. The resulting structure is depicted in Fig. 4.37.

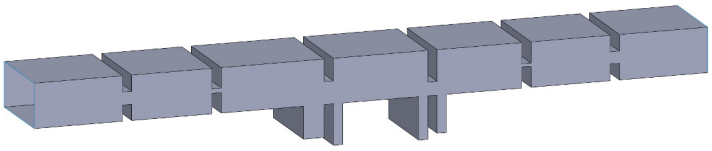

Figure 4.37: All-capacitive quasi-elliptic filter. The two central couplings are implemented by stub-iris combinations.

Initially, the filter is designed without stubs, thus it becomes a simple all-pole filter. Only the passband specifications are considered in this initial design. From the coupling matrix, the equivalent circuit formed by inverters and transmission lines is obtained by application of the formulas (4.5)-(4.9). Then, it is transformed into a physical structure where inverters are substituted by capacitive windows (with a fixed length of 2 mm) and transmission lines by WR-75 rectangular waveguides. Once this structure fulfills the passband specifications, the stubs are added. Any coupling window in the structure is able to include stubs. In this example, the two central windows are selected to contain them. This choice is not arbitrary. In a symmetrical all-pole Chebyshev filter, the weakest couplings are located in the center of the structure. Since they are implemented by capacitive windows, which tend to provide rather strong couplings, the resulting windows have a very small height. As previously shown, the introduction of stubs forces the capacitive window to increase its height to compensate the stub effect. Therefore, we can take advantage of this fact to increase the robustness of the filter to manufacturing deviations, by placing the stubs in the capacitive windows that implement the smallest couplings.

EM simulations are employed to obtain initial values for the stub lengths. The thickness l_s of all the stubs is set to 2 mm. Given this thickness and the dimensions of the resonator waveguide, a T-junction is constructed and analyzed. From the fundamental-mode admittance matrix values Y_{ij}, the susceptances of the equivalent circuit model of the T-junction can be computed as:

$$jB_c^T = Y_{31} \tag{4.20a}$$
$$jB_b^T = Y_{21} - jB_c^T \tag{4.20b}$$
$$jB_a^T = Y_{11} + jB_b^T + jB_c^T \tag{4.20c}$$
$$jB_a^T = Y_{33} + jB_c^T. \tag{4.20d}$$

From these parameters, a good starting point for the stub lengths is obtained by solving (4.16). Slight adjustments are made using EM simulations, so the four TZs are located between 11 GHz and 12 GHz. Stubs of 7, 8, 8.3 and 9 mm are employed. With these values, the physical structure of the two stub-iris combinations can be constructed. Each capacitive window height d is then adjusted until it has the same behavior (at the center frequency) as the corresponding iris in the all-pole filter. Having determined the geometrical dimensions of all the irises, resonators are finally tuned to recover the original resonances of the all-pole filter.

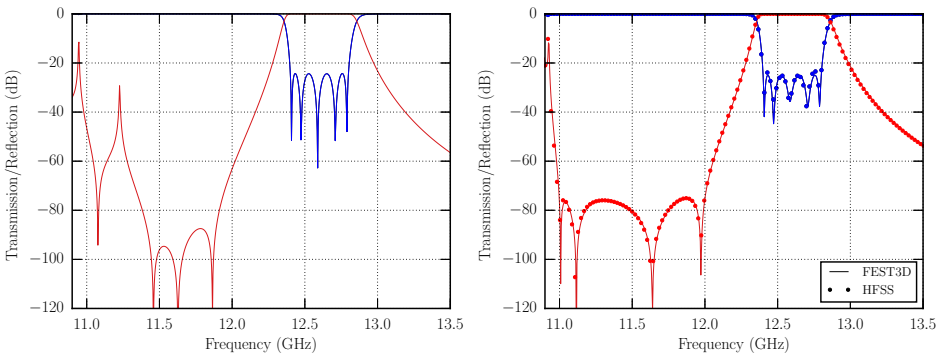

(a) **(b)**

Figure 4.38: **(a)** Optimized filter with the original stub lengths of $h = 7$, 8, 8.3, and 9 mm. An undesired resonance can be identified within the stopband, at 11.2 GHz. **(b)** Final response after optimization is successfully compared with HFSS.

The resulting structure only requires minor adjustments to provide the response depicted in Fig. 4.38a. The four TZs are located in the prescribed stopband,

but the specific lengths still require certain fine-tuning to create an equiripple response in the stopband. Furthermore, an undesired resonance appears within this stopband at 11.2 GHz. This resonance is due to high-order modes that are excited in the stub with the shortest length. To move this resonance outside the stopband, the thickness l_s of the corresponding stub is modified to shift this undesired resonances to lower frequencies. An additional round of optimization is run. This time, the length of the stubs are also adjusted to provide an equiripple stopband. Without much computational effort, the final response depicted in Fig. 4.38b is obtained. To validate the design, this response is successfully compared with the one provided by HFSS for the same structure. The dimensions of the filter are summarized in Table 4.3 and Fig. 4.39.

Resonators					
l_1	l_2	l_3	l_4	l_5	b
17.318	22.226	20.365	18.277	17.088	9.525
Capacitive Windows					
d_1	d_2	d_3	d_4	d_5	d_6
2.747	0.968	4.811	2.891	0.668	2.541
Stubs					
h_1	h_2	h_3	h_4	l_{s1}	l_s
6.895	8.701	9.093	7.992	4.5	2

Table 4.3: Dimensions of the all-capacitive quasi-elliptic filter in mm. The width of the complete structure is 19.05 mm.

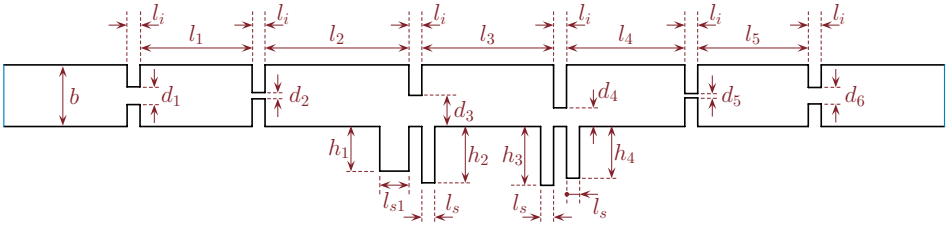

Figure 4.39: Lateral view of the all-capacitive quasi-elliptic filter and physical meaning of dimensions contained in Table 4.3.

4.2.1.2 HFRW filter with TZs in both stopbands

The proposed stub-iris connection can also be employed in combination with HFRW triplets to realize filters that have TZs both in the upper and lower stopbands. This second example involves a filter employed in passive intermodulation measurements at Ku-band. The channel filter (with a passband that spans 400 MHz between 12.5 GHz and 12.9 GHz) must realize one TZ below the passband to prevent signal leakages from an adjacent channel, between 11.4 GHz and 12.2 GHz. Simultaneously, four TZs have to be located above the passband to isolate the frequency band where a low-level PIM signal is generated (between 13.8 GHz and 14.6 GHz). The structure selected is a four-pole HFRW filter with two stub-iris sections. Its physical structure is depicted in Fig. 4.40a.

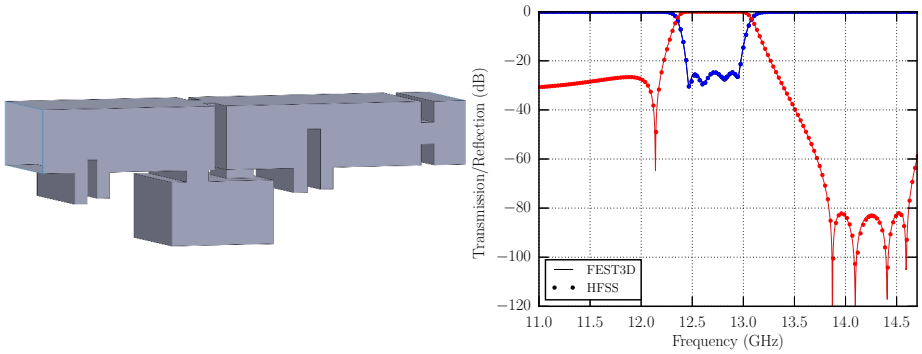

(a) **(b)**

Figure 4.40: Four-pole HFRW filter with five TZs. Four of them are realized by stubs connected to capacitive windows. The TZ below the passband is realized by the HFRW trisection.

The design procedure is equivalent to the one explained in the previous example. First, the structure is designed without any stubs, and they are only introduced once the passband and lower-stopband TZ fulfill the requirements. The novel capacitive coupling windows are then readjusted to recover the passband response. A final optimization cycle is also applied to obtain the response shown in Fig. 4.40b. The successful comparison of this response with results provided by HFSS validate the design process. The dimensions of the final structure are summarized in Table 4.4 and Fig. 4.41.

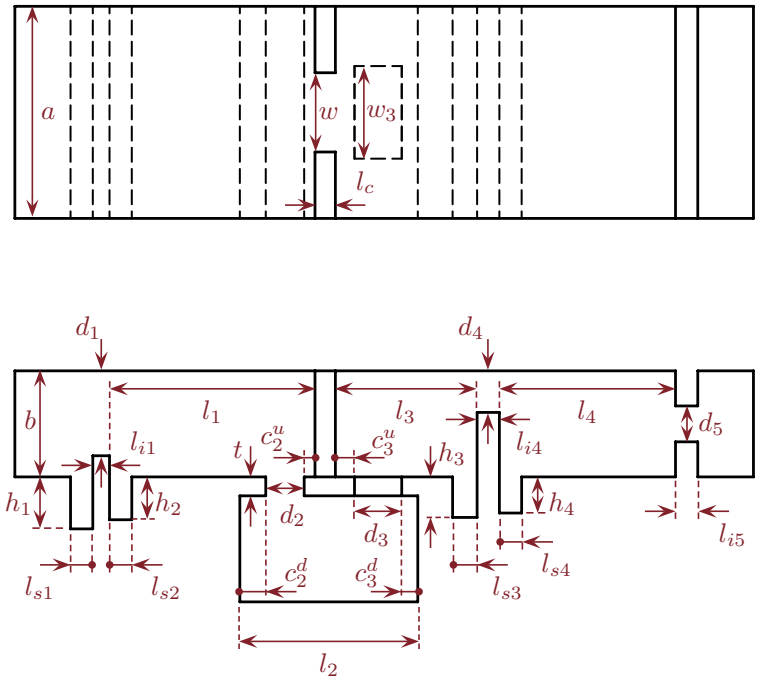

Figure 4.41: Lateral view of the HFRW filter with TZs above and below the passband.

Resonators and cross-coupling							
l_1	l_2	l_3	l_4	a	b	l_c	w
18.451	15.980	12.725	15.815	19.050	9.525	1.831	7.118
HFRW direct-couplings							
d_2	c_2^u	c_2^d	d_3	c_3^u	c_3^d	w_3	t
3.449	0.972	2.328	4.241	1.717	1.442	8.317	1.700
Capacitive direct-coupling windows							
	d_1	l_{i1}	d_4	l_{i4}	d_5	l_{i5}	
	7.626	1.500	3.733	2.000	3.223	2.000	
Stubs							
h_1	l_{s1}	h_2	l_{s2}	h_3	l_{s3}	h_4	l_{s4}
4.668	2.000	3.848	2.000	3.641	2.2	3.245	2.000

Table 4.4: Dimensions, in mm, of the HFRW filter with TZs above and below the passband.

Chapter 5

Design of wideband manifold-coupled multiplexers

Multiplexers are multiport components widely used in communication systems at microwave and millimeter-wave frequencies. Multiplexers can be employed either to combine multiple frequency bands into a single one, or, alternatively, to divide a common frequency band into multiple sub-bands (or channels). The most commonly used implementations for these components are [96]:

- Hybrid-coupled filter combiner module (HCFM) multiplexers.
- Circulator-coupled multiplexers.
- Manifold-coupled multiplexers.

On the one hand, HCFM and circulator-coupled multiplexers are modular implementations that can accommodate changes in the frequency plan, but tend to be bulky. On the other hand, manifold-coupled multiplexers are the optimal choice in terms of insertion losses, volume and mass. However, their design is much more complex and does not allow modifications in the number of channels [102]. Depending on the application, one implementation may be favored over the others. For example, because of their modularity, high-power channel multiplexers in large earth stations are usually realized by means of HCFM structures. Input multiplexers (IMUX) for satellite payloads, in contrast, are typically implemented as circulator-coupled multiplexers due to their relatively simple design. In the same context, satellite output multiplexers (OMUX) are implemented with the

manifold-coupled configuration because of the low-loss requirement of these subsystems, combined with their capability to sustain high power levels.

Due to the complexity of their design, manifold-coupled multiplexers have been the subject of extensive research over the last four decades [115, 157–163]. These multiplexers employ a common transmission line, usually a rectangular waveguide, that acts as the manifold. This transmission line is either short-circuited or has one end connected to one of the channel filters. The remaining channel filters are then connected along the manifold at (quasi) regular intervals.

The design of these components starts with the stand-alone channel filters. They are designed either as singly- or doubly-terminated, independently of each other. However, once they are connected to the manifold, the multiplexer has to be designed as a whole, not as individual channels, in order to account for the mutual interactions between the filters and the manifold [152]. To obtain the final geometry, modern design procedures apply extensive optimization to the structure. Therefore, design methodologies that provide a good starting point for this optimization are highly valuable.

Wideband multiplexers have certain requirements that are at odds with classical narrowband design techniques. Likewise, some of these requirements have not been properly addressed in the literature, mainly focused on conventional narrowband designs. Consequently, this chapter presents a systematic methodology for the most delicate part of a wideband multiplexer design: the connection of filters to the manifold. Simple steps are described to connect the filters, and adjust a limited number of dimensions to achieve a good starting point for the final optimization. The proposed methodology will be compared with existing design techniques to demonstrate its superiority. Finally, it will be applied to the design of a wideband multiplexer to be used within a passive intermodulation (PIM) measurement set-up. Measurements from a manufactured prototype will be provided to validate the design procedure.

5.1 Comparison between wideband and narrowband multiplexer design

Table 5.1 summarizes the main characteristics that make narrowband (fractional bandwidth $< 10\%$) multiplexer design significantly different from wideband multiplexer (fractional bandwidth $> 20\%$) design.

Narrowband multiplexers typically combine a large number of narrowband channel filters. Given the sensitivity of narrowband filters to manufacturing deviations, tuning elements are usually added and manually adjusted after fabrication to fulfill specifications. Hence, these types of multiplexers do not require an extremely accurate modeling of the different parts, since most deviations from ideal behavior can be accounted for by the final tuning process. Channel filters can

Narrowband Multiplexers	Wideband Multiplexers
Large number of channels	Reduced number of channels
Tuning required	Tuning-less structures
Low-accuracy modeling	High-accuracy modeling
Small impedance variation in adjacent passbands	Large impedance variation in adjacent passbands
Reduced number of spurious in-band resonances	Large number of spurious in-band resonances
Low input coupling levels	High input coupling levels

Table 5.1: Main differences associated with the design of narrowband and wideband multiplexers.

be simply substituted by their equivalent models based on coupling matrices or lumped elements. Furthermore, a fundamental-mode characterization of the manifold and its junctions is accurate enough, in most cases, to achieve successful results [163].

Due to the narrow bandwidth of the filters involved, there are two effects that aid in the matching of all the filters in narrowband multiplexers. On the one hand, the loading effect of one filter in the narrow passband of any other filter does not exhibit an important dependence with frequency. Therefore the manifold is able to provide a good matching for all channels. On the other hand, it is easy to implement the first inverter of each narrowband filter attached to the manifold, due to the low coupling level required. From the previous discussion it can be concluded that the interconnection of narrowband filters to a manifold-coupled multiplexer is not a severe issue. This does not mean that designing narrowband multiplexer is a simple task, but rather that a good starting point for the optimization can be easily found. In fact, classical design techniques [96, 102] prescribe analytical values for the initial dimensions of the interconnection:

- Filters are connected to the manifold through half-wavelength stubs at the channels center frequency (or an integer multiple of this value).
- The distance between the short circuit and the first stub depends on the type of manifold. For E-plane multiplexers, the stubs must be connected where there is a maximum of the magnetic field along the manifold. Consequently, the initial separation from the short circuit is set at $\lambda_g/2$, where λ_g is the

manifold wavelength. In contrast, H-plane multiplexers require the filters to be connected where the electric field is maximum, therefore the initial separation from the short-circuit is $\lambda_g/4$.

- The rest of the filters are connected to the manifold separated by $\lambda_g/2$ (or an integer multiple of this value).

As it can be seen, the part of the multiplexer performing the interconnection has many degrees of freedom. Therefore, this excess of parameters can be exploited to obtain a good matching of the different channels with only minor adjustments in the very first stages of each filter. To obtain such flexibility, the resulting interconnecting network (manifold and stubs) is normally long and bulky. As an example, Fig. 5.1 depicts an 8-channel narrowband multiplexer [164]. The initial distribution of filters along the manifold is indicated.

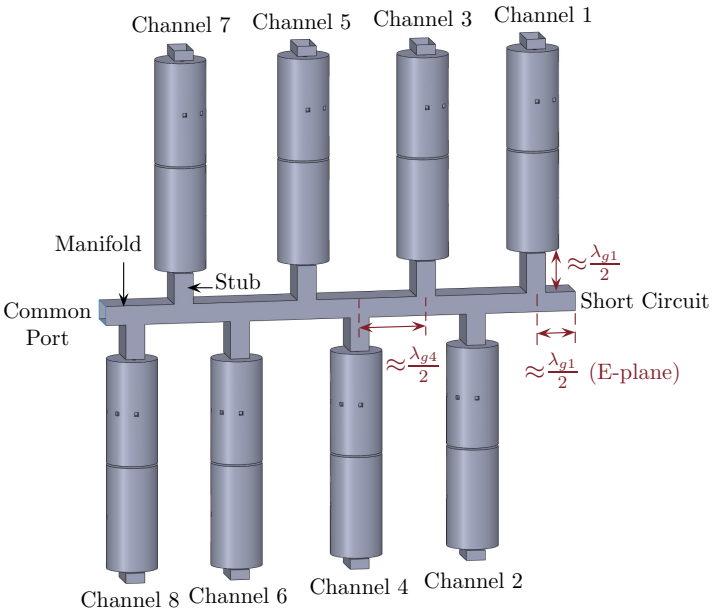

Figure 5.1: Classical narrowband multiplexer.

Since most applications in the space sector do not handle very wide frequency bands, design techniques for wideband multiplexers have been scarcely developed. However, certain applications require multiplexers with a wide frequency band of operation, such as measurement set-ups and electronic warfare equipment. A series of issues arise during the design of these wideband components. The main one is due to the interaction between the different filters and the manifold, which is much

stronger than in the narrowband case. Undesired resonances are more troubling and must be avoided in a wider frequency range. For instance, Fig. 5.2 shows the out-of-band response of the narrowband multiplexer of Fig. 5.1. As it can be seen, the spurious resonances due to the stubs and manifold appear around 11.7 GHz, not very far from the passband. However, since the passband of the multiplexer is small (3%), these resonances do not interfere with the normal operation of the multiplexer.

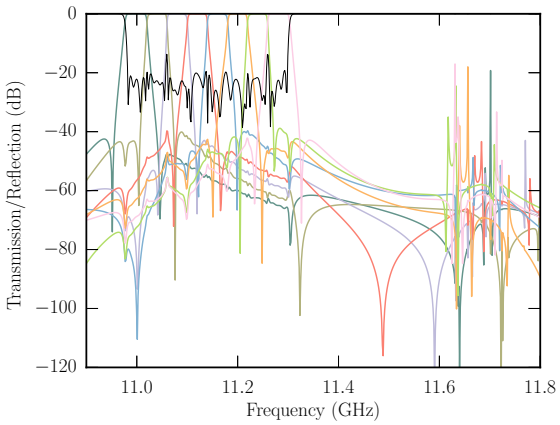

Figure 5.2: Out-of-band response of the narrowband multiplexer shown in Fig. 5.1. Undesired spikes, due to the interaction between the stubs and the manifold can be identified around 11.7 GHz.

Another issue involves the physical implementation of the input coupling for each filter. Wideband filters tend to have much larger input coupling levels than their narrowband counterpart. The physical structure that implements this input coupling must provide a high coupling level and, at the same time, compensate for the frequency-dependent loading effect of adjacent filters. These two issues become more troublesome as the number of channels increases. For that reason, most publications related to the design of wideband multiplexers have been focused on diplexers [124–126]. As far as multiplexers are concerned, a manifold based on a cascade connection of Y-junctions for wideband applications has been proposed in [98] together with a tailored design technique. The solution requires interconnecting stubs and a bulky and intricate manifold (that can reduce the available coupling from the common port to the last channel filters). However, the component designed in [98] included only moderate bandwidth filters, whereas the frequency range covered by the entire multiplexer was not very wide. As it has been demonstrated, there is still room for improvement in the area of wideband

multiplexer design. The following section presents a new design procedure that addresses most of the issues that arise when designing this family of multiplexers.

5.2 Design methodology for wideband multiplexers

The design methodology presented in this thesis is tailored to manifold-coupled multiplexers. As it is usually the case in these structures, one end of the manifold contains either a filter or a short circuit, while the other end constitutes the common port (CP). The main benefit of connecting a filter inline with the manifold is that the input coupling level that can be achieved is higher than in a lateral connection. The rest of the filters are spaced along the manifold and directly connected to it via H- or E-plane T-junctions. No stubs are located between the first coupling window of each filter and the manifold. As previously mentioned, the use of these additional stubs is widely adopted by multiplexer designers, mainly because it offers a simple way of increasing the degrees of freedom in the structure. Therefore, it is easier to achieve an adequate matching between filters and manifold without readjusting most of the filters dimensions (typically, only the first two resonators and couplings of each filter are modified). Compared with the classical configuration, the proposed connection of filters considered in this work leads to more compact designs. In addition, undesired resonances (which may interfere with other filters in the multiplexer) can be largely mitigated by removing such stubs, since they enhance the frequency variation of the filter input impedance over adjacent channels.

Solutions to cope with unwanted spikes generated by the manifold have been presented in the past, for instance [165]. They included reducing the height of the manifold waveguide and reducing the size of the coupling slots. The configuration proposed in this section is compatible with making use of a reduced-height manifold, although additional effort must be done to design the transition from the common port to a standard waveguide. Furthermore, as the height of the manifold is reduced, so does the power handling capability of the multiplexer. Regarding the reduction of size in the coupling slots, this solution is only suitable for narrowband multiplexers. Otherwise, reducing the size of the input coupling slot is detrimental to the implementation of the high coupling values that wideband filters require for these particular slots. As an alternative, the authors in [166] cleverly proposed to take advantage of the unwanted resonances and used them as additional poles of the channel filter function. However, the extension of this technique to wideband multiplexers is not direct. The implementation in a wide frequency band of the input coupling and first resonator, by simply adjusting sections of transmission line while simultaneously avoiding undesired extra resonances, is a difficult task.

In this thesis, a different approach is developed. The idea is to connect filters

directly to the manifold, one by one, as depicted in Fig. 5.3. At each iteration, the spacing between the filter to be attached and the previous junction is adjusted, in order to achieve a strong coupling to the branching arm where the filter is connected. This also contributes to a reduction in size of the input irises, limiting unwanted interactions in the multiplexer. Once this length is set, the first coupling iris and resonator of the connected filter are adjusted, so the overall structure behaves (in magnitude and phase) like the first impedance inverter $\overline{K}_{01}$ of the stand-alone filter. To summarize, three dimensions are adjusted in each iteration, as illustrated in Fig. 5.3: the distance to the previous junction, the size of the first coupling iris, and the length of the first resonator.

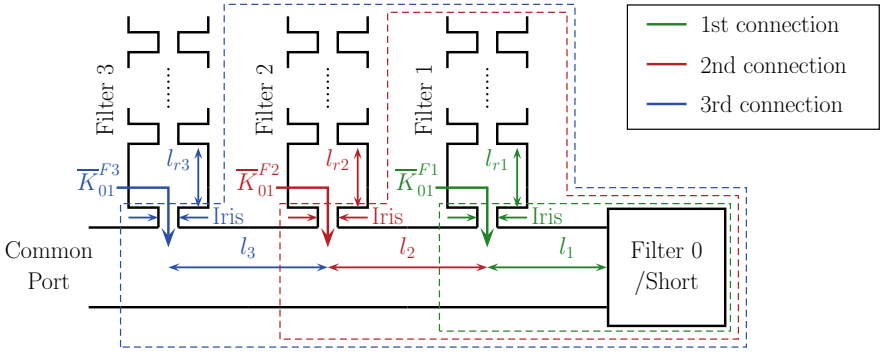

Figure 5.3: Schematic view of the sequential filter connection to the manifold.

The idea of designing a junction to behave like the first inverter of a filter was already applied in [167] to the design of compact diplexers. In that work both filters were directly connected to a star-junction. The design of the junction was driven by formulas based on the value of the first impedance inverter extracted from each filter. A basic condition for the application of these formulas was that the interaction between both filters of the diplexer must be close to zero, measured from the first resonator. This condition was verified using narrowband filters with passbands located far apart, but its suitability for other applications is questionable, especially in the case of wideband filters. In addition, the technique in [167] limits its scope to star-junction multiplexers, since it does not define a way to separate the filters if a manifold waveguide were to be employed. In contrast, the methodology proposed in this thesis determines the physical distance between filters in the manifold, and does not require filters to have great mutual isolation. Therefore, it can be applied to both contiguous and non-contiguous multiplexers.

The proposed methodology does not avoid the need for optimization of the multiplexer. Instead, it is able to provide a good initial point for the trickiest part of the design: the adjustment of the manifold and the first variables of each filter

dominating the multiplexer interactions. As it will be demonstrated, for wideband multiplexers this starting point is better than the starting point of classical narrowband techniques.

To sum up, the proposed design procedure for wideband manifold-coupled multiplexers can be described as:

1. Sequential connection of the filters to the manifold. For each filter, three adjustments (separation along the manifold, first iris and first resonant cavity) are made. This is the *First Cycle* of the design, explained in section 5.2.1.

2. Once all filters are connected to the manifold, successive rounds of adjustments are made. These are the *Additional Cycles* explained in section 5.2.2. In those additional rounds, the separation between filters along the manifold is not adjusted.

3. Then, a filter-by-filter optimization of the multiplexer is performed until specifications are fulfilled. This is the classical last step in narrowband multiplexer design [96], as well.

5.2.1 First cycle

This first cycle provides the initial connection of all the filters to the manifold. A flowchart summarizing this first cycle is depicted in Fig. 5.4. It involves the sequential connection of the filters, starting from one end of the manifold and then moving towards the common port. The connection of each new filter is divided in three steps that are explained next. The objective of these three steps is to replace the behavior of the filter first iris by the part of the multiplexer that has already been connected. In preparation for this first cycle, the T-junctions for the connection of the filters to the manifold are simulated at the center frequency of each channel, and results are stored. Likewise, the reflection coefficient of the element that terminates the manifold (either a short-circuit or Filter 0) is simulated at the center frequency of the first filter to be connected.

Step 1: Adjustment of separation between filters

To initiate the connection of a new filter (for instance Filter n) to the manifold, the physical length of transmission line l_n that separates the T-junction of this filter from the already-connected network N_{n-1} has to be determined. N_{n-1} contains the section of the multiplexer that has already been adjusted in previous iterations of the first cycle, namely, all filters from $n-1$ to 0 and the corresponding part of the manifold attached to them. As mentioned before, N_0 may either be a filter (connected in-line with the manifold) or a short-circuit. The physical structure used in this first step to determine l_n is depicted in Fig. 5.5. Port 2 is the arm where filter n will be directly connected, whereas Port 1 is the common port.

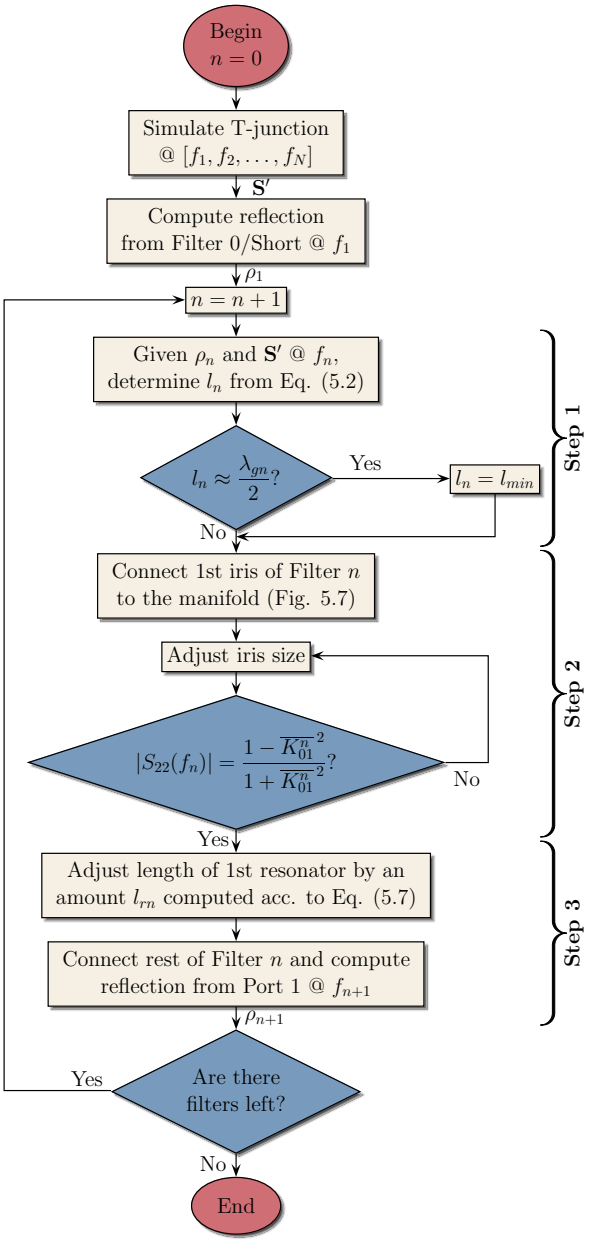

Figure 5.4: Detailed flowchart summarizing the first cycle of the design procedure. This cycle starts with all the filters independently designed and sequentially connects them to the manifold.

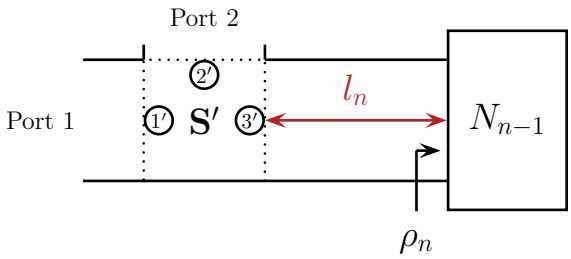

Figure 5.5: Schematic view of the structure used to adjust the spacing between junctions for filter n. Circled numbers indicate $\mathbf{S}'$ reference port numbers.

Classical multiplexer design calls for an initial separation between filters that is a multiple of half the manifold wavelength, as explained in section 5.1. These classical techniques assume that the locations of maximum electric/magnetic field within the manifold are barely affected by the connection of the filters. In narrow-band cases, where the input coupling is small, this may be an adequate assumption. However, as the input coupling increases, the coupling windows have a stronger effect in the field distribution along the manifold. For that reason, it is important to use EM models in determining the optimal value of l_n. Otherwise, the manifold may not be able to couple enough energy to the corresponding filter, particularly for a wide passband channel. The optimal value of length l_n is the one that minimizes the return loss at Port 2 of Fig. 5.5 at the filter center frequency f_n. If the dimensions of Port 2 are the same as those of the input/output port of the channel filter, the minimum value of $|S_{22}|$ gives an indication of the maximum normalized impedance inverter parameter $\overline{K}$ that can be achieved by adjusting the coupling iris.

Given the fundamental-mode scattering parameters $\mathbf{S}'$ of the T-junction, as well as the reflection coefficient ρ_n from the previously connected network, the return loss at Port 2 of Fig. 5.5 can be expressed as:

$$S_{22} = S'_{22} + \frac{S'^2_{23}\,\rho_n\,e^{-2j\beta_n l_n}}{1 - S'_{33}\,\rho_n\,e^{-j2\beta_n l_n}} \tag{5.1}$$

where β_n is the manifold phase constant at f_n. To simplify the computation it has been assumed that the network is loss-less.

The goal is to find a solution for l_n that minimizes (5.1). An analytical solution for this length was proposed in [168], however, it assumed that $|\rho_n| = 1$. As mentioned earlier, in wideband and contiguous multiplexers there can be a stronger interaction between filters. For that reason, a more general case (where ρ_n can

take any value) is considered here. The optimal length l_n in this case is:

$$l_n = \frac{\varphi_n - \psi + 2m\pi}{2\beta_n} \tag{5.2}$$

where φ_n is the phase of ρ_n, m is an integer value and phase ψ is computed as:

$$\psi = 2\tan^{-1}\left(\frac{B + \sqrt{A^2 + B^2 - C^2}}{A + C}\right). \tag{5.3}$$

Parameters A, B and C are extracted from $\mathbf{S}'$ and ρ_n:

$$\begin{aligned} A &= a_{33}\left(a_{22}^2 + a_{11}^2\,|\rho_n|^2\right)\sin\phi_{33} \\ &+ a_{11}\,a_{22}\left(1 + a_{33}^2\,|\rho_n|^2\right)\sin\left(\phi_{11} + \phi_{22} - \phi_s\right) \\ B &= a_{33}\left(a_{22}^2 + a_{11}^2\,|\rho_n|^2\right)\cos\phi_{33} \\ &- a_{11}\,a_{22}\left(1 + a_{33}^2\,|\rho_n|^2\right)\cos\left(\phi_{11} + \phi_{22} - \phi_s\right) \\ C &= 2\,a_{11}\,a_{22}\,a_{33}\,|\rho_n|\,\sin\left(\phi_{11} + \phi_{22} + \phi_{33} - \phi_s\right) \end{aligned} \tag{5.4}$$

where a_{ii} and ϕ_{ii} are, respectively, the magnitude and phase of the S'_{ii} parameter of the T-junction, and ϕ_s is the phase of the determinant of $\mathbf{S}'$.

As (5.2) shows, multiple solutions for l_n can be found, separated by half the manifold wavelength ($\lambda_{gn} = 2\pi/\beta_n$). The greater length l_n is, the more troublesome the presence of spurious resonances becomes. In addition, the operational bandwidth of the T-junction decreases as l_n increases. Consequently, the smaller positive value of l_n that meets the physical and mechanical constraints of the multiplexer is selected. Occasionally, one of the solutions given by (5.2) may be very close to $\lambda_{gn}/2$. In those cases, it is suggested to use a non-optimal solution to avoid unwanted resonances. A length value closer to the minimum separation between filters that fulfills all mechanical constraints l_{min} should be chosen. Certainly, this solution can only be used as long as it is able to provide enough coupling for the implementation of the first inverter. Otherwise, the optimal but longer solution should be adopted. Figure 5.6 illustrates an example where the optimal l_n is very close to $\lambda_{gn}/2$, prompting the choice of a different (and less optimal) value.

In the usual case where the optimal l_n solution is chosen, the value obtained by application of (5.2) is normally a good approximation to the desired solution. In wideband multiplexers, the filters can be placed close to each other, thus the interaction between them typically involves the fundamental but also higher-order modes. For that reason, it is recommended to perform a final refinement of l_n based on full-wave EM simulations. Once the EM-based solution for l_n is found, the aforementioned rule regarding solutions that are close to $\lambda_{gn}/2$ must also be applied.

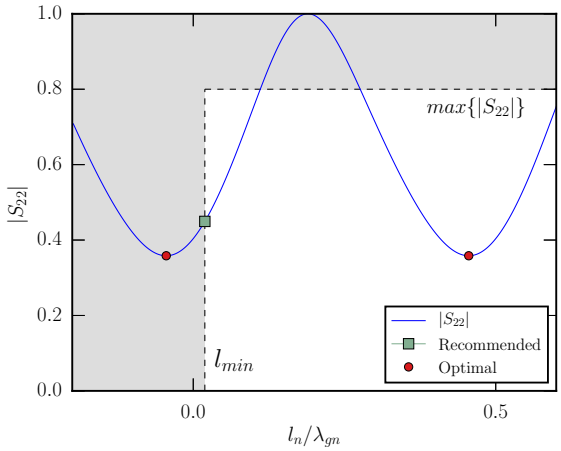

Figure 5.6: Case example where the recommended length l_n differs from the optimal value. Magnitude of the S_{22} parameter is depicted as a function of length l_n, normalized by the manifold wavelength. The shaded area defines the region where the normalized length is too small to fulfill mechanical specifications, or the magnitude of $|S_{22}|$ is not low enough to implement the first inverter (in this particular example, $\overline{K}_{01} = 0.33$).

Step 2: Adjustment of the filter first coupling iris

After setting the appropriate separation between filters, the first coupling iris is connected directly to the manifold (see Fig. 5.7). The iris is placed at the center of what is marked as Port 2 in Fig. 5.5. The size of this iris is then adjusted until the behavior of the structure at f_n is equivalent to the first inverter of filter n. The equivalent $\overline{K}_{01}^{n}$ inverter value is obtained from the full-wave simulation of the first iris of filter n as:

$$\overline{K}_{01}^{n} = \sqrt{\frac{1 - |\rho_{\text{iris}}(f_n)|}{1 + |\rho_{\text{iris}}(f_n)|}} \tag{5.5}$$

where ρ_{iris} is the reflection coefficient of the first iris detached from the rest of the filter. The iris size can be manually adjusted, or an automatic optimization procedure launched, until the magnitude of S_{22} is:

$$|S_{22}(f_n)| = \frac{1 - \overline{K}_{01}^{n\,2}}{1 + \overline{K}_{01}^{n\,2}}. \tag{5.6}$$

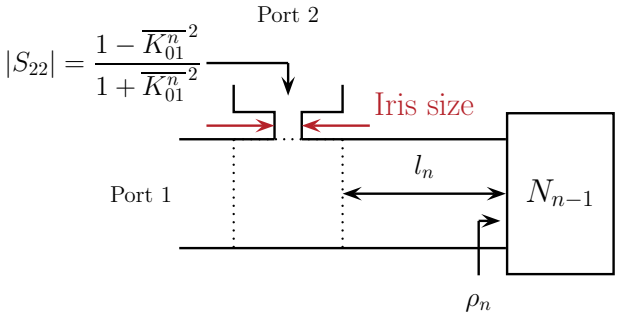

Figure 5.7: Schematic view of the structure used to adjust the size of the first coupling element of filter n, in order to match the first inverter of the stand-alone filter. Dotted line indicates the reference plane of the T-junction with all ports having the same size, as shown in Fig. 5.5.

Step 3: Adjustment of the filter first cavity

Once the dimensions of the first iris are adjusted, the structure yields the same $|S_{22}|$ as the first coupling element of the original filter. However, the phase of S_{22} (φ_{22}) does not equal the phase of the first coupling element. Comparing φ_{22} with the objective phase $\varphi_{22}^{\text{obj}}$ of the original first coupling element, a certain length of transmission line l_{rn} is added to the filter first resonator (see Fig. 5.8). Generally, this length is negative, so it will be automatically absorbed by the resonator. It can be computed as:

$$l_{rn} = \frac{\varphi_{22} - \varphi_{22}^{\text{obj}}}{2\beta'_n} \tag{5.7}$$

where β'_n is the phase constant of the waveguide that implements the first resonator of the filter (i.e. the waveguide connected to Port 2 of Fig. 5.7) at frequency f_n.

Finally, the remainder of the filter (second and subsequent resonators and coupling elements) is attached to the structure without altering its dimensions. This three-step procedure is repeated until all filters are connected to the manifold. The particular arrangement of filters has an important effect in the performance of a wideband multiplexer. With the proposed methodology, by the end of the first cycle (when all filters are connected to the manifold) the designer is able to spot potential problems in terms of spikes, or not enough coupling from the manifold to one of the filters. Since this methodology is very cost-effective, the designer can rearrange the filters in a different order and run the process once again, to see if problems have disappeared or there are additional benefits derived from the new arrangement.

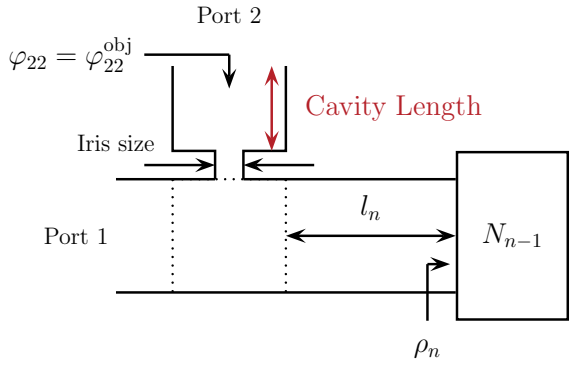

Figure 5.8: Schematic view of the structure used in Step 3 of the design procedure.

5.2.2 Additional design cycles

Once this first cycle has ended, the response from the output port of the last filter connected must be very similar to the return loss of the stand-alone filter at its central frequency. During the first cycle, the loading effect of all filters up to filter $n-1$ was considered when adjusting filter n. However, the opposite effect (i.e. the loading of filter n when connecting any of the previous filters) was not taken into account. To account for the mutual interactions both ways, at least one additional cycle must be run.

The first cycle has already provided an adequate distribution of the filters along the manifold and reasonably good dimensions of the first irises. Small adjustments to these iris dimensions are not expected to change considerably the field distribution along the manifold. Therefore, the separation between filters is not re-adjusted during the additional cycles.

Instead, the first coupling iris and first resonator length of each filter are sequentially readjusted to match the response of the corresponding first inverter of the isolated filter. In contrast with the first cycle, during the additional cycles all the filters (with the exception of the one that is being adjusted) are simultaneously connected to the manifold (see Fig. 5.9). In the first cycle, though, only the filters that had been previously adjusted were connected to the manifold. In short, the additional cycles consists on repeating Step 2 and Step 3 of the flowchart in Fig. 5.4 until all filters are adjusted.

The number of additional design cycles depends on the particular structure. Normally, after the second or third complete cycle, the benefits in terms of response improvement does not justify the time spent on an additional iteration (in fact, sometimes the results start to oscillate after each cycle, meaning that this simple procedure has reached its limit). In general, this methodology tends to benefit

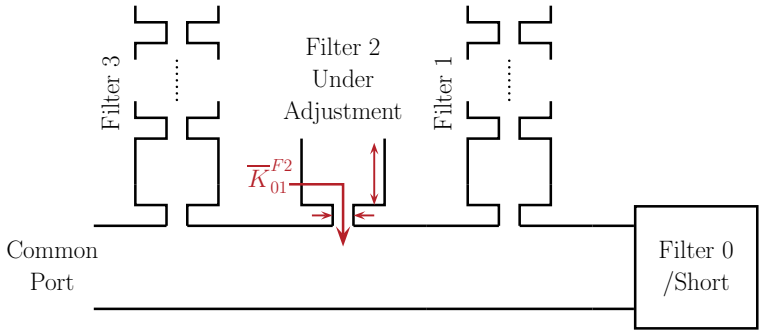

Figure 5.9: Adjustment of filter 2 during one of the additional design cycles.

the last filter readjusted, in the sense that it mainly improves the response of the multiplexer in this filter passband. As a result, the last cycle should not be fully completed, instead it must end after readjusting the most poorly matched filter (this is often filter 1 since it normally has the worst loading effect from the rest of the multiplexer).

5.2.3 Example: design of a Ka-band triplexer

This example illustrates the proposed design procedure through the simple triplexer shown in Fig. 5.10.

The three channel filters of order 4 are centered at 36.5 GHz, 38 GHz and 39.5 GHz, respectively, with 1 GHz bandwidth and 25 dB return losses. The relative bandwidth of the three filters is slightly above 2.5% but, overall, the relative bandwidth of the multiplexer is 10%. Although it is not a wideband example, but one with a moderate bandwidth, it is useful to clarify and understand the design steps. Furthermore, its simple topology enables the comparison of this method with existing ones proposed in the literature. The three standalone filters have been designed as doubly-terminated structures, given the separation between bands. Singly-terminated implementations can be employed in multiplexers involving adjacent channels, in order to facilitate their matching once they are connected to the manifold. In any case, the filters are directly connected to the short-circuited manifold by their inductive irises. In addition, the presence of rounded corners, which typically appear when components are fabricated by milling [137], has been explicitly considered in the whole structure, including also the short-circuit at the end of the manifold.

The connection of the filters to the manifold follows the guidelines described in previous sections. Starting from the lower frequency filter, each one is sequentially connected to the manifold and its first iris and resonator are conveniently adjusted.

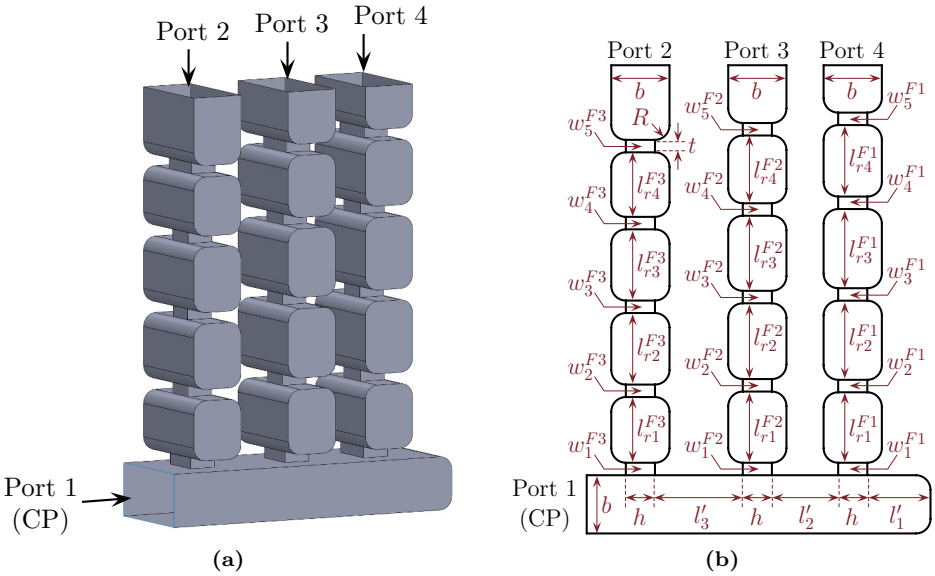

Figure 5.10: **(a)** Triplexer with rounded corners used to illustrate the design procedure. **(b)** Lateral view of the designed triplexer, along with key dimensions. w_i^{Fj} indicates the width of the i-th inductive window of filter j. The thickness (in the direction of propagation) of all inductive windows is t.

Figure 5.11 depicts the evolution of the reflection coefficient from the common port during the first cycle. In each iteration, a new filter is connected and adjusted.

At the first iteration, the adjusted manifold behaves similarly to the first inverter of filter 1 in most of its passband. Therefore, the common port return loss (CPRL) parameter of the multiplexer is almost equivalent to the return loss of the stand-alone filter (see *First Iteration* in Fig. 5.11).

Once a second filter is added, though, the mutual loading between filter 1 and filter 2 deteriorates the response in both passbands (see *Second Iteration* in Fig. 5.11). For filter 1 this implies that the first iris no longer behaves like the first inverter of the filter, thus the matching of the structure within its passband is worse than in the first iteration. Even if the matching is far from ideal, all four poles are still visible. For filter 2, the response at its center frequency is recovered thanks to the adjustment of the first iris and resonator. Within its passband, however, the variation of the reactance of the previous filter (i.e. filter 1) is not smooth. This affects how well filter 2 can be matched with the rest of the multiplexer. Around the center frequency, the filter is considerably well matched, but closer to the edges of the passband the response is significantly different from its stand-

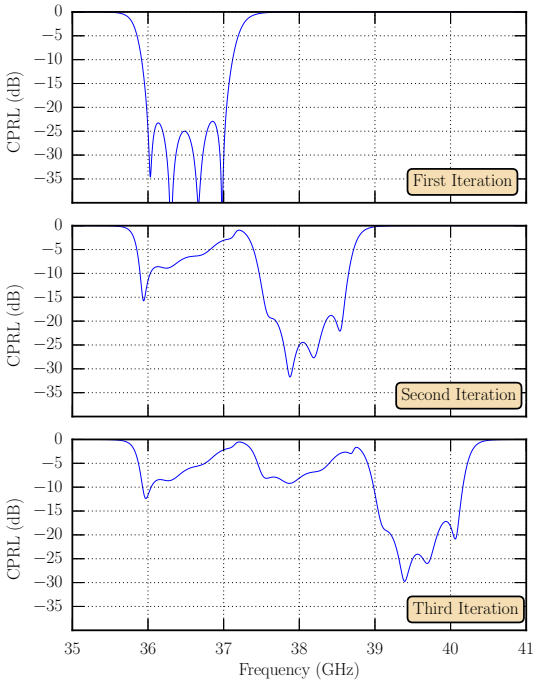

Figure 5.11: Magnitude of the reflection coefficient at the common port of the triplexer in Fig. 5.10, after each filter is assembled into the manifold. In each iteration, three dimensions are adjusted: the separation from the previous network, the first iris size, and the first resonator length.

alone version. Nevertheless, the return losses are better than 10 dB in the whole passband. Similarly, by the end of the third iteration (see *Third Iteration* in Fig. 5.11), filter 3 is considerably well matched, whereas the matching of filters 1 and 2 has been deteriorated. It is worth noting that all poles can still be identified.

After the third iteration, two additional cycles are run. Figure 5.12 shows how the CPRL improves after the application of each additional cycle. In this example, any additional cycle beyond the third one does not improve significantly the overall response. Thus, it is assumed that the method has reached convergence and the procedure finishes. The response obtained after the third cycle is considered as starting point of the optimization procedure.

It is interesting to compare this starting point, with the one provided by classical design techniques proposed in the literature. Figure 5.13a contains this comparison. Three classical techniques have been considered. In the first case, labeled *Uher et al.*, filters are directly connected to the manifold and separated along the

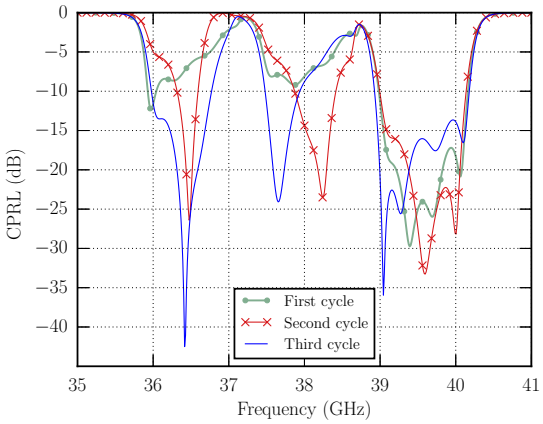

Figure 5.12: Evolution of the CPRL in the different cycles of the design process.

manifold according to the formulas in [102]. No filter dimensions are altered. This technique is normally used for narrowband multiplexer and, as it can be seen, does not provide a very good starting point if applied to wideband multiplexers. In the second case, labeled *Morini (adapted)*, the design method of [167] is applied. Since [167] is focused on diplexers using star-junctions (rather than a manifold), the equations included in it cannot be exactly extrapolated to this example. Instead, the formulas of [168] are used to separate the filters along the manifold. Once this is done, the design criteria defined in [167] is applied to adjust the first coupling window and resonator of each filter. In contrast with our proposed methodology, the remaining filters are not connected to the manifold while adjusting the dimensions of each input iris. Thus, mutual filter interactions from the first and subsequent resonators are being neglected. As can be seen in Fig. 5.13a, the two classical techniques yield similar results, whereas our proposed methodology considerably improves the initial multiplexer response. Finally, the third case, labeled *Cameron et al.*, corresponds to the classical starting point for narrowband multiplexers explained in [96]. It includes half-wavelength stubs between the filter and the manifold. The initial response with this methods seems to be better than the aforementioned classical techniques. However, this improvement can be misleading, since it comes mainly at the expense of introducing multiple resonances within the operating range of the multiplexer. Once the optimization procedure starts, it will be costly for the designer to prevent them from interfering with the multiplexer response. In conclusion, the more adequate starting point for this multiplexer is obtained with the methodology presented in this thesis.

In order to test the performance of the proposed method, an alternative solution

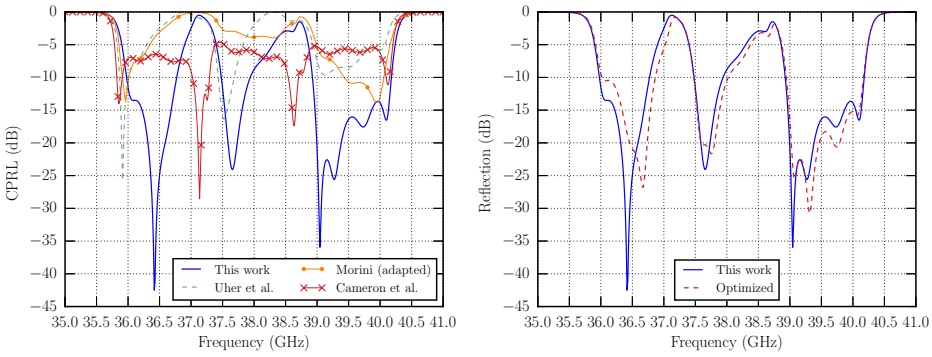

Figure 5.13: CPRL of the triplexer with rounded corners after application of the design method. This initial response (solid line) is compared with alternative procedures. **(a)** Dashed line is obtained by connecting the filters directly to the manifold and separating them according to the expressions of [102]. Solid line with circular markers is obtained by spacing the filters according to [168] and adjusting the first coupling irises to fit formulae in [167]. Solid line with cross markers corresponds to the design procedure that includes half-wavelength stubs between each filter and the manifold [96]. **(b)** The initial response (solid line) obtained with the proposed methodology is compared with the one (dashed line) obtained after a global optimization of the first stages (iris and resonator).

has been considered as well. It has been obtained by optimization of the first iris and resonator of each filter using the simplex method. The separation between filters, though, has been fixed to the same value as our proposed initial design. The optimization goals have been set to achieve return losses better than 25 dB over the bandwidth of the three filters. In contrast with the proposed design methodology, this alternative procedure actually takes into account the loading effect of all filters at the same time. As shown in Fig. 5.13b, this solution is a slightly better option than our proposed methodology, but the differences between the two responses are certainly small. Furthermore, our proposed methodology is less CPU-intensive since, in each step, only one dimension is adjusted and the full-wave simulations are just performed at one frequency point (center frequency of the filter being adjusted).

Starting from the proposed initial response, the conventional multiplexer design procedure described in [96] (sequential adjustment of filters until specifications are fulfilled) is applied. Without much effort, the final response depicted in Fig. 5.14

is obtained. The final dimensions of the triplexer are summarized in Table 5.2.

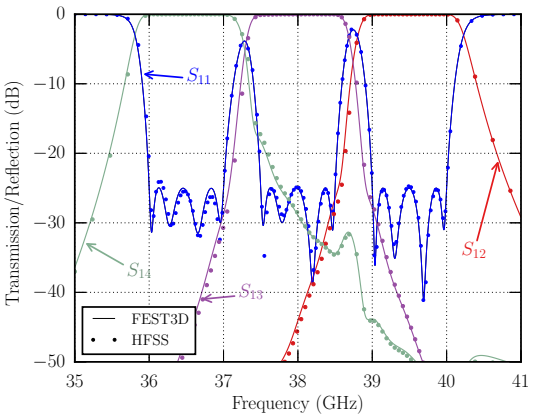

Figure 5.14: Magnitude of the scattering parameters after optimization of the triplexer with rounded corners. Design results are compared with HFSS.

Filter 1									
l'_1	w_1^{F1}	l_{r1}^{F1}	w_2^{F1}	l_{r2}^{F1}	w_3^{F1}	l_{r3}^{F1}	w_4^{F1}	l_{r4}^{F1}	w_5^{F1}
3.858	3.294	4.303	2.420	4.833	2.216	4.835	2.416	4.364	3.409
Filter 2									
l'_2	w_1^{F2}	l_{r1}^{F2}	w_2^{F2}	l_{r2}^{F2}	w_3^{F2}	l_{r3}^{F2}	w_4^{F2}	l_{r4}^{F2}	w_5^{F2}
4.046	2.906	4.348	2.119	4.628	2.084	4.584	2.315	4.138	3.280
Filter 3									
l'_3	w_1^{F3}	l_{r1}^{F3}	w_2^{F3}	l_{r2}^{F3}	w_3^{F3}	l_{r3}^{F3}	w_4^{F3}	l_{r4}^{F3}	w_5^{F3}
5.361	2.905	4.012	2.122	4.370	2.018	4.349	2.220	3.940	3.151
Additional dimensions									
		a	b		R	t	h		
		7.112	3.556		0.889	0.762	1.778		

Table 5.2: Final dimensions of the designed triplexer with rounded corners in mm. Dimension a refers to the width of the manifold and resonators.

5.3 Design of a C-band quadruplexer for PIM measurement set-ups

The proposed design methodology has been presented and validated through the application to the design of a simple triplexer. Now it is applied to the design of a much more complicated structure, this is a quadruplexer that covers practically the entire recommended band of the WR-229 waveguide. This component is to be employed as the key element of a PIM measurement set-up at C-band. A schematic view of this set-up can be seen in Fig. 5.15. Up to three carriers (each in a different frequency band) are amplified and then combined. The resulting signal is routed to the common port, where the device under test (DUT) is connected. The third-order passive intermodulation generated by this device is then reflected back and redirected to the output port (Rx), where a vector network analyzer measures the PIM level. Consequently, the role of the quadruplexer is to combine the input signals, direct them to the common port and transfer the reflected PIM signal to the output (Rx) port.

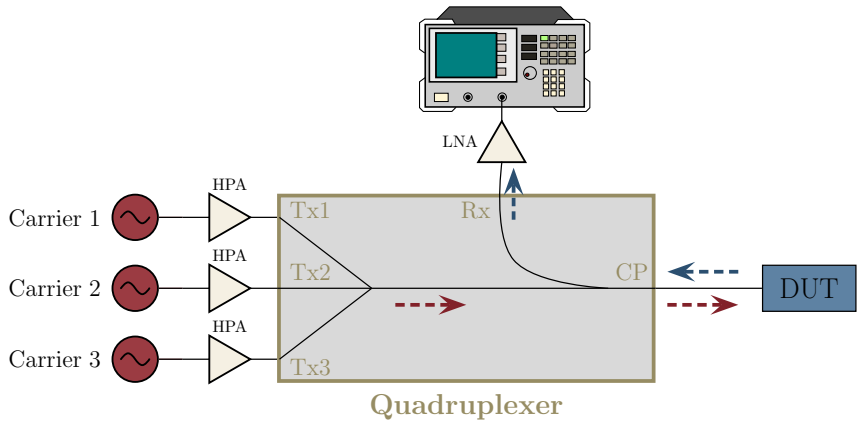

Figure 5.15: Scheme of a PIM measurement set-up.

The transmission (Tx) and reception (Rx) frequency bands of operation for this multiplexer are:

- Tx1 band: 3.4 GHz to 3.61 GHz
- Tx2 band: 3.81 GHz to 3.98 GHz
- Tx3 band: 4.13 GHz to 4.26 GHz
- Rx (PIM) band: 4.5 GHz to 4.85 GHz

The passive intermodulation generated by the DUT is very weak. The set-up must be able to detect signals with a minimum level of -139 dBm. Considering that the high-power amplifiers may introduce noise in the Rx band with a maximum power level of 10 dBm, the isolation from the input ports to the Rx port in this band must be greater that 149 dB. Since this is a critical design parameter, a safety margin of 16 dB is added, thus the objective isolation from the three Tx signals in the Rx band is 165 dB. In contrast, the isolation of the Rx signal in the Tx bands is set to 160 dB (including margins). This is done to prevent input-carrier leakages from reaching the low noise-amplifier (LNA) placed between the quadruplexer and the spectrum analyzer. If the isolation was much lower, active intermodulation could be generated in the LNA, which would unequivocally harm the measurement set-up. Furthermore, the maximum insertion losses allowed for the set-up are 1.35 dB, in order to maximize its performance, given the available high power amplifiers (HPA), and also avoid unwanted thermal issues.

As can be seen from the stringent specifications, the complexity of this design, in terms of bandwidth (36% overall, with filters of 3.6%, 4.9%, 6% and 8.3% relative bandwidth, after the inclusion of design margins) and rejection levels, is unprecedented in the technical literature for manifold-coupled multiplexers. Under these circumstances, the use of a proper design methodology is fundamental.

First, the different filters that compose the manifold are designed. Since the quadruplexer must be as low-PIM as possible, the tuning-less implementation of the filters is fundamental. Low order structures are preferred, in order to minimize the manufacturing deviations in the final response. At the same time, these filters must be able to create high-isolation stopbands to fulfill the rejection requirements. HFRW filters are employed for the Tx channel filters. In some instances, the number of TZs generated by these low-order HFRW filters is not enough to fulfill the stringent rejection requirements. Consequently, corrugated lowpass filters are cascaded to increase the overall rejection in the PIM band. In contrast, the Rx channel is implemented by the combination of a bandpass and a high-pass filter. The implementation of each channel filter is considered next.

5.3.1 Channel filters

Tx1 channel

The channel filter operating in the Tx1 band is depicted in Fig. 5.16a. This sixth-order filter is composed of two cascaded HFRW triplets, thus providing two additional TZs. In addition, the novel iris-stub coupling structure presented in section 4.2 is used to implement the output coupling, and simultaneously provide 2 TZs. The six cavities are implemented as stepped-impedance resonators [169], instead of the classical rectangular cavities. This choice allows certain additional control over the location of the spurious passband, due to higher-order resonances of the filter cavities. Since this is the filter located the furthest from the PIM

band, the aforementioned spikes fall closer to the critical reception band. Thus, it is specially important to be able to shift such spurious passband towards higher frequencies, obtaining the maximum filter rejection at the reception band. As can be seen in the response depicted in Fig. 5.16b, the rejection requirements over the PIM band are fulfilled. Consequently, additional low-pass filters are not required.

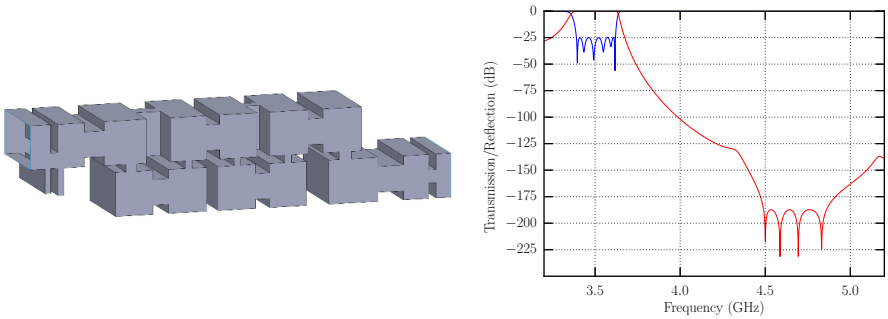

(a) **(b)**

Figure 5.16: **(a)** Physical structure of the Tx1 channel filter. Stepped-impedance resonators are employed to implement the six cavities of the filter. Stubs are connected to the output iris to generate two additional TZs. **(b)** S-parameter response.

Tx2 and Tx3 channels

The Tx2 and Tx3 channels contain fifth-order bandpass filters implemented in the HFRW topology. These structures can be seen at the top of Fig. 5.17a and Fig. 5.18a. Cascading two triplets, each filter is able to provide two TZs, located within the Rx band. The isolation generated by these structures is not enough to fulfill the stringent requirements of the set-up. For that reason, a lowpass stub filter capable of increasing the number of TZs (and, consequently, the rejection) is connected to each filter. In the Tx2 case, the 11-th order corrugated structure shown in Fig. 5.17b is used. This structure generates five TZs in the passband. Regarding the Tx3 channel, the lowpass filter employed is a 15-th order structure that generates seven TZs. The first two are double zeros to improve sensitivity to manufacturing [170]. The need for additional TZs are justified by the fact that this channel is adjacent to the PIM band and requires a much steeper rejection slope. This structure and its S-parameter response can be seen at the bottom of Fig. 5.18.

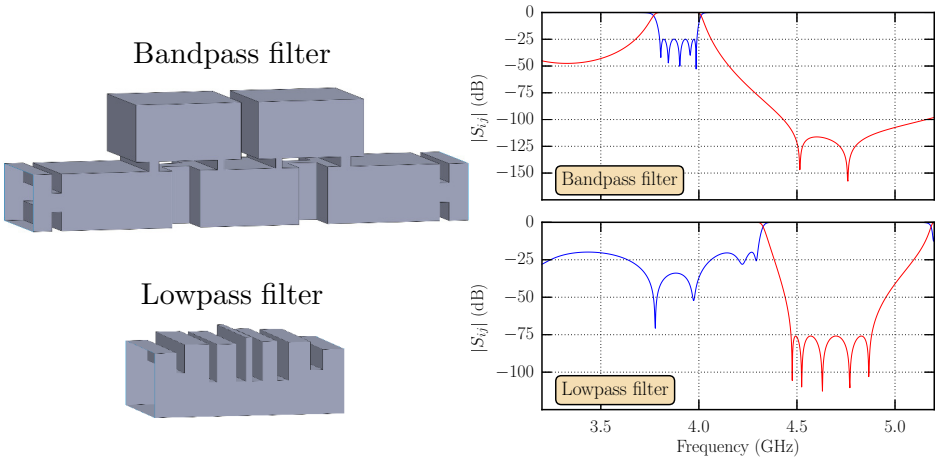

(a) **(b)**

Figure 5.17: **(a)** Physical structure of the HFRW bandpass and lowpass filter of channel Tx2. **(b)** S-parameter response of both filters.

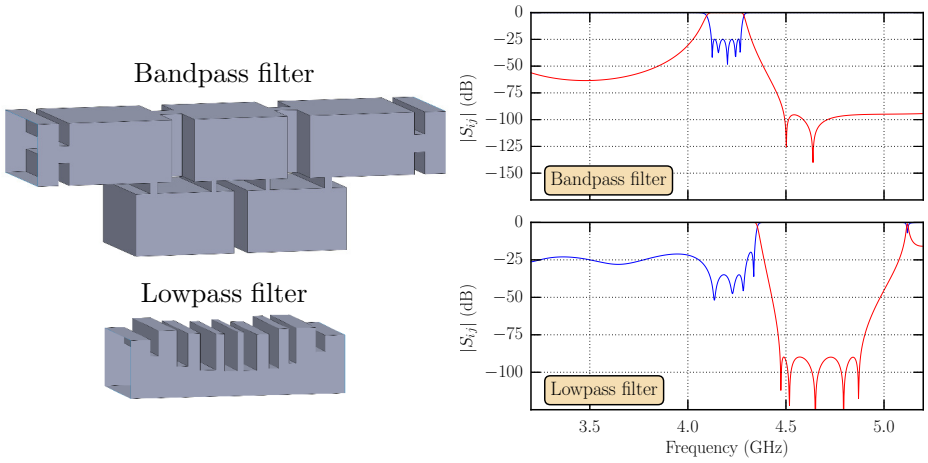

(a) **(b)**

Figure 5.18: **(a)** Physical structure of the HFRW bandpass and lowpass filter of channel Tx3. **(b)** S-parameter response of both filters.

Rx channel

The Rx channel must filter the signal in the frequency band where the third-order PIM is generated, and prevent a potential harmful leakage from the Tx carriers to reach the low-noise amplifier placed before the spectrum analyzer. The Rx band is realized by the classical inductive bandpass filter structure shown in Fig. 5.19. As it can be seen, the input coupling window is capacitive to facilitate its connection to an E-plane manifold multiplexer. In addition, the last cavity of this filter has a reduced width. This is done to adapt the output port to a reduced-width rectangular waveguide. The bulk of the isolation is provided by this reduced-width waveguide, equivalent to a high-pass filter. In order to generate enough attenuation in the stopband, this waveguide has to be extremely long. The waveguide is twisted, forming the meandering block shown in Fig. 5.19a. By doing so, the footprint of the overall quadruplexer (this is, the area occupied by the component when seen in projection on a mounting surface) is reduced, thus leading to a more compact structure.

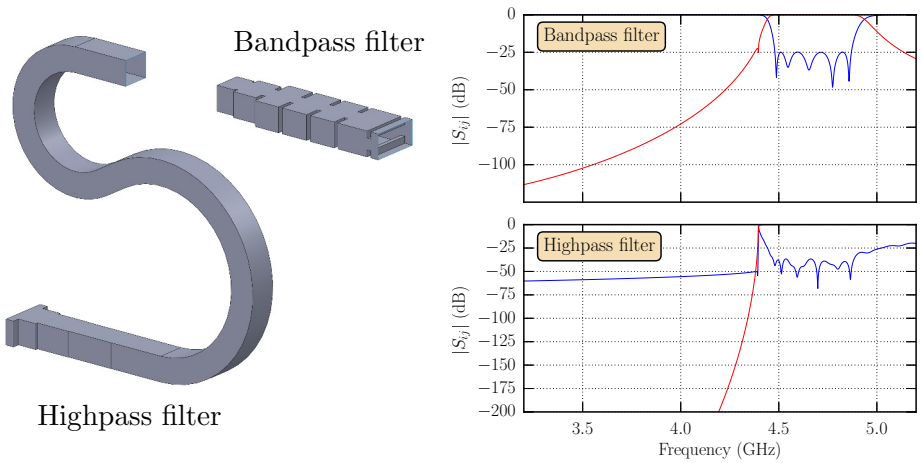

(a) **(b)**

Figure 5.19: **(a)** Physical structure of the bandpass and highpass filters that compose the Rx channel. **(b)** S-parameter response of both filters.

5.3.2 Final design

Once the channel filters are designed, the methodology proposed in section 5.2 is applied to connect them to the manifold. The resulting structure is depicted in Fig. 5.20. As can be seen, the manifold is extremely short. In order to keep this element as short as possible, a non-optimal but minimal separation between the Tx2 and Tx3 channel filters has been chosen (instead of the optimal separation close to $\lambda_g/2$). This choice has some undesired consequences: the physical separation between the Tx1 and Tx3 filters is very small. Such a small gap between filters limits the amount of heat that can be dissipated in that area of the component, and prevents the introduction of assembling/alignment screws. To overcome this problem, the first coupling window of both of these filters has been shifted with respect to the center of the cavity, effectively increasing the gap between them (note this in the detail of Fig. 5.20).

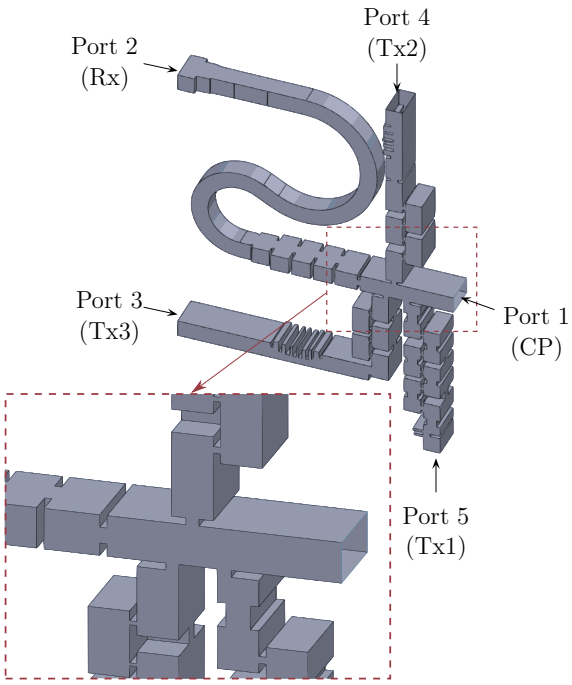

Figure 5.20: Quadruplexer for PIM measurements at C-band. Detail of the manifold is included.

After application of the initial design procedure, a global optimization is run, considering only the variables of the four bandpass filters and without re-adjusting the manifold. The final optimized response, simulated with FEST3D [37], can be

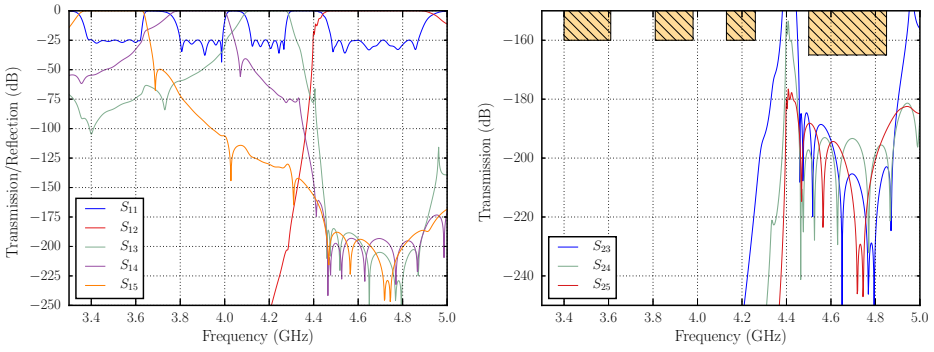

Figure 5.21: **(a)** Magnitude of the scattering parameters of the designed quadruplexer at C-band. Results are generated with FEST3D. **(b)** Isolation between the transmission and reception ports. Shaded areas indicate the design threshold for the isolation parameter.

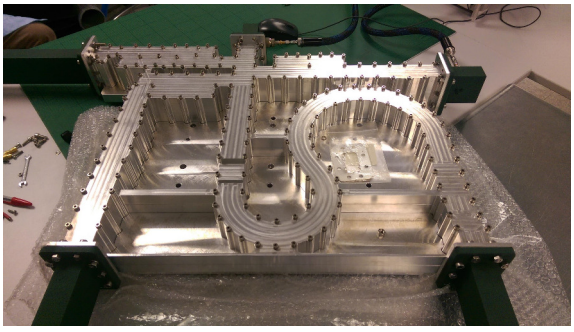

Figure 5.22: Photograph of the manufactured quadruplexer.

seen in Fig. 5.21. As expected, the quadruplexer is able to fulfill the stringent requirements imposed by the working conditions of this component.

The quadruplexer has been manufactured from bare aluminum (using alloy 6082) in two identical halves and assembled with clam-shell technology. Due to the high sensitivity to manufacturing deviations of the Tx3 channel, silver coating (typically used to reduce insertion losses) is avoided. To improve heat transfer, it has been attached to a base plate. A photograph of this component can be seen in Fig. 5.22.

Measured results from the manufactured quadruplexer are depicted in Fig.

5.23. A very good agreement is found between this results and the designed response computed with FEST3D. Due also to the efficient design technique proposed in this paper, which provides a good starting point after application of the fast algorithm for interconnecting the filters, it is possible to successfully carry out the design of such a large tuning-less multiplexer in reasonable CPU times. Note that no tuning has been performed on the multiplexer.

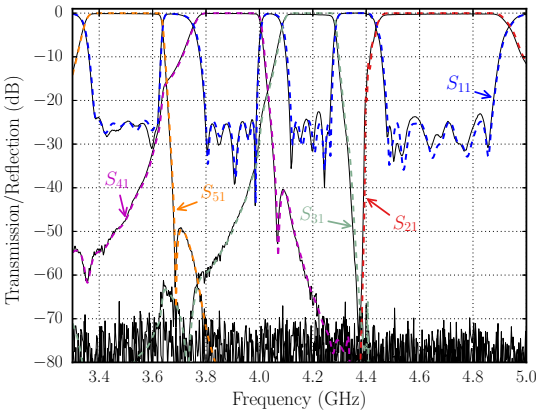

Figure 5.23: Comparison between the designed (dashed lines) and measured (solid lines) responses of the C-band quadruplexer.

As shown, return losses are better than 22.3 dB and insertion losses are smaller than 0.5 dB in all passbands (see Fig. 5.24), satisfying the desired specifications by a wide margin. These results also enable the inclusion of other elements in the PIM measurement set-up (such as isolators, waveguide sections or directional couplers), if necessary. The rejection level has been successfully validated up to 150 dB, which was the limit of the measurement system due to undesired leakages between cables and instrumentation equipment. In any case, this rejection level guarantees the successful performance of this component for the intended application.

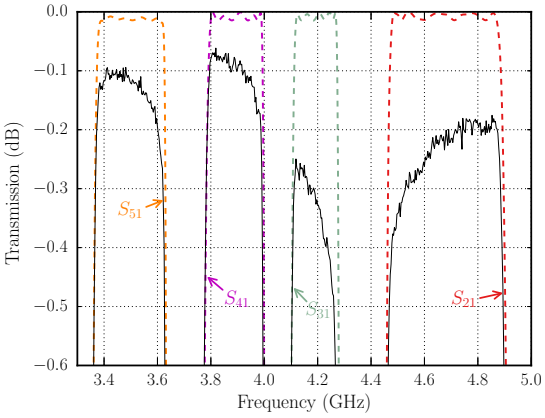

Figure 5.24: Insertion losses of the measured quadruplexer (solid lines) compared with simulations (dashed lines).

Chapter 6

Conclusions and future work

The design of a C-band quadruplexer for PIM measurements explained in section 5.3 can be considered the pinnacle of this PhD thesis. It combines in a single structure all the developments presented in this work, and certainly puts in perspective the different achievements. The particular application for which it was conceived required the multiplexer to cover a very wide frequency band. Thus the adoption of a consistent design methodology, specifically the one presented in chapter 5, was critical to the success of its design. Simultaneously, the isolation and low-PIM requirements set particular constraints on the type of channel filters that could be employed. The quasi-elliptic filter implementations studied in chapter 4 were uniquely qualified to fulfill these constraints. Consequently, their choice to implement the channel filters was direct. At the same time, the use of an adequate EM simulation tool in such a complex design, involving a large amount of optimization, is crucial. Being heavily based on a succession of bi-dimensional blocks, the quadruplexer was an ideal candidate to benefit from the accurate and fast modeling provided by the EM analysis tool presented in chapter 2. As a matter of fact, prior results presented in chapter 3 were encouraging. They showed that the use of the developed software tool in a triplexer with the same intended application had actually reduced the time for a typical EM analysis, when compared with previously existing formulations. Therefore, it was decided to rely on this tool throughout the design process. As a result, the complete design cycle was largely accelerated and, in turn, the delivery of the final component could be done ahead of schedule.

The C-band quadruplexer is just one example of the possibilities that this PhD thesis offers. In fact, the scope of application of this thesis is much broader, as reflected by the objectives described in section 1.2. After presenting the complete body of work in chapters 2 to 5, it is time to revisit these objectives and assess the degree of fulfillment of each one.

The first objective of this thesis was to develop an efficient software tool for the EM analysis of bi-dimensional cavities of arbitrary shape. To fulfill this goal, a new formulation was developed. The EM problem was divided into two independent sub-problems thanks to the adoption of an adequate family of modes (the Longitudinal Section family). By applying a specific frequency transformation, it was demonstrated in chapter 2 that the size of both sub-problems could be reduced by an important factor. Kurokawa's field expansion was first considered to solve both problems, but its application was proved to be inefficient and impractical. Instead, an alternative solution based on the combination of the Boundary Integral - Resonant Mode Expansion method with an Integral Equation technique was implemented. It reduced considerably the number of modes to solve in the arbitrary cross-section of the cavity and accelerated the computation of the electromagnetic field. In addition, this formulation was fully compatible with the computation of the Generalized Admittance Matrix. Making use of certain matrices employed in the field solution, an equivalent network representation could be obtained with very little computational overhead. Therefore, the second objective of this thesis was also fulfilled. A point of emphasis throughout the formulation development was to ensure that the contour of the cavity could be described with straight, circular and elliptical segments. Thanks to the solution of certain singular integrals performed in Appendix C, this objective was accomplished as well.

This new formulation was integrated into FEST3D, enabling the analysis and design of a wide range of microwave components. Chapter 3 displayed simulation results for certain structures, from filters and multiplexers to orthomode transducers, that fully validated the new EM formulation. Some of these components were extracted from the technical literature, whereas others were designed ad hoc. In any case, results were always compared with measured data or simulations generated by general-purpose EM solvers, such as HFSS and CST. At the same time, the fields provided by the new analysis tool were used in combination with SPARK3D to study the high-power performance of two waveguide components. Consequently, the third and fourth objectives of this thesis were also fulfilled.

The fifth objective was to apply the aforementioned formulation to HFRW filters and perform an in-depth study of these structures. Different coupling apertures were proposed in the first part of chapter 4 to implement the direct and cross-couplings. In particular, seven different aperture combinations were studied, highlighting the advantages and limitations of each one. By doing so, designers were granted enough flexibility to choose the coupling combination that better fits their requirements. At the same time, it was shown how the resonant nature of the direct-coupling apertures of HFRW filters affects the number of TZs that can be realized in the stopband of a given filter. As demonstrated, each triplet is able to realize two additional TZs associated with the two resonant direct-coupling apertures. However, not all of them are located in desired stopband, and thus their use is not always practical. In any case, a specific design procedure for these types of

filters was proposed and applied to a five-pole structure realizing four TZs. Measurements from a manufactured prototype were employed to validate this study, thus fulfilling the fifth objective.

In addition, a coupling structure formed by the connection of stubs to a capacitive window was proposed in the second part of chapter 4. It was presented as an interesting alternative to increase the number of TZs in waveguide filters. As demonstrated, the structure is able to realize a given coupling level as well as generate one TZ per stub at a prescribed frequency. Therefore, any capacitive inline connection between rectangular resonators can be substituted by this coupling structure and realize two TZs without implementing any cross coupling. Two examples were given to illustrate its use, comparing design results with simulations. Consequently, the sixth objective was also accomplished.

Finally, the last objective was focused on developing an efficient methodology to design wide-band multiplexers. The special characteristics of these components makes their design slightly different from their narrowband counterparts. Taking into account these differences, a step-by-step procedure was proposed in chapter 5. It is based on the adjustment of a few dimensions per filter in order to make the rest of the multiplexer behave as the first inverter of the corresponding standalone filter. Even though this procedure does not avoid a final optimization, it certainly provides a good starting point, as evidenced in the triplexer design example included in this chapter. To culminate this thesis, the aforementioned C-band quadruplexer was successfully designed and results compared with measurements.

In conclusion, all the objectives initially proposed for this PhD thesis were accomplished. As a result, this thesis has generated multiple publications in relevant journals and conferences dedicated to microwave engineering, as summarized in appendix E. Likewise, most of the advances and technology developed in the framework of this thesis has been transferred to the European space industry. The electromagnetic analysis technique for bi-dimensional cavities presented in chapter 2 has been integrated into FEST3D, a commercial software tool developed and commercialized by the Valencia-based company Aurorasat. Furthermore, the C-band quadruplexer designed in chapter 5, which includes some of the filters studied in chapter 4, was commissioned by the European Space Agency (ESA) and is, currently, employed at the ESA-Val Space Consortium (VSC) High-Power RF laboratory[1] located in Valencia.

Nevertheless, this work has opened up new research possibilities that could be explored in the future. The main ones are summarized next:

1. Analysis of bi-dimensional cavities with apertures both in the lateral and top (or bottom) walls. This extension enables the analysis of magic Ts with an arbitrary base (for example, a transformer), turnstile junctions, OMTs with dual junctions, etc. This problem basically requires a formulation that

[1] Information about this facility can be found at `http://www.val-space.com/highpowerlabrf/`

combines the field solution from a short circuited waveguide of arbitrary cross-section (case where the excitation is introduced by the port in the top/bottom wall) with the formulation presented in this thesis.

2. Extension of the analysis formulation to enable the introduction of dielectric elements. Initially, these elements may occupy the total height or width of the cavity. But, given the practical interest of dielectric resonators (typically manufactured as cylindrical disks of a certain dielectric material) a notable contribution would involve the analysis of these elements within arbitrarily-shaped cavities. In order to do so, the full 3D version of the BI-RME method, combining multiple dielectric and metallic elements (to represent the contour of the cavity and additional tuning elements), should be developed.

3. Automatic synthesis and design procedure for HFRW filters. Even though the design procedure presented in chapter 4 has been shown to be adequate for these filters, the designer still has to adjust some dimensions to achieve the desired response. An elaborated synthesis technique tailored to this family of filters, which can automatize many of the adjustments, can be of interest to facilitate and speed up the design.

4. Synthesis of coupling structures based on the iris-stub concept with more than two stubs. In theory, it is possible to attach more than two stubs to a given capacitive window. As more stubs are attached, the maximum coupling provided by the overall structure decreases, but the number of TZs increases. The distance between stubs is one parameter that has not been considered in this thesis, but can be very important as more stubs are added. Moreover, a synthesis of the initial dimensions of the stubs and capacitive window would be of great help in extending the use of this novel coupling structure.

5. Study of alternative connections between filters and manifold for wideband multiplexers. Theoretically, the direct connection of filters to the manifold minimizes undesired resonances. But, occasionally, the design methodology presented in this thesis does not provide enough degrees of freedom to move these resonances outside the passband. In these situations, two alternatives can be studied:

    - Effect of the distribution of filters along the manifold on the undesired resonances. Traditionally, filters have been connected in ascending order (regarding their center frequency) from the short-circuit to the common port. This solution tends to provide an adequate match in adjacent bands. However, altering the distribution of filters can lead to significant changes in the manifold length, which, in turn can shift the undesired resonances outside of the passband.

- Shorter manifolds can also be achieved by introducing short fixed-length stubs between the manifold and the filters. In this case, the design procedure presented in this thesis can be directly applied while considering these stubs as belonging to the corresponding manifold T-junction. Practical design strategies that clearly define when to consider each option would be of great interest for multiplexer designers.

6. Systematic design of star-junction multiplexers. A design procedure, equivalent to the one presented in this thesis, can be developed for star-junction multiplexers. Furthermore, star-junctions are a typical example of bi-dimensional cavities. Thus, the design of these components could also be largely accelerated through the use of the analysis technique presented in chapter 2 to model the interconnection.

7. New multiplexer designs in forward configuration. The multiplexer designs included in this thesis work in the reverse configuration. This means that the PIM signal routed to the spectrum analyzer is the one that has been reflected by the DUT. Another configuration for PIM measurements is the forward PIM measurement, where the spectrum analyzer receives the PIM signal that is transmitted by the DUT. The hardware involved in this second configuration is slightly different, mainly because the routing has to be done in two separate places: at the input (to combine the high-power carriers) and at the output (to separate the PIM signal and deliver it to the spectrum analyzer). Therefore, the design of novel high-end components for the forward measurement of PIM is a promising research topic.

Appendix A

Transformation between Longitudinal Section and Transverse modes in rectangular waveguides

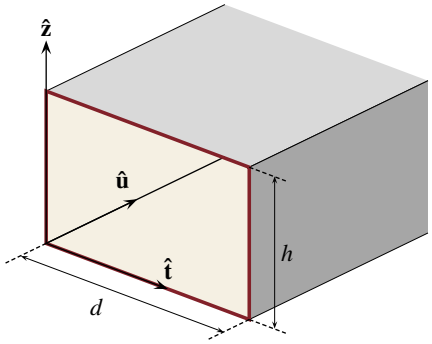

Figure A.1: Rectangular waveguide and coordinate system.

Longitudinal modes (LSE and LSM) oriented with regard to z (see Fig. A.1) can be expressed as a superposition of transverse-to-u (TE or TM) modes as:

$$\mathbf{h}_{lm}^{\text{LSE/LSM}} = A^{\text{TE-LSE/LSM}}\,\mathbf{h}_{lm}^{\text{TE}} + A^{\text{TM-LSE/LSM}}\,\mathbf{h}_{lm}^{\text{TM}} \tag{A.1a}$$

$$\mathbf{e}_{lm}^{\text{LSE/LSM}} = B^{\text{TE-LSE/LSM}}\,\mathbf{e}_{lm}^{\text{TE}} + B^{\text{TM-LSE/LSM}}\,\mathbf{e}_{lm}^{\text{TM}}. \tag{A.1b}$$

The indices (l,m) of both sets of modes must be equal, otherwise no coupling is possible (amplitudes A and B are null). Despite the different field orientation, both sets of modes propagate in the u-direction and fulfill $\mathbf{e}_{lm} \times \mathbf{h}_{lm} = \hat{\mathbf{u}}$. The specific expressions for the different field components are:

LSE modes

$$\mathbf{e}_{lm}^{\mathrm{LSE}} = C_{lm} \cos\left(\frac{m\pi}{d}t\right) \sin\left(\frac{l\pi}{h}z\right) \hat{\mathbf{t}} \tag{A.2a}$$

$$\mathbf{h}_{lm}^{\mathrm{LSE}} = \frac{C_{lm}\, lm\pi^2}{dh\left[k^2 - \left(\frac{l\pi}{h}\right)^2\right]} \sin\left(\frac{m\pi}{d}t\right) \cos\left(\frac{l\pi}{h}z\right) \hat{\mathbf{t}} - C_{lm} \cos\left(\frac{m\pi}{d}t\right) \sin\left(\frac{l\pi}{h}z\right) \hat{\mathbf{z}} \tag{A.2b}$$

LSM modes

$$\mathbf{e}_{lm}^{\mathrm{LSM}} = \frac{-C_{lm}\, lm\pi^2}{dh\left[k^2 - \left(\frac{l\pi}{h}\right)^2\right]} \cos\left(\frac{m\pi}{d}t\right) \sin\left(\frac{l\pi}{h}z\right) \hat{\mathbf{t}} + C_{lm} \sin\left(\frac{m\pi}{d}t\right) \cos\left(\frac{l\pi}{h}z\right) \hat{\mathbf{z}} \tag{A.3a}$$

$$\mathbf{h}_{lm}^{\mathrm{LSM}} = C_{lm} \sin\left(\frac{m\pi}{d}t\right) \cos\left(\frac{l\pi}{h}z\right) \hat{\mathbf{t}} \tag{A.3b}$$

TE modes

$$\mathbf{e}_{lm}^{\mathrm{TE}} = -\frac{l}{h} C_{lm} \sin\left(\frac{l\pi\, z}{h}\right) \cos\left(\frac{m\pi\, t}{d}\right) \hat{\mathbf{t}} + \frac{m}{d} C_{lm} \cos\left(\frac{l\pi\, z}{h}\right) \sin\left(\frac{m\pi\, t}{d}\right) \hat{\mathbf{z}} \tag{A.4a}$$

$$\mathbf{h}_{lm}^{\mathrm{TE}} = \frac{m}{d} C_{lm} \cos\left(\frac{l\pi\, z}{h}\right) \sin\left(\frac{m\pi\, t}{d}\right) \hat{\mathbf{t}} + \frac{l}{h} C_{lm} \sin\left(\frac{l\pi\, z}{h}\right) \cos\left(\frac{m\pi\, t}{d}\right) \hat{\mathbf{z}} \tag{A.4b}$$

TM modes

$$\mathbf{e}_{lm}^{\mathrm{TM}} = -\frac{m}{d} C_{lm} \sin\left(\frac{l\pi\, z}{h}\right) \cos\left(\frac{m\pi\, t}{d}\right) \hat{\mathbf{t}} - \frac{l}{h} C_{lm} \cos\left(\frac{l\pi\, z}{h}\right) \sin\left(\frac{m\pi\, t}{d}\right) \hat{\mathbf{z}} \tag{A.5a}$$

$$\mathbf{h}_{lm}^{\mathrm{TM}} = -\frac{l}{h} C_{lm} \cos\left(\frac{l\pi\, z}{h}\right) \sin\left(\frac{m\pi\, t}{d}\right) \hat{\mathbf{t}} + \frac{m}{d} C_{lm} \sin\left(\frac{l\pi\, z}{h}\right) \cos\left(\frac{m\pi\, t}{d}\right) \hat{\mathbf{z}} \tag{A.5b}$$

where

$$C_{lm} = \begin{cases} \sqrt{\dfrac{2\epsilon_m}{dh}} & \text{for LSE modes} \\ \sqrt{\dfrac{2\epsilon_l}{dh}} & \text{for LSM modes} \\ \sqrt{\dfrac{\epsilon_l \epsilon_m \, hd}{(ld)^2 + (mh)^2}} & \text{for TE and TM modes.} \end{cases} \tag{A.6}$$

ϵ_l/ϵ_m are defined in (2.53). Using these expressions, the coupling between the different pair of modes can be computed.

A.1 Coupling between LSE and TE modes

The coupling coefficients between LSE and TE modes are:

$$A^{\text{TE-LSE}} = \int_0^h \int_0^d \mathbf{h}_{lm}^{\text{TE}} \cdot \mathbf{h}_{lm}^{\text{LSE}} dz \, dt = \frac{-l\,d \;\left[k^2 - (l\pi/h)^2 - (m\pi/d)^2\right]}{\sqrt{(ld)^2 + (mh)^2}\;\left[k^2 - (l\pi/h)^2\right]} \tag{A.7}$$

$$B^{\text{TE-LSE}} = \int_0^h \int_0^d \mathbf{e}_{lm}^{\text{TE}} \cdot \mathbf{e}_{lm}^{\text{LSE}} dz \, dt = \frac{-l\,d}{\sqrt{(ld)^2 + (mh)^2}}. \tag{A.8}$$

A.2 Coupling between LSE and TM modes

The coupling coefficients between LSE and TM modes are:

$$A^{\text{TM-LSE}} = \int_0^h \int_0^d \mathbf{h}_{lm}^{\text{TM}} \cdot \mathbf{h}_{lm}^{\text{LSE}} dz \, dt = \frac{-m\,h\,k^2}{\left[k^2 - (l\pi/h)^2\right]\sqrt{(ld)^2 + (mh)^2}} \tag{A.9}$$

$$B^{\text{TM-LSE}} = \int_0^h \int_0^d \mathbf{e}_{lm}^{\text{TM}} \cdot \mathbf{e}_{lm}^{\text{LSE}} dz \, dt = \frac{-m\,h}{\sqrt{(ld)^2 + (mh)^2}}. \tag{A.10}$$

A.3 Coupling between LSM and TE modes

The coupling coefficients between LSM and TE modes are:

$$A^{\text{TE-LSM}} = \int_0^h \int_0^d \mathbf{h}_{lm}^{\text{TE}} \cdot \mathbf{h}_{lm}^{\text{LSM}} \, dz \, dt = \frac{m\,h}{\sqrt{(ld)^2 + (mh)^2}} \tag{A.11}$$

$$B^{\text{TE-LSM}} = \int_0^h \int_0^d \mathbf{e}_{lm}^{\text{TE}} \cdot \mathbf{e}_{lm}^{\text{LSM}} \, dz \, dt = \frac{m\,h\,k^2}{[k^2 - (l\pi/h)^2]\,\sqrt{(ld)^2 + (mh)^2}}. \tag{A.12}$$

A.4 Coupling between LSM and TM modes

The coupling coefficients between LSM and TM modes are:

$$A^{\text{TM-LSM}} = \int_0^h \int_0^d \mathbf{h}_{lm}^{\text{TM}} \cdot \mathbf{h}_{lm}^{\text{LSM}} \, dz \, dt = \frac{-l\,d}{\sqrt{(ld)^2 + (mh)^2}} \tag{A.13}$$

$$B^{\text{TM-LSM}} = \int_0^h \int_0^d \mathbf{e}_{lm}^{\text{TM}} \cdot \mathbf{e}_{lm}^{\text{LSM}} \, dz \, dt = \frac{-l\,d\,\left[k^2 - (l\pi/h)^2 - (m\pi/d)^2\right]}{\sqrt{(ld)^2 + (mh)^2}\,\left[k^2 - (l\pi/h)^2\right]}. \tag{A.14}$$

Appendix B

Derivation of the Integral Equation for the scalar potential

B.1 General Integral Equation

This appendix describes the procedure followed to obtain the Integral Equation that enables the computation of the scalar potential φ_s at points P within S and on its contour. The procedure explained here can be found in Appendix A3.1 and A3.2 of [171] particularized in the case of the classical two-dimensional Green's function (i.e. the zero-order Hankel's function of the second kind). Instead, the more general expression of the two-dimensional Green's function proposed in [135] is considered in this appendix. The final integral equations are equal in both cases.

The derivation starts with Green's second identity particularized for the functions φ_s and G:

$$\oint_{\partial S} \left(\varphi_s \frac{\partial G}{\partial n} - G \frac{\partial \varphi_s}{\partial n} \right) dr' = \int_S \left(\varphi_s \nabla^2 G - G \nabla^2 \varphi_s \right) dS \tag{B.1}$$

where S is a surface bounded by the contour ∂S as shown in Fig. B.1, and φ_s and G are functions that depend on the distance R from a certain fixed point P. If φ_s and G, along with their first and second derivatives, are continuous within S and on ∂S, and satisfy

$$\nabla^2 \Omega + k_0^2 \Omega = 0 \tag{B.2}$$

(with Ω being either φ_s or G), then Green's identity becomes:

$$\oint_{\partial S} \left(\varphi_s \frac{\partial G}{\partial n} - G \frac{\partial \varphi_s}{\partial n} \right) dr' = 0 \tag{B.3}$$

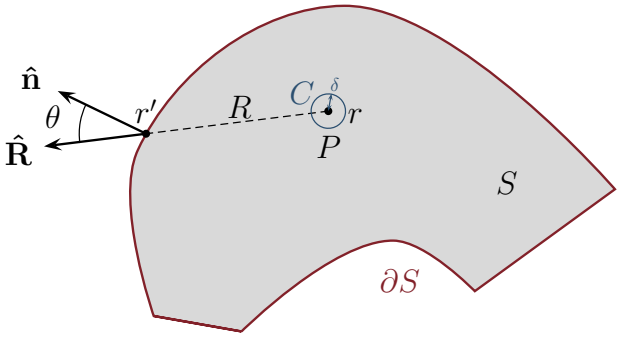

Figure B.1: Parameters used in the derivation of the integral equation.

provided that P and the singularities of φ_s and G lie outside of S.

The two-dimensional Green's function associated with the zero-order Bessel's equation (B.2) is the well known Hankel function:

$$G(k_0, R) = \frac{H_0^{(2)}(k_0 R)}{4j} \tag{B.4}$$

where $H_0^{(2)}$ is the zero-order Hankel function of the second kind. However, any proper combination of Bessel functions can also provide a valid Green's function for the two-dimensional problem. In general, we consider the function:

$$G(k_0, R) = C_0 J_0(k_0 R) + B_0 Y_0(k_0 R) \tag{B.5}$$

where J_0 is the Bessel function of the first kind and zero order, Y_0 is the Bessel function of the second kind and zero order. C_0 and B_0 are arbitrary constants. To determine one of them, the boundary condition at $R = 0$ is imposed. Both functions, (B.4) and (B.5), must have the same behavior around the origin [172]. Since the behavior of (B.4) is of the type $-\ln(R)/2\pi$ around $R = 0$, the constant B_0 is determined to be $B_0 = -1/4$ [135]. Consequently, the Green's function for the problem becomes:

$$G(k_0, R) = C_0 J_0(k_0 R) - \frac{1}{4} Y_0(k_0 R). \tag{B.6}$$

The problem does not have any other boundary conditions associated with $G(k_0, R)$. Consequently, the constant C_0 may take any value. In particular, the choice $C_0 = -j/4$ results into the classical two-dimensional Green's function of (B.4).

Regardless of the value of C_0, it is clear that if the point P lies within S, (B.3) will not hold since $Y_0(k_0 R)$ becomes singular at P and the surface integral of (B.1) does not vanish. To avoid this problem, we apply Green's identity (B.1) to the

surface S bounded externally by ∂S and internally by the circle C of center P and small radius δ:

$$\oint_{\partial S}\left[\varphi_s\frac{\partial G(k_0,R)}{\partial n}-G(k_0,R)\frac{\partial\varphi_s}{\partial n}\right]dr'=\oint_{C}\left[\varphi_s\frac{\partial G(k_0,R)}{\partial R}-G(k_0,R)\frac{\partial\varphi_s}{\partial R}\right]dr'. \tag{B.7}$$

Note that, on C, vectors $\hat{\mathbf{n}}$ and $\hat{\mathbf{R}}$ have opposite directions, thus the partial derivatives in the direction of both vectors have opposite signs. This explains the sign change in the right hand side of (B.7). Using the following small-argument approximations for G and its normal derivative:

$$G(k_0,R) \approx C_0-\frac{1}{2\pi}\left[\gamma+\ln\left(\frac{k_0}{2}\right)\right]-\frac{1}{2\pi}\ln(R) \tag{B.8a}$$

$$\frac{\partial G(k_0,R)}{\partial R} \approx \frac{-1}{2\pi R} \tag{B.8b}$$

where $\gamma=0.57721566490153286\ldots$ is the Euler-Mascheroni constant, the right-hand side of (B.7) becomes

$$\begin{aligned}\oint_{C}\left[\varphi_s\frac{\partial G(k_0,R)}{\partial R}-G(k_0,R)\frac{\partial\varphi_s}{\partial R}\right]dr' &= \int_0^{2\pi}\frac{-\varphi_s}{2\pi}d\theta+\frac{\delta\ln(\delta)}{2\pi}\int_0^{2\pi}\frac{\partial\varphi_s}{\partial R}d\theta\\ &\quad-\delta\left\{C_0-\frac{1}{2\pi}\left[\gamma+\ln\left(\frac{k_0}{2}\right)\right]\right\}\int_0^{2\pi}\frac{\partial\varphi_s}{\partial R}d\theta.\end{aligned} \tag{B.9}$$

Assuming that φ_s and its normal derivative do not change considerably in C, and taking the limit $\delta\to 0$, we have

$$\oint_{C}\left[\varphi_s\frac{\partial G(k_0,R)}{\partial R}-G(k_0,R)\frac{\partial\varphi_s}{\partial R}\right]dr'=-\varphi_s \tag{B.10}$$

This expression is the integral equation for the potential φ_s used in the field formulation for bi-dimensional cavities for points P within S (i.e. (2.92)):

$$\varphi_s(k,\mathbf{r})=\oint_{\partial S}\left[G(k_0,R)\frac{\partial\varphi_s(k,\mathbf{r}')}{\partial n}-\varphi_s(k,\mathbf{r}')\frac{\partial G(k_0,R)}{\partial n}\right]dr' \tag{B.11}$$

B.2 Integral Equation for points on the contour

Up until this point we have determined the integral equation that allows to compute the value of potential φ_s for points within S. What is left to determine is an equivalent equation valid for points P' located on the contour ∂S. It has been shown that from Green's theorem we can write:

$$\varphi_s(k,\mathbf{r})=\oint_{\partial S}\left[G(k_0,R)\frac{\partial\varphi_s(k,\mathbf{r}')}{\partial n}-\varphi_s(k,\mathbf{r}')\frac{\partial G(k_0,R)}{\partial n}\right]dr' \tag{B.12}$$

where $\mathbf{r} = \mathbf{r}(r)$ is the position of a certain point P within surface S located at a small distance δ from the contour ∂S (see Fig. B.2). Given that $R = \sqrt{r'^2 + \delta^2}$, $\cos\theta = \delta/R$ and assuming that $\delta << \alpha << k_0^{-1}$, we approximate the Green's function and its normal derivative by:

$$G(k_0, R) \approx C_0 - \frac{\gamma}{2\pi} - \frac{1}{2\pi} \ln \frac{k_0\sqrt{r'^2 + \delta^2}}{2} \tag{B.13a}$$

$$\frac{\partial G(k_0, R)}{\partial n} = \frac{\partial G(k_0, R)}{\partial R} \cos\theta \approx \frac{-\delta}{2\pi\,(r'^2 + \delta^2)}. \tag{B.13b}$$

Now, we take (B.12) and split the contour integral in two parts: one integral in the infinitesimal region between α and $-\alpha$, and another integral on the rest of the contour Γ.

$$\begin{aligned}\varphi_s(k, \mathbf{r}) = &\int_{-\alpha}^{\alpha} \left\{ \frac{\partial \varphi_s(k, \mathbf{r}')}{\partial\, n} \left[C_0 - \frac{\gamma}{2\pi} - \frac{1}{2\pi} \ln \frac{k_0\sqrt{r'^2 + \delta^2}}{2} \right] + \frac{\varphi_s(k, \mathbf{r}')\ \delta}{2\pi\,(r'^2 + \delta^2)} \right\} dr' \\ &+ \int_{\Gamma} \left[G(k_0,\, R) \frac{\partial \varphi_s(k, \mathbf{r}')}{\partial\, n} - \varphi_s(k, \mathbf{r}') \frac{\partial G(k_0,\, R)}{\partial n} \right] dr'. \end{aligned} \tag{B.14}$$

The potential φ_s and its normal derivative are considered to be constant between α and $-\alpha$. In addition, the remaining integrals are expressed as:

$$\int_{-\alpha}^{\alpha} \left(C_0 - \frac{\gamma}{2\pi} \right) dr' = \left(C_0 - \frac{\gamma}{2\pi} \right) 2\alpha \tag{B.15a}$$

$$\begin{aligned}\frac{1}{2\pi} \int_{-\alpha}^{\alpha} \ln \left(\frac{k_0\sqrt{r'^2 + \delta^2}}{2} \right) dr' = &\frac{1}{\pi} \left\{ \alpha \left[\ln \left(\frac{k_0\sqrt{\alpha^2 + \delta^2}}{2} \right) - 1 \right] \right. \\ &\left. - \frac{k\delta}{2} \left[\operatorname{arc\,csc} \left(\frac{\sqrt{\alpha^2 + \delta^2}}{\delta} \right) - \frac{\pi}{2} \right] \right\} \end{aligned} \tag{B.15b}$$

$$\frac{1}{2\pi} \int_{-\alpha}^{\alpha} \frac{\delta}{r'^2 + \delta^2} dr' = \frac{1}{\pi} \arctan \left(\frac{\alpha}{\delta} \right). \tag{B.15c}$$

Substituting (B.15) into (B.14) and making $\alpha \to 0$ and $\delta \to 0$ (so point P' coincides with P), the terms in (B.15a) and (B.15b) vanish, whereas (B.15c) tends to $1/2$. As a result, the integral equation for points P' on the contour ∂S becomes:

$$\varphi_s(k, \mathbf{r}) = 2 \oint_{\partial S} \left[G(k_0,\, R) \frac{\partial \varphi_s(k, \mathbf{r}')}{\partial\, n} - \varphi_s(k, \mathbf{r}') \frac{\partial G(k_0,\, R)}{\partial n} \right] dr'. \tag{B.16}$$

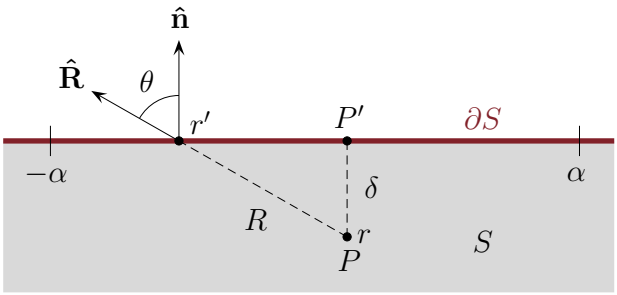

Figure B.2: Parameters used in the derivation of the integral equation on the contour.

Appendix C

Computation of singular integrals

C.1 Fields under LSE excitation

The process that leads to obtain α_{s1}^F and β_{s1}^F requires the numerical computation of certain integrals in order to fill the different matrices of the linear system of equations. Some of these integrals involve modified Bessel functions K_0 and K_1, which are singular for $R = 0$. Therefore, standard numerical integration techniques fail to provide an accurate value for the integral. In those cases, the limit as $R \to 0$ of the integrand will be computed analytically. The evaluation of the function at that point will be substituted by its limit. Depending on the type of segment (linear, circular or elliptical) where the integral is being performed, the limit value may change.

C.1.1 Singularity of $\mathbf{M}^F$

As we have shown, the expression of the position (i, j) of matrix $\mathbf{M}^F$ is:

$$M_{ij}^F = \frac{-1}{2h} \oint_{\partial S} \oint_{\partial S} \cos\theta \; K_1\left(\frac{\pi R}{h}\right) \; f_i(\mathbf{r}) \, f_j(\mathbf{r}') \; dr \; dr' \tag{C.1}$$

As $\mathbf{r} \to \mathbf{r}'$ (i.e. $R \to 0$), $K_1 \to \infty$, thus rendering the integration by numerical techniques impossible. In order to avoid this problem, the modified Bessel function will be grouped with the $\cos\theta$ term and the limit of this integrand I_M

$$I_M = \cos\theta \; K_1\left(\frac{\pi R}{h}\right) \tag{C.2}$$

will be computed analytically according to the segment type.

The term $\cos\theta$ can be related to $\mathbf{R}$ and $\hat{\mathbf{n}}$ (see Fig. 2.7) as:

$$\cos\theta = \frac{\mathbf{R}\cdot\hat{\mathbf{n}}}{R} \tag{C.3}$$

Near $R = 0$, we can approximate the modified Bessel function by the first term of its series expansion:

$$K_1\left(\frac{\pi R}{h}\right) \approx \frac{h}{\pi R} + O(R^2) \tag{C.4}$$

Combining (C.3) and (C.4), the limit as $R \to 0$ of the integrand is:

$$\lim_{R\to 0} \; I_M = \frac{h}{\pi} \lim_{R\to 0} \; \frac{\mathbf{R}\cdot\hat{\mathbf{n}}}{R^2} \tag{C.5}$$

Now, we proceed to evaluate this limit for the three type of segments that are considered for defining the contour ∂S. In order to do that, the segments will be parametrized according to a variable $u \in [-1/2, 1/2]$ as described in (2.116).

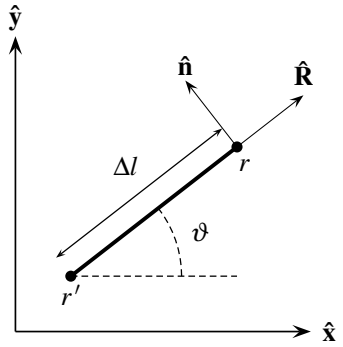

Figure C.1: Linear segment.

Linear segments

Figure C.1 shows the variables involved in the definition of a linear segment. As it is clear, when $\mathbf{r}$ and $\mathbf{r}'$ belong to the same linear segment, $\cos\theta = 0$ since $\mathbf{R} \perp \hat{\mathbf{n}}$. Therefore, for linear segments the limit of the integrand when $R \to 0$ is:

$$\lim_{R\to 0} \; I_M = 0 \tag{C.6}$$

Circular arcs

The parametrization of circular arcs (see Fig. C.2) is:

$$\begin{aligned} x &= x_0 + a\,\cos\phi(u) \\ y &= y_0 + a\,\sin\phi(u) \end{aligned} \tag{C.7}$$

with

$$\begin{aligned} \phi(u) &= \phi_1 + \Delta\phi\,(u + 0.5) \\ \Delta\phi &= \phi_2 - \phi_1 \end{aligned} \tag{C.8}$$

The length differential dr in this case is:

$$dr = a\,d\phi = a\,\Delta\phi\,du \tag{C.9}$$

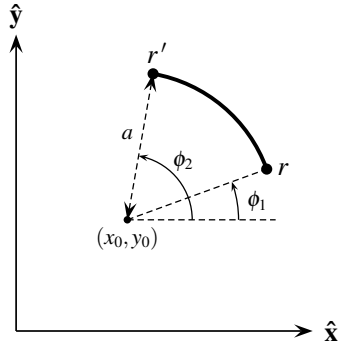

Figure C.2: Circular arc.

Vectors $\mathbf{R}$ and $\hat{\mathbf{n}}$ are:

$$\mathbf{R} = \mathbf{r}' - \mathbf{r} = a\,[(\cos\phi' - \cos\phi)\,\hat{\mathbf{x}} + (\sin\phi' - \sin\phi)\,\hat{\mathbf{y}}] \tag{C.10}$$

$$\hat{\mathbf{n}} = \cos\phi'\,\hat{\mathbf{x}} + \sin\phi'\,\hat{\mathbf{y}} \tag{C.11}$$

and the dot product between them is:

$$\mathbf{R}\cdot\hat{\mathbf{n}} = a\,[1 - \cos(\phi - \phi')] \tag{C.12}$$

where $\phi = \phi(u)$ and $\phi' = \phi(u')$. Finally, the expression for R^2 is:

$$R^2 = a^2\left[(\cos\phi' - \cos\phi)^2 + (\sin\phi' - \sin\phi)^2\right] \tag{C.13}$$

Therefore, the limit of the integrand as $R \to 0$ is:

$$\lim_{R\to 0}\ I_M = \frac{h}{\pi}\lim_{\phi\to\phi'}\ \frac{a\,[1 - \cos(\phi - \phi')]}{a^2\left[(\cos\phi - \cos\phi')^2 + (\sin\phi - \sin\phi')^2\right]} = \frac{h}{2\pi a} \tag{C.14}$$

obtained via the application of L'Hôpital's rule.

Elliptical arcs

The parametrization of elliptical arcs makes use of a local coordinate system (w, v) rotated an angle α with respect to the Cartesian coordinate system (see Fig. C.3). In this system, the elliptical arcs are described by:

$$\begin{aligned} w &= a_e \cos\eta(u) \\ v &= b_e \sin\eta(u) \end{aligned} \tag{C.15}$$

where

$$\begin{aligned} \eta(u) &= \eta_1 + \Delta\eta(u + 0.5) \\ \Delta\eta &= \eta_2 - \eta_1 \end{aligned} \tag{C.16}$$

To compact the notation, η and η' will be used from now on to represent $\eta(u)$ and $\eta(u')$, respectively. a_e y b_e are the major and minor semi-axis of the ellipse. This local coordinate system is related to the Cartesian one by:

$$\begin{pmatrix} x \\ y \end{pmatrix} = \begin{pmatrix} x_0 \\ y_0 \end{pmatrix} + \begin{pmatrix} \cos\alpha & -\sin\alpha \\ \sin\alpha & \cos\alpha \end{pmatrix} \cdot \begin{pmatrix} w \\ v \end{pmatrix} \tag{C.17}$$

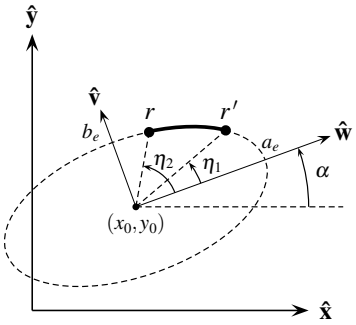

Figure C.3: Elliptical arc.

The length differential dr for these arcs is:

$$dr' = a_e \, \Delta\eta \sqrt{1 - e^2 \cos^2\eta'} \, du' \tag{C.18}$$

where e is the eccentricity of the ellipse, defined as:

$$e = \sqrt{1 - \frac{b_e^2}{a_e^2}} \tag{C.19}$$

The unitary normal vector $\hat{\mathbf{n}}$ and vector $\mathbf{R}$ take the following expressions:

$$\hat{\mathbf{n}} = \frac{-a_e \sin\alpha \sin\eta' + b_e \cos\alpha \cos\eta'}{a_e\sqrt{1-e^2\cos^2\eta'}}\,\hat{\mathbf{x}} + \frac{a_e \cos\alpha \sin\eta' + b_e \sin\alpha \cos\eta'}{a_e\sqrt{1-e^2\cos^2\eta'}}\,\hat{\mathbf{y}} \tag{C.20}$$

$$\begin{aligned}\mathbf{R} &= \left[a_e\cos\alpha\,(\cos\eta'-\cos\eta) - b_e\sin\alpha\,(\sin\eta'-\sin\eta)\right]\hat{\mathbf{x}} \\ &+ \left[a_e\sin\alpha\,(\cos\eta'-\cos\eta) + b_e\cos\alpha\,(\sin\eta'-\sin\eta)\right]\hat{\mathbf{y}}\end{aligned} \tag{C.21}$$

and the dot product between them is

$$\mathbf{R}\cdot\hat{\mathbf{n}} = \frac{b_e\left[1-\cos(\eta-\eta')\right]}{\sqrt{1-e^2\cos^2\eta'}} \tag{C.22}$$

The distance between source and field points is:

$$R^2 = a_e^2\left(\cos\eta'-\cos\eta\right)^2 + b_e^2\left(\sin\eta'-\sin\eta\right)^2 \tag{C.23}$$

Substituting (C.22) and (C.23) into (C.5), and after applying L'Hôpital's rule twice, the limit of I_M is finally expressed as:

$$\lim_{R\to 0} I_M = \frac{a_e\, b_e}{2\pi\sqrt{1-e^2\cos^2\eta'}\left(a_e^2\sin^2\eta' + b_e^2\cos^2\eta'\right)} \tag{C.24}$$

C.1.2 Singularity of $\mathbf{G}^F$

The second integral that requires some additional manipulations to avoid singularity problems is associated with the computation of $\mathbf{G}^F$. The expression of the i-th position of this vector is:

$$G_i^F = \frac{A_{1m}}{2\pi}\oint_{\partial S}\int_0^{d_p}\cos\left(\frac{m\pi}{d_p}t_p'\right)K_0\left(\frac{\pi\,R_p}{h}\right)\,f_i(\mathbf{r})\;dr\;dt_p' \tag{C.25}$$

When the length differential dr is taken over a segment that belongs to port p, the singularity may arise. The problem is due to the fact that

$$\lim_{R_p\to 0} K_0\left(\frac{\pi\,R_p}{h}\right) = +\infty \tag{C.26}$$

The procedure to overcome this problem involves separating the two line integrals. One of them (associated with dr) will be computed analytically, whereas the other one will be numerically integrated with classical quadrature techniques.

The modified Bessel function can be expanded in series at $R_p = 0$ as:

$$K_0\left(\frac{\pi\, R_p}{h}\right) \approx -\ln\left(\frac{\pi\, R_p}{h}\right) - \gamma + \ln(2) + R_p^2\, \frac{\pi^2}{4\, h^2}\left[-\ln\left(\frac{\pi\, R_p}{h}\right) - \gamma + 1 + \ln(2)\right] + R_p^4\, \frac{\pi^4}{128\, h^4}\left[-2\ln\left(\frac{\pi\, R_p}{h}\right) - 2\gamma + 3 + 2\ln(2)\right] + R_p^6\, \frac{\pi^6}{13824\, h^6}\left[-6\ln\left(\frac{\pi\, R_p}{h}\right) - 6\gamma + 11 + 6\ln(2)\right] + O\left[(\pi R_p/h)^8\right] \tag{C.27}$$

where $\gamma = 0.57721566490153286\ldots$ is the Euler-Mascheroni constant. The integral I_g intended to be solved analytically is:

$$I_g(t_p') = \int_{\Delta S} K_0\Big(\frac{\pi}{h}\, R_p\Big)\; f_i(\mathbf{r})\; dr = \int_{-0.5}^{0.5} K_0\Big(\frac{\pi}{h}\, R_p\Big)\; \big(c_1\, u^2 + c_2\, u + c_3\big)\, \Delta l\; du \tag{C.28}$$

where ΔS is a linear segment located on port p and $c_1,\ c_2,\ c_3$ are the coefficients of the parabolic basis function defined on ΔS. Making use of the series expansion of K_0 (and assuming that it is accurate in the segment) the integral I_g can be separated in a regular part I_g^r and a singular part I_g^s

$$I_g = I_g^r + I_g^s \tag{C.29}$$

where

$$I_g^r = \int_{-0.5}^{0.5} \Bigg\{ \ln(2) - \gamma - \ln(\pi/h) + R_p^2 \frac{\pi^2}{4\, h^2}\left[1 - \gamma + \ln 2 - \ln(\pi/h)\right] + R_p^4 \frac{\pi^4}{128\, h^4}\left[3 - 2\gamma + 2\ln 2 - \ln(\pi/h)\right] + R_p^6\, \frac{\pi^6}{13824\, h^6}\left[11 - 6\gamma - 6\ln 2 - \ln(\pi/h)\right] \Bigg\} \big(c_1\, u^2 + c_2\, u + c_3\big)\, \Delta l\; du \tag{C.30a}$$

$$I_g^s = \frac{-1}{2} \int_{-0.5}^{0.5} \ln R_p^2 \left(1 + \frac{R_p^2 \pi^2}{4\, h^2} + \frac{R_p^4 \pi^4}{128\, h^4} + \frac{R_p^6 \pi^6}{13824\, h^6}\right) \big(c_1\, u^2 + c_2\, u + c_3\big)\, \Delta l\; du \tag{C.30b}$$

The regular part I_g^r can be computed numerically. Regarding the singular part, it can be split into four different integrals and each one solved analytically:

$$I_g^s = \frac{-\Delta l}{2}\left(I_g^{s0} + I_g^{s2} + I_g^{s4} + I_g^{s6}\right) \tag{C.31}$$

Substituting $R_p = \Delta l^2 \left(t_p' - u\right)^2$ in (C.30b), the solution to I_g^{s0} can be expressed as:

$$
\begin{aligned}
I_g^{s0} &= \int_{-0.5}^{0.5} \ln\left[\Delta l^2 \left(t'_p - u\right)^2\right] \left[c_1\, u^2 + c_2\, u + c_3\right] du \\
&= \left\{ \frac{1}{12} \left[8\, c_1\, t'^3_p + 12\, c_2\, t'^2_p + 24\, c_3\, t'_p + c_1 - 3\,(c_2 - 4\, c_3)\right] \ln|2t_p + 1| \right. \\
&- \frac{1}{12} \left[8\, c_1\, t'^3_p + 12\, c_2\, t'^2_p + 24\, c_3\, t'_p - c_1 - 3\,(c_2 + 4\, c_3)\right] \ln|2t_p - 1| \\
&+ \left. \left(\frac{c_1}{6} + 2\, c_3\right) \ln\left|\frac{\Delta l}{2}\right| - \frac{1}{18} \left(12\, c_1\, t'^2_p + 18\, c_2\, t'_p + c_1 + 36\, c_3\right) \right\} \qquad \text{(C.32)}
\end{aligned}
$$

The second integral I_g^{s2}, involving the term R_p^2, is:

$$
\begin{aligned}
I_g^{s2} &= \frac{\pi^2 \Delta l^2}{4\, h^2} \int_{-0.5}^{0.5} \ln\left[\Delta l^2 \left(t'_p - u\right)^2\right] \left(t'_p - u\right)^2 \left[c_1\, u^2 + c_2\, u + c_3\right] du \\
&= \frac{\pi^2 \Delta l^2}{4\, h^2} \frac{1}{1800} \\
&\quad \left\{ (0.5 - t'_p)^3 \left[-112.5 c_2 - 400 c_3 - 175 c_2\, t'_p - 36 c_1 - 81\, c_1\, t'_p - 94\, c_1\, t'^2_p \right.\right. \\
&\quad + 2 \ln\left[\Delta l (0.5 - t'_p)\right] \left(90\, c_1 + 225 c_2 + 600 c_3 + 150 c_2\, t'_p + 90\, c_1\, t'_p + 60\, c_1\, t'^2_p\right)\Big] \\
&\quad + (0.5 + t'_p)^3 \left[112.5 c_2 - 400 c_3 - 175 c_2\, t'_p - 36\, c_1 + 81\, c_1\, t'_p - 94\, c_1\, t'^2_p \right. \\
&\quad \left.\left. + 2 \ln\left[\Delta l (0.5 + t'_p)\right] \left(90\, c_1 - 225 c_2 + 600 c_3 + 150 c_2\, t'_p - 90\, c_1\, t'_p + 60\, c_1\, t'^2_p\right)\right] \right\}
\end{aligned}
\qquad \text{(C.33)}
$$

Likewise, the integral involving the term R_p^4 is:

$$
\begin{aligned}
I_g^{s4} &= \frac{\pi^4 \Delta l^4}{128\, h^4} \int_{-0.5}^{0.5} \ln\left[\Delta l^2 \left(t'_p - u\right)^2\right] \left(t'_p - u\right)^4 \left[c_1\, u^2 + c_2\, u + c_3\right] du \\
&= \frac{\pi^4 \Delta l^4}{128\, h^4} \frac{1}{22050} \\
&\quad \left\{ (0.5 - t'_p)^5 \left[-612.5\, c_2 - 1764\, c_3 - 539\, c_2\, t'_p - 225\, c_1 - 325\, c_1\, t'_p \right.\right. \\
&- 214\, c_1\, t'^2_p + 2 \ln\left[\Delta l (0.5 - t'_p)\right] \left(1837.5\, c_2 + 4410\, c_3 + 735\, c_2\, t'_p + 787.5\, c_1\right. \\
&+ \left.\left. 525\, c_1\, t'_p + 210\, c_1\, t'^2_p\right)\Big] \\
&+ (0.5 + t'_p)^5 \left[612.5\, c_2 - 1764\, c_3 - 539\, c_2\, t'_p - 225\, c_1 + 325\, c_1\, t'_p - 214\, c_1\, t'^2_p \right. \\
&+ 2 \ln\left[\Delta l (0.5 + t'_p)\right] \left(-1837.5\, c_2 + 4410\, c_3 + 735\, c_2\, t'_p + 787.5\, c_1\right. \\
&- \left.\left. \left. 525\, c_1\, t'_p + 210\, c_1\, t'^2_p\right)\right] \right\}
\end{aligned}
\qquad \text{(C.34)}
$$

Finally, the integral involving the term R_p^6 is:

$$
\begin{aligned}
I_g^{s6} = & \frac{\pi^6 \Delta l^6}{13824\, h^6} \int_{-0.5}^{0.5} \ln\left[\Delta l^2 \left(t'_p - u\right)^2\right] \left(t'_p - u\right)^6 \left[c_1\, u^2 + c_2\, u + c_3\right] du \\
= & \frac{\pi^6 \Delta l^6}{13824\, h^6} \frac{1}{127008} \\
& \left\{(0.5 - t'_p)^7 \left[-1984.5\, c_2 - 5184\, c_3 - 1215\, c_2\, t'_p - 784\, c_1 - 833\, c_1\, t'_p - 382\, c_1\, t'^2_p \right.\right. \\
& + 2 \ln\left[\Delta l (0.5 - t'_p)\right] (7938\, c_2 + 18144\, c_3 + 2268\, c_2\, t'_p + 3528 c_1 \ + 1764 c_1\, t'_p \\
& \left. + 504\, c_1\, t'^2_p)\right] \\
& + (0.5 + t'_p)^7 \left[1984.5\, c_2 - 5184\, c_3 - 1215\, c_2\, t'_p - 784\, c_1 + 833\, c_1\, t'_p - 382\, c_1\, t'^2_p \right. \\
& + 2 \ln\left[\Delta l (0.5 + t'_p)\right] (-7938\, c_2 + 18144\, c_3 + 2268\, c_2\, t'_p + 3528 c_1 \ - 1764 c_1\, t'_p \\
& \left.\left. + \ 504\, c_1\, t'^2_p)\right]\right\}
\end{aligned}
\tag{C.35}
$$

C.1.3 Singularity of $\mathbf{N}^F$

The third singular integral is related to the computation of $\mathbf{N}^F$. The (i, j) position of this matrix is computed as:

$$
N_{ij}^F = \frac{1}{4\pi} \oint_{\partial S} \oint_{\partial S} R\, K_0\left(\frac{\pi\, R}{h}\right) \cos\theta\, f_i(\mathbf{r})\, f_j(\mathbf{r}')\, dr\, dr' \tag{C.36}
$$

As it will be shown, the limit when $R \to 0$ of the integrand has a finite value for the three types of segments. Therefore, the integral of matrix $\mathbf{N}^F$ can be solved numerically just by substituting the evaluation of the integrand in $R = 0$ by its limit. The expression of this limit is:

$$
I_N = \lim_{u \to u'} \left\{ \cos\theta(u, u')\, R(u, u')\, K_0\left[\frac{\pi\, R(u, u')}{h}\right] \right\} = \lim_{u \to u'} \left\{ \mathbf{R} \cdot \hat{\mathbf{n}}\ K_0\left[\frac{\pi\, R(u, u')}{h}\right] \right\} \tag{C.37}
$$

Substituting the first term of the expansion of the modified Bessel function shown in (C.27), the limit I_N becomes:

$$
I_N = \frac{-1}{2} \lim_{u \to u'} \mathbf{R} \cdot \hat{\mathbf{n}}\ \ln\left[R^2(u, u')\right] \tag{C.38}
$$

Now, this limit will be computed for each segment type.

Linear segments

For linear segments, $\mathbf{R}$ is always perpendicular to $\hat{\mathbf{n}}$, therefore the integrand I_N is null.

Circular arcs

As it was shown before for circular arcs while studying the singularity of matrix $\mathbf{M}^F$, the dot product of $\mathbf{R}$ and $\hat{\mathbf{n}}$ can be written as:

$$\mathbf{R}\cdot\hat{\mathbf{n}} = a\left[1-\cos\left(\phi-\phi'\right)\right] = a\left\{1-\cos\left[\Delta\phi\left(u-u'\right)\right]\right\} \tag{C.39}$$

Likewise, R^2 can be approximated by:

$$R^2 \approx a^2\Delta\phi^2\left(u-u'\right)^2 \tag{C.40}$$

thus, $\ln R^2$ can be written as the sum of two terms: one regular[1] and the other one singular:

$$\ln R^2 = \ln\left[\frac{(x-x')^2+(y-y')^2}{\Delta\phi^2\left(u-u'\right)^2}\right] + \ln\left[\Delta\phi^2(u-u')^2\right] \tag{C.41}$$

The regular term, once it is multiplied by $\mathbf{R}\cdot\hat{\mathbf{n}}$, becomes null. Substituting (C.39) and the singular term of (C.41) into (C.38), the limit becomes:

$$I_N = -a\lim_{u\to u'}\left\{1-\cos\left[\Delta\phi\left|u-u'\right|\right]\right\}\ln\left[\Delta\phi\left|u-u'\right|\right] \tag{C.42}$$

Since this limit takes an indeterminate form, L'Hôpital's rule is successively applied until the actual limit value is obtained. In this case, it is

$$I_N\big|_{\text{Circ.}} = -0.5\lim_{u\to u'}\mathbf{R}\cdot\hat{\mathbf{n}}\ \ln\left[R^2(u,u')\right] = 0 \tag{C.43}$$

Elliptical arcs

It was shown earlier that with the parametrization of elliptical arcs, the dot product of $\mathbf{R}$ and $\hat{\mathbf{n}}$ can be expressed as:

$$\mathbf{R}\cdot\hat{\mathbf{n}} = \frac{b_e\left[1-\cos\left(\eta-\eta'\right)\right]}{\sqrt{1-e^2\cos^2\eta'}} = \frac{b_e\left\{1-\cos\left[\Delta\eta\left(u-u'\right)\right]\right\}}{\sqrt{1-e^2\cos^2\eta'}} \tag{C.44}$$

As it was done for circular arcs, $\ln R^2$ can be expressed as the sum of two terms: a regular one[2] and a singular one:

$$\ln R^2 = \ln\left[\frac{(x-x')^2+(y-y')^2}{\Delta\eta^2\left(u-u'\right)^2}\right] + \ln\left[\Delta\eta^2(u-u')^2\right] \tag{C.45}$$

[1] As shown in [62], the limit of the regular part when $r\to r'$ is:

$$\lim_{(x,y)\to(x',y')}\ln\left[\frac{(x-x')^2+(y-y')^2}{\Delta\phi^2\left(u-u'\right)^2}\right] = \ln a^2$$

[2] As shown in [62], the limit of the regular part of $\ln R^2$ when $r\to r'$ is:

$$\lim_{(x,y)\to(x',y')}\ln\frac{(x-x')^2+(y-y')^2}{\Delta\eta^2\left(u-u'\right)^2} = \ln\left[a_e^2\sin^2\eta'+b_e^2\cos^2\eta'\right]$$

Likewise, the limit of the regular term multiplied by the dot product of $\mathbf{R}$ and $\hat{\mathbf{n}}$ becomes null. Therefore, only the singular part may contribute to the limit. It can be rewritten as:

$$I_N = \frac{2b_e}{\sqrt{1-e^2\cos^2\eta'}} \lim_{u\to u'} \{1-\cos\left[\Delta\eta\,(u-u')\right]\} \ln\left[\Delta\eta\,|u-u'|\right] \tag{C.46}$$

This expression is equivalent to (C.42), therefore, I_N for elliptical arcs is also:

$$I_N\big|_{\text{Ellip.}} = \frac{-1}{2} \lim_{u\to u'} \mathbf{R}\cdot\hat{\mathbf{n}}\ \ln\left[R^2(u,u')\right] = 0 \tag{C.47}$$

C.1.4 Singularity of $\mathbf{T}^F$

The last problematic integral is associated with the computation of $\mathbf{T}^F$:

$$T_i^F = \frac{A_{1m}h}{4\pi^2} \oint_{\partial S} \int_0^{d_p} \cos\left(\frac{m\pi}{d_p}t_p'\right) R_p\, K_1\!\left(\frac{\pi\, R_p}{h}\right)\, f_i(\mathbf{r})\ dr\, dt_p' \tag{C.48}$$

We can group the modified Bessel function $K_1(\pi R_p/h)$ with R_p and compute the limit when $R_p \to 0$:

$$I_T = \lim_{R_p\to 0} R_p\ K_1\!\left(\frac{\pi\, R_p}{h}\right) \tag{C.49}$$

Making use of the expansion of $K_1(\pi R_p/h)$ at $R_p = 0$ (C.4), the limit I_T simply becomes:

$$I_T = \lim_{R_p\to 0} R_p \frac{h}{\pi\, R_p} = \frac{h}{\pi} \tag{C.50}$$

C.2 Fields under LSM excitation

Four matrices ($\mathbf{M}^A$, $\mathbf{G}^A$, $\mathbf{N}^A$ y $\mathbf{T}^A$) involved in the computation of α_{s0}^A and β_{s0}^A contain singular integrands. In this section, the singular integrands are treated, once again, to allow the solution of the different integrals by classical quadrature techniques.

C.2.1 Singularity of $\mathbf{M}^A$

The (i,j) position of matrix $\mathbf{M}^A$ is computed as:

$$M_{ij}^A = \oint_{\partial S} \oint_{\partial S} f_i(\mathbf{r})\, f_j(\mathbf{r}')\, \ln R\ dr'\, dr \tag{C.51}$$

This double integral can be rewritten as:

$$M_{ij}^{A} = \oint_{\partial S} f_i(\mathbf{r}) I_M(\mathbf{r}) dr \tag{C.52}$$

where the integral involving the singularity is:

$$I_M(\mathbf{r}) = \frac{1}{2} \oint_{\partial S} f_j(\mathbf{r}') \, \ln R^2 \; dr' \tag{C.53}$$

This same integral was solved in [62] for linear, circular and elliptical segments. For completeness, only the final results are included here.

Linear segments

With the parametrization of linear segments, the integral I_M becomes:

$$I_M(u) = \frac{1}{2} \int_{-0.5}^{0.5} \ln \left[\Delta l^2 (u - u')^2 \right] (c_1 \, u'^2 + c_2 \, u' + c_3) \Delta l \; du' \tag{C.54}$$

The analytical solution of this integral is:

$$\begin{aligned} I_M^{\text{rect}}(u) = \frac{\Delta l}{2} \Bigg\{ & \frac{1}{12} \left[8c_1 u^3 + 12 c_2 u^2 + 24 c_3 u + c_1 - 3 \left(c_2 - 4 c_3 \right) \right] \ln |2u + 1| \\ & - \frac{1}{12} \left[8c_1 u^3 + 12 c_2 u^2 + 24 c_3 u - c_1 - 3 \left(c_2 + 4 c_3 \right) \right] \ln |2u - 1| \\ & + \left(\frac{c_1}{6} + 2 c_3 \right) \ln \left| \frac{\Delta l}{2} \right| - \frac{1}{18} \left(12 c_1 u^2 + 18 c_2 u + c_1 + 36 c_3 \right) \Bigg\} \end{aligned} \tag{C.55}$$

Circular arcs

For circular arcs, the integral I_M can be split into two parts:

$$\begin{aligned} I_M^{\text{circ}}(u) = I_{M-r}^{\text{circ}} + I_{M-s}^{\text{circ}} = & \frac{1}{2} \int_{-0.5}^{0.5} \ln \left[\frac{R^2}{\Delta \varphi^2 (u - u')^2} \right] (c_1 \, u'^2 + c_2 \, u' + c_3) a \Delta \varphi \; du' \\ & + \frac{1}{2} \int_{-0.5}^{0.5} \ln \left[\Delta \varphi^2 (u - u')^2 \right] (c_1 \, u'^2 + c_2 \, u' + c_3) a \Delta \varphi \; du' \end{aligned} \tag{C.56}$$

where I_{M-r}^{circ} is regular, since

$$\lim_{u' \to u} \ln \left[\frac{R^2}{\Delta \varphi^2 (u - u')^2} \right] = \ln a^2 \tag{C.57}$$

and I^{circ}_{M-s} is equivalent to (C.54), thus its solution is:

$$\begin{aligned} I^{\text{circ}}_{M-s}(u) = \frac{a\Delta\varphi}{2}\Bigg\{ & \frac{1}{12}\left[8c_2u^3+12c_2u^2+24c_3u+c_1-3\left(c_2-4c_3\right)\right]\ln|2u+1| \\ & -\frac{1}{12}\left[8c_2u^3+12c_2u^2+24c_3u-c_1-3\left(c_2+4c_3\right)\right]\ln|2u-1| \\ & +\left(\frac{c_1}{6}+2c_3\right)\ln\left|\frac{\Delta\varphi}{2}\right|-\frac{1}{18}\left(12c_2u^2+18c_2u+c_1+36c_3\right)\Bigg\} \end{aligned} \tag{C.58}$$

Elliptical arcs

Similarly, the integral I_M is also split into two parts when computed over elliptical arcs:

$$\begin{aligned} I^{\text{ellip}}_{M}(u) &= I^{\text{ellip}}_{M-r}+I^{\text{ellip}}_{M-s} \\ &= \frac{1}{2}\int_{-0.5}^{0.5}\ln\left[\frac{R^2}{\Delta\eta^2(u-u')^2}\right]\left(c_1\,u'^2+c_2\,u'+c_3\right)a_e\Delta\eta\sqrt{1-e^2\cos^2\eta'}\;du' \\ &+\frac{1}{2}\int_{-0.5}^{0.5}\ln\left[\Delta\eta^2(u-u')^2\right]\left(c_1\,u'^2+c_2\,u'+c_3\right)a_e\Delta\eta\sqrt{1-e^2\cos^2\eta'}\;du' \end{aligned} \tag{C.59}$$

where I^{ellip}_{M-r} is regular, since

$$\lim_{u'\to u}\ln\left[\frac{R^2}{\Delta\eta^2(u-u')^2}\right]=\ln\left(a_e^2\sin^2\eta+b_e^2\cos^2\eta\right) \tag{C.60}$$

However, I^{ellip}_{M-s} still requires a second subdivision:

$$\begin{aligned} I^{\text{ellip}}_{M-s}(u) &= I^{\text{ellip}}_{M-s-r}+I^{\text{ellip}}_{M-s-s} \\ &= \frac{a_e\,\Delta\eta}{2}\int_{-0.5}^{0.5}\ln\left[\Delta\eta^2(u-u')^2\right]\left(c_1\,u'^2+c_2\,u'+c_3\right)\gamma(u')\left(1-\frac{\gamma(u)}{\gamma(u')}\right)du' \\ &+\gamma(u)\,\frac{a_e\,\Delta\eta}{2}\int_{-0.5}^{0.5}\ln\left[\Delta\eta^2(u-u')^2\right]\left(c_1\,u'^2+c_2\,u'+c_3\right)\,du' \end{aligned} \tag{C.61}$$

where I^{ellip}_{M-s-r} is regular due to $\lim_{u'\to u}\left(1-\frac{\gamma(u)}{\gamma(u')}\right)=0$ and, even though the logarithmic term is singular, it is also well known that $\lim_{x\to 0}x^\alpha\ln x=0$ for any

$\alpha > 0$. Regarding I^{ellip}_{M-s-s}, it is equivalent to (C.54), therefore:

$$\begin{aligned} I^{\text{ellip}}_{M-s-s}(u) = & \frac{a_e\,\Delta\eta\,\gamma(u)}{2} \\ & \cdot \left\{ \frac{1}{12}\left[8c_1u^3 + 12c_2u^2 + 24c_3u + c_1 - 3\,(c_2 - 4c_3)\right] \ln|2u+1| \right. \\ & - \frac{1}{12}\left[8c_1u^3 + 12c_2u^2 + 24c_3u - c_1 - 3\,(c_2 + 4c_3)\right] \ln|2u-1| \\ & \left. + \left(\frac{c_1}{6} + 2c_3\right) \ln\left|\frac{\Delta\eta}{2}\right| - \frac{1}{18}\left(12c_1u^2 + 18c_2u + c_1 + 36c_3\right) \right\} \end{aligned} \tag{C.62}$$

C.2.2 Singularity of $\mathbf{G}^A$

The expression for the components of $\mathbf{G}^A$ is

$$G^A_i = \sqrt{\frac{2}{h\,d_p}} \oint_{\partial S} \int_0^{d_p} \sin\left[\frac{m\pi}{d_p} t'_p\right]\, I_G(\mathbf{r}, \mathbf{r}'_p)\, f_i(\mathbf{r})\; dr\; dt'_p \tag{C.63}$$

with $I_G(\mathbf{r}, \mathbf{r}'_p) = \cos\theta / R_p$. The singularity of the integrand occurs when dr and dt'_p are applied over the same segment of port p. Since the port is a linear segment, $\cos\theta = 0$, thus, the integrand I_G is always null over the port.

C.2.3 Singularity of $\mathbf{N}^A$

Matrix $\mathbf{N}^A$ is filled according to

$$N^A_{ij} = \oint_{\partial S} \oint_{\partial S} I_N(\mathbf{r}, \mathbf{r}') f_i(\mathbf{r})\, f_j(\mathbf{r}')\; dr\; dr' \tag{C.64}$$

where

$$I_N(\mathbf{r}, \mathbf{r}') = \frac{R^2}{4}\,(1 - \ln R) \tag{C.65}$$

As $R \to 0$, the limit of I_N is:

$$\lim_{R \to 0} I_N(\mathbf{r}, \mathbf{r}') = 0 \tag{C.66}$$

C.2.4 Singularity of $\mathbf{T}^A$

The expression of vector $\mathbf{T}^A$ is

$$T^A_i = \frac{-1}{4} \sqrt{\frac{2}{h\,d_p}} \oint_{\partial S} \int_0^{d_p} \sin\left[\frac{m\pi}{d_p} t'_p\right]\, I_T(\mathbf{r}, \mathbf{r}'_p)\, f_i(\mathbf{r})\, dt'_p dr \tag{C.67}$$

with $I_T(\mathbf{r}, \mathbf{r}'_p) = \cos\theta R_p\,(1 - 2\ln R_p)$. As it is the case with vector $\mathbf{G}^A$, the singularity of the integrand is located on the port. Since $\cos\theta = 0$ for linear segments, the integrand I_T is always null over the port.

Appendix D

Relationships between scalar potentials and current densities in the BI-RME method

This appendix is aimed at providing the TE and TM potentials on the lateral walls of arbitrarily-shaped waveguides according to the solution (current densities) generated by the BI-RME method. The electric field (not normalized) provided by the Boundary Integral - Resonant Mode Expansion (BI-RME) method is defined as:

$$\mathbf{E}(\mathbf{r}) = -j\eta k \oint_{\partial S} \bar{\mathbf{G}}_e(\mathbf{r}, \mathbf{r}') \cdot \mathbf{J}_\sigma(\mathbf{r}')\, dr' \tag{D.1}$$

where $\bar{\mathbf{G}}_e$ is the two-dimensional dyadic Green's function of the problem [26]. The current density $\mathbf{J}_\sigma$ can be split into a tangential ($J_t\,\hat{\mathbf{t}}$) and a longitudinal ($J_z\,\hat{\mathbf{z}}$) contribution (see Fig. D.1). Depending on the family of modes (TE or TM), the BI-RME method is able to provide one of these contributions as a series expansion of basis functions.

D.1 TE modes

As it is well known, on a Perfect Electric Conductor (PEC) the current density $\mathbf{J}_\sigma$ is directly related to the magnetic field $\mathbf{H}$ as:

$$\mathbf{J}_\sigma = \hat{\mathbf{n}} \times \mathbf{H} \tag{D.2}$$

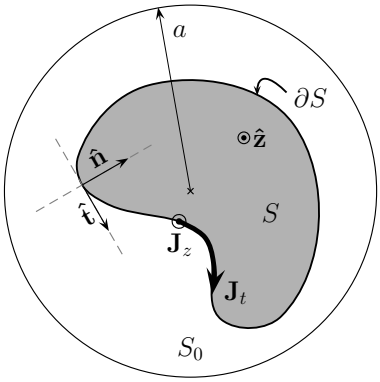

Figure D.1: Cross-section S of an arbitrarily-shaped waveguide located within a canonical circular waveguide of radius a for application of the BI-RME method.

where $\hat{\mathbf{n}}$ is the inward normal vector (see Fig. D.1). The magnetic field for TE modes has two components: one axial H_z and one tangential to the contour H_t. Therefore, the current density can be split in two parts:

$$\mathbf{J}_\sigma = \mathbf{J}_z + \mathbf{J}_t \tag{D.3a}$$

$$\mathbf{J}_z = J_z\hat{\mathbf{z}} = \hat{\mathbf{n}} \times \left(\mathbf{H} \cdot \hat{\mathbf{t}}\right) = -H_t\,\hat{\mathbf{z}} \tag{D.3b}$$

$$\mathbf{J}_t = J_t\hat{\mathbf{t}} = \hat{\mathbf{n}} \times (\mathbf{H} \cdot \hat{\mathbf{z}}) = H_z\,\hat{\mathbf{t}}. \tag{D.3c}$$

The BI-RME method is able to provide the tangential current density on the perturbed contour for each waveguide TE mode at its resonant frequency. The current density is expressed as a series of basis functions:

$$J_t(\mathbf{r}') = \sum_{\kappa=1}^{\mathcal{K}} B_\kappa^{\mathrm{TE}} f_\kappa(\mathbf{r}'). \tag{D.4}$$

where B_κ^{TE} are coefficients obtained after application of the BI-RME method.

On the one hand, this current generates a transverse electric field given by [26]:

$$\begin{aligned}\mathbf{E}_{\mathrm{T}}(\mathbf{r}) &= -j\eta\left[\frac{1}{k}\nabla_{\mathrm{T}}\oint_{\partial S} g(\mathbf{r},\mathbf{r}')\frac{\partial J_t}{\partial t}dr' + k\oint_{\partial S}\bar{\mathbf{G}}_{st}(\mathbf{r},\mathbf{r}')\cdot\hat{\mathbf{t}}\;J_t(\mathbf{r}')\,dr'\right.\\ &+ \left. k\sum_{m=1}^{M}\frac{a_m}{k_m^2}\,\mathbf{e}_m(\mathbf{r})\right]\end{aligned} \tag{D.5}$$

where g and $\bar{\mathbf{G}}_{st}$ are, respectively, the scalar and dyadic two-dimensional Green's function of the auxiliary canonical resonator used for the resonant mode expansion.

$\mathbf{e}_m$ is the electric modal vector for the m-th TE mode of this auxiliary resonator with cutoff wavenumber k_m. a_m are unknown expansion coefficients obtained after application of the method. The subindex T indicates the transverse-to-z components. At $k = \chi^{\mathrm{TE}}$ (the wavenumber at which the current density J_t and modal vectors are defined) this field does not correspond directly with the normalized electric modal vector in the S domain. The normalized electric $\mathbf{e}^{\mathrm{TE}}$ and magnetic modal $\mathbf{h}^{\mathrm{TE}}$ vectors can be derived from the scalar TE potential φ^{TE} employed in chapter 2 as [133]:

$$\mathbf{h}^{\mathrm{TE}} = \frac{-\nabla_{\mathrm{T}}\varphi^{\mathrm{TE}}}{\chi^{\mathrm{TE}}} \tag{D.6a}$$

$$\mathbf{e}^{\mathrm{TE}} = \frac{-\nabla_{\mathrm{T}}\varphi^{\mathrm{TE}} \times \hat{\mathbf{z}}}{\chi^{\mathrm{TE}}}. \tag{D.6b}$$

The scalar TE potential satisfies[1]

$$\int_S \left|\varphi^{\mathrm{TE}}\right|^2 dS = 1 \tag{D.7}$$

as previously determined in (2.42). Comparing (D.5) with Ec. (1) in [173], it is simple to determine that the normalized and unnormalized transverse components of the electric field are related as:

$$\mathbf{E}_{\mathrm{T}} = -j\eta\, \mathbf{e}^{\mathrm{TE}}. \tag{D.8}$$

On the other hand, the magnetic field can be expressed as the curl of the electric field, from Maxwell's equations. Therefore, the axial magnetic field is given by:

$$H_z = \frac{j}{k\eta}\nabla_{\mathrm{T}} \cdot \left(\mathbf{E}_{\mathrm{T}} \times \hat{\mathbf{z}}\right). \tag{D.9}$$

According to (D.3c), the axial magnetic field on the contour ∂S can be directly identified with the tangential current density $J_t = H_z$. Substituting (D.6b) and

[1] It is frequent to define the relationship between the magnetic modal vector and the scalar potential as:

$$\mathbf{h} = \hat{\mathbf{z}} \times \mathbf{e} = -\nabla_{\mathrm{T}}\varphi^{\mathrm{TE}}.$$

This implies that, if the modal vectors are normalized to the cross-section of the waveguide as

$$\int_S (\mathbf{e} \times \mathbf{h}) \cdot \hat{\mathbf{z}} dS = \int_S \mathbf{h} \cdot \mathbf{h} dS = \int_S \left|\nabla_{\mathrm{T}}\varphi^{\mathrm{TE}}\right|^2 dS = \left(\chi^{\mathrm{TE}}\right)^2 \int_S \left|\varphi^{\mathrm{TE}}\right|^2 dS = 1$$

the scalar potential must satisfy a normalization condition that is different from (D.7):

$$\int_S \left|\varphi^{\mathrm{TE}}\right|^2 dS = \frac{1}{(\chi^{\mathrm{TE}})^2}.$$

(D.8) into (D.9) and operating, the scalar TE potential on the contour is related to the tangential current density as:

$$\varphi^{\mathrm{TE}}\Big|_{\partial S} = -J_t. \tag{D.10}$$

D.2 TM modes

As in the TE case, the current density can be obtained from the magnetic field on the walls of a waveguide as:

$$\mathbf{J}_\sigma = \hat{\mathbf{n}} \times \mathbf{H} = \mathbf{J}_z \longrightarrow J_z = -H_t. \tag{D.11}$$

This current density generates an axial electric field E_z in the form [26]:

$$E_z(\mathbf{r}) = -j\eta k \left[\oint_{\partial S} g(\mathbf{r}, \mathbf{r}')\ J_z(\mathbf{r}')\, dr' + \sum_{m=1}^{m} \frac{a_m}{k_m^2} \psi_m(\mathbf{r}) \right]. \tag{D.12}$$

Comparing this expression with Ec. (3) in [173], the unnormalized electric field component evaluated at $k = \chi^{\mathrm{TM}}$ can be related to the scalar TM potential as:

$$E_z = -j\eta\, \varphi^{\mathrm{TM}}. \tag{D.13}$$

From the scalar TM potential, which fulfills the normalization condition expressed in (2.51), the normalized modal vectors are obtained:

$$\mathbf{e}^{\mathrm{TM}} = \frac{-\nabla_{\mathrm{T}} \varphi^{\mathrm{TM}}}{\chi^{\mathrm{TM}}} \tag{D.14a}$$

$$\mathbf{h}^{\mathrm{TM}} = \frac{\hat{\mathbf{z}} \times \left(-\nabla_{\mathrm{T}} \varphi^{\mathrm{TM}}\right)}{\chi^{\mathrm{TM}}}. \tag{D.14b}$$

From Maxwell's equations, and knowing that $\nabla \times \mathbf{E}_{\mathrm{T}} = 0$ (since the transverse electric field can be expressed as the gradient of the scalar TM potential), the tangential magnetic field can be expressed as:

$$-jk\eta H_t = (\nabla \times E_z\, \hat{\mathbf{z}}) \cdot \hat{\mathbf{t}} = \frac{\partial E_z}{\partial n} \tag{D.15}$$

Substituting (D.11) and (D.13) into (D.15) and evaluating at $k = \chi^{\mathrm{TM}}$, the relationship between the normal derivative of the scalar TM potential on the contour ∂S and the axial current density is given by:

$$\frac{\partial\, \varphi^{\mathrm{TM}}}{\partial n}\Big|_{\partial S} = -\chi^{\mathrm{TM}} J_z. \tag{D.16}$$

Appendix E

List of publications

E.1 Journal publications

- P. Soto, V. E. Boria, **C. Carceller**, C. Vicente, J. Gil, B. Gimeno, "EM based synthesis and design of bandpass waveguide filters including manufacturing effects with FEST3D", in *International Journal of RF and Microwave Computer-Aided Engineering*, vol. 22, no. 1, pp. 93-103, Jan. 2012.

- **C. Carceller**, S. Cogollos, P. Soto, J. Gil, V. E. Boria, C. Vicente, and B. Gimeno, "Efficient boundary integral-resonant mode expansion method implementation for full-wave analysis of passive devices based on circular waveguides with arbitrary perturbations," in *IET Microwave, Antennas and Propagation*, vol. 7, no. 1, pp. 44-53, Jan. 2013.

- S. Cogollos, **C. Carceller**, M. Taroncher, V. E. Boria, M. Guglielmi, C. Vicente, M. Brumos, "Correction of manufacturing deviations in waveguide filters and manifold multiplexers using metal insertions", in *International Journal of Microwave and Wireless Technologies*, vol. 7, no. 3-4, pp. 219-227, Jun. 2015.

- **C. Carceller**, P. Soto, V. E. Boria, M. Guglielmi, J. Gil, "Design of compact wideband manifold-coupled multiplexers", in *IEEE Transactions on Microwave Theory and Techniques*, vol. 63, no. 10, pp. 3398 - 3407, Sep. 2015.

- **C. Carceller**, P. Soto, V. E. Boria, M. Guglielmi, "Design of hybrid folded rectangular waveguide filters with transmission zeros below the passband", in *IEEE Transactions on Microwave Theory and Techniques*, vol. 64, no. 2, pp. 475-485, Feb. 2016.

E.2 Conference publications

- **C. Carceller**, M. Brumos, S. Cogollos, P. Soto, J. Gil, V. E. Boria, C. Vicente, B. Gimeno, "Análisis modal de componentes pasivos basados en guías circulares con contornos arbitrarios", in *XXVI Simposio Nacional de la Unión Científica Internacional de Radio*, Leganés, Spain, Sep. 2011, pp. 1-4.

- F. J. Pérez, **C. Carceller**, L. Roglá, S. Anza, T. Pinheiro, F. Quesada, J. Gil, C. Vicente. S. Sobrino, V. E. Boria, B. Gimeno, "High-power analysis in coaxial combline resonator filters", in *Proc. 7th ESTEC International Workshop on Multipactor, Corona and Passive Intermodulation in Space RF Hardware*, Valencia, Spain, Sep. 2011, pp. 1-8.

- **C. Carceller**, F. J. Pérez, J. Gil, C. Vicente, V. E. Boria, B. Gimeno, M. Guglielmi, "A commercial EM solver using the BI-RME method", in *IEEE International Conference on Numerical Electromagnetic Modeling and Optimization for RF, Microwave, and Terahertz Applications*, Pavia, Italy, May 2014, pp. 1-4.

- **C. Carceller**, J. Gil, C. Vicente, V. E. Boria, P. Soto, S. Anza, T. Pinheiro, B. Gimeno, "High-power analysis in H- and E-plane waveguide components", in *Proc. 8th ESTEC International Workshop on Multipactor, Corona and Passive Intermodulation in Space RF Hardware*, Valencia, Spain, Sep. 2014, pp. 1-8.

- M. Guglielmi, P. Soto, **C. Carceller**, V. E. Boria, D. Smacchia, M. Brumos, S. Cogollos, B. Gimeno, D. Raboso, "A novel Ku-band test bed for passive intermodulation measurements", in *Proc. 8th ESTEC International Workshop on Multipactor, Corona and Passive Intermodulation in Space RF Hardware*, Valencia, Spain, Sep. 2014, pp. 1-8.

- **C. Carceller**, P. Soto, V. E. Boria, M. Guglielmi, and D. Raboso, "New folded configuration of rectangular waveguide filters with asymmetrical transmission zeros," in *Proc. 44th European Microwave Conference*, Rome, Italy, Oct. 2014, pp. 183-186.

- P. Soto, **C. Carceller**, V. E. Boria, M. Guglielmi, D. Smacchia, B. Gimeno, J. Gil, C. Vicente and D. Raboso, "CAD of multiplexers for PIM measurement set-ups," in *Proc. 6th CNES/ESA International Workshop on Microwave Filters*, Toulouse, France, Mar. 2015, pp. 1-4.

- P. Soto, V. E. Boria, **C. Carceller**, S. Cogollos, M. Guglielmi, and D. Smacchia, "Practical design of rectangular waveguide filters with a capacitive

building block providing an extra transmission zero," in *IEEE MTT-S Int. Microwave Symp. Dig.*, Phoenix, AZ, May 2015, pp. 1-4.

- P. Soto, **C. Carceller**, V. E. Boria, M. Guglielmi, D. Smacchia, J. Gil, C. Vicente, B. Gimeno and D. Raboso, "CAD of multiplexers for PIM measurement set-ups," in *XXX Simposio Nacional de la Unión Científica Internacional de Radio*, Pamplona, Spain, Sep. 2015, pp. 1-4.

- **C. Carceller**, P. Soto, J. Gil, V. E. Boria, "Direct full-wave modeling of bidimensional structures combining E-plane and H-plane analysis techniques," in *IEEE MTT-S Int. Microwave Symp. Dig.*, San Francisco, CA, May 2016, pp. 1-4.

Bibliography

[1] M. Yu, A. Panariello, M. Ismail, and J. Zheng, "Passive 3-D simulators," *IEEE Microw. Mag.*, vol. 9, no. 6, pp. 50–61, Dec. 2008.

[2] S. B. Cohn, "Direct-coupled-resonator filters," *Proc. IRE*, vol. 45, no. 2, pp. 187–196, Feb. 1957.

[3] N. Marcuvitz, *Waveguide Handbook*. New York: McGraw-Hill, 1951.

[4] N. Marcuvitz and J. Schwinger, "On the representation of electric and magnetic fields produced by the currents and discontinuities in waveguides," *J. Appl. Phys.*, vol. 22, no. 6, pp. 806–819, Jun. 1951.

[5] G. Matthaei, E. M. T. Jones, and L. Young, *Microwave Filters, Impedance-Matching Networks, and Coupling Structures*. New York: McGraw-Hill, 1964.

[6] J. D. Rhodes, "The generalized direct-coupled cavity linear phase filter," *IEEE Trans. Microw. Theory Techn.*, vol. 18, no. 6, pp. 308–313, Jun. 1970.

[7] A. E. Atia and A. E. Williams, "New types of bandpass filters for satellite transponders," *COMSAT Tech. Rev.*, vol. 1, pp. 21–43, Fall 1971.

[8] ——, "Narrow-bandpass waveguide filters," *IEEE Trans. Microw. Theory Techn.*, vol. 20, no. 4, pp. 258–265, Apr. 1972.

[9] E. G. Cristal and G. L. Matthaei, "A technique for the design of multiplexers having contiguous channels," *IEEE Trans. Microw. Theory Techn.*, vol. 12, no. 1, pp. 88–93, Jan. 1964.

[10] M. H. Chen, F. Assal, and C. Mahle, "A contiguous band multiplexer," *COMSAT Tech. Rev.*, vol. 6, pp. 285–307, Fall 1976.

[11] C. Kudsia, R. Cameron, and W.-C. Tang, "Innovations in microwave filters and multiplexing networks for communications satellite systems," *IEEE Trans. Microw. Theory Techn.*, vol. 40, no. 6, pp. 1133–1149, Jun. 1992.

[12] J. W. Bandler, "Computer optimization of a stabilizing network for a tunnel-diode amplifier," *IEEE Trans. Microw. Theory Techn.*, vol. 16, no. 6, pp. 326–333, Jun. 1968.

[13] ——, "Optimization methods for computer-aided design," *IEEE Trans. Microw. Theory Techn.*, vol. 17, no. 8, pp. 533–552, Aug. 1969.

[14] J. B. Castillo and L. E. Davis, "Computer-aided design of three-port waveguide junction circulators," *IEEE Trans. Microw. Theory Techn.*, vol. 18, no. 1, pp. 25–34, Jan. 1970.

[15] A. E. Atia, "Computer-aided design of waveguide multiplexer," *IEEE Trans. Microw. Theory Techn.*, vol. 22, no. 3, pp. 332–336, Mar. 1974.

[16] S. Maas, "Circuit simulation in the dark ages," *IEEE Microw. Mag.*, vol. 13, no. 4, pp. 89–99, May 2012.

[17] D. G. Swanson and W. Hoefer, *Microwave Circuit Modeling Using Electromagnetic Field Simulation*. Norwood, MA: Artech House, 2003.

[18] A. Wexler, "Solution of waveguide discontinuities by modal analysis," *IEEE Trans. Microw. Theory Techn.*, vol. 15, no. 9, pp. 508–517, Sep. 1967.

[19] R. F. Harrington, *Field Computation by Moment Method*. New York: Macmillan, 1968.

[20] P. Silvester, "A general high-order finite-element waveguide analysis program," *IEEE Trans. Microw. Theory Techn.*, vol. 17, no. 4, pp. 204–210, Apr. 1969.

[21] K. Yee, "Numerical solution of initial boundary value problems involving Maxwell's equations in isotropic media," *IEEE Trans. Antennas Propag.*, vol. 14, no. 3, pp. 302–307, May 1966.

[22] P. B. Johns and R. L. Beurle, "Numerical solution of 2-dimensional scattering problems using a transmission-line matrix," *Proc. IEE*, vol. 118, no. 9, pp. 1203–1208, Sep. 1971.

[23] HFSS. Ansys Inc., Pittsburgh, PA, 2015.

[24] Sonnet. Sonnet Software, Syracuse, NY, 2015.

[25] H. Patzelt and F. Arndt, "Double-plane steps in rectangular waveguides and their application for transformers, irises, and filters," *IEEE Trans. Microw. Theory Techn.*, vol. 30, no. 5, pp. 771–776, May 1982.

[26] G. Conciauro, M. Bressan, and C. Zuffada, "Waveguide Modes Via an Integral Equation Leading to a Linear Matrix Eigenvalue Problem," *IEEE Trans. Microw. Theory Techn.*, vol. 32, no. 11, pp. 1495–1504, Nov. 1984.

[27] F. Arndt, B. Koch, H.-J. Orlok, and N. Schroder, "Field theory design of rectangular waveguide broad-wall metal-insert slot coulplers for millimeter-wave applications," *IEEE Trans. Microw. Theory Techn.*, vol. 33, no. 2, pp. 95–104, Feb. 1985.

[28] H.-W. Yao, K. A. Zaki, A. E. Atia, and R. Hershtig, "Full wave modeling of conducting posts in rectangular waveguides and its applications to slot coupled combline filters," *IEEE Trans. Microw. Theory Techn.*, vol. 43, no. 12, pp. 2824–2830, Dec. 1995.

[29] R. Beyer and F. Arndt, "Efficient modal analysis of waveguide filters including the orthogonal mode coupling elements by an MM/FE method," *IEEE Microw. Guided Wave Lett.*, vol. 5, no. 1, pp. 9–11, Jan. 1995.

[30] J. W. Bandler and S. H. Chen, "Circuit optimization: the state of the art," *IEEE Trans. Microw. Theory Techn.*, vol. 36, no. 2, pp. 424–443, Feb. 1988.

[31] F. Alessandri, M. Dionigi, and R. Sorrentino, "A fullwave CAD tool for waveguide components using a high speed direct optimizer," *IEEE Trans. Microw. Theory Techn.*, vol. 43, no. 9, pp. 2046–2052, Sep. 1995.

[32] F. Arndt, T. Sieverding, T. Wolf, and U. Papziner, "Optimization-oriented design of rectangular and circular waveguide components with the use of efficient mode-matching simulators in commercial circuit CAD tools," *Int. J. RF and Microwave CAE*, vol. 7, no. 1, pp. 37–51, Jan. 1997.

[33] Q. J. Zhang and K. C. Gupta, *Neural Networks for RF and Microwave Design*. Boston, MA: Artech House, 2000.

[34] Y. Rahmat-Samii and E. Michielssen, *Electromagnetic Optimization by Genetic Algorithms*. New York: John Wiley & Sons, Inc., 1999.

[35] J. W. Bandler, R. Biernacki, S. H. Chen, R. H. Hemmers, and K. Madsen, "Electromagnetic optimization exploiting aggressive space mapping," *IEEE Trans. Microw. Theory Techn.*, vol. 43, no. 12, pp. 2874–2882, Dec. 1995.

[36] CST Microwave Studio. CST, Darmstadt, Germany, 2015.

[37] FEST3D Full-wave Electromagnetic Simulation Tool v.6.8.6. Aurora Software and Testing, Valencia, Spain, 2015. [Online]. Available: http://www.fest3d.com

[38] μWave Wizard. Mician GmbH, Bremen, Germany, 2015.

[39] WASP-NET. MiG GmbH, Bremen, Germany, 2015.

[40] G. L. James, "Analysis and design of TE_{11}-to-HE_{11} corrugated cylindrical waveguide mode converters," *IEEE Trans. Microw. Theory Techn.*, vol. 29, no. 10, pp. 1059–1066, Oct. 1981.

[41] F. Alessandri, G. Bartolucci, and R. Sorrentino, "Admittance matrix formulation of waveguide discontinuity problems: computer aided design of branch guide directional couplers," *IEEE Trans. Microw. Theory Techn.*, vol. 36, no. 2, pp. 394–403, Feb. 1988.

[42] X.-P. Liang, K. A. Zaki, and A. E. Atia, "A rigorous three plane mode-matching technique for characterizing waveguide T-junctions, and its application in multiplexer design," *IEEE Trans. Microw. Theory Techn.*, vol. 39, no. 12, pp. 2138–2147, Dec. 1991.

[43] J. M. Rebollar, J. Esteban, and J. E. Page, "Fullwave analysis of three and four-port rectangular waveguide junctions," *IEEE Trans. Microw. Theory Techn.*, vol. 42, no. 2, pp. 256–263, Feb. 1994.

[44] D. B. Davidson, *Computational Electromagnetics for RF and Microwave Engineering*. Cambridge, UK: Cambridge University Press, 2010.

[45] J. P. Webb and S. Parihar, "Finite element analysis of H-plane rectangular waveguide problems," *IEE Microw. Antennas Propag.*, vol. 133, no. 2, pp. 91–94, 1986.

[46] M. Koshiba, M. Sato, and M. Suzuki, "Application of finite-element method to H-plane waveguide discontinuities," *Electron. Lett.*, vol. 18, no. 9, pp. 364–365, Feb. 1982.

[47] M. Koshiba and M. Suzuki, "Finite-element analysis of H-plane waveguide junction with arbitrarily shaped ferrite post," *IEEE Trans. Microw. Theory Techn.*, vol. 34, no. 1, pp. 103–109, Jan. 1986.

[48] J. Abdulnour and L. Marildon, "Boundary elements and analytic expansions applied to H-plane waveguide junctions," *IEEE Trans. Microw. Theory Techn.*, vol. 42, no. 6, pp. 1038–1045, Jun. 1994.

[49] W. Yong and D. Yaogen, "Boundary element analysis of H-plane rectangular waveguide discontinuities," in *Int. Conf. Micro. Mil. Wave Tech.*, Aug. 1998, pp. 1064–1067.

[50] W. K. Gwarek, "Analysis of arbitrarily-shaped two-dimensional microwave circuits by finite-difference time-domain method," *IEEE Trans. Microw. Theory Techn.*, vol. 36, no. 4, pp. 738–744, Apr. 1988.

[51] E. A. Navarro, V. Such, B. Gimeno, and J. L. Cruz, "Analysis of H-plane waveguide discontinuities with an improved finite-difference time domain algorithm," *IEE Microw. Antennas Propag.*, vol. 139, no. 2, pp. 183–185, Apr. 1992.

[52] R. Beyer and F. Arndt, "The generalized scattering matrix separation technique combined with the MM/FE method for the efficient modal analysis of a comprehensive class of 3D passive waveguide circuits," in *IEEE MTT-S Int. Microwave Symp. Dig.*, vol. 1, May 1995, pp. 277–280.

[53] F. Arndt, J. Brandt, V. Catina, J. Ritter, I. Rullhusen, J. Dauelsberg, U. Hilgefort, and W. Wessel, "Fast CAD and optimization of waveguide components and aperture antennas by hybrid MM/FE/MoM/FD methods — state-of-the-art and recent advances," *IEEE Trans. Microw. Theory Techn.*, vol. 52, no. 1, pp. 292–305, Jan. 2004.

[54] R. R. Mansour and R. H. Macphie, "An improved transmission matrix formulation of cascaded discontinuities and its application to E-plane circuits," *IEEE Trans. Microw. Theory Techn.*, vol. 34, no. 12, pp. 1490–1498, Dec. 1986.

[55] H.-W. Yao, A. E. Abdelmonem, J.-F. Liang, X.-P. Liang, K. A. Zaki, and A. Martin, "Wide-band waveguide and ridge waveguide T-junctions for diplexer applications," *IEEE Trans. Microw. Theory Techn.*, vol. 41, no. 12, pp. 2166–2173, Dec. 1993.

[56] J. M. Reiter and F. Arndt, "Rigorous analysis of arbitrarily shaped H- and E-plane discontinuities in rectangular waveguides by a full-wave boundary contour mode-matching method," *IEEE Trans. Microw. Theory Techn.*, vol. 43, no. 4, pp. 796–801, Apr. 1995.

[57] O. A. Peverini, G. Addamo, G. Virone, R. Tascone, and R. Orta, "A spectral-element method for the analysis of 2-D waveguide devices with sharp edges and irregular shapes," *IEEE Trans. Microw. Theory Techn.*, vol. 59, no. 7, pp. 1685–1695, Jul. 2011.

[58] P. Arcioni, M. Bressan, and G. Conciauro, "Generalized admittance matrix of arbitrary E-plane waveguide junctions by the BI-RME method," in *IEEE MTT-S Int. Microwave Symp. Dig.*, vol. 4, Jun. 1999, pp. 1699–1702.

[59] P. Arcioni, M. Bressan, G. Conciauro, and L. Perregrini, "Generalized Y-matrix of arbitrary H-plane waveguide junctions by the BI-RME method," in *IEEE MTT-S Int. Microwave Symp. Dig.*, vol. 1, Jun. 1997, pp. 211–214.

[60] T. Okoshi and T. Miyoshi, "The Planar Circuit - An Approach to Microwave Integrated Circuitry," *IEEE Trans. Microw. Theory Techn.*, vol. 20, no. 4, pp. 245–252, Apr. 1972.

[61] E. Anderson, Z. Bai, C. Bischof, S. Blackford, J. Demmel, J. Dongarra, J. Du Croz, A. Greenbaum, S. Hammarling, A. McKenney, and D. Sorensen, *LAPACK Users' Guide (Third ed.)*. Philadelphia, PA: Society for Industrial and Applied Mathematics, 1999.

[62] S. Cogollos, S. Marini, V. E. Boria, P. Soto, A. Vidal, H. Esteban, J. V. Morro, and B. Gimeno, "Efficient modal analysis of arbitrarily shaped waveguides composed of linear, circular, and elliptical arcs using the BI-RME method," *IEEE Trans. Microw. Theory Techn.*, vol. 51, no. 12, pp. 2378–2390, Dec. 2003.

[63] P. Arcioni, M. Bozzi, M. Bressan, G. Conciauro, and L. Perregrini, "Frequency/time-domain modelling of 3D waveguide structures by a BI-RME approach," *Int. J. Numer. Model.*, vol. 15, pp. 3–21, Jan. 2002.

[64] F. Mira, M. Bressan, G. Conciauro, B. G. Martinez, and V. E. Boria, "Fast S-domain modeling of rectangular waveguides with radially symmetric metal insets," *IEEE Trans. Microw. Theory Techn.*, vol. 53, no. 4, pp. 1294–1303, Apr. 2005.

[65] A. San Blas, F. Mira, V. E. Boria, B. Gimeno, M. Bressan, and P. Arcioni, "On the fast and rigorous analysis of compensated waveguide junctions using off-centered partial-height metallic posts," *IEEE Trans. Microw. Theory Techn.*, vol. 55, no. 1, pp. 168–175, Jan. 2007.

[66] J. Gil, A. San Blas, C. Vicente, B. Gimeno, M. Bressan, V. E. Boria, G. Conciauro, and M. Maestre, "Full-wave analysis and design of dielectric-loaded waveguide filters using a state-space integral-equation method," *IEEE Trans. Microw. Theory Techn.*, vol. 57, no. 1, pp. 109–120, Jan. 2009.

[67] G. Conciauro, P. Arcioni, M. Bressan, and L. Perregrini, "Wideband modeling of arbitrarily shaped H-plane waveguide components by the boundary integral-resonant mode expansion method," *IEEE Trans. Microw. Theory Techn.*, vol. 44, no. 7, pp. 1057–1066, Jul. 1996.

[68] P. Arcioni, M. Bressan, G. Conciauro, and L. Perregrini, "Wideband modeling of arbitrarily shaped E-plane waveguide components by the boundary

integral-resonant mode expansion method," *IEEE Trans. Microw. Theory Techn.*, vol. 44, no. 11, pp. 2083–2092, Nov. 1996.

[69] K. Kurokawa, "The expansions of electromagnetic fields in cavities," *IRE Trans. Microw. Theory Techn.*, vol. 6, no. 2, pp. 178 –187, Apr. 1958.

[70] P. Arcioni, M. Bressan, G. Conciauro, and L. Perregrini, "ANAPLAN-W on a Sun platform," ESA Contract 10966/94/NL/NB, Final Report, Mar. 1995.

[71] ——, "ANAPLAN-W: a CAD tool for E/H-plane waveguide circuits," *ESA - Preparing for the Future*, vol. 6, no. 1, pp. 12–13, Mar. 1996.

[72] A. D. MacDonald, *Microwave breakdown in gases.* New York: Wiley, 1996.

[73] C. Vicente, M. Mattes, D. Wolk, B. Mottet, H. L. Hartnagel, J. R. Mosig, and D. Raboso, "Multipactor breakdown prediction in rectangular waveguide based components," in *IEEE MTT-S Int. Microwave Symp. Dig.*, Jun. 2005, pp. 1–4.

[74] M. Yu, "Power-handling capability for RF filters," *IEEE Microw. Mag.*, vol. 8, no. 5, pp. 88–97, Oct. 2007.

[75] S. Anza, C. Vicente, J. Gil, M. Mattes, D. Wolk, U. Wochner, V. E. Boria, B. Gimeno, and D. Raboso, "Prediction of multipactor breakdown for multicarrier applications: The quasi-stationary method," *IEEE Trans. Microw. Theory Techn.*, vol. 60, no. 7, pp. 2093–2105, Jul. 2012.

[76] M. Guglielmi, G. Gheri, M. Calamia, and G. Pelosi, "Rigorous multimode network numerical representation of inductive step," *IEEE Trans. Microw. Theory Techn.*, vol. 42, no. 2, pp. 317–326, Feb. 1994.

[77] T. Rozzi, A. Morini, F. Ragusini, and M. Mongiardo, "Analytical solution and frequency extraction of iris problems in waveguide by separation of variables," *IEEE Trans. Microw. Theory Techn.*, vol. 45, no. 2, pp. 253–259, Feb. 1997.

[78] Y. Leviatan, P. G. Li, A. T. Adams, and J. Perini, "Single-post inductive obstacle in rectangular waveguide," *IEEE Trans. Microw. Theory Techn.*, vol. 31, no. 10, pp. 806–812, Oct. 1983.

[79] T. Rozzi, F. Moglie, A. Morini, W. Gulloch, and M. Politi, "Accurate full-band equivalent circuits of inductive posts in rectangular waveguide," *IEEE Trans. Microw. Theory Techn.*, vol. 40, no. 5, pp. 1000–1009, May 1992.

[80] C. Valagiannopoulos and N. Uzunoglu, "Rigorous analysis of a metallic circular post in a rectangular waveguide with step discontinuity of sidewalls," *IEEE Trans. Microw. Theory Techn.*, vol. 55, no. 8, pp. 1673–1684, Aug. 2007.

[81] R. Bunger and F. Arndt, "Moment-method analysis of arbitrary 3-D metallic N-port waveguide structures," *IEEE Trans. Microw. Theory Techn.*, vol. 48, no. 4, pp. 531–537, Apr. 2000.

[82] K. L. Wu, G. Y. Delisle, D. G. Fang, and M. Lecours, "Waveguide discontinuity analysis with a coupled finite-boundary element method," *IEEE Trans. Microw. Theory Techn.*, vol. 37, no. 6, pp. 993–998, Jun. 1989.

[83] F. Alessandri, M. Dionigi, and R. Sorrentino, "Rigorous analysis of compensated E-plane junctions in rectangular waveguide," in *IEEE MTT-S Int. Microwave Symp. Dig.*, vol. 2, May 1995, pp. 987–990.

[84] M. Mongiardo, A. Morini, and T. Rozzi, "Analysis and design of full-band matched waveguide bends," *IEEE Trans. Microw. Theory Techn.*, vol. 43, no. 12, pp. 2965–2971, Dec. 1995.

[85] A. A. San Blas, B. Gimeno, V. E. Boria, H. Esteban, S. Cogollos, and A. Coves, "A rigorous and efficient full-wave analysis of uniform bends in rectangular waveguide under arbitrary incidence," *IEEE Trans. Microw. Theory Techn.*, vol. 51, no. 2, pp. 397–405, Feb. 2003.

[86] H. J. Riblet, "An alternate derivation of Lewin's formula (letters)," *IEEE Trans. Microw. Theory Techn.*, vol. 25, no. 8, pp. 711–712, Aug. 1977.

[87] M. Cecchi, A. Morini, T. Rozzi, and L. Zappelli, "An efficient CAD for the design of enlarged waveguide feeds," in *Eur. Microwave Conf.*, vol. 1, Oct. 1998, pp. 701–706.

[88] L. Lewin, "Calculation of waveguide junction and diaphragm interactions," *IEEE Trans. Microw. Theory Techn.*, vol. 17, no. 10, pp. 785–788, Oct. 1969.

[89] T. Rozzi and M. Mongiardo, "E-plane steps in rectangular waveguide," *IEEE Trans. Microw. Theory Techn.*, vol. 39, no. 8, pp. 1279–1288, Aug. 1991.

[90] R. Levy, "Analysis of practical branch-guide directional couplers (correspondence)," *IEEE Trans. Microw. Theory Techn.*, vol. 17, no. 5, pp. 289–290, May 1969.

[91] T. Kawai, M. Kishihara, Y. Kokubo, and T. Ohta, "Cavity-type directional couplers with simple structure," in *IEEE MTT-S Int. Microwave Symp. Dig.*, vol. 2, Jun. 1997, pp. 413–416.

[92] M. E. Bialkowski, J. Bornemann, V. P. Waris, and P. W. Davis, "Simplified mode-matching techniques for the analysis of coaxial-cavity-coupled radial E-plane power dividers," *IEEE Trans. Microw. Theory Techn.*, vol. 43, no. 8, pp. 1875–1880, Aug. 1995.

[93] M. Kishihara, T. Kawai, Y. Kokubo, and I. Ohta, "Analysis and design of radial waveguide E-plane hybrids," in *Asia Pac. Microwave Conf.*, vol. 2, Nov. 1999, pp. 500–503.

[94] J. Dittloff, J. Bornemann, and F. Arndt, "Computer aided design of optimum E- or H-plane N-furcated waveguide power dividers," in *Eur. Microwave Conf.*, Sep. 1987, pp. 181–186.

[95] T. Shen, Y. Rong, K. A. Zaki, and T. Dolan, "Full-wave modeling of waveguide dividers with rounded corners and its applications in millimeter-wave diplexers," in *Eur. Microwave Conf.*, vol. 3, Oct. 1999, pp. 110–113.

[96] R. J. Cameron and M. Yu, "Design of manifold-coupled multiplexers," *IEEE Microw. Mag.*, vol. 8, no. 5, pp. 46–59, Oct. 2007.

[97] W. A. Edson and J. Wakabayashi, "Input manifolds for microwave channelizing filters," *IEEE Trans. Microw. Theory Techn.*, vol. 18, no. 5, pp. 270–276, May 1970.

[98] A. Morini, T. Rozzi, and M. Mongiardo, "Efficient CAD of wideband contiguous channel multiplexers," in *IEEE MTT-S Int. Microwave Symp. Dig.*, vol. 3, Jun. 1996, pp. 1651–1654.

[99] G. P. Kefalas, "Frequency diplexing with waveguide bifurcations," *IRE Trans. Microw. Theory Techn.*, vol. 10, no. 3, pp. 221–222, May 1962.

[100] B. Auld, "The synthesis of symmetrical waveguide circulators," *IRE Trans. Microw. Theory Techn.*, vol. 7, no. 2, pp. 238–246, Apr. 1959.

[101] A. Morini, T. Rozzi, and G. Venanzoni, "Analytical formulas for the design of orthomode transducers," in *Eur. Microwave Conf.*, vol. 1, Oct. 2004, pp. 273–276.

[102] J. Uher, J. Bornemann, and U. Rosenberg, *Waveguide components for antenna feed systems: theory and CAD.* Artech House, 1993.

[103] A. M. Bøifot, E. Lier, and T. Schaug-Pettersen, "Simple and broadband orthomode transducer (antenna feed)," *IEE Microw. Antennas Propag.*, vol. 137, no. 6, pp. 396–400, Dec. 1990.

[104] O. A. Peverini, R. Tascone, G. Virone, A. Olivieri, and R. Orta, "Orthomode transducer for millimeter-wave correlation receivers," *IEEE Trans. Microw. Theory Techn.*, vol. 54, no. 5, pp. 2042–2049, May 2006.

[105] A. Navarrini and R. Nesti, "Symmetric reverse-coupling waveguide orthomode transducer for the 3-mm band," *IEEE Trans. Microw. Theory Techn.*, vol. 57, no. 1, pp. 80–88, Jan. 2009.

[106] D. Henke and S. Claude, "Minimizing RF performance spikes in a cryogenic orthomode transducer (OMT)," *IEEE Trans. Microw. Theory Techn.*, vol. 62, no. 4, pp. 840–850, Apr. 2014.

[107] T. Sieverding and F. Arndt, "Field theoretical CAD of open or aperture matched T-junction coupled rectangular waveguide structures," *IEEE Trans. Microw. Theory Techn.*, vol. 40, no. 2, pp. 353–362, Feb. 1992.

[108] A. Morini, T. Rozzi, and M. Mongiardo, "Curved filters in rectangular waveguide," in *Eur. Microwave Conf.*, vol. 1, Sep. 1996, pp. 153–154.

[109] C. Vale, P. Meyer, and K. Palmer, "A design procedure for bandstop filters in waveguides supporting multiple propagating modes," *IEEE Trans. Microw. Theory Techn.*, vol. 48, no. 12, pp. 2496–2503, Dec. 2000.

[110] F. De Paolis, R. Goulouev, J. Zheng, and M. Yu, "CAD procedure for high-performance composite corrugated filters," *IEEE Trans. Microw. Theory Techn.*, vol. 61, no. 9, pp. 3216–3224, Sep. 2013.

[111] I. Arregui, F. Teberio, I. Arnedo, A. Lujambio, M. Chudzik, D. Benito, T. Lopetegi, R. Jost, F.-J. Gortz, J. Gil, C. Vicente, B. Gimeno, V. E. Boria, D. Raboso, and M. A. G. Laso, "High-power low-pass harmonic filters with higher-order TE_{n0} and non-TE_{n0} mode suppression: Design method and multipactor characterization," *IEEE Trans. Microw. Theory Techn.*, vol. 61, no. 12, pp. 4376–4386, Dec. 2013.

[112] C. Tang, "Nonuniform waveguide high-pass filters with extremely steep cutoff," *IEEE Trans. Microw. Theory Techn.*, vol. 12, no. 3, pp. 300–309, May 1964.

[113] J. R. Montejo-Garai, J. A. Ruiz-Cruz, J. M. Rebollar, and T. Estrada, "In-line pure E -plane waveguide band-stop filter with wide spurious-free response," *IEEE Microw. Wireless Compon. Lett.*, vol. 21, no. 4, pp. 209–211, Apr. 2011.

[114] J. D. Rhodes and R. J. Cameron, "General extracted pole synthesis technique with applications to low-loss TE_{011} mode filters," *IEEE Trans. Microw. Theory Techn.*, vol. 28, no. 9, pp. 1018–1028, Sep. 1980.

[115] A. E. Atia, A. E. Williams, and R. W. Newcomb, "Narrow-band multiple-coupled cavity synthesis," *IEEE Trans. Circuits Syst.*, vol. 21, no. 5, pp. 649–655, Sep. 1974.

[116] S. Amari and G. Macchiarella, "Synthesis of inline filters with arbitrarily placed attenuation poles by using nonresonating nodes," *IEEE Trans. Microw. Theory Techn.*, vol. 53, no. 10, pp. 3075–3081, Oct. 2005.

[117] S. Cogollos, R. J. Cameron, R. R. Mansour, M. Yu, and V. E. Boria, "Synthesis and design procedure for high performance waveguide filters based on nonresonating nodes," in *IEEE MTT-S Int. Microwave Symp. Dig.*, Jun. 2007, pp. 1297–1300.

[118] O. Glubokov and D. Budimir, "Extraction of generalized coupling coefficients for inline extracted pole filters with nonresonating nodes," *IEEE Trans. Microw. Theory Techn.*, vol. 59, no. 12, pp. 3023–3029, Dec. 2011.

[119] S. Amari, U. Rosenberg, and J. Bornemann, "Singlets, cascaded singlets, and the nonresonating node model for advanced modular design of elliptic filters," *IEEE Microw. Wireless Compon. Lett.*, vol. 14, no. 5, pp. 237–239, May 2004.

[120] R. Levy and P. Petre, "Design of CT and CQ filters using approximation and optimization," *IEEE Trans. Microw. Theory Techn.*, vol. 49, no. 12, pp. 2350–2356, Dec. 2001.

[121] G. Macchiarella, "Accurate synthesis of inline prototype filters using cascaded triplet and quadruplet sections," *IEEE Trans. Microw. Theory Techn.*, vol. 50, no. 7, pp. 1779–1783, Jul. 2002.

[122] M. Guglielmi, "Hybrid folded rectangular waveguide filter," ESA Patent WO 2 015 058 809 A1, 25 Oct. 2013.

[123] S. Amari and J. Bornemann, "Using frequency-dependent coupling to generate finite attenuation poles in direct-coupled resonator bandpass filters," *IEEE Microw. Guided Wave Lett.*, vol. 9, no. 10, pp. 404–406, Oct. 1999.

[124] L. Accatino, "Computer-aided design of a Ku-band antenna diplexer," in *Eur. Microwave Conf.*, Sep. 1993, pp. 544–546.

[125] K.-L. Wu and W. Meng, "A direct synthesis approach for microwave filters with a complex load and its application to direct diplexer design," *IEEE Trans. Microw. Theory Techn.*, vol. 55, no. 5, pp. 1010–1017, May 2007.

[126] U. Rosenberg, A. Bradt, M. Perelshtein, and P. Bourbonnais, "Extreme broadband waveguide diplexer design for high performance antenna feed systems," in *Eur. Microwave Conf.*, Sep. 2010, pp. 1249–1252.

[127] L. Accatino and M. Mongiardo, "Hybrid circuit-full-wave computer-aided design of a manifold multiplexers without tuning elements," *IEEE Trans. Microw. Theory Techn.*, vol. 50, no. 9, pp. 2044–2047, Sep. 2002.

[128] SPARK3D v.1.5.1. Aurora Software and Testing, Valencia, Spain, 2015. [Online]. Available: http://www.fest3d.com/spark3d.php

[129] K. Kurokawa, *An Introduction to the Theory of Microwave Circuits*. New York: Academic Press, 1969.

[130] J. V. Bladel, *Electromagnetic Fields*. Washington: Hemisphere, 1985.

[131] C. Balanis, *Advanced Engineering Electromagnetics*. New York: John Wiley & Sons., 1989.

[132] S. Ramo, J. R. Whinnery, and T. V. Duzer, *Fields and Waves in Communication Electronics*. New York: John Wiley & Sons., 1994.

[133] G. Conciauro, M. Guglielmi, and R. Sorrentino, *Advanced Modal Analysis — CAD Techniques for Waveguide Components and Filters*. Chichester, UK: John Wiley & Sons, 2000.

[134] H. M. Altschuler and L. Goldstone, "On network representations of certain obstacles in waveguide regions," *IRE Trans. Microw. Theory Techn.*, vol. 7, no. 2, pp. 213–221, Apr. 1959.

[135] Y. Ayasli, "Analysis of wide-band stripline circulators by integral equation technique," *IEEE Trans. Microw. Theory Techn.*, vol. 28, no. 3, pp. 200–209, Mar. 1980.

[136] C. Carceller, S. Cogollos, P. Soto, J. Gil, V. E. Boria, C. Vicente, and B. Gimeno, "Efficient boundary integral - resonant mode expansion method implementation for full-wave analysis of passive devices based on circular waveguides with arbitrary perturbations," *IET Microw. Antennas Propag.*, vol. 7, no. 1, pp. 44–53, Jan. 2013.

[137] P. Soto, V. E. Boria, C. Carceller, C. Vicente, J. Gil, and B. Gimeno, "EM-based synthesis and design of bandpass waveguide filters including manufacturing effects with FEST3D," *Int. J. RF and Microwave CAE*, vol. 22, no. 1, pp. 93–103, Jan. 2012.

[138] G. Gerini and M. Guglielmi, "Efficient integral equation formulations for admittance or impedance representation of planar waveguide junctions," in *IEEE MTT-S Int. Microwave Symp. Dig.*, vol. 3, Jun. 1998, pp. 1747–1750.

[139] V. E. Boria, S. Cogollos, H. Esteban, M. Guglielmi, and B. Gimeno, "Efficient analysis of a cubic junction of rectangular waveguides using the admittance-matrix representation," *IEE Microw. Antennas Propag.*, vol. 147, no. 6, pp. 417–422, Dec. 2000.

[140] M. S. Tong and P. Pramanick, "Personal computer-based direct synthesis of optimum rectangular waveguide E-, H-, and EH-plane transformers," *Int. J. RF and Microwave CAE*, vol. 7, no. 4, pp. 289–308, Jul. 1997.

[141] A. Navarrini and R. L. Plambeck, "A turnstile junction waveguide orthomode transducer," *IEEE Trans. Microw. Theory Techn.*, vol. 54, no. 1, pp. 272–277, Jan. 2006.

[142] J. R. M. Vaughan, "Multipactor," *IEEE Trans. Electron Devices*, vol. 35, no. 7, pp. 1172–1180, Jul. 1988.

[143] S. Anza, C. Vicente, D. Raboso, J. Gil, B. Gimeno, and V. E. Boria, "Enhanced prediction of multipaction breakdown in passive waveguide components including space charge effects," in *IEEE MTT-S Int. Microwave Symp. Dig.*, Jun. 2008, pp. 1095–1098.

[144] T. Pinheiro-Ortega, J. Monge, S. Marini, J. Sanz, E. Sorolla, M. Mattes, C. Vicente, J. Gil, V. E. Boria, and B. Gimeno, "Microwave corona breakdown prediction in arbitrarily-shaped waveguide based filters," *IEEE Microw. Wireless Compon. Lett.*, vol. 20, no. 4, pp. 214–216, Apr. 2010.

[145] R. Levy, "Compact waveguide bandstop filters for wide stopbands," in *IEEE MTT-S Int. Microwave Symp. Dig.*, Jun. 2009, pp. 1245–1248.

[146] J. Thomas, "Cross-coupling in coaxial cavity filters – a tutorial overview," *IEEE Trans. Microw. Theory Techn.*, vol. 51, no. 4, pp. 1368–1376, Apr. 2003.

[147] C. Carceller, P. Soto, V. E. Boria, M. Guglielmi, and D. Raboso, "New folded configuration of rectangular waveguide filters with asymmetrical transmission zeros," in *Eur. Microwave Conf.*, Oct. 2014, pp. 183–186.

[148] I. A. Eshrah, A. A. Kishk, A. B. Yakovlev, A. W. Glisson, and C. E. Smith, "Analysis of waveguide slot-based structures using wide-band equivalent-circuit model," *IEEE Trans. Microw. Theory Techn.*, vol. 52, no. 12, pp. 2691–2696, Dec. 2004.

[149] G. F. Craven and F. Skedd, *Evanescent Mode Microwave Components*. Norwood, MA: Artech House, 1987.

[150] S. Cogollos, P. Soto, M. Brumos, V. E. Boria, and M. Guglielmi, "Novel rectangular waveguide structures for advanced filter characteristics," in *IEEE MTT-S Int. Microwave Symp. Dig.*, Jun. 2014, pp. 1–4.

[151] P. Soto, V. E. Boria, C. Carceller, S. Cogollos, M. Guglielmi, and D. Smacchia, "Practical design of rectangular waveguide filters with a capacitive building block providing an extra transmission zero," in *IEEE MTT-S Int. Microwave Symp. Dig.*, May 2015, pp. 1–4.

[152] R. J. Cameron, C. M. Kudsia, and R. R. Mansour, *Microwave Filters for Communication Systems: Fundamentals, Design and Applications.* New Jersey: John Wiley & Sons, 2007.

[153] V. E. Boria, P. Soto, and S. Cogollos, "Distributed models for filter synthesis," *IEEE Microw. Mag.*, vol. 12, no. 6, pp. 87–100, Oct. 2011.

[154] S. Cogollos, M. Brumos, V. E. Boria, C. Vicente, J. Gil, B. Gimeno, and M. Guglielmi, "A systematic design procedure of classical dual-mode circular waveguide filters using an equivalent distributed model," *IEEE Trans. Microw. Theory Techn.*, vol. 60, no. 4, pp. 1006–1017, Apr. 2012.

[155] W. Menzel, F. Alessandri, A. Plattner, and J. Bornemann, "Planar integrated waveguide diplexer for low-loss millimeter-wave applications," in *Eur. Microwave Conf.*, vol. 2, Sep. 1997, pp. 676–680.

[156] S. Amari, J. Bornemann, and U. Rosenberg, "Pseudo-elliptic waveguide filters without cross coupling," in *Eur. Microwave Conf.*, Sep. 2001, pp. 1–4.

[157] J. D. Rhodes and R. Levy, "Design of general manifold multiplexers," *IEEE Trans. Microw. Theory Techn.*, vol. 27, no. 2, pp. 111–123, Feb. 1979.

[158] M. Guglielmi, "Simple CAD procedure for microwave filters and multiplexers," *IEEE Trans. Microw. Theory Techn.*, vol. 42, no. 7, pp. 1347–1352, Jul. 1994.

[159] R. R. Mansour, B. Jolley, V. Dokas, S. Ye, and F. Thomson, "Design of high power superconductive output multiplexers," in *IEEE MTT-S Int. Microwave Symp. Dig.*, vol. 3, Jun. 1996, pp. 1485–1488.

[160] M. Ismail, D. Smith, A. Panariello, Y. Wang, and M. Yu, "EM-based design of large-scale dielectric-resonator filters and multiplexers by space mapping," *IEEE Trans. Microw. Theory Techn.*, vol. 52, no. 1, pp. 386–392, Jan. 2004.

[161] J. R. Montejo-Garai, J. A. Ruiz-Cruz, and J. M. Rebollar, "Full-wave design of H-plane contiguous manifold output multiplexers using the fictitious reactive load concept," *IEEE Trans. Microw. Theory Techn.*, vol. 53, no. 8, pp. 2628–2632, Aug. 2005.

[162] Y. Wang, S. Li, and M. Yu, "Hybrid models for effective design and optimization of large-scale multiplexing networks," *IEEE Trans. Microw. Theory Techn.*, vol. 61, no. 5, pp. 1839–1849, May 2013.

[163] M. Brumos, S. Cogollos, M. Martinez, P. Soto, V. E. Boria, and M. Guglielmi, "Design of waveguide manifold multiplexers with dual-mode filters using distributed models," in *IEEE MTT-S Int. Microwave Symp. Dig.*, Jun. 2014, pp. 1–4.

[164] S. Cogollos, C. Carceller, M. Taroncher, V. E. Boria, M. Guglielmi, C. Vicente, and M. Brumos, "Correction of manufacturing deviations in waveguide filters and manifold multiplexers using metal insertions," *Int. J. Microw. Wireless Technol.*, vol. 7, no. 3-4, pp. 219–227, Jun. 2015.

[165] H. Hu and K.-L. Wu, "Coping with spurious effects in full-wave electromagnetic design of a wide-band waveguide multiplexer," in *IEEE MTT-S Int. Microwave Symp. Dig.*, Jun. 2012, pp. 1–3.

[166] M. Yu and Y. Wang, "Enhanced microwave multiplexing network," *IEEE Trans. Microw. Theory Techn.*, vol. 59, no. 2, pp. 270–277, Feb. 2011.

[167] A. Morini, T. Rozzi, M. Farina, and G. Venanzoni, "A new look at the practical design of compact diplexers," *IEEE Trans. Microw. Theory Techn.*, vol. 9, no. 54, pp. 3515–3520, Sep. 2006.

[168] A. Morini, T. Rozzi, and M. Morelli, "New formulae for the initial design in the optimization of T-junction manifold multiplexers," in *IEEE MTT-S Int. Microwave Symp. Dig.*, vol. 2, Jun. 1997, pp. 1025–1028.

[169] M. Morelli, I. Hunter, R. Parry, and V. Postoyalko, "Stopband performance improvement of rectangular waveguide filters using stepped-impedance resonators," *IEEE Trans. Microw. Theory Techn.*, vol. 50, no. 7, pp. 1657–1664, Jul. 2002.

[170] M. Guglielmi and G. Connor, "Chained function filters," *IEEE Microw. Guided Wave Lett.*, vol. 7, no. 12, pp. 390–392, Dec. 1997.

[171] T. Okoshi, *Planar Circuits For Microwaves and Lightwaves.* Berlin, Heidelberg: Springer-Verlag, 1985.

[172] B. B. Baker and E. T. Copson, *The Mathematical Theory of Huygens' Principle.* Oxford: Clarendon Press, 1939.

[173] P. Arcioni, "Fast evaluation of modal coupling coefficients of waveguide step discontinuities," *IEEE Microw. Guided Wave Lett.*, vol. 6, no. 6, pp. 232–234, Jun. 1996.